Heat Transfer Measurements and Optimization Studies Relevant to Louvered Fin Compact Heat Exchangers

Ryan A. Stephan

Thesis submitted to the Faculty of the Virginia Polytechnic
and State University in partial fulfillment of the requirements
for the degree of

Master of Science
in
Mechanical Engineering

Dr. Karen A. Thole, Chair
Dr. Clinton L. Dancey
Dr. Danesh K. Tafti

21 August 2002
Blacksburg, Virginia

Keywords: Louvered Fins, Compact Heat Exchangers, Optimization

Heat Transfer Measurements and Optimization
Studies Relevant to Louvered Fin Compact Heat Exchangers

Abstract

Ryan A. Stephan

A compact heat exchanger is a device used to transfer thermal energy between two or more fluids. The most extensive use of compact heat exchangers occurs in the commercial trucking industry. Most compact heat exchanger designs contain tubes carrying one fluid and external fins through which passes another fluid. To enhance the fin-side heat transfer in a compact heat exchanger, which is typically the air side of the heat exchanger, louvers are manufactured into the fins. Louvered fins initiate the growth of new boundary layers such that the average convective heat transfer coefficient is higher than that which would occur for a continuous fin. Approximately 85% of the total thermal resistance occurs on the air side of the heat exchanger. To design more space and weight efficient heat exchangers, it is imperative to gain a fundamental understanding of the mechanisms that serve to increase the heat transfer on the air side.

This thesis presents the heat transfer results of three scaled-up louvered fin geometries and compares these results to six additional models in which the louver angle, fin pitch and Reynolds number were varied. Two experiments were performed to determine the reference temperature used for the calculation of the heat transfer coefficients. The use of two reference temperatures allowed the effects of the flow field and thermal field to be separated. This thesis also presents details of an optimization study performed for a louvered fin array.

The results of the experimental study showed that the hot thermal wakes formed at the entrance louver have an adverse effect on the heat transfer of downstream louvers. Measuring the adiabatic wall temperature of the louvers in the array showed the effect of these thermal wakes. The experimental study showed that the optimal louver geometry was Reynolds number dependent. For the lower two Reynolds numbers of Re_{Lp} = 230 and 370, the F_p/L_p = 1.52, θ = 27° model was found to be the best performer, which does not agree with previous studies. For Re_{Lp} = 1016, the F_p/L_p = 0.91, θ = 39° model was shown to have optimal heat transfer performance, which is in agreement with a previous study performed by Chang and Wang (1996).

Acknowledgments

The writing of this document has been the most challenging undertaking of my life to date. I could not have completed this work without the support and help of many other people. I would first like to thank my contract monitors at Modine, Inc., Dr. Steve Memory, and Dr. Winston Zhang.

I would also like to thank my advisor, Dr. Karen Thole for sticking with me through this long process; you will never know how much I truly appreciate that. She has taught me the importance of hard work and, most importantly, patience. Much of what I have completed to this point is due to the lessons of professionalism and perseverance that she has taught me. This thesis has been a growing process for me as both a professional and a person.

I would like to thank my mom and dad for forcing me to go into the field of engineering when I didn't know what I wanted to do. I also want to thank my parents for supporting me throughout my entire life, both academically and personally. I would also like to thank my beautiful wife, Kim, for putting up with all the long hours; for that I am forever indebted to her.

Finally, I would like to thank all of the people at Virginia Tech that helped me. First, I would like to thank Drew and Andy for helping me with the completion of this work. I would also like to thank Wil for supporting the only team that is worse than Cleveland and keeping life in the laboratory loose. Lastly, I would like to thank Mike for being the only other person in the world that appreciates my taste in music. I wish all of you luck in the future.

Table of Contents

Nomenclature

A	Surface area of one side of a heated louver
A_{ff}	Minimum cross sectional free flow area
$A_{louvers}$	Sum of all the louver surface areas exposed to flow
A_{in}	Cross sectional area at inlet to test section
C	Constant value
C_p	Specific heat of air
D_h	Hydraulic Diameter of duct
F_p	Fin pitch
F_l	Fin length
G	Maximum mass velocity, $G = \dot{m} / A_{ff}$
h	Convective heat transfer coefficient
h_b	Convective heat transfer coefficient based on the bulk flow temperature, $h_b = q'' / (T_w - T_b)$
h_{aw}	Convective heat transfer coefficient based on the bulk flow temperature, $h_{aw} = q'' / (T_w - T_{aw})$
H_l	Vertical distance between louver surfaces measured normal to inlet flow, $H_l = F_p - t/\cos\theta$
i	Current in heating circuits
j	Colburn factor, $j = h*Pr^{2/3}/(G*C_p)$
j_b	Colburn factor based on the bulk flow temperature, $j_b = h_b*Pr^{2/3}/(G*C_p)$
j_{aw}	Colburn factor based on the adiabatic wall temperature, $j_{aw} = h_{aw}*Pr^{2/3}/(G*C_p)$
k	Thermal conductivity
L_p	Louver pitch, length of louver
L_H	Height of entrance louver
L	Streamwise length of entire louver array
$\dot{m}$	Mass flow rate through wind tunnel
n	Number of louver rows
Nu	Nusselt number, $Nu = h*L_p/k$
Nu_b	Nusselt number based on the bulk flow temperature, $Nu_b = h_b*L_p/k$

Nu_{aw}	Nusselt number based on the adiabatic wall temperature, $Nu_{aw} = h_{aw}*L_p/k$
Pr	Prandtl number
P	Pumping power required
Q	Heat dissipated by the louver array
q''	Louver surface heat flux
R	Electrical resistance of louver surface
R_{total}	Total thermal resistance of a heat exchanger
R_{air}	Thermal resistance on the air side of a heat exchanger
R_{fin}	Thermal resistance of the fin in a heat exchanger
R_{fluid}	Thermal resistance of fluid side of a heat exchanger
Re_{Lp}	Reynolds number based on the louver pitch, $Re_{Lp} = U_{in}*L_p/\nu$
Re_x	Reynolds number based on streamwise length on a flat plate, $Re_x = U_{in}*L_p/\nu$
t	Fin thickness
T_d	Tube depth
T_p	Tube pitch
T_w	Louver wall temperature with fully heated boundary condition
T_{ref}	Reference temperature used for heat transfer coefficient
T_{in}	Temperature at inlet to wind tunnel
T_b	Bulk flow temperature calculated at entrance to louver passage
T_{aw}	Louver wall temperature with adiabatic wall boundary condition
U_{in}	Fluid velocity at entrance to test section
V	Volume of louver array
w	Spanwise width of louver surfaces
x^*	Distance along streamwise direction of the louver surface
Greek	
θ	Louver angle
ν	Kinematic viscosity
Δp	Pressure drop through louver array
η	Non-dimensional adiabatic wall temperature, $\eta = (T_{aw} - T_{in})/(T_b - T_{in})$

List of Figures

List of Tables

Chapter 1

Introduction and Literature Review

Heat exchanger efficiency is critically important for the financially competitive commercial trucking industry. Heat exchangers are used as the radiators to remove the excess thermal energy from the truck's engine. Fuel is one of the leading operating costs and fuel economy is becoming even more important with the rising fuel prices. At a highway speed of 55 mph approximately one-half of the energy used by a truck is to overcome the aerodynamic drag (PACCAR, 2002). The vehicle's shape and frontal area influence the aerodynamic drag. One of the major limitations to the aerodynamic shape of a truck is the large grill frontal area required to allow enough flow to pass through the radiator for the engine to sufficiently cooled. Improvements to the heat exchanger efficiency will permit smaller radiator heat exchangers that can lead to a reduced frontal grill area and still provide the same cooling capacity leading to substantial fuel savings.

Compact heat exchangers with louvered rather than continuous fins on the airside, similar to that shown in Figure 1.1, are used extensively in the trucking industry because of their superior heat transfer performance. Louvered fins typically have a higher overall heat transfer as compared with continuous fins for uses in compact heat exchangers. Unlike continuous fins, louvered fins produce increased heat transfer because of the new start of the boundary layer formation on each louver surface.

In a typical louvered fin compact heat exchanger, there are three important aspects of heat transfer. The first is that of convection of heat from the fluid in the tube side to the walls of the tubes located in the heat exchanger. The heat is then conducted through the walls of the tube and along the fins. The heat is then removed from the heat exchanger by the fluid flowing through the louvered array by convection. The thermal circuit analogy for this energy transfer is shown schematically in Figure 1.2. Considering water as the fluid inside the tubes and air on the external side, as with most compact heat exchanger designs, over 85% of the total thermal resistance occurs on the airside of a heat exchanger. It is for this reason, that it is important to study the fundamental mechanisms of the convective heat transfer on the airside of louvered fin heat exchangers.

The primary goal of this study, therefore, was to understand the fundamental mechanisms affecting the heat transfer along the louvered surfaces in this complicated

flow and thermal field. The current study explores the local heat transfer characteristics of louvered fin arrays to determine how geometry and Reynolds numbers affect the heat transfer performance. The first chapter in this document will discuss previous studies involving compact heat exchangers as well as the goals of the current study.

1.1 Literature Review

The majority of the data currently available for compact heat exchangers focuses on the heat exchanger as an entire system. As such, these heat exchangers are characterized using the ε-NTU and LMTD methods. As previously mentioned, the current study focuses on the local heat transfer on louver surfaces. Although most of the published data is for full-scale heat exchanger tests, several papers have been published in which detailed studies relevant to a louver fin heat exchanger have been discussed. These papers are briefly described in the following section.

Beauvais (1965) performed flow field experiments on scaled-up louvered fin geometries and his data showed that flow entering a louvered fin array quickly becomes louver directed. The flow measurements of Beauvais were repeated by Davenport (1980) and Davenport showed that the degree to which the flow is louver directed was a strong function of the operating Reynolds number. The flow tended to remain more axially (duct) directed for low Reynolds numbers when compared with higher Reynolds numbers. The cause of this, he hypothesized, was because the boundary layers on the louvers were thicker for the slower inlet velocity. These thicker boundary layers deflected the flow from becoming louver directed in the array.

The exact manner in which air enters a louver array and becomes axially directed was shown in a detailed study performed by Springer and Thole (1998a, 1998b, 1999). The length required for the flow to become fully developed, was found to increase with increasing fin pitch. The flow required a longer streamwise distance to become fully louver directed with increasing fin pitch. Through their extensive study of the flow field in a louvered fin array, Springer and Thole (1998a) mapped the progression of velocity wakes that formed on upstream louvers (specifically the entrance louver). The velocity wakes were found to be stronger, narrower, and maintain form further downstream at high Reynolds numbers ($Re_{Lp} \approx 1000$).

The measurements performed by Springer and Thole (1998a, 1998b, 1999) were completed for the same louver geometries as those studied by Lyman (2000). The models studied by Lyman (2000) were compared with the three geometries studied in this thesis. Comparing the work between Springer and Thole (1999) with that completed by Lyman (2000) offers meaningful insight into the data obtained for the three models presented in this document. These and other flow field studies have concluded that, except for Reynolds numbers below $Re_{Lp} = 200$ or very large ratios of the fin pitch to louver pitch (F_p/L_p), most louver geometries that have been studied have indicated that the flow is strongly louver directed. It is for this reason, that much of the heat transfer data that pertains to louvered fin heat exchangers is in the form of inline and staggered parallel plate studies where the plates are oriented parallel to the flow.

One relevant study to the current work was performed by Zhang et al. (1997). They performed computational simulations of inline and staggered parallel plates that simulated infinite fin arrays. The predicted thermal and velocity profiles around the plates at various Reynolds numbers showed that the wakes from upstream louvers remained stronger and narrower as they progressed downstream at high Reynolds numbers when compared with those at low Reynolds numbers. The presence of these thermal and velocity wakes around the parallel plates was shown to have a significant effect on the heat transfer performance of downstream plates. Deviations from simple exponential decay, as would be expected for a flat plate solution, from the leading edge to the trailing edge of the plates at high Reynolds numbers were attributed to vortex contributions. The results indicated that effects of upstream plates in fully developed flow influence the convective heat transfer performance of downstream plates.

The effects of thermal wakes on heat transfer of downstream louvers in various arrangements of parallel plates were studied by Kurosaki et al. (1988). They used laser holographic interferometry to visualize the isothermal contours of the wakes off of the back of the plates. By using this technique, they were able to observe the manner in which the thermal wakes from upstream plates progressed downstream and interacted with the subsequent louvers. The thermal wake visualizations showed that increasing the Reynolds number caused the wake to narrow and maintain form further downstream, which agreed with the data of Springer and Thole (1998a) as well the predictions of

Zhang et al. (1997). Heat transfer measurements taken on the downstream plates indicated that direct interactions with thermal wakes had an adverse effect on the convective heat transfer of the plates. The explanation of this is that the local temperature field surrounding a particular downstream plate in a thermal wake is increased thereby decreasing the heat transfer on that surface. By simply shifting the plates to avoid the wakes of upstream plates, the heat transfer of the downstream louvers was increased due to the relatively cooler fluid surrounding the plates. Except at high operating Reynolds numbers, increasing the streamwise distance between aligned plates was shown to have a minimal effect on the heat transfer of the downstream plates. The reason for this is that because the thermal wakes at low Reynolds numbers are more diffuse and do not have as much of an effect on the heat transfer of downstream plates as compared with high Reynolds number flows. Increasing the streamwise distance between aligned plates had a minimal effect on the heat transfer of the downstream louver at high Reynolds numbers.

The importance of considering the thermal wake effects on louver heat transfer is most clearly described by the computational study performed by Zhang and Tafti (2001). In their results, they describe an inter-fin interference for highly louver directed flows and an intra-fin interference for duct directed flows. They found that the thermal wake effects could be expressed as a function of the flow efficiency and the fin pitch to louver pitch ratio. Most importantly, they state that neglecting thermal wake effects at low flow efficiencies (duct directed flows) can introduce errors as high as 100% in the heat transfer. Their results point to the necessity of heating both the louver of interest as well as the upstream and adjacent louvers when performing heat transfer studies in louvered fins.

Sparrow and Hajiloo (1980) studied the heat transfer performance of staggered plate arrays aligned parallel to the flow. During the study, they varied the Reynolds number and the plate thickness. Using naphthalene sublimation, the heat transfer characteristics of the plates were quantified. As the Reynolds number was increased for the plate geometries, the mass transfer (which is equivalent to the heat transfer) was increased. Using uncoated steel plates with the same thickness of the naphthalene coated plates at all locations other than the plate of interest, the heat transfer was observed to be

the same for all plate positions past the entrance plate. This finding showed that the flow fields surrounding the plates downstream of the entrance plate were similar for all of the plates. As discussed in the study performed by Zhang and Tafti (2001), it is critical that the thermal wakes from upstream louvers are included in any analysis. By not coating the upstream plates with naphthalene, Sparrow and Hajiloo (1980) neglected the effect of thermal wakes in their study.

Suga and Aoki (1991) showed the results of a numerical study on a two-dimensional heat exchanger geometry in which they attempted to determine the optimal geometry for heat exchanger performance. Suga and Aoki's study focused on the slower flow regime corresponding to Reynolds numbers between 64 and 450. They determined that the heat transfer of a louver was adversely affected if the louver was placed in a thermal wake formed from an upstream louver. For this reason, they concluded that the optimal geometry would be one in which the thermal wake of an upstream louver would pass directly between the smallest gap between downstream louvers. In this conclusion, Suga and Aoki assumed the flow through the array to be fully louver directed. Several geometries were studied with this concept in mind. In these studies, the louver angle and the ratio of the fin pitch to louver pitch were varied. To find the optimal geometry, Suga and Aoki correlated the released heat per unit volume to the amount of pumping power required. From the perspective of combined heat transfer and pressure drop, smaller louver angles were found to perform better and as such, the optimal geometry was determined to be the $F_p/L_p = 0.50$, $\theta = 20°$ model. The louver geometries studied in this thesis, as well as the research performed by Lyman (2000) and Springer (1998), were designed based on the results of Suga and Aoki (1991).

After studying the data from several earlier studies performed by Davenport (1983), Achaichaia and Cowell (1988), Webb and Jung (1992), and Rugh et al. (1992), Chang and Wang (1997) presented a prediction for the convective heat transfer performance of louvered fin heat exchangers from the data released from these studies. Several earlier studies developed heat transfer correlations for louvered fin heat exchangers, but they were not often very accurate according to Chang and Wang (1997). The correlation by Chang and Wang developed a more comprehensive predictor of the heat transfer performance by using a large amount of available data. The correlation was

valid for an operating Reynolds number range of $100 < Re_{Lp} < 3000$. The correlation predicted 89% of the louvered fin data within 15% and a mean deviation of 7.6%. Their final published correlation is as follows:

$$j = Re_{Lp}^{-0.49}\left(\frac{\theta}{90}\right)^{0.27}\left(\frac{F_p}{L_p}\right)^{-0.14}\left(\frac{F_l}{L_p}\right)^{-0.29}\left(\frac{T_d}{L_p}\right)^{-0.23}\left(\frac{L_l}{L_p}\right)^{0.68}\left(\frac{T_p}{L_p}\right)^{-0.28}\left(\frac{\delta_f}{L_p}\right)^{-0.05} \quad 1.1$$

In Equation 1.1, F_l refers to the fin length, T_d refers to the tube depth, L_l refers to the louver length, T_p refers to the tube pitch, and δ_f refers to the fin thickness. The other variables in Equation 1.1 represent the same parameters used in the current study. The remaining variables have the same meaning as in the current study. Only the first three terms of Equation 1.1 are relevant to the current study as the remaining terms describe heat exchanger dimensions that were not varied or simulated in the current experimental test facility. Of the nine louver geometries discussed in this thesis, the $F_p/L_p = 0.91$, $\theta = 39°$ model was predicted by the Chang and Wang correlation to result in the highest heat transfer performance.

In 1990, Sunden and Svantesson also derived a correlation for the average Colburn factor in a louvered array. The louvered fin geometry used in their study was identical to that being presented here. Sunden and Svantesson's proposed correlation for a corrugated louver array with a rectangular channel was as follows:

$$j = 3.67\,Re_{Lp}^{-.591}\left(\frac{\theta}{90}\right)^{0.239}\left(\frac{F_p}{L_p}\right)^{0.0206}\left(\frac{F_l}{L_p}\right)^{-0.285}\left(\frac{L_h}{L_p}\right)^{0.0671}\left(\frac{T_p}{L_p}\right)^{-0.243} \quad 2.1$$

In the previous equation, L_h is the louver height of the entrance louver and the other variables have the same meaning as Equation 1.1. As was the case for Equation 1.1, only the first three terms in Equation 2.1 were varied and simulated in the current study. It is also important to note that Sunden and Svantesson's correlation is valid for $100 < Re_{Lp} < 800$. The correlation presented by Sunden and Svantesson predicted that

the $F_p/L_p = 1.52$, $\theta = 39^o$ model, would perform the best of the geometries studied in this thesis.

Huihua and Xuesheng (1989) determined that the flow became fully developed after the fifth louver position based on their mass transfer experiments. Their results were obtained with only three fin rows in which only one louver was coated with naphthalene during a particular test. Only the effect of the flow field for a particular louver position could be determined without the effects of the local thermal field as a result of coating only one louver.

Given the large number of variables that must be considered when studying a louvered fin array (such as transition from duct directed to louver directed, thermal wake effects, flow field effects, Reynolds number effects, etc.) it is imperative to perform row-by-row analyses for louvered fins. There have only been three studies that have completed analyses on a row-to-row basis for louvered fin geometries. Huihua and Xuesheng (1989), Suga and Aoki (1991), and Zhang and Tafti (2001) performed these studies. The lack of studies performed on a row-by-row basis for louvered fin arrays indicates a need for the current work to be performed.

1.2 Objectives of the Current Study

As shown in the previous section, several relevant studies have been completed to characterize the fluid mechanics and heat transfer of geometries similar to those being presented by this study. While some of these studies focused on the local heat transfer of the individual louver surfaces, most did not. It is for this reason, that the current study was completed. The work presented in this document is an extension of the research performed by Lyman (2000). During his study, he focused on six louver geometries while the current study performed measurements for three additional louver geometries.

The first objective of the current research was to quantify the local heat transfer coefficients for three louver geometries. After obtaining these results, nine different louver geometries were compared in an effort to determine the best performing louver geometry. Another objective of the current study was to perform an optimization of the louvers with computational fluid dynamics and an optimization package. The purpose of

this optimization was to find the combination of louver angle and fin pitch to maximize the performance of a louvered fin heat exchanger.

The current document is divided into seven chapters. Chapter 2 describes in detail the experimental and computational methodologies used. Chapter 3 details the data analysis methods used to quantify the performance of the louver arrays, while chapter 4 presents the experimental heat transfer results for the $\theta = 20°$ louver models. The next chapter, Chapter 5, shows a comparison of the nine different louver models and discusses the effect of several geometrical parameters. Chapter 6 presents the set-up and results for the optimization study and Chapter 7 summarizes the results from the study and gives recommendations for future work.

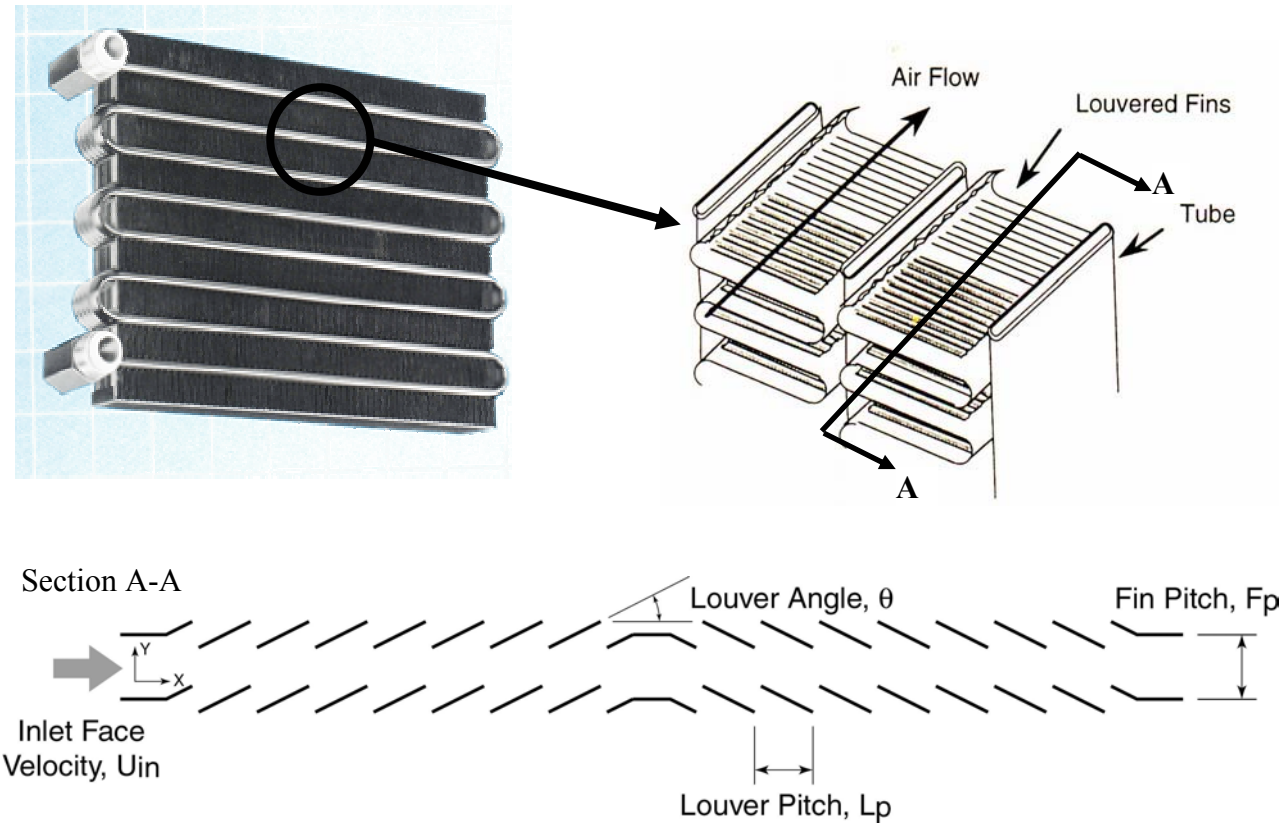

Figure 1.1 Typical geometry for a louvered fin heat exchanger used in the trucking industry as a truck radiator.

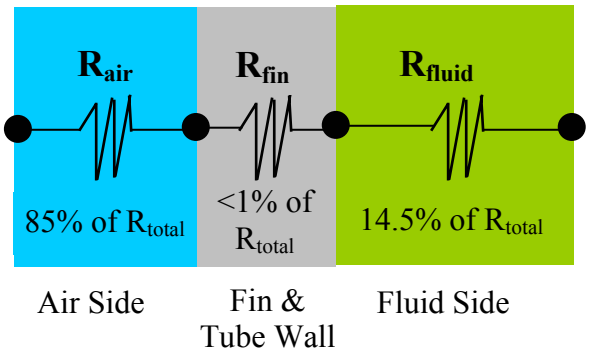

$$R_{total} = R_{air} + R_{fin} + R_{fluid}$$

$$R_{total} = \frac{1}{\eta_a h_a A_a} + \frac{b}{k_m A_m} + \frac{1}{h_w A_w}$$

$$R_{total} = \frac{1}{0.92 * 164.7 * 2.88} + \frac{1.00584 * 10^{-4}}{103.8 * 0.353} + \frac{1}{7381.3 * 0.348}$$

$$R_{total} = 0.23*10^{-2} + 2.74*10^{-6} + 3.89*10^{-4}\ [°C/W]$$

Figure 1.2 Distribution of the thermal resistance in a typical louvered fin compact heat exchanger (Beauvais, 1965)

Chapter 2
Experimental and Computational Methodologies

This chapter describes the experimental flow facility that was designed for this study as well as the computational methods that were used. To provide the spatial resolution needed for this in-depth study, scaled-up louver models were used with constant heat flux surfaces. Optimization studies were also performed for the scaled-up louvered fins using two commercial packages. Springer (1998) performed thorough flowfield measurements using louvers that were of the same scale used for the heat transfer measurements presented in this document. At the conclusion of Springer's study, Lyman (2000) performed heat transfer measurements on the same six louver geometries. The current study used the same test facility and measurement methods developed by Lyman but for three additional louver geometries.

The first section of this chapter describes the experimental facility as well as the geometry of the three primary louver models that were studied. The second section presents the instrumentation that was used to obtain the heat transfer data for this study. The following part details the benchmarking experiments that were performed with the louver array and the flow facility. Section 2.4 discusses the uncertainty analyses that were used for the experimental measurements. The next section describes the computational simulations that were used to support the experimental results obtained during this study. The sixth, and final, section of this chapter presents the optimization simulations that were performed on the louver geometries.

2.1 Description of Louver Models and Experimental Facility

The experimental design was made to insure that meaningful, spatially-resolved heat transfer coefficients could be made along several streamwise louver positions over a range of Reynolds numbers. To insure good measurement resolution, the louver models were scaled up by a factor of 20. The flow conditions were also scaled to match the relevant Reynolds numbers. The Reynolds number was based on the louver pitch (L_p) and the inlet velocity (U_{in}) and was defined as:

$$\mathrm{Re}_{Lp} = \frac{U_{in} L_p}{\nu}$$

Three separate Reynolds numbers were considered for this study by changing the inlet velocity and they corresponded to $Re_{Lp} = 230$, $Re_{Lp} = 370$, and $Re_{Lp} = 1016$.

A schematic of a sample louver array along with a detail drawing labeling the nomenclature used for louver arrays can be found in Figure 2.1. This document will primarily focus on three louver models, however comparisons will be made between these three models and six other models that were analyzed in a previous study performed by Lyman (2000). The geometric features of the nine models are listed in Table 2.1. The models with a louver angle of 20° are the models that are original to the current study, while the other six models (θ = 27° and 39°) were investigated by Lyman (2000). It should be noted from Table 2.1 that the louver pitch (L_P) and the louver thickness (t) are constant for all of the models while the fin pitch and the louver angle vary.

Figures 2.2 – 2.4 show the louver geometries for each of the models in Table 2.1. The geometry for the θ = 20° models can be found in Figure 2.2 a-c. The geometry for the θ = 27° and θ = 39° models can be found in Figure 2.3 a-c and Figure 2.4 a-c respectively. The aforementioned figures will be helpful when reviewing the heat transfer results presented in Chapter 4 as they show the relations between the louvers in the array.

A schematic of the open-loop test rig used for this study is shown in Figure 2.5. The test rig consisted of four sections: an inlet nozzle with a screen and honeycomb at the entrance, a louver test section, a laminar flow element, and a centrifugal fan.

The first section of the experimental facility consisted of the inlet nozzle. Three different inlet nozzle geometries were used for this study. Each of the inlet nozzles had the same 16:1 area reduction from the front of the nozzle to the entrance to the test section. The 16:1 area reduction allowed the velocity profile at the entrance to the louver array to be uniform. The nozzle geometry was designed using a commercially available computational fluid dynamics package called Fluent 5.0 (1998). The first and smallest inlet nozzle contracted from an area of 0.387m^2 to 0.024m^2. Nozzle two contracted from an area of 0.610 m^2 to 0.0381 m^2 while nozzle three contracted from 0.893 m^2 to 0.0558 m^2. The nozzle used for each model investigated during this study can be found in Table

2.1. As mentioned in the preceding paragraph, a honeycomb section was attached to the inlet of the contraction nozzle. This honeycomb coupled with a piece of window screen forced the flow at the inlet of the nozzle to be uniform. The velocity distribution at the inlet of the test section was proven to be uniform in the previous study done by Lyman (2000) using laser Doppler velocimeter measurements.

The next section of the test facility consisted of the louver test section containing the louver array. The louver test section was a two dimensional idealization of an actual heat exchanger. The width of the test section was 14.5 cm while the height depended on the fin pitch for the various models. The number of fin rows varied between models ranging from 9 rows for the largest fin pitch to 11 rows for the smallest fin pitch for the 20° models, which is shown in Table 2.1. The number of louvers in the streamwise direction remained 17 for all of the models tested. The test section was made using Lexan sheets with slots cut into either side. The louvers were held in place by the slots during the testing sequence. The slots were covered with tape and the side walls were thermally insulated using Styrofoam. The flowfield was observed by Springer and Thole to be very much louver directed for all of the models. For this reason, Styrofoam plates that matched the louver angle were used on the interior of the test section to create a periodic flow condition, which more accurately simulated an infinite stack of louver rows. The Styrofoam plates helped to reduce endwall effects associated with the top and bottom of the test section as well as minimize any conduction losses through the top and bottom of the test section.

The next section of the experimental facility was the laminar flow element (LFE), which was used to measure the flowrate of the air through the test section. The LFE was a Meriam 50MC2-2 model that was rated for a flowrate range up to 2.787 m^3/min with a corresponding pressure drop of 203.2 mmH_2O. During the testing process, the pressure drop was measured across the LFE using a Meriam 2110F digital manometer. Using a correlation provided by the manufacturer of the LFE, a flowrate was calculated.

The final part of the test rig was the centrifugal fan. A Dayton model 4C108 fan was used to draw the air through the test facility. As was shown in Figure 2.5, the fan was located at the exit of the test rig. The fan speed was controlled by a Dayton 3HX72 AC inverter, which allowed the speed of the fan to be controlled to a resolution of 0.01

Hz. All three of the studied Reynolds numbers were obtained by adjusting the speed of the fan using the AC inverter.

2.2 Louver Design and Instrumentation

A constant heat flux boundary condition was applied to all of the louvers upstream of the turning louver by using thin heating foils. These studies focused only on heat transfer measurements upstream of the turning louver. In addition, Springer and Thole (1998a) determined that the flowfield in the louver array was mirrored about the turning louver. A detailed drawing of the heated louver design can be seen in Figure 2.6. The heated louvers consisted of a low thermally conductive balsa wood core sandwiched between two sheets of file folder paper. The balsa wood was 1.58 mm thick and the file folder paper was 0.30 mm thick. Epoxied to each piece of file folder paper was a 0.038 mm thick stainless steel foil. Copper bus bars were soldered onto the ends of the heater foils to ensure a uniform current distribution and provide a location to attach the electrical lead wires.

The heat flux boundary conditions for $Re_{Lp} = 230$, $Re_{Lp} = 370$, and $Re_{Lp} = 1016$ were $q'' = 60$, 95, and 160 W/m^2, respectively. The heat flux values were chosen so that the temperature distribution across the louver surface would be the same for each of the Reynolds number. The resistive heating elements were connected in series to ensure a constant current through each louver. Because the surface area of the entrance louvers was 1.94 times larger than that of the downstream louvers, two separate circuits were needed. Each of the circuits were connected to a singular DC power supply. The circuit for the entrance louver was powered by a Wagner R24-6M power supply. The power supply used for louvers 2 through 8 was a Hewlett-Packard 6024. A separate precision resistor was connected in series with each of the louver circuits. Using a multimeter, the voltage drop across each resistor was measured and the current for each circuit was calculated by applying Ohm's law. A diagram of the electrical circuit used for the entrance louvers can be found in Figure 2.7. Figure 2.8 shows the electrical circuit for the remaining louvers (louvers 2-8). The heat flux boundary condition (q'') was determined by using the following relation:

$$q'' = \frac{i^2 R}{A}$$

In the preceding equation, i represents the current through the circuit, R is the electrical resistance of one side of the louver, and A is the surface area of that corresponding side.

Two boundary conditions were used for each louver position at each Reynolds number. These two boundary conditions consisted of a constant heat flux and an adiabatic wall condition on the louver surface. For the constant heat flux, the entire louver array was heated including the louver of interest. For the second boundary condition, the entire array was heated except for the particular louver of interest. The second boundary condition represented an adiabatic wall condition. For both of the boundary conditions, streamwise temperature distributions along the louver were recorded on both the front and back sides.

To adequately measure the streamwise temperature distributions along the louver, instrumented louvers were constructed. Two separate instrumented louvers were made for this study. The first of these louvers were used to measure the temperature distribution in the spanwise direction at a given streamwise position. The purpose of the spanwise instrumented louver was to insure thermal two-dimensionality within the flow facility. A schematic of the spanwise instrumented louver can be found in Figure 2.9. The spanwise louver had 12 thermocouples on each side. Six thermocouples were aligned in the spanwise direction and they were located at 40% of the louver pitch from the leading edge. Another six were located at 80% of the louver pitch from the leading edge.

The second instrumented louver was the streamwise instrumented louver and its primary purpose was to measure the temperature distribution in the streamwise direction. A detailed drawing of the instrumented streamwise louver can be found in Figure 2.10. As can be seen in Figure 2.10, 27 thermocouples were located on each side of the louver in the spanwise center of the test section. These thermocouples were located 1 mm apart in the streamwise direction beginning 1 mm from the leading of the louver. All of the thermocouples used for this study were type E. The thermocouples were accurately calibrated using an ice water bath. The thermocouples were imbedded into the balsa wood by cutting narrow grooves in the instrumented louvers and placing the

thermocouple wire in the grooves. High thermally conductive paste was used to minimize the thermal resistance between the thermocouple bead and the louver surface. The paste allowed for the temperature of the thermocouple bead to be as close as possible to that of the louver surface. A cross section of the streamwise instrumented louver can be found in Figure 2.11. Conduction corrections were made to the data to account for the temperature differences between the front and back side of the louvers. These corrections were minimal in most cases except near the leading edge of the louvers.

National Instruments data acquisition hardware was used to acquire thermocouple voltages and National Instruments LabVIEW hardware was used to process the voltages. The data acquisition system for the thermocouple measurements consisted of an SCXI-1000 chassis into which three SXCI-1102 modules were inserted. An SXCI-330 terminal block was inserted into each of the modules. The data acquisition card used was a National Instruments PCI-MIC-16XE-50.

2.3 Benchmarking of the Test Rig

This section of the chapter will present the benchmarking of the louver array and the flow facility. Lyman's (2000) earlier study focused on the benchmarking of the flowfield experiments. Therefore, the primary focus for the current work was the benchmarking of the heat transfer experiments including repeatability, periodicity, and insuring an energy balance.

Repeatability of the heat transfer results was performed several times during this study and all of these results agreed with the original data obtained by Lyman (2000) to within the uncertainty of the measurements. Figures 2.12 and 2.13 show a plot of the heat transfer coefficients taken on separate days in one of the louver models. The repeated data was obtained after the test facility was completely disassembled and then re-assembled. The time period between the two measurements was about four months. At least one of the louver positions were repeated for each of the models in this study and all of the repeated data agreed well with the original data.

Experiments were performed in order to be sure that the heat transfer results were periodic in the louver array. In order to accomplish this, temperature measurements were made at a vertically central louver position and then the instrumented louver was moved

up one position and the measurements were repeated. The two models that the tests were performed on was the $\theta = 39°$, $F_p/L_p = 1.22$ and the $\theta = 27°$, $F_p/L_p = 0.76$ model. Measurements were taken at louver 3 and 7 in the $\theta = 39°$ model, while louver 7 was focused on for the $\theta = 27°$ model.

The differences in the heat transfer coefficients for different vertical louver positions were not noticeable in either model for $Re_{Lp} = 1016$ as can be seen in Figures 2.14 and 2.15. The minimal differences between the heat transfer coefficients indicated acceptable periodicity between the vertically adjacent fin rows at $Re_{Lp} = 1016$. For the lower Reynolds number of $Re_{Lp} = 230$, the periodicity of the heat transfer results was quite good near the entrance louver. However, sensitivity to the vertical row developed as the flow moved further away from the entrance louver. The heat transfer coefficients for louver position 3 in the $\theta = 39°$, $F_p/L_p = 1.22$ model can be found in Figure 2.16. In studying this figure, it can be seen that neither h_{aw} or h_b changed by more than 3% when the instrumented louver was moved up two louver positions. This showed that the periodicity of louver 3 was acceptable for all of the test conditions. However, this was not the case for louver positions further downstream. Figures 2.17 and 2.18 show the heat transfer results at louver position 7 for the $\theta = 39°$, $F_p/L_p = 1.22$ and the $\theta = 27°$, $F_p/L_p = 0.76$ model, respectively. Figure 2.17 shows that the heat transfer coefficient based on the adiabatic wall temperature, h_{aw}, remained nearly constant when the instrumented louver was moved two rows up. The heat transfer coefficient based on the bulk temperature decreased by approximately 15% when the measurements were taken at a position two rows up. The same basic trends occurred for the $\theta = 27°$, $F_p/L_p = 0.76$ model as depicted in Figure 2.18. This figure shows that while h_{aw} essentially remained constant, h_b decreased by about 10% when the instrumented louver was moved up one position. The heat transfer coefficients were measured on the center row when possible noting there is a slight natural convection effect at the lower Reynolds numbers at the center position of the louver array.

As will be discussed in the following chapter, the heat transfer coefficient based on the adiabatic wall temperature, h_{aw}, shows effects of the flow field while the heat transfer coefficient based on the bulk temperature is indicative of the thermal field surrounding a louver. Because h_{aw} does not change when an instrumented louver is

moved up the changes in the heat transfer measurements are not due to changes in the surrounding flow field. The changes in the heat transfer coefficient can be attributed to differences in the surrounding thermal field. As the flow moves through the louver array, its temperature is increased by the energy being added to the fluid and buoyancy causes the less dense air to rise. The heat transfer based on the bulk temperature does not take into account the buoyancy of the flow. h_b is based on assuming a bulk temperature average at the entrance of each louver passage and it is not affected by the hot air rising while the coefficient's other parameter, the local wall temperature, is affected by the buoyancy of the flow. The heat transfer coefficient based on the adiabatic wall temperature does not change because both of its parameters, the adiabatic wall temperature and the wall temperature similarly increase.

In order to show that the thermal losses in the flow facility were minimal, an energy balance was performed on the flow facility. After performing the energy balance, the calculated temperatures were compared with the temperatures measured by a thermocouple located at the exit of the test section for all of the models tested. The maximum difference in the calculated exit temperature and the measured temperature was 10.7% and occurred at $Re_{Lp} = 230$. For $Re_{Lp} = 1016$, the maximum difference between the two values was 5%. The measured values were always the lower of the two, which can be explained by thermal losses in the test facility. This difference could also be attributed to the thermal and velocity gradients measured at the exit of the test section. LDV measurements were made at the exit of the louver array and the measurements showed a 6% velocity increase at the top of the section when compared to the bottom. The temperature of this high velocity flow was also found to be greater than the temperature of the slower moving flow at the bottom of the exit section. If a mass averaged technique was performed on the measured temperature values, the average would be increased. This increase in the measured temperature would contribute to the difference between the calculated values and the measured exit temperatures.

2.4 Experimental Uncertainty analysis

Kline and McClintock (1953) presented the method used in the current study to determine the uncertainties on the experimental measurements. The uncertainty results

discussed in this section took into account both the precision and bias uncertainties of the temperature measurements made during the research. The precision uncertainties in the measurements were based on a 95% confidence interval. The general equation presented by Kline and McClintock showing the magnitude of the uncertainty in R (u_R) is

$$u_R = \pm\left[\left(\frac{\partial R}{\partial x_1}u_{x1}\right)^2 + \left(\frac{\partial R}{\partial x_2}u_{x2}\right)^2 + \ldots\ldots + \left(\frac{\partial R}{\partial x_n}u_{xn}\right)^2\right]^{1/2} \tag{2.1}$$

where $R = R(x_1, x_2, \ldots, x_n)$ and x_n is the variables that affect the results of R.

The most dominating of the uncertainties in the experimental set-up was the temperature measurements along the louver surfaces. The combined precision and bias uncertainties of the individual temperature measurements was ±0.15 °C. Lyman (2000) determined the uncertainties of the temperature measurements by performing tests in a water bath. The tests showed that the thermocouple biases were channel dependent only. For this reason, a bias correction scheme was used. The voltage bias of the thermocouples was determined by comparing a voltage reading to a single reference thermocouple located at the entrance of the wind tunnel while the system was at room temperature before the heat transfer experiments.

The uncertainties in the Colburn factor based on the bulk flow temperature were typically highest at the leading edge of louver 2. At $Re_{Lp} = 230$, the uncertainty at the leading edge for j_b was calculated to be approximately 12.5%. The high uncertainty values were caused by the temperature difference between the surface and fluid being small. This uncertainty value quickly decreased to only 5.3% at the trailing edge of louver 2 with the average uncertainty on the louver surface being 6.8%. The uncertainty values for the Colburn factor based on the adiabatic wall temperature were lower. At the leading edge of louver 2, the uncertainty was 9.1% and that value decreased to 5.4% at the trailing edge with an average value along the louver surface of 6.3%. The uncertainties were much lower for $Re_{Lp} = 1016$. For example, the uncertainty in j_b at the leading edge was only 6.4% and decreased to 3.9% at the trailing edge of louver 2. The average uncertainty in j_b for this louver was 4.3%. The uncertainties in j_{aw} for the same louver were very similar to the j_b uncertainties with an average of 4.5%.

The uncertainties for the non-dimensional adiabatic wall temperature were higher than those calculated for the Colburn factors. The highest uncertainty occurred for louver 2 where the η values were relatively low ($0.4 < \eta < 0.5$). These high uncertainty values are due to the fact that the adiabatic wall temperature measurements were on the order of the ±0.15°C uncertainty in the temperature measurements. The uncertainties for these values were 17.5% at the leading edge and decreased to 10.5% at the trailing edge for $Re_{Lp} = 230$. For the higher η values corresponding to $0.8 < \eta < 1.0$, the uncertainties are much lower. For example, on louver 3, the uncertainty at the leading edge is only 6.9% and it decreases to a value of 6.0%. Unfortunately, the uncertainty values for louver 2 at $Re_{Lp} = 1016$ are higher than those calculated for the $Re_{Lp} = 230$. Again, the cause of this is because the duct directed flow that impacts the surface of the louver is very close to that measured at the inlet to the test facility. At this location, the η values are only measured to be approximately 0.2 and the corresponding uncertainties are upwards of 56% and decrease to value of 28.8% at the trailing edge. A summary of the uncertainty values for the $F_p/L_p = 0.91$, $\theta = 20°$ model can be found in Table 2.2.

2.5 Description of the Computational Simulations

Computational fluid dynamics (CFD) was used in this study to perform an optimization on the louver geometry using a commercially available CFD code in parallel with optimization software. Lyman (2000) benchmarked the CFD methodology used for the current study. In his study, he showed that two-dimensional CFD techniques accurately predicted heat transfer coefficients on all of the louver surfaces.

The two-dimensional Navier-Stokes equations were solved using the commercially available Fluent 5.0 (1998). The CFD predictions were obtained by solving the mass, momentum, and energy equations using second order discretization on an SGI Origin 2000 using parallel processors. The flow was assumed to be two-dimensional, laminar, and steady. The computational models consisted of a single fin row with 17 streamwise louvers including one entrance louver, one exit louver, and one flow reversal (turning) louver. The model was built and meshed in the pre-processor program Gambit, which is a mesh generation program packaged with Fluent. To computationally simulate an infinite stack of louvers, periodic boundary conditions were

used. A constant velocity was applied at three louver pitches upstream of the entrance louver while an outflow boundary condition was applied at seven louver pitches downstream of the exit louver. To simulate the experimental set-up, a constant heat flux was assigned to the front and back side of each louver in the array. The value of the heat flux was set to match the different heat flux values for each Reynolds number as stated for the experiments.

The mesh for the model consisted of a triangular grid for the majority of the louver passage with a quadrilateral grid placed along the surface boundaries of the louvers. Figure 2.19 shows the quadrilateral mesh around the louvers. The detailed quadrilateral mesh around the louver consisted of ten rows and was used to provide smoother temperature measurements than those that would be obtained with a triangular mesh. The grid-independent mesh, which was verified through a number of grid studies, consisted of approximately 505,000 cells.

In order to expedite the solving process, 800 iterations were run solving the momentum equations then the energy was turned on and allowed to converge. This process usually took approximately 1100 iterations to ensure acceptable convergence. Acceptable convergence occurred when the momentum and energy residuals dropped by less than 10^{-3} and 10^{-4}, respectively between iterations.

2.6 Description of the Optimization Simulations

Optimization simulations were performed on the louver array in an attempt to design a more effective louvered fin heat exchanger. In doing this, it was desirable to find a way to automate the optimization cycle. This was accomplished by integrating an optimization routine with the aforementioned CFD code, Fluent (Lethander, 2003). The optimization software that was used for this study was also a commercially available product called iSIGHT.

In a typical design problem an engineer must be actively involved in the process. Unfortunately, this can be very time consuming and expensive and for this reason, it is desirable to replace the engineer with a more automated process. The responsibility of the engineer for these problems is to retrieve the design objectives and evaluate the design feasibility. The optimization routine, iSIGHT, allows the engineer to focus on

other tasks while the program retrieves the design objectives and evaluates the design feasibility based on parameters set-up in advance by the user. Other than eliminating the time-consuming human interaction with the design problem, another advantage to using an automated optimization code is a thorough exploration of the entire design space. ISIGHT is also capable of optimization through objective weighting. That is, it is possible to force the program to view some components as being more important than others. For example, if an engineer is designing a satellite and he or she decides that reducing weight is twice as important as thermal performance, it is possible to program that stipulation into iSIGHT's cost or optimization function.

As mentioned in the opening paragraph to this section, the optimization of the louver geometry was performed by integrating iSIGHT with the Gambit and Fluent journal files. The Gambit journal files were used by Gambit to create the louver geometry and mesh the ensuing geometry. The Fluent journal files, on the other hand existed in order to run the CFD simulation. The optimization process began with iSIGHT entering the input parameters describing the louver geometry into the Gambit journal files. After the geometry was changed according to the new parameters, both Gambit and Fluent were allowed to run. The optimization objectives were then obtained from the output files. iSIGHT would then retrieve the objectives and change the input parameters according to the optimization technique.

Louver Model Number	1*	2*	3*	4**	5**	6**	7**	8**	9**
Louver Angle, θ	20°	20°	20°	27°	27°	27°	39°	39°	39°
Louver Pitch, L_p (m)	0.0279	0.0279	0.0279	0.0279	0.0279	0.0279	0.0279	0.0279	0.0279
Ratio of fin pitch to louver pitch, F_p/L_p	0.54	0.91	1.52	0.76	0.91	1.52	0.91	1.22	1.52
Ratio of fin thickness to louver pitch, t/L_p	0.082	0.082	0.082	0.082	0.082	0.082	0.082	0.082	0.082
Nozzle number used	1	2	3	2	2	3	2	3	3
Number of louver rows in test section	11	10	10	12	10	9	10	11	9
Test section inlet area, A_{in} (m^2)	0.024	0.0381	0.0558	0.0381	0.0381	0.0558	0.0381	0.0558	0.0558
Free flow area, A_{ff} (m^2)	0.0204	0.0348	0.0525	0.0341	0.0348	0.0528	0.0348	0.0522	0.0528

*Denotes models original to the current research study
**Denotes models researched by Lyman (2000)

Table 2.1 Geometric parameters and test set up for the louvered fin models researched.

		Re_{Lp} = 230			Re_{Lp} = 370			Re_{Lp} = 1016		
		j_b (%)	j_{aw} (%)	η (%)	j_b (%)	j_{aw} (%)	η (%)	j_b (%)	j_{aw} (%)	η (%)
Louver 2	Minimum	5.50	4.76	15.01	3.99	4.42	17.24	3.59	3.88	28.83
	Maximum	11.59	8.42	34.09	5.03	6.82	40.08	5.93	6.41	56.48
	Average	6.63	6.15	23.16	4.28	4.98	27.75	4.09	4.41	44.28
Louver 3	Minimum	5.00	5.43	6.00	3.99	4.42	4.80	3.51	3.98	4.33
	Maximum	6.80	8.35	6.12	5.03	6.82	5.01	3.93	6.09	4.70
	Average	5.46	6.13	6.06	4.28	4.98	4.92	3.62	4.41	4.53
Louver 7	Minimum	6.82	3.20	4.55	4.81	4.49	3.89	3.67	3.92	4.11
	Maximum	11.60	8.40	4.56	7.05	6.75	3.93	5.00	6.44	4.22
	Average	7.89	6.21	4.56	5.33	5.00	3.92	4.00	4.47	4.16

Table 2.2 Summary of uncertainty values for $F_p/L_p = 0.91$, $\theta = 20°$ model.

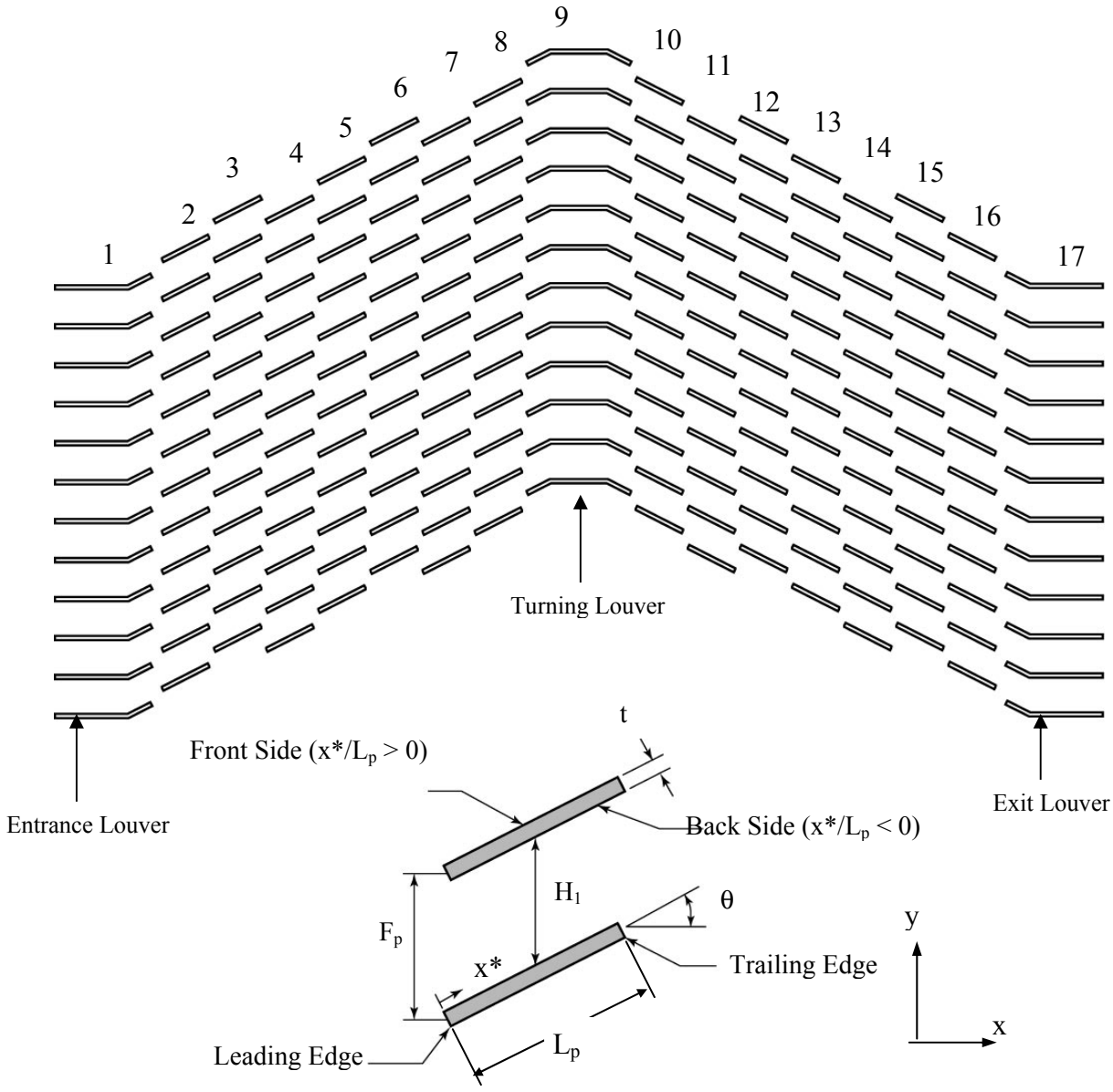

Figure 2.1 Typical louver array geometry detailing louver numbers and geometry nomenclature.

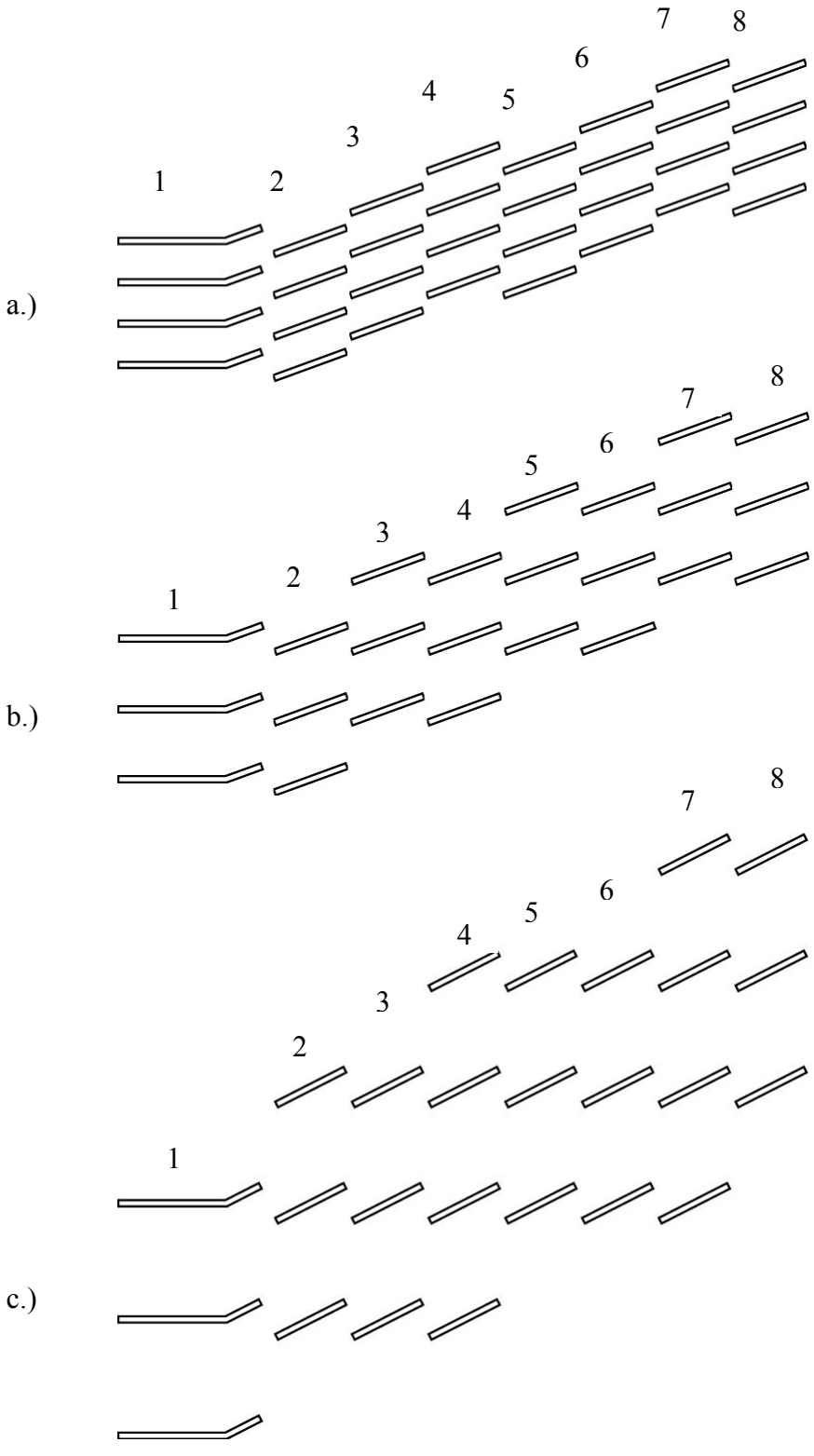

Figure 2.2 a – c Louver arrangements for geometries with θ = 20° a.) $F_p/L_p = 0.54$, b.) $F_p/L_p = 0.91$, and c.) $F_p/L_p = 1.52$

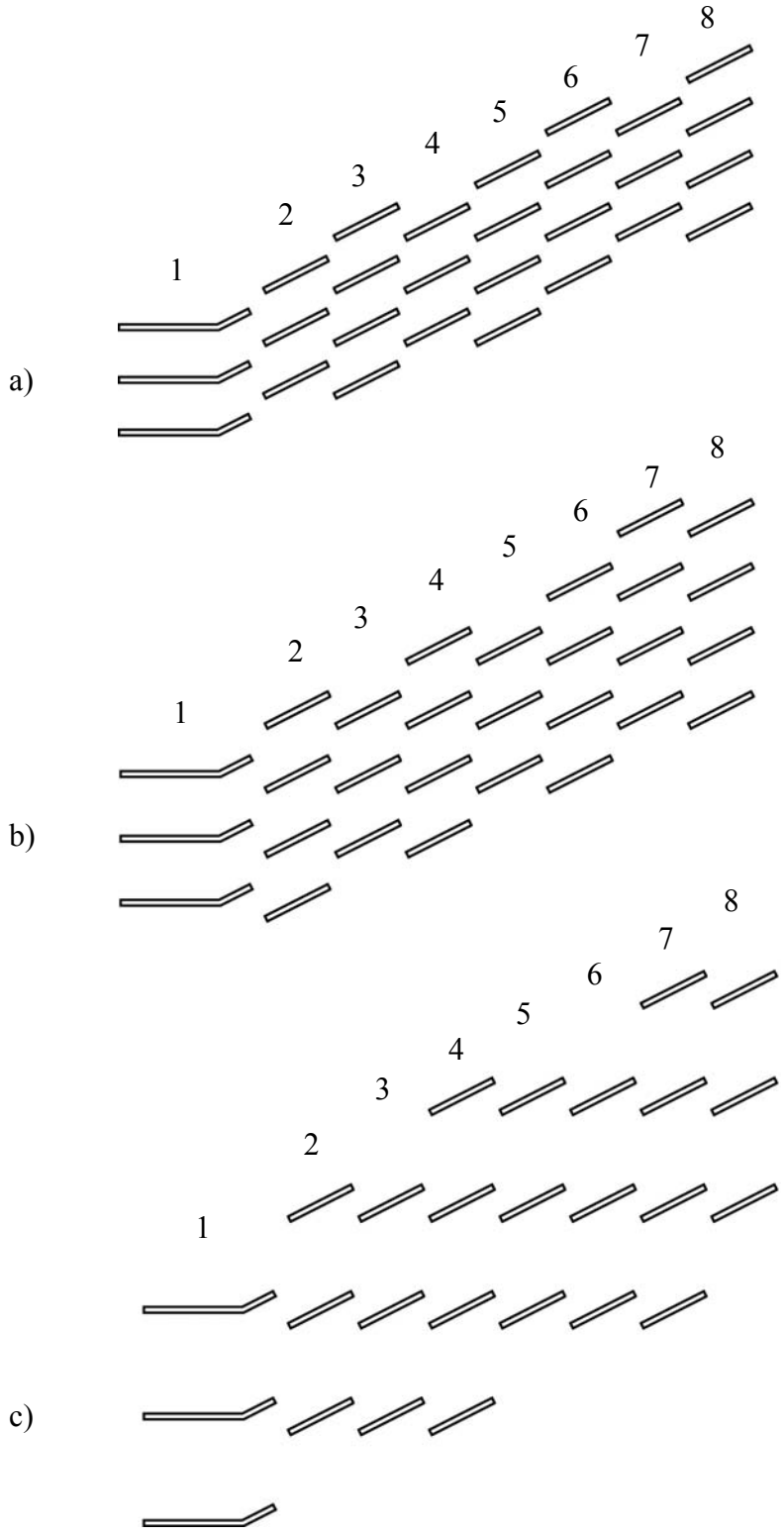

Figure 2.3 a – c Louver arrangements for geometries with θ = 27° a.) $F_p/L_p = 0.76$, b.) $F_p/L_p = 0.91$, and c.) $F_p/L_p = 1.52$

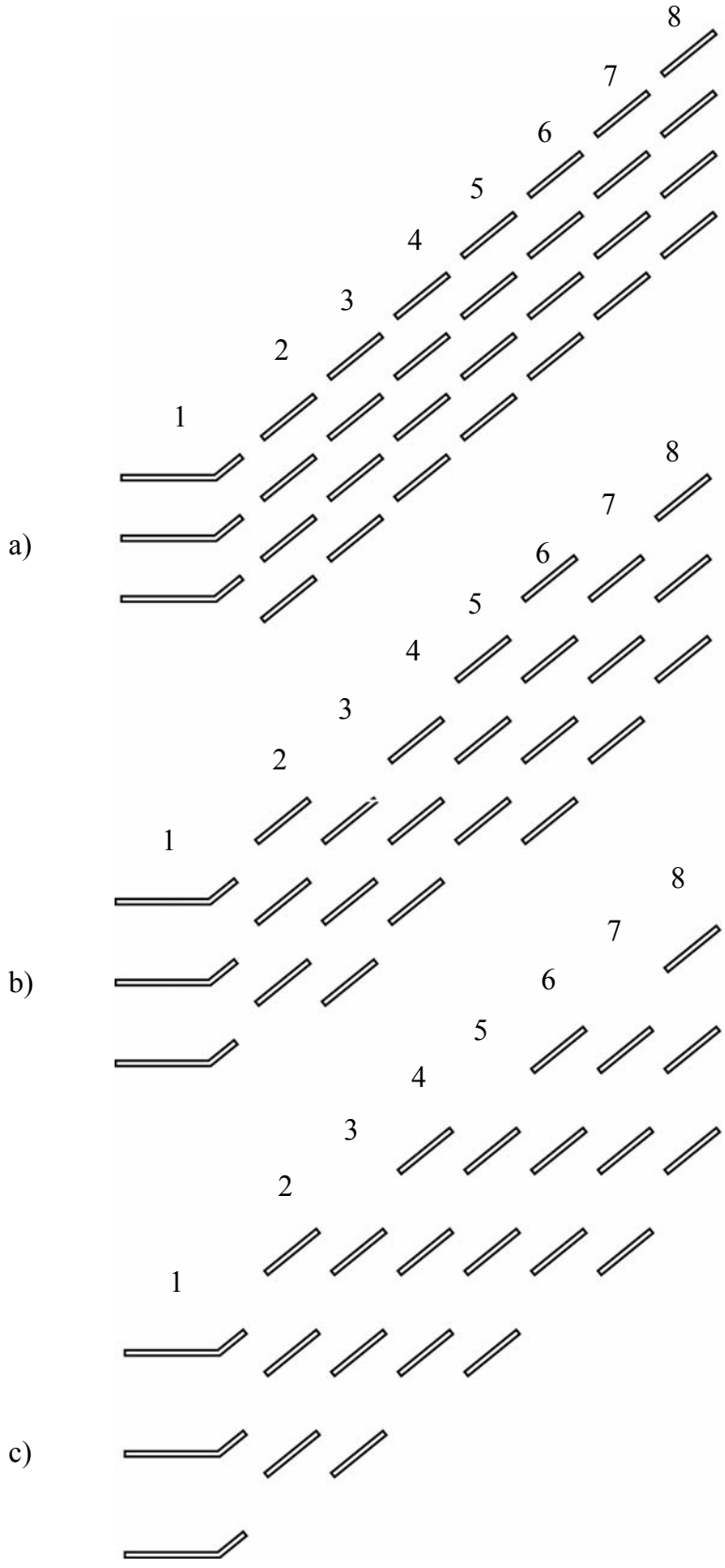

Figure 2.4 a – c Louver arrangements for geometries with θ = 39° a.) $F_p/L_p = 0.91$, b.) $F_p/L_p = 1.22$, and c.) $F_p/L_p = 1.52$

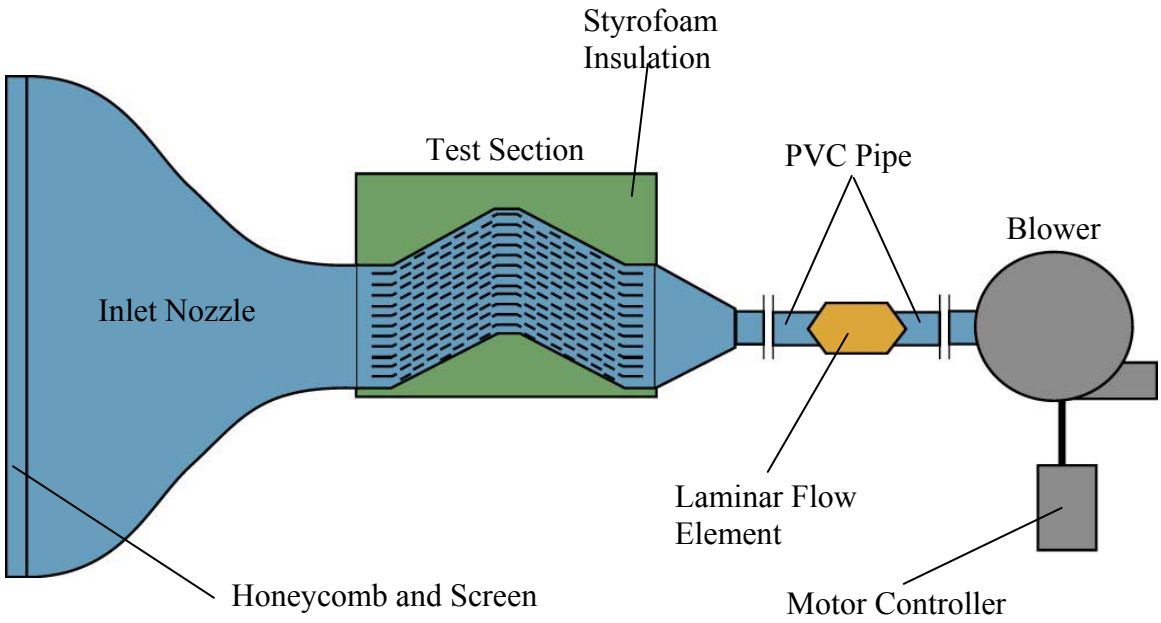

Figure 2.5 The test facility used for the heat transfer measurements along the scaled-up louvers.

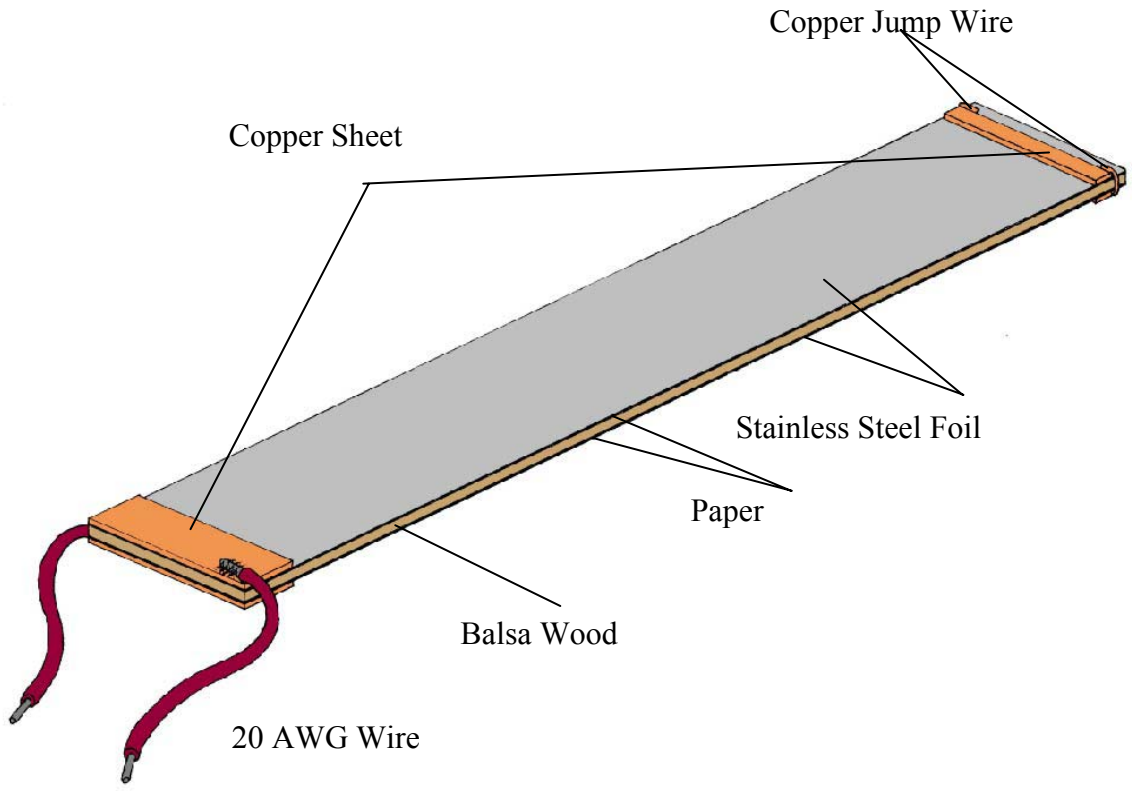

Figure 2.6 The heated louver design.

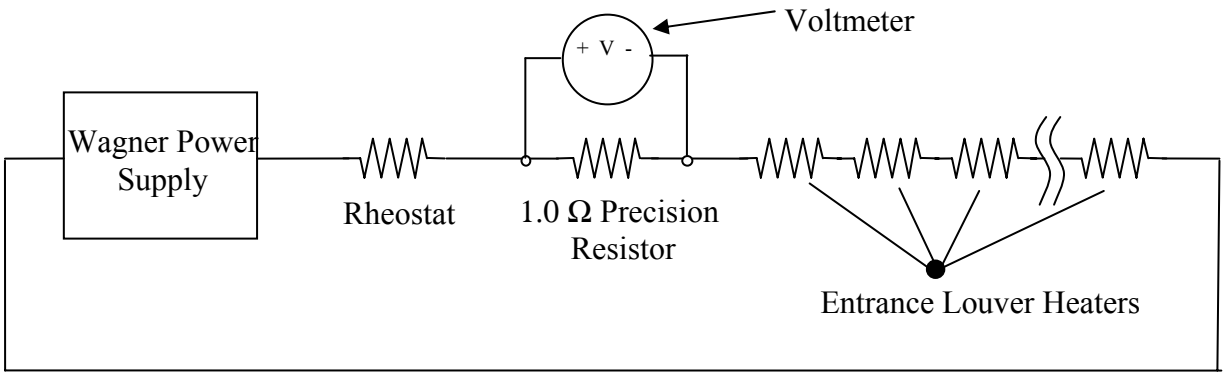

Figure 2.7 Electrical circuit diagram for the entrance louver heaters.

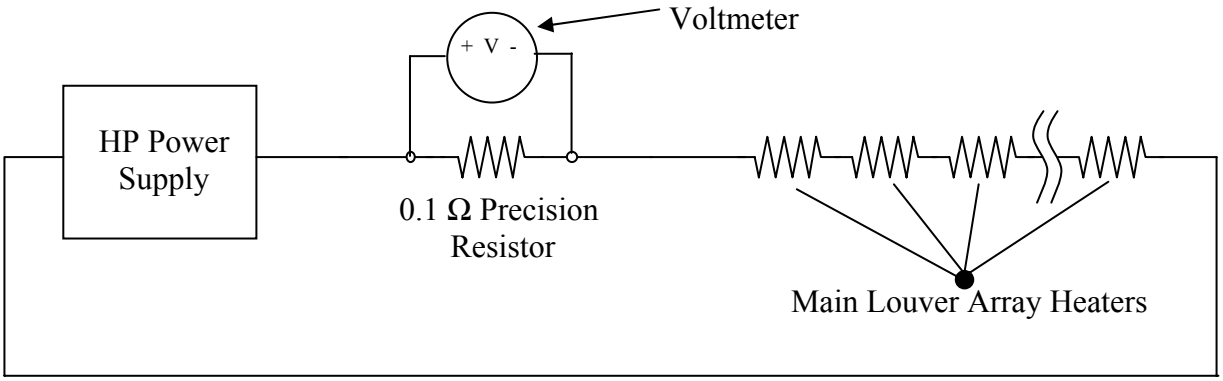

Figure 2.8 Electrical circuit diagram for the main louver array heaters (louvers 2-8).

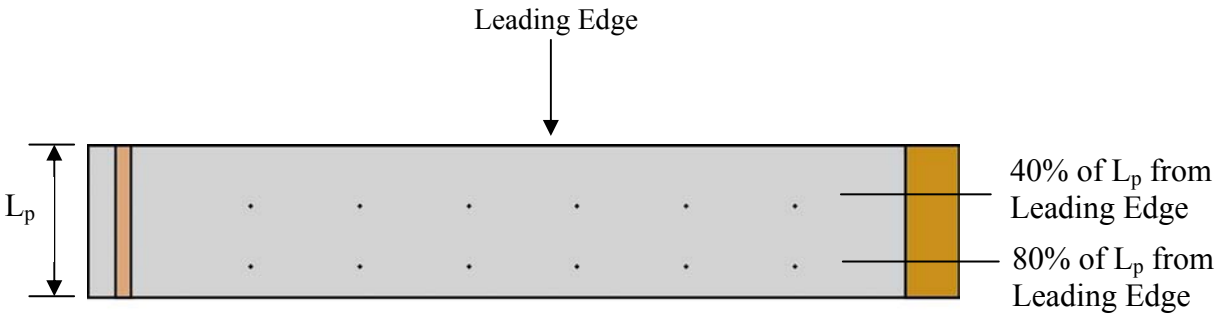

Figure 2.9 Thermocouple locations on the instrumented spanwise louver.

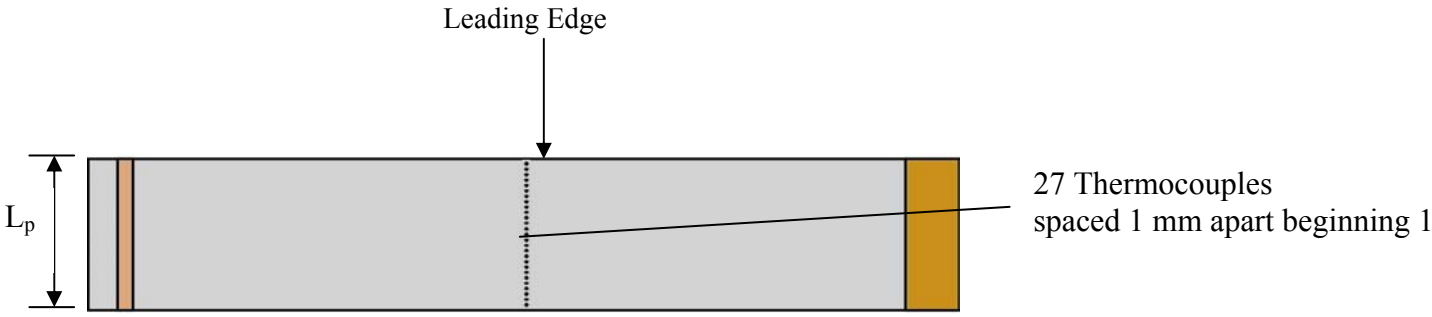

Figure 2.10 Thermocouple locations on the instrumented streamwise louver.

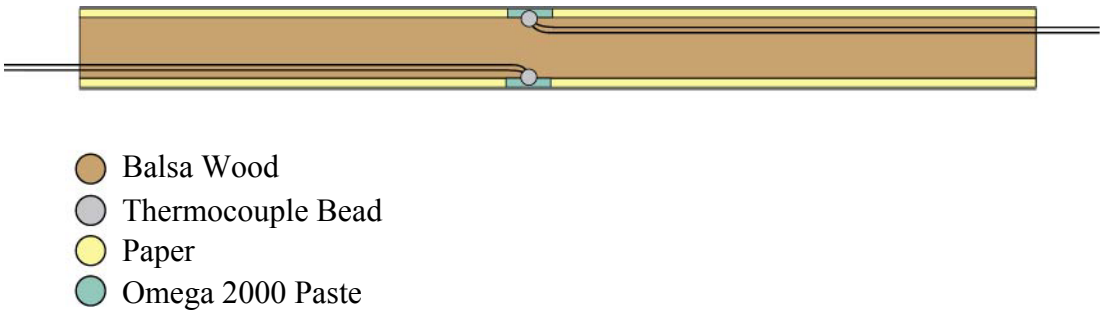

Figure 2.11 Cross-sectional view of an instrumented louver.

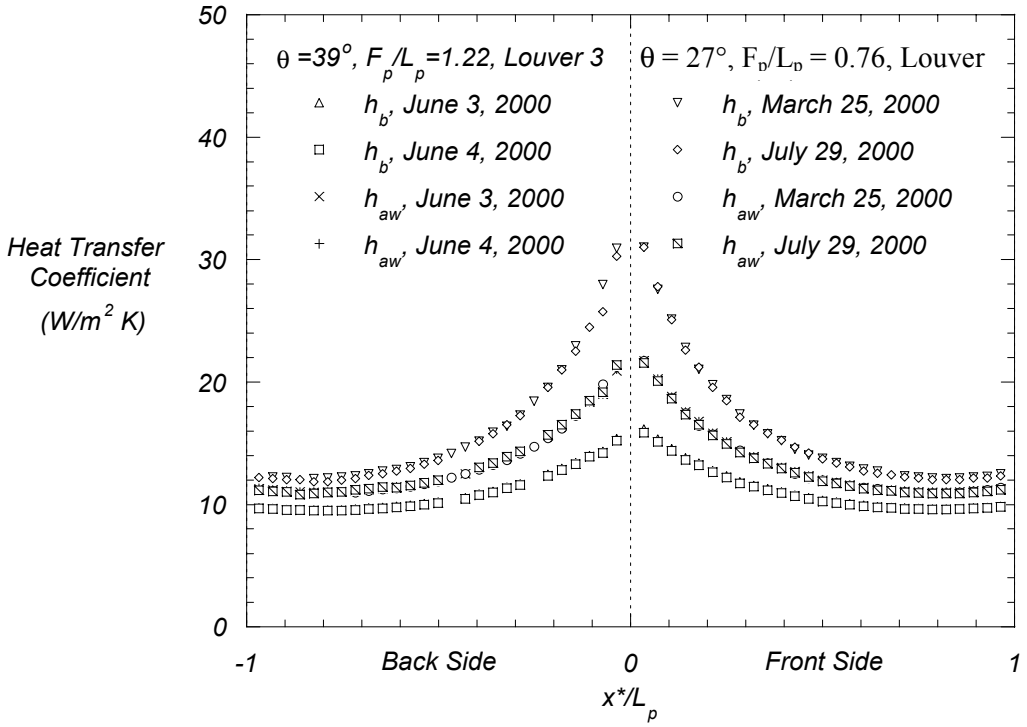

Figure 2.12 Repeatability of the heat transfer coefficients for louver 3 at Re_{Lp} = 230 in the θ = 39°, F_p/L_p = 1.22 model (Lyman, 2000) and louver 7 in the θ = 27°, F_p/L_p = 0.76 model.

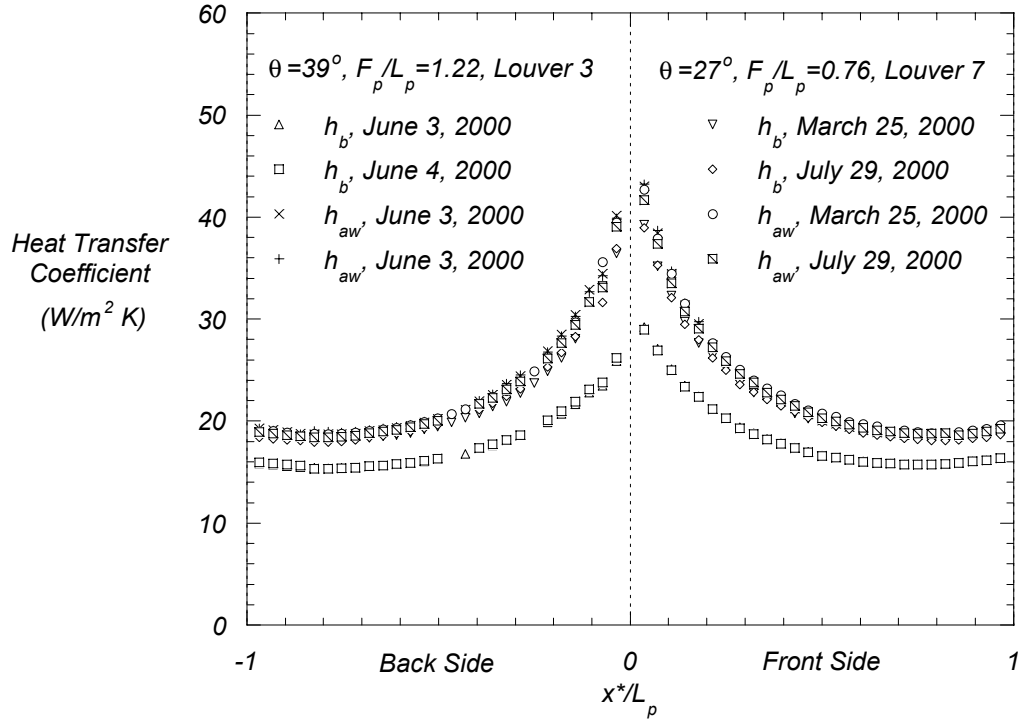

Figure 2.13 Repeatability of the heat transfer coefficients for louver 3 at Re_{Lp} = 1016 in the θ = 39°, F_p/L_p = 1.22 model (Lyman, 2000) and louver 7 in the θ = 27°, F_p/L_p = 0.76 model.

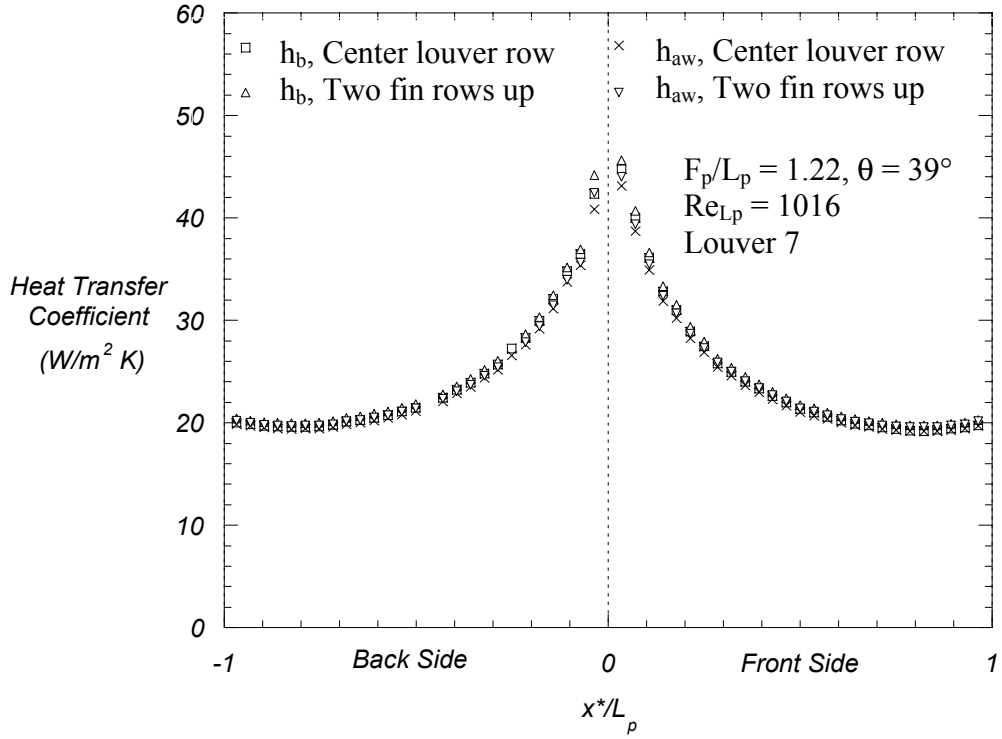

Figure 2.14 Periodicity of the heat transfer coefficients between vertically adjacent fin rows for Re_{Lp} = 1016 at louver 7 in the θ = 39º, F_p/L_p = 1.22 model. Center louver row Lyman (2000)

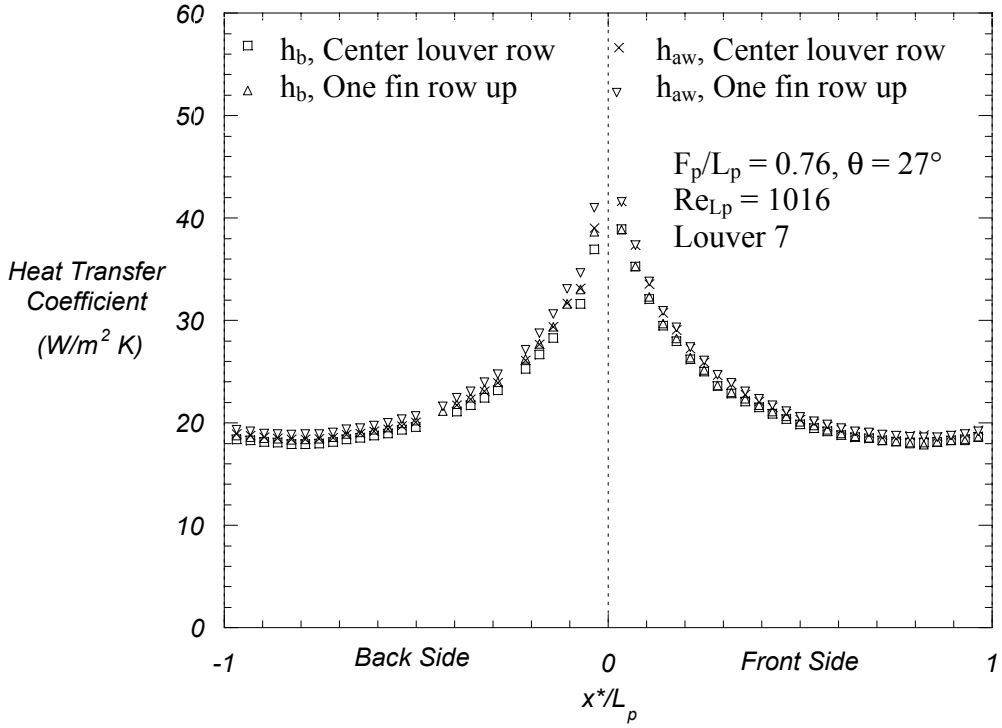

Figure 2.15 Periodicity of the heat transfer coefficients between vertically adjacent fin rows for Re_{Lp} = 1016 at louver 7 in the θ = 27º, F_p/L_p = 0.76 model. Center louver row Lyman (2000)

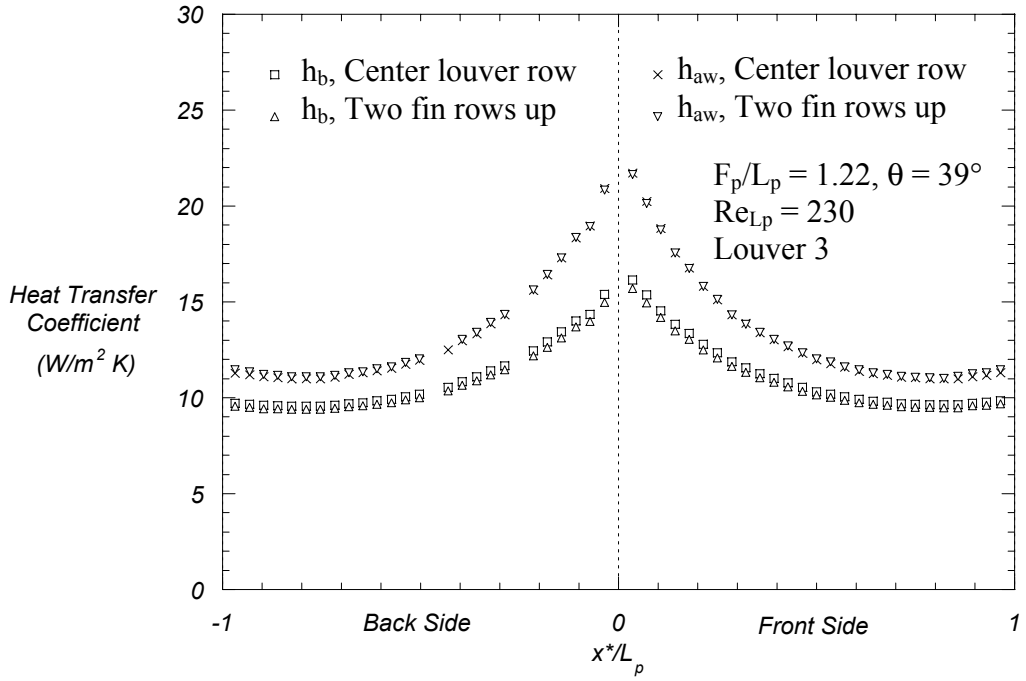

Figure 2.16 Periodicity of the heat transfer coefficients between vertically adjacent fin rows for Re_{Lp} = 230 at louver 3 in the θ = 39º, F_p/L_p = 1.22 model. Center louver row Lyman (2000)

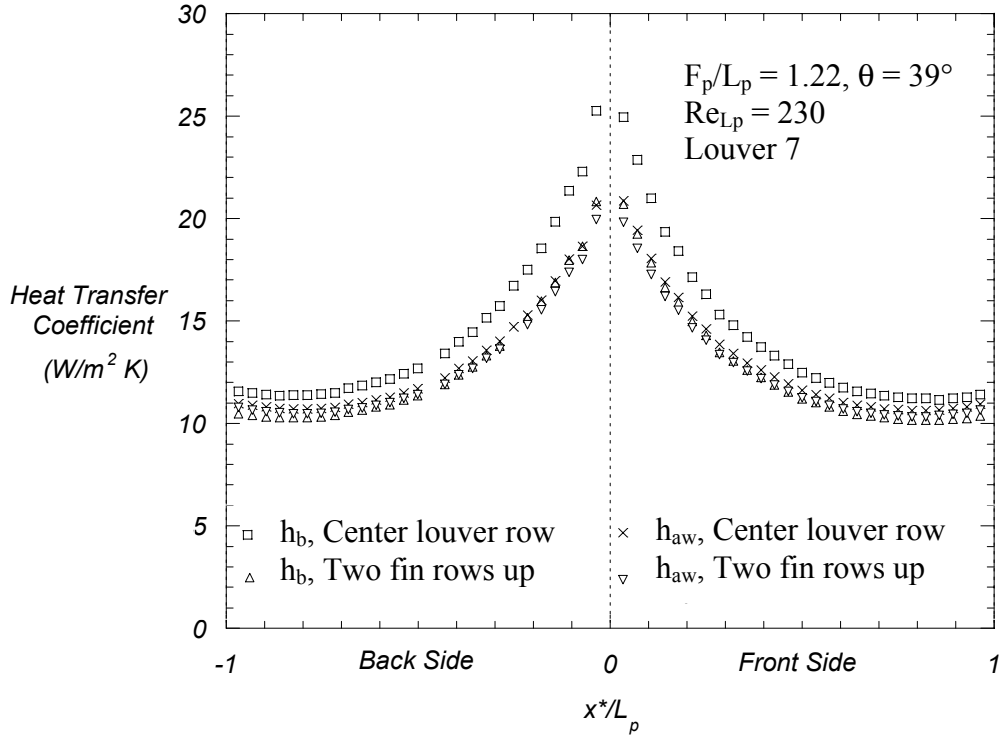

Figure 2.17 Periodicity of the heat transfer coefficients between vertically adjacent fin rows for Re_{Lp} = 230 at louver 7 in the θ = 39º, F_p/L_p = 1.22 model. Center louver row Lyman (2000)

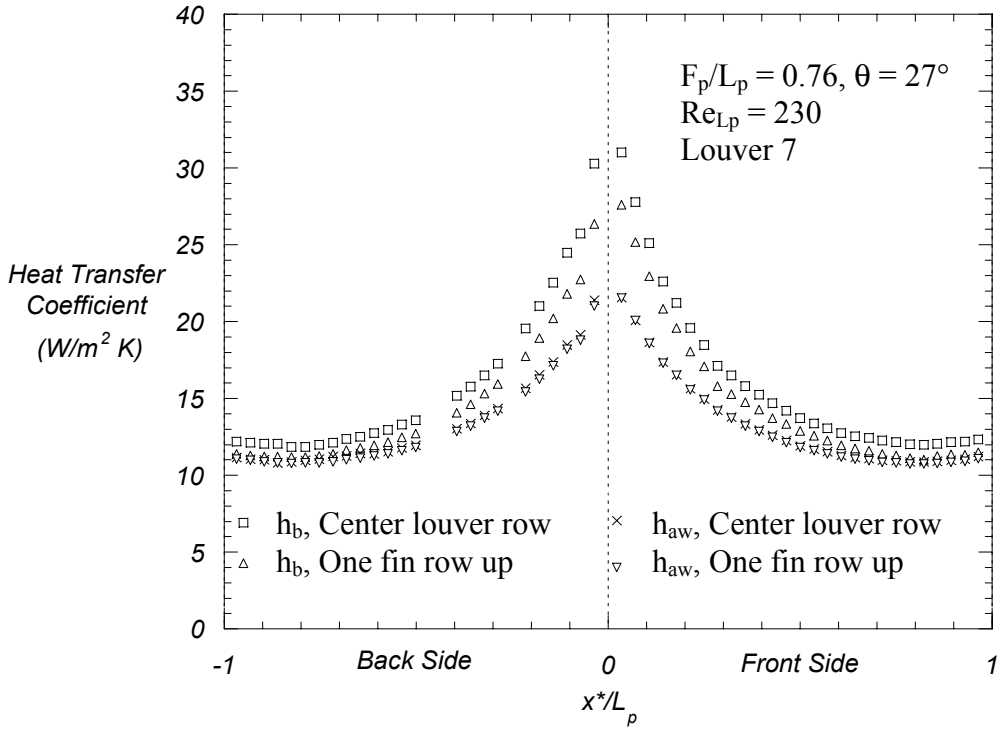

Figure 2.18 Periodicity of the heat transfer coefficients between vertically adjacent fin rows for Re_{Lp} = 230 at louver 7 in the θ = 27°, F_p/L_p = 0.76 model. Center louver row Lyman (2000)

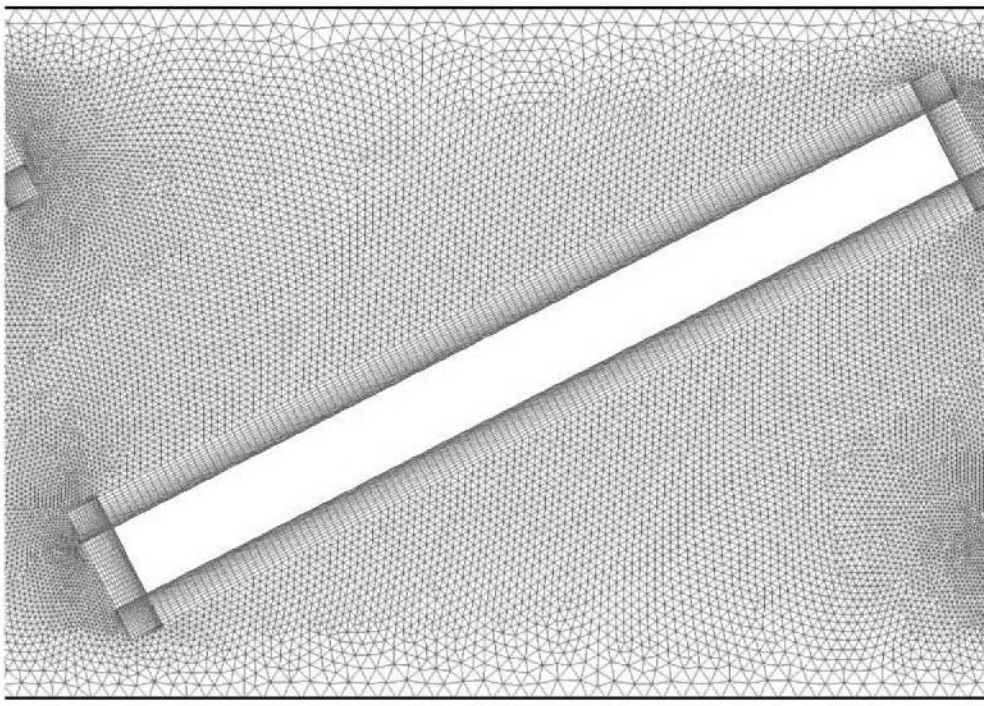

Figure 2.19 A portion of the CFD grid showing a detailed section of the quadrilateral grid used around each of the louvers.

Chapter 3
Data Analysis Methods

This chapter details how the heat transfer data was analyzed. A method was previously devised by Lyman (2000) in which two different reference temperatures were used in the definition of the heat transfer coefficients. The definition of the heat transfer coefficient is made difficult by the fact that the driving temperature differential between the louver and the fluid is not clear. As was briefly alluded to in the previous chapter, two different heat transfer coefficients were used to analyze the data. Both of these heat transfer coefficients and the meaning of each will be described in the first section of this chapter. The next section of this chapter will describe the non-dimensional adiabatic wall temperatures that were used to better understand the thermal field surrounding a particular louver. Chapter 3 will conclude with a section defining the average values used throughout this document.

3.1 Description of the Heat Transfer Coefficients

Sir Isaac Newton is credited with making the observation that objects cool at a rate proportional to the temperature difference between the surrounding fluid and the surface of that object (Moffatt, 1997). The proportionality constant is referred to as the convective heat transfer coefficient. The classical definition of the heat transfer coefficient is given by Newton's law of cooling, which is typically written as

$$h = \frac{q''}{T_w - T_{ref}} \tag{3.1}$$

In the preceding equation q'' represents the surface heat flux in W/m^2, T_w is the surface temperature of the object being considered, and T_{ref} is a representative reference temperature of the surrounding fluid. The question arises as to what temperature should be used as the reference temperature in a complex heat transfer problem such as the one being considered in the present study.

For the current study, two reference temperatures were used in the definition of the heat transfer coefficient. The first reference temperature was that of the computed bulk air temperature at the entrance to the particular louver position of interest. The bulk air temperature at the entrance to a particular louver position was determined by performing an energy balance defined as

$$T_b = T_{in} - \frac{q}{\dot{m} C_p} \tag{3.2}$$

In Equation 3.2, T_{in} represents the temperature of the flow at the inlet to the test section, q is the total heat added by the upstream louvers, $\dot{m}$ is the flowrate through the test facility, and C_p is the specific heat of air. The heat transfer coefficient based on the bulk air temperature, h_b, was then defined as

$$h_b = \frac{q''}{T_w - T_b} \tag{3.3}$$

when the bulk temperature of the flow is used as a reference temperature, the h_b value becomes a strong function of the local fluid temperature which allows the effects of heated wakes from upstream louvers to appear in the heat transfer coefficient data. For instance, if a hot wake from an upstream louver directly impacts a downstream louver, the surrounding fluid temperature of a louver will be increased above that of the bulk flow temperature at the entrance to the particular louver position of interest. This increase in fluid temperature increases the temperature difference ($T_w - T_b$) thereby increasing the magnitude of the denominator in Equation 3.3 and decreasing h_b.

The second of the two reference temperatures used to calculate the heat transfer coefficient is the local adiabatic wall temperature along an individual louver. This reference temperature was obtained by performing a second experiment in which a zero heat flux boundary condition was applied to the particular louver of interest and a non-zero heat flux boundary condition was applied to all other louvers. The corresponding wall temperature was measured along the unheated louver to yield the adiabatic wall

temperature. The heat transfer coefficient based on the adiabatic wall temperature, h_{aw}, was then defined as

$$h_{aw} = \frac{q''}{T_w - T_{aw}} \tag{3.4}$$

Using the adiabatic temperature as a reference temperature removes the effects of the local thermal field resulting from upstream louvers. The adiabatic wall reference temperature allows any flow field effects that might be present to be distinguished. The elimination of the thermal field effects can be explained by looking at the denominator in the definition of the adiabatic wall heat transfer coefficient. A thermal wake from an upstream louver affects both the adiabatic wall temperature and the fully heated wall temperature. The corresponding rise in these temperatures is subtracted out when calculating the adiabatic wall heat transfer coefficient using Equation 3.4. Common flow field effects found in this study are velocity wakes, flow separation, and boundary layer development.

3.2 Definition of Non-Dimensional Values

This section will describe several non-dimensional parameters that were used in this study to accurately compare and contrast the nine different models. The heat transfer coefficients for each of the models could not be directly compared because the flowrate in each louver row differed between the models. The flowrates differed because the number of fin rows varied between the nine models and because different Reynolds numbers were studied. To accurately compare the heat transfer performance between the nine models, it was necessary to account for these differing flowrates through the use of the Colburn factor, j. The Colburn factor is a non-dimensional heat transfer coefficient and is defined as

$$j = \frac{hPr^{\frac{2}{3}}}{GC_p} \tag{3.5}$$

where h is the heat transfer coefficient, Pr is the Prandtl number of air evaluated at the film temperature, and G is the maximum mass velocity. The maximum mass velocity is defined as

$$G = \frac{\dot{m}}{A_{ff}} \tag{3.6}$$

In equation 3.6, $\dot{m}$ represents the flowrate through the entire flow facility and A_{ff} is the free flow area of each louver model. The free flow area is calculated by

$$A_{ff} = A_{in} - ntw \tag{3.7}$$

where A_{in} represents the inlet area to the test section, n is the number of louver rows, t is the thickness of each louver, and w is the spanwise width of each louver. Note that both of the two heat transfer coefficients (h_b and h_{aw}) were used in the Colburn factors (j_b and j_{aw}).

Another non-dimensional value that was used for this study was a non-dimensional value for the adiabatic wall temperature, η. This non-dimensional adiabatic wall temperature was previously defined by Lyman (2000) as

$$\eta = \frac{T_{aw} - T_{in}}{T_b - T_{in}} \tag{3.8}$$

Because the adiabatic wall temperature represents the local temperature surrounding a louver, an η value of 1 represents a fully mixed out flowfield where the local fluid temperature is the bulk temperature. A η value greater than unity occurs if the local temperature surrounding a louver was greater than the calculated bulk temperature at the entrance to that louver passage. A value greater than unity transpires when a heated wake from an upstream louver impinges on the downstream louver. When the thermal field surrounding a louver is cooler than the calculated bulk temperature, η is less than 1. Having an η less than unity occurs when the fluid entering the louver passage is less than

the bulk temperature. Increased heat transfer performance for a louver would be expected for low values of η.

3.3 Definition of Average Values

One of the goals for this study was to create an experimental database of all nine louver models and to compare the overall performance of each of the models to determine the optimal louver geometry. To better understand the heat transfer results and compare the overall performance of the models, several average values were defined. The first average value used was the louver-averaged Colburn factor, $\bar{j}$. The louver-averaged Colburn factor is defined as

$$\bar{j} = \frac{1}{L_p}\int_0^{L_p} j(x)dx \tag{3.9}$$

Upon substituting equation 3.5 for the definition of the Colburn factor, Equation 3.9 becomes

$$\bar{j} = \frac{Pr^{\frac{2}{3}}}{L_p C_p G}\int_0^{L_p} h(x)dx \tag{3.10}$$

Note that both the Colburn factor based on the adiabatic wall temperature and that based on the bulk temperature were louver-averaged. The average values were calculated for both the front and the back side of the louver surfaces. Another louver-averaged value that was used in this study was the louver-averaged value of the non-dimensional adiabatic wall temperature. This average value is defined as

$$\bar{\eta} = \frac{1}{L_p}\int_0^{L_p} \eta(x)dx\,. \tag{3.11}$$

As was briefly alluded to in the introduction to this section, one of the primary goals of this study was to compare the overall performance of the different louver geometries. To sufficiently make this comparison, a few more average values were defined. A louver-averaged value, as was mentioned in the previous paragraph, is simply an arithmetic mean of the front and back sides of one louver. A louver and model-averaged value, on the other hand, is an average Colburn factor or non-dimensional adiabatic wall temperature for an entire model. This value is determined by taking the arithmetic mean of all 7 louver-averaged values in one model. The louver and model-averaged value is for only one Reynolds number. A Reynolds number-averaged value, on the other hand, is an average of all the louver positions for all 3 of the experimentally tested Reynolds numbers. The average values for each of the 9 louver geometries will be presented and discussed in more detail in chapter 4.

Chapter 4

Experimental Heat Transfer Results for the Louver Models

To better understand the heat transfer along louvered fins, a set of nine different scaled-up louver models were designed. The designs of these models were based on the computational results of Suga and Aoki (1991). Lyman (2000) reported the results for six of the nine models, and the current study focused on the remaining three louver models. Chapter 4 details the spatially resolved heat transfer results obtained for the models having a louver angle of $\theta = 20°$ with fin pitch to louver pitch ratios of F_p/L_p = 0.54, 0.91, and 1.52. The first section of this chapter presents the spatially resolved heat transfer coefficients of the three models. The following section details the average heat transfer coefficients for the $\theta = 20°$ models. Following the second section is a conclusion of the experimental results for the three models.

4.1 Spatially resolved heat transfer coefficients for the $\theta = 20°$ models

This section will primarily focus on the heat transfer coefficients as well as the non-dimensional adiabatic wall temperatures obtained for all three of the $\theta = 20°$ models. To better understand these results, the reader is advised to refer to the louver geometry figures located in Chapter 2 (Figure 2.2a-c) of this document. Figures 4.1 through 4.27 show the spatially resolved Colburn factor data and the non-dimensional adiabatic wall temperature measurements for the $\theta = 20°$ models. As was expected from simple flat plate theory, high heat transfer coefficients existed at the leading edge of each of the louvers. As the boundary layer developed along the louver in the streamwise direction, the heat transfer coefficient decreased.

Figures 4.1 and 4.2 show the local Colburn factors based on the bulk flow temperature and the adiabatic wall temperature, respectively, for the $\theta = 20°$, $F_p/L_p = 0.54$ model at $Re_{Lp} = 230$. The heat transfer coefficients based on the bulk flow temperature on the front side of louver 2 and both sides of louver 3 appear to be higher than the heat transfer coefficients at the other louver positions. The increased heat transfer on these surfaces can be explained by studying Figure 4.3, the localized η values. It is evident from this figure that the η values for louver 2 and 3 are below unity. As mentioned in the

previous chapter, this corresponds to a relatively cool thermal field surrounding the louvers thereby increasing the heat transfer coefficients on these surfaces. The η values surrounding these louvers are below unity because the fluid is the cool inlet flow entering the louver array.

The rest of the heat transfer coefficients based on the bulk flow temperature in the louver array appear to be very similar, which means that the thermal field surrounding the louvers is without any dominating thermal wakes. Figure 4.3 verifies this by showing that the η values for most of the louvers is approximately equal to 1. Remember from the previous chapter that an η value of 1 represents a mixed out thermal field surrounding the louver.

The spatially resolved heat transfer coefficients based on the adiabatic wall temperature (j_{aw}) can be found in Figure 4.2. The j_{aw} values shown in this figure collapse to a tight band, showing that the adiabatic wall temperature is a good reference temperature in terms of scaling the heat transfer data. As was mentioned in Chapter 4, using the adiabatic wall temperature as the reference temperature eliminates the effect of thermal wakes on the heat transfer coefficient. Therefore, any lack of collapsing the data of the j_{aw} can be attributed to the flow field surrounding a particular louver. Because the j_{aw} data shown in Figure 4.2 collapses to a very tight band, it can be concluded that the flow field surrounding each of the louvers is very similar. The same trends that were described above for the $Re_{Lp} = 230$ case are evident for $Re_{Lp} = 370$ in Figures 4.4 and 4.5. Figures 4.4 through 4.6 show the heat transfer coefficients and η values for the same louver model at $Re_{Lp} = 370$.

Figure 4.7 through 4.9 show the heat transfer results for the $\theta = 20°$, $F_p/L_p = 0.54$ model at $Re_{Lp} = 1016$. Figure 4.7 shows the local Colburn factors based on the bulk flow temperature at each louver position. As was evident from the $Re_{Lp} = 230$ case, the heat transfer coefficient on the front side of louver 2 and both sides of louver 3 is higher than the other louver positions. This increased heat transfer can be attributed to the low η values shown in Figure 4.9. The relatively cool thermal field surrounding these louvers results in a higher potential for the louvers to transfer heat. Louvers 4 and 7, on the other hand, have relatively low Colburn factors (j_b). These low heat transfer coefficients can be explained by reviewing Figure 4.9 and 2.2a. Figure 4.9 shows η values significantly

greater than 1 for louver position 4. A high η value is attributed to a thermal wake surrounding a particular louver. Figure 2.2a shows that louver 4 is directly aligned with the entrance louver. Because the surface area on each side of the entrance louver is approximately twice (exactly 1.96 times) that of the other louvers and the surface heat flux is the same, the thermal wake produced by that louver is much hotter than the wake produced by the other louvers. Therefore, when a louver is aligned with the angled portion of entrance louver, a lower heat transfer coefficient is expected because the measured wall temperature is higher than if the louver were exposed to a mixed-out thermal field. It is also apparent from Figure 2.2a that louver 7 is aligned with louver 4 and subsequently the entrance louver. This alignment explains the lower heat transfer coefficient of louver 7. These figures support the claim made by Lyman (2000) that the thermal wakes from the entrance louver are much hotter and progress further downstream at high Reynolds numbers. For the $Re_{Lp} = 230$ case a lower Colburn factor was not evident at louver 4 or 7. However, for the $Re_{Lp} = 1016$ case, the Colburn factor for louver 4 and 7 were lower than the values measured at the other louver positions.

Figure 4.8 shows the j_{aw} values for the $\theta = 20°$, $F_p/L_p = 0.54$ model at $Re_{Lp} = 1016$. As was true for the $Re_{Lp} = 230$ case, the j_{aw} data collapses to a tight band for $Re_{Lp} = 1016$ except for louvers 2 and 3. The collapsing of the data shows that the flow field surrounding the louvers is very similar regardless of the louver position. For most of the louver positions, the j_{aw} values are symmetric between the front and back sides of the louver. However, this is not the case for louver 2 and 3. The asymmetric nature of the data is due to entrance effects of the flow. Because the flow is changing from axial to louver directed, it tends to attach to the front side of louver 2 and separate away from the back side. The separation of the flow from the back side of louver 2 has the effect of slightly decreasing the overall heat transfer of that surface as shown in Figure 4.8. On the other hand, the impingement of the flow on the front surface had the effect of increasing the overall heat transfer. The entrance effects are still evident at louver position 3 by the asymmetric j_{aw} data. The heat transfer coefficients on the front side of louver 3 are much lower than those on the back side. From this, it is concluded that the flow along the front surface of louver 2 also flows along to the back side of louver 3, which is aligned with the front surface of louver 2.

The heat transfer data for the $\theta = 20°$, $F_p/L_p = 0.91$ louvered model at $Re_{Lp} = 230$ can be found in Figures 4.10 through 4.12. Several observations can be made from studying Figure 4.10. The first thing that is apparent from this figure is the high Colburn factor on both sides of louver 3. This relatively high heat transfer can be explained by viewing Figure 4.12. The η values for louver 3 are well below unity, which occurs for a relatively cool thermal field surrounding a particular louver. This cooler thermal field increases the potential for heat transfer resulting in high heat transfer coefficients (j_b). From Figure 4.10, it is also evident that the front side of louver 2 has a low heat transfer coefficient. Springer and Thole (1998b) determined that it took a longer streamwise distance for flow to become fully louver directed for large fin pitches and low Reynolds numbers. This phenomenon explains why the heat transfer coefficient is low on the front side of louver 2. From studying the louver geometry in Figure 2.2b, it is seen that the thermal wake from the bottom of the entrance louver impinges directly upon the front surface of louver 2, thereby decreasing the heat transfer coefficient of that surface. Figure 4.12 supports this claim by showing that the η value increases dramatically towards the trailing edge of the front surface of louver 2.

Figure 4.11 shows that j_{aw} is slightly lower on the front surface of louver 2 as compared with the other louver positions. As explained above, any discrepancies in the adiabatic Colburn factor are primarily attributed to flow field effects. This decreased Colburn factor shows entrance effects on the front surface of louver 2. These entrance effects are caused by the low speed wake from the entrance louver impinging on the front surface of louver 2 causing a thicker boundary layer. Other than louver 2, the j_{aw} data collapses to a very tight band showing that the flow field surrounding the downstream louvers is similar. A low heat transfer coefficient on the back side of louver 4 is also seen in Figure 4.10, which is caused by the thermal wake from the front side of louver 2 impinging upon the back surface of louver 4. Remember from above, the hot wake from the entrance louver impacted louver 2, which is aligned with the back side of louver 4. This local hot thermal field is shown by the high η values on the back side of louver 4 as shown in Figure 4.12. The same heat transfer results for the $Re_{Lp} = 370$ case can be found in Figures 4.13 through 4.15.

The resultant heat transfer plots for the $\theta = 20°$, $F_p/L_p = 0.91$ louvered model at $Re_{Lp} = 1016$ can be found in Figures 4.16 through 4.18. It can be seen from Figure 4.16 that the Colburn factor based on the bulk flow temperature for louver 3 is high compared to the other louver positions in the array. This occurs because of the relatively cool thermal field surrounding the louver, which is shown in Figure 4.18 by the η values less than unity. This cool thermal field occurs because the fluid entering the louver array interacts with louver 3. Figure 4.16 also shows low heat transfer coefficients for both louver 4 and louver 7. These low values can again be explained by the presence of thermal wakes surrounding the louvers of interest. In studying Figure 4.18, it is apparent that the η values surrounding louver 4 and 7 are much greater than 1, verifying the existence of hot fluid. Figure 4.18 shows η values close to 1.8 for louver 4 meaning that the adiabatic wall temperatures are almost twice as hot as the bulk flow temperatures at the entrance to that particular louver passage. These high non-dimensional adiabatic wall temperature measurements lead to lower heat transfer coefficients on the surfaces. As would be expected, the η values surrounding louver 4 are higher than those surrounding louver 7. This shows that while the thermal wake from the entrance louver continues through the entire louver array, it gets weaker as it progresses. Unlike the previous model, there does not appear to be any flow field differences between the louver positions. Figure 4.17 shows the j_{aw} data for the $Re_{Lp} = 1016$ case and all of the data collapses to a tight band.

Figures 4.19 through 4.21 show the heat transfer results for the $\theta = 20°$, $F_p/L_p = 1.52$ louvered fin model at $Re_{Lp} = 230$. When looking at Figure 4.19, a plot of j_b, it is immediately apparent that there is a wide range of values. In particular, the j_b for louver 2 is much lower than the other louver positions. This can be explained by looking at Figure 4.21. In this Figure, the η values for louver 2 are greater than 2.2 showing that louver 2 experiences a very strong thermal wake from the upstream louvers, which in this case is the entrance louver. As previously mentioned, for large fin pitches it takes longer for the flow to become fully louver directed. This geometry has the largest fin pitch of all the $\theta = 20°$ models. The results in the entry region indicate that the flow is primarily duct directed causing the thermal wake from the entrance louvers to impinge upon the surfaces of louver 2 thereby causing it to have a high η value. As was the case with the $F_p/L_p =$

0.91 model, the j_{aw} plot shows a flow field effect on the front side of louver 2. This effect is caused primarily by the duct directed flow coming off of the entrance louver and impinging upon the front surface of louver 2. This impingement causes a thicker boundary layer on the front side of louver 2 thereby decreasing the heat transfer coefficient on this surface. The flow development distance also explains why louver 3 has a high η value. Louver 3 is protected from the entrance louver's thermal wake by louver 2. This allows the flow entering the louver array to directly hit louver 3 and 4 without gaining much thermal energy from the upstream louvers causing both of these louvers to experience high heat transfer coefficients.

It is apparent from Figure 4.20 that this model has the largest variation in the j_{aw} values. This variation is due to the fact that this model has the largest fin pitch of the three louver models. As mentioned before, the flow tends to take a longer streamwise distance to become louver directed for large fin pitches. Figure 4.20 shows that the primary outliers in the j_{aw} data are louver 2, 3, and 4. From this it is concluded that each of these 3 louver positions experience slight entrance effects. The same trends that occurred for the $Re_{Lp} = 230$ case are evident in Figures 4.22 through 4.24 for the $Re_{Lp} = 370$ case.

Figures 4.25 through 4.27 show the results for the $Re_{Lp} = 1016$ condition in the $F_p/L_p = 1/52$, $\theta = 20°$ model. From Figure 4.25, it is clear that j_b for louver 2 is significantly lower than the rest of the louver positions. These low heat transfer coefficients can be explained by studying the other two figures for this operating condition. Figure 4.27 shows that the thermal field surrounding louver 2 is relatively hot near the trailing edge of both sides of the louver. This is caused by the thermal wake from the bottom side of the entrance louver impinging onto the front surface of louver 2. The trailing edge of the back side of louver 2 is hot due to the thermal wake from the top side of the entrance louver striking it. The fact that the j_{aw} curve for louver 2 in Figure 4.26 does not collapse with the other curves shows that there are entrance effects associated with louver 2, which are also causing the decrease in heat transfer from that louver. The flow field surrounding the other 6 louver positions appears to be very similar from Figure 4.26. Figure 4.25 also depicts a lower j_b for louver 4. This decreased heat transfer coefficient can be attributed to the thermal wake from the entrance louver. From

Figure 2.2c, it is apparent that the entrance louver's wake impacts both louver 4 and louver 7. Therefore, the louver directed thermal wake from the entrance louver is flowing along both louver 4 and 7 at $Re_{Lp} = 1016$. The low j_b values for louver 4 and 7 are in agreement with the high η values presented in Figure 4.27. Louver 4 and 5 have high heat transfer coefficients, as can be seen from Figure 4.25. These high j_b values correspond with low η values in Figure 4.27, which show that these louver surfaces experience no thermal wakes.

4.2 Average heat transfer coefficients for the $\theta = 20°$ models

The following section presents the average heat transfer coefficients calculated for each of the three $\theta = 20°$ models tested during this study. The average values being discussed in this section have been previously defined and discussed in Chapter 3 of this document. The values that will be discussed here include; the louver-averaged Colburn factor based on the bulk temperature $(\bar{j}_b)$, the louver-averaged Colburn factor based on the adiabatic wall temperature $(\bar{j}_{aw})$, and the louver-averaged non-dimensional adiabatic wall temperature $(\bar{\eta})$. These average values will be used to support and explain the spatially resolved heat transfer coefficients explained in the previous section. As was the case with the spatially resolved heat transfer data, it will be very helpful to periodically refer to the louver geometry figures located in Chapter 2.

The average heat transfer values based on the adiabatic wall temperature in increasing F_p/L_p order can be found in Figures 4.29, 4.32, and 4.35, respectively. The most obvious and interesting observation made when studying these figures is the fact that most of the $\bar{j}_{aw}$ curves are flat. There are, of course, instances where this is not completely true. It is apparent that $\bar{j}_{aw}$ is not flat in Figure 4.32 at louver 2 for $Re_{Lp} = 230$. Because $\bar{j}_{aw}$ at louver 2 is not the same as the other louver positions, one can conclude that there are flow field effects present at this location. The entrance effects that occur at louver 2 were detailed in the previous section. However, in that same figure, $\bar{j}_{aw}$ at $Re_{Lp} = 1016$ is constant through the entire louver array. This verifies the findings of Davenport (1980) and Lyman (2000). The flow through a louver array tends

to remain more duct directed at low Reynolds numbers than at high Reynolds numbers. The entrance effects shown in Figure 4.32 at $Re_{Lp} = 230$ are caused because the flow is changing from duct to louver directed. This same trend can be found in Figure 4.35. Figure 4.35 shows the $\bar{j}_{aw}$ values for the $\theta = 20°$, $F_p/L_p = 1.52$ louvered fin model. In this figure, the $\bar{j}_{aw}$ values for the $Re_{Lp} = 230$ do not reach a constant value until louver position 5. Therefore, the flow does not become fully louver directed until further downstream. However, for the $Re_{Lp} = 1016$ case, the $\bar{j}_{aw}$ values reach a constant at louver position 3, which verifies the results presented by Davenport (1980) and Lyman (2000) that the flow tends to remain duct directed (causing adverse entrance effects) at low Reynolds numbers. Another important conclusion that can be made from the $\bar{j}_{aw}$ results is that the flow tends to remain duct directed for high values of F_p/L_p. This is evidenced by the fact that the $\bar{j}_{aw}$ values are constant for each of the louver positions for $F_p/L_p = 0.54$ and they vary significantly for $F_p/L_p = 1.52$ at $Re_{Lp} = 230$.

The $\bar{j}_b$ and $\bar{\eta}$ values for each of the three $\theta = 20°$ models can be found in Figures 4.28-4.36. The $\bar{\eta}$ values for each of the models show a similar trend in that there are significant peaks in the data for $Re_{Lp} = 1016$. For the $Re_{Lp} = 230$ case there do not appear to be any dramatic peaks. A peak in the $\bar{\eta}$ values at the higher Reynolds number show the effect that Reynolds number has on the thermal field. The increased $\bar{\eta}$ values are caused by a hot thermal wake surrounding a particular louver. One common peak in the data occurs at louver 7 for all of the models, and it is concluded that a thermal wake from the angled portion of the entrance louver impacts louver 7. It can also be concluded that the thermal wakes propagate further downstream at high Reynolds numbers. For the lower Reynolds numbers of $Re_{Lp} = 230$ and $Re_{Lp} = 370$ there are no significant peaks apparent at the louvers located downstream of the entrance louver.

The previously mentioned figures show many other interesting phenomena. It has been mentioned numerous times throughout this document that any flow field effects on the heat transfer coefficient are contained in the j_{aw} data. On the other hand, j_b and η contain both flow field and thermal field effects. As was mentioned above, $\bar{j}_{aw}$ approaches a constant value for all three of the models at each Reynolds number. This

indicates that the flow field surrounding each louver is fully developed before louver position 8, but that a thermally fully-developed flow never really transpires. Figures 4.28-4.38 show the louver-averaged bulk heat transfer coefficients for the three $\theta = 20°$ louvered fin models. In viewing these figures, it is immediately obvious that the $\bar{j}_b$ and $\bar{\eta}$ patterns do not approach a constant value for any of the three louver models by louver position 8.

4.3 Summary of the experimental heat transfer results for the $\theta = 20°$ models

The previous two sections presented all of the heat transfer results for the three $\theta = 20°$ models. The F_p/L_p ratios ranged between 0.54 and 1.52. From these results, several important conclusions can be made. The non-dimensional adiabatic wall temperature introduced in this thesis shows the influence of the thermal wakes surrounding a louver surface. The data also showed that using the adiabatic wall temperature as the reference temperature collapses the heat transfer coefficient data to a single curve provided that no flow field effects are present. The thermal wakes formed at the entrance louver are stronger and maintained form further downstream at $Re_{Lp} = 1016$ as compared with $Re_{Lp} = 230$.

The results also showed that the thermal wakes from the entrance louver have an adverse effect on the heat transfer for downstream louvers that are impacted by these thermal wakes. Flow field effects were more apparent at the entry region of the louver array at larger fin pitch spacing because the flow tends to remain duct directed as was shown by Springer and Thole (1998) and Lyman (2000). The results presented in this chapter also showed that the flow tends to remain more duct directed at $Re_{Lp} = 230$ rather than $Re_{Lp} = 1016$ as shown by Davenport (1980).

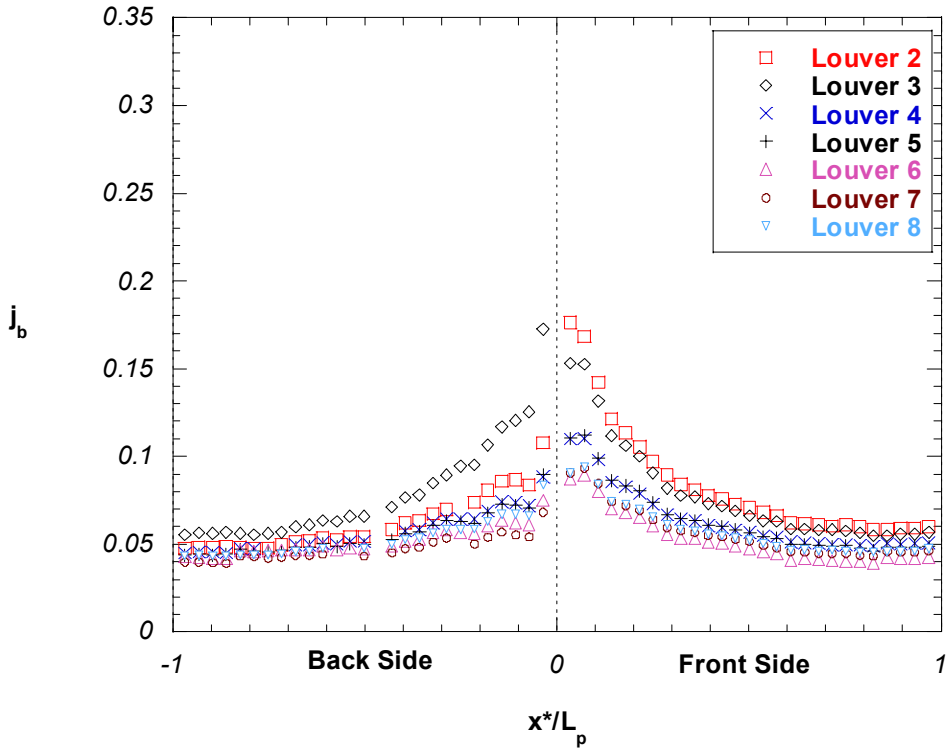

Figure 4.1 Colburn factor measurements based on the bulk flow temperature for the $\theta = 20°$, $F_p/L_p = 0.54$ louvered fin model at $Re_{Lp} = 230$.

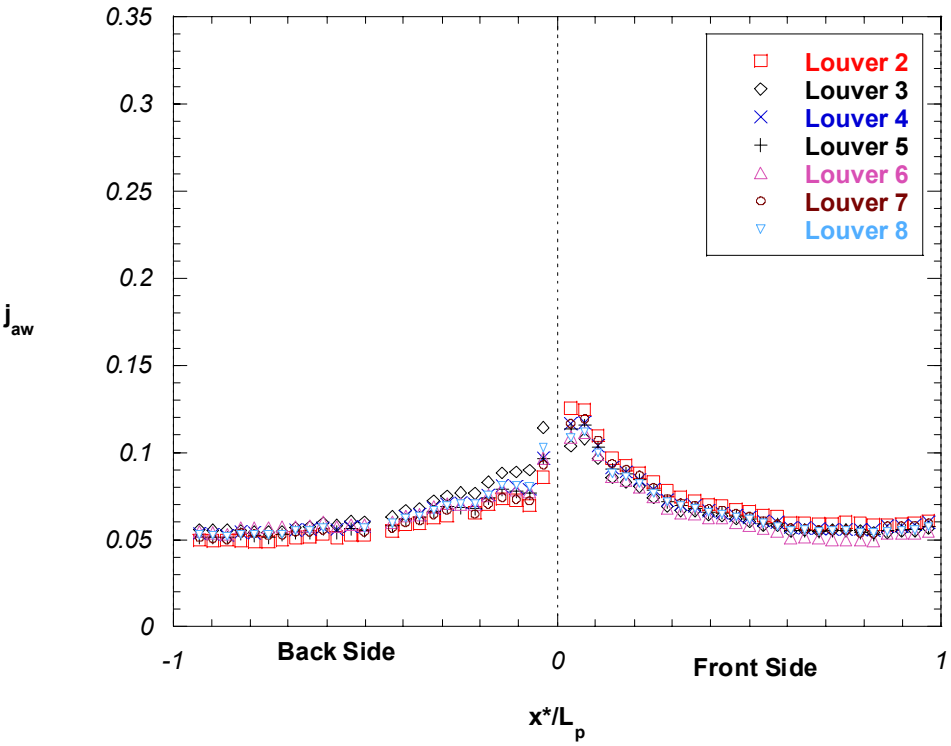

Figure 4.2 Colburn factor measurements based on the adiabatic wall temperature for the $\theta = 20°$, $F_p/L_p = 0.54$ louvered fin model at $Re_{Lp} = 230$.

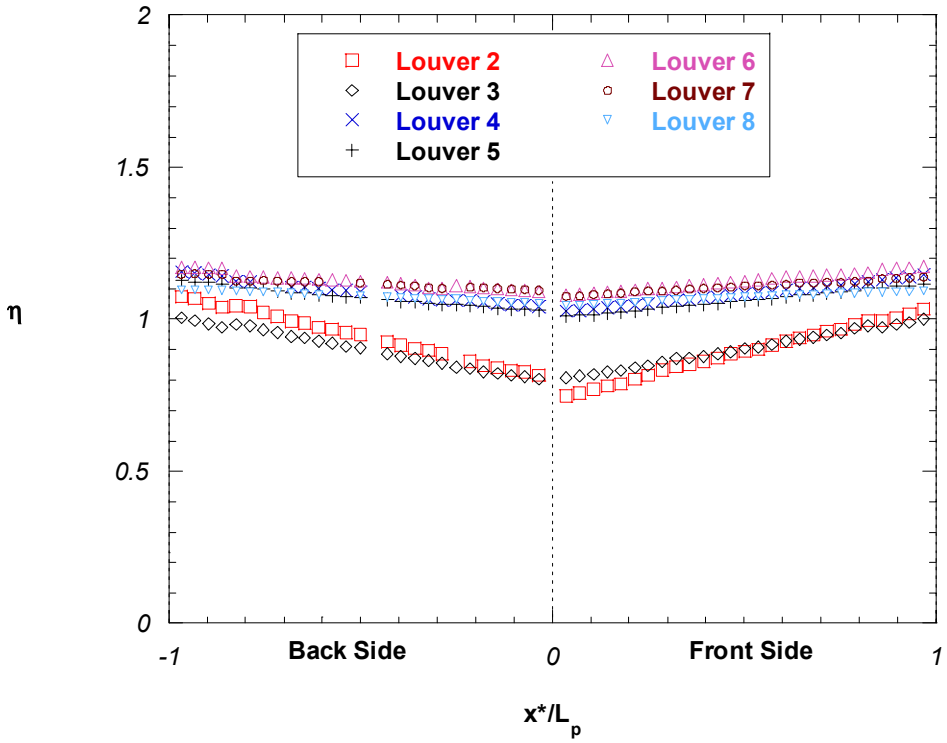

Figure 4.3 Non-dimensional adiabatic wall temperature measurements for the $\theta = 20°$, $F_p/L_p = 0.54$ louvered fin model at $Re_{Lp} = 230$.

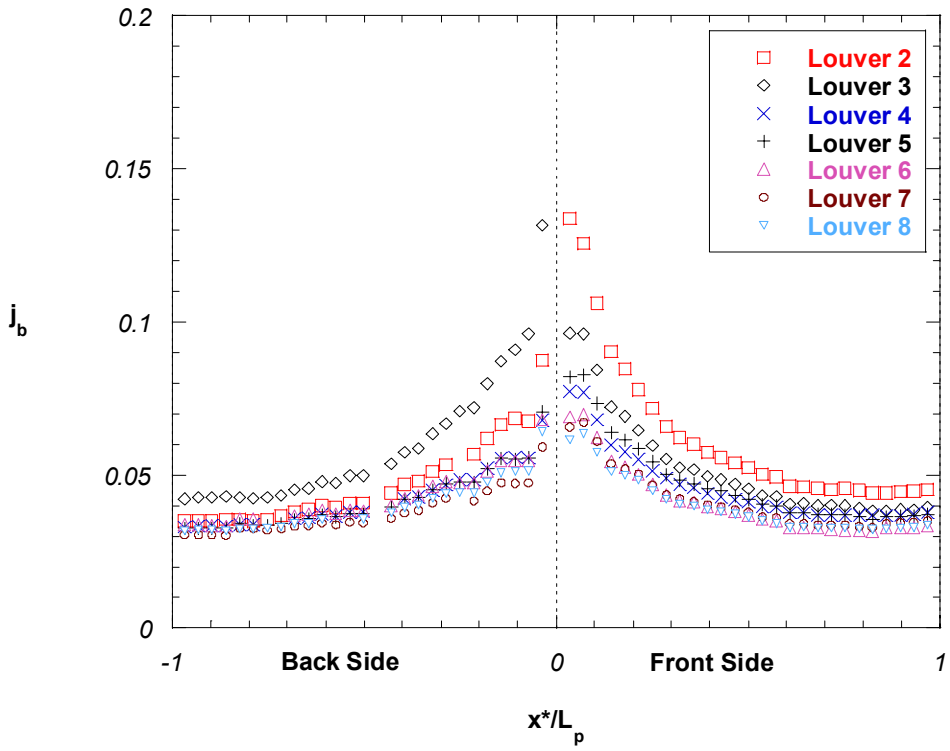

Figure 4.4 Colburn factor measurements based on the bulk flow temperature for the $\theta = 20°$, $F_p/L_p = 0.54$ louvered fin model at $Re_{Lp} = 370$.

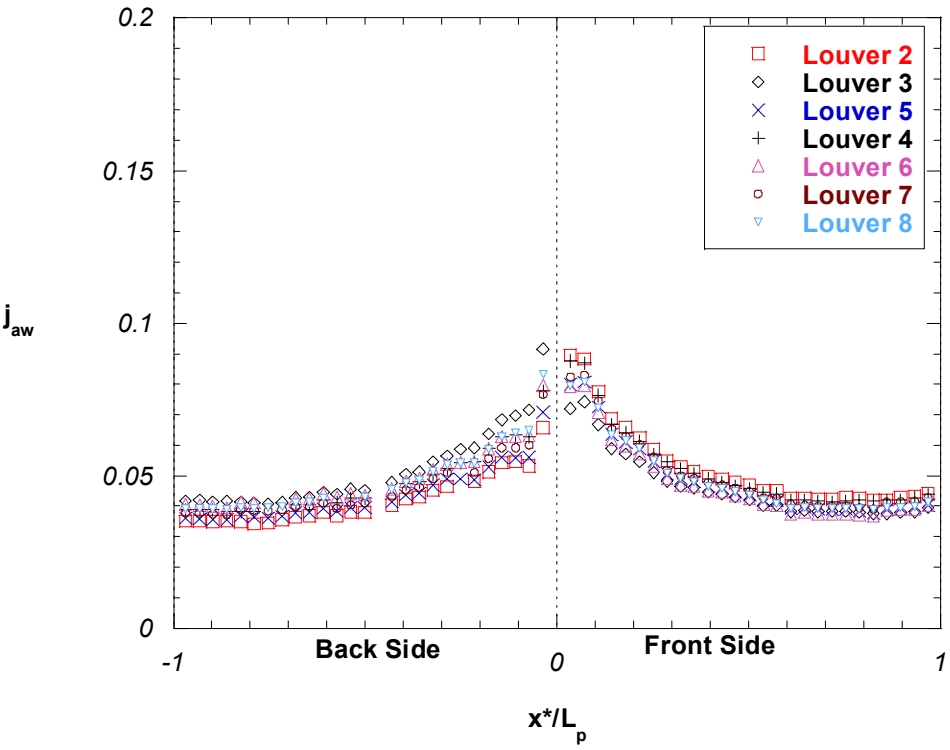

Figure 4.5 Colburn factor measurements based on the adiabatic wall temperature for the $\theta = 20°$, $F_p/L_p = 0.54$ louvered fin model at $Re_{Lp} = 370$.

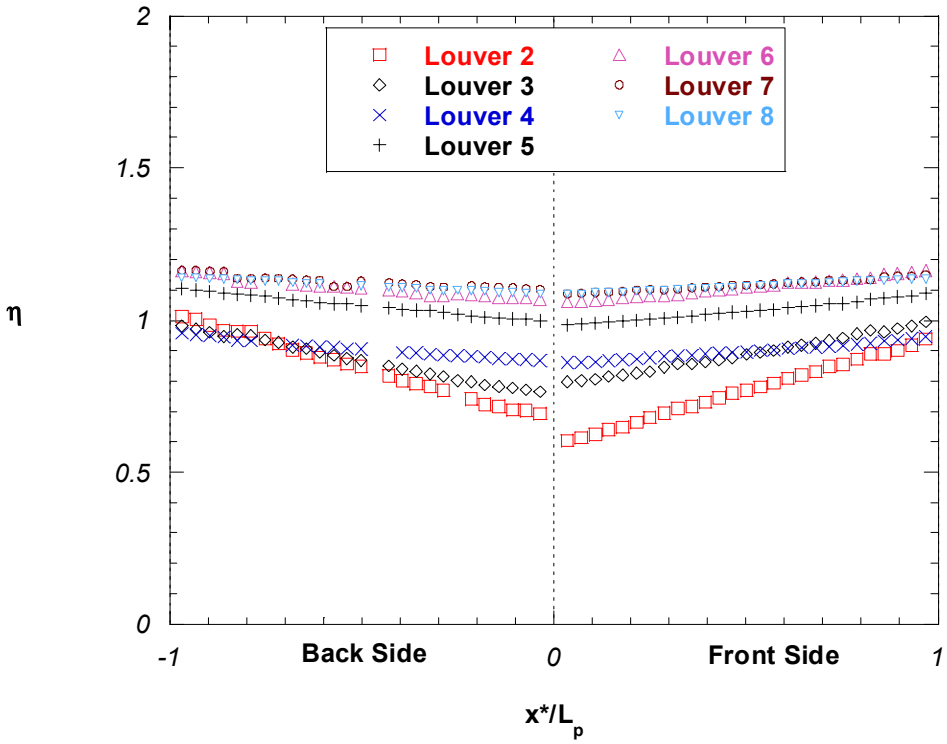

Figure 4.6 Non-dimensional adiabatic wall temperature measurements for the $\theta = 20°$, $F_p/L_p = 0.54$ louvered fin model at $Re_{Lp} = 370$.

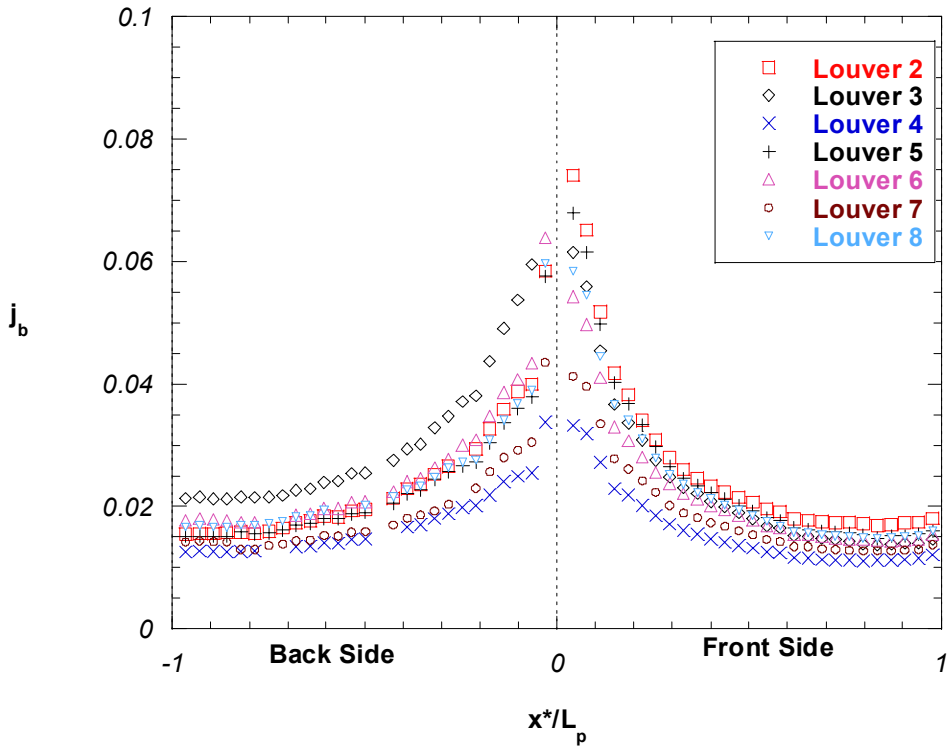

Figure 4.7 Colburn factor measurements based on the bulk flow temperature for the $\theta = 20°$, $F_p/L_p = 0.54$ louvered fin model at $Re_{Lp} = 1016$.

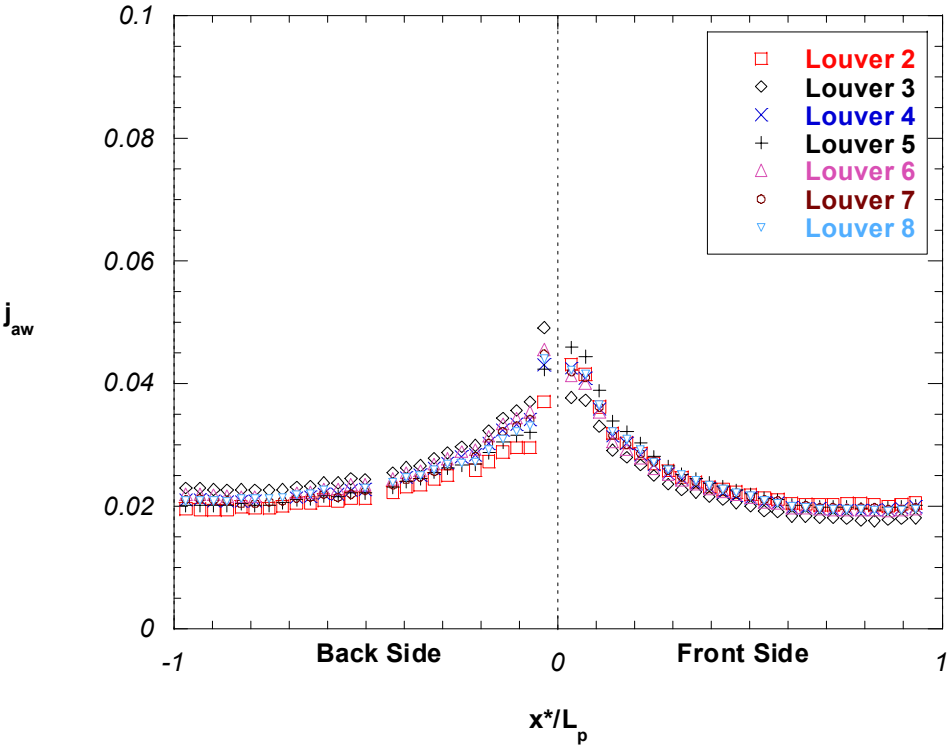

Figure 4.8 Colburn factor measurements based on the adiabatic wall temperature for the $\theta = 20°$, $F_p/L_p = 0.54$ louvered fin model at $Re_{Lp} = 1016$.

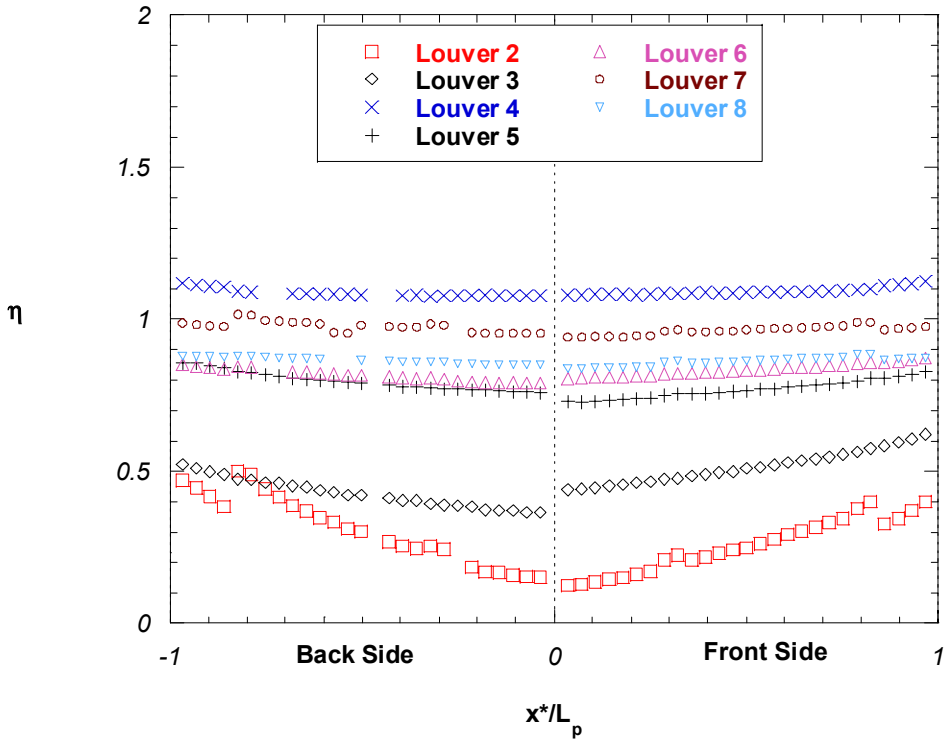

Figure 4.9 Non-dimensional adiabatic wall temperature measurements for the $\theta = 20°$, $F_p/L_p = 0.54$ louvered fin model at $Re_{Lp} = 1016$.

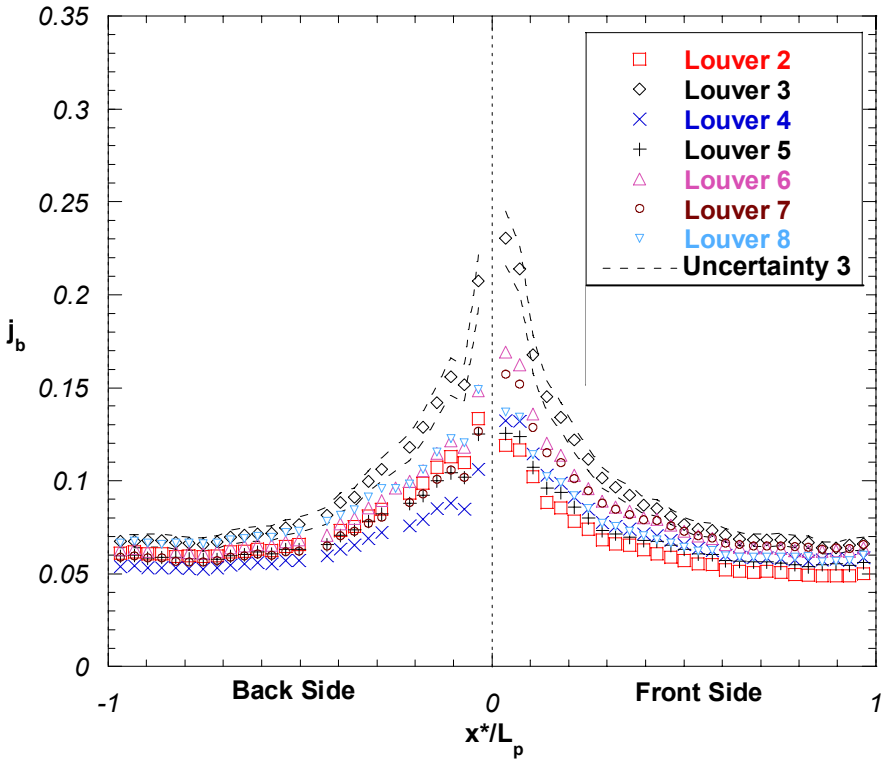

Figure 4.10 Colburn factor measurements based on the bulk flow temperature for the $\theta = 20°$, $F_p/L_p = 0.91$ louvered fin model at $Re_{Lp} = 230$.

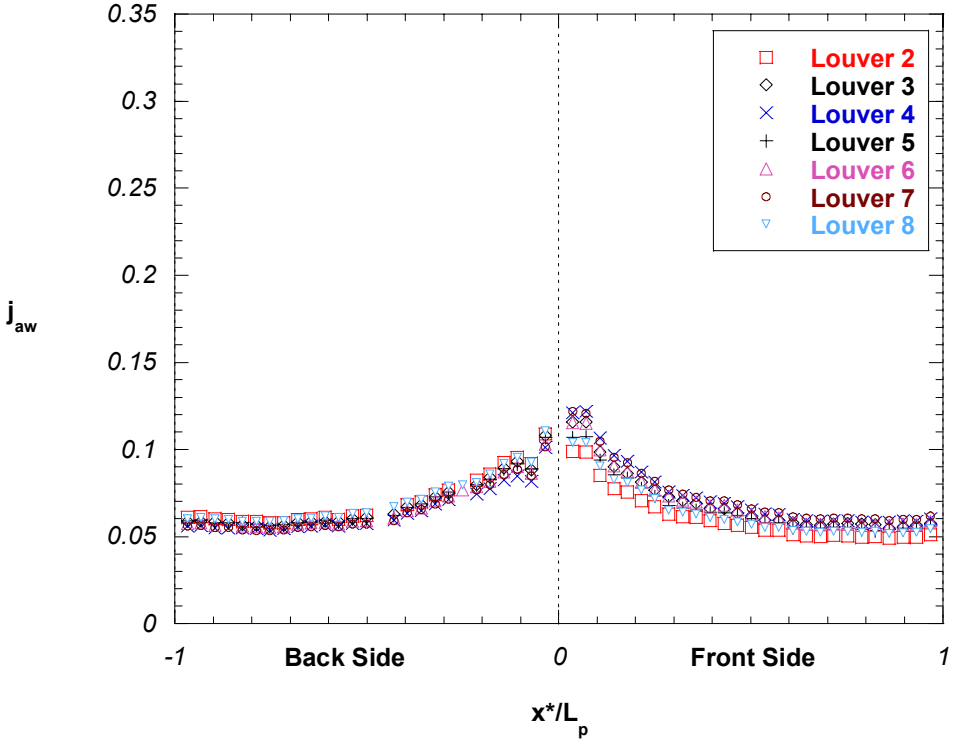

Figure 4.11a Colburn factor measurements based on the adiabatic wall temperature for the $\theta = 20°$, $F_p/L_p = 0.91$ louvered fin model at $Re_{Lp} = 230$.

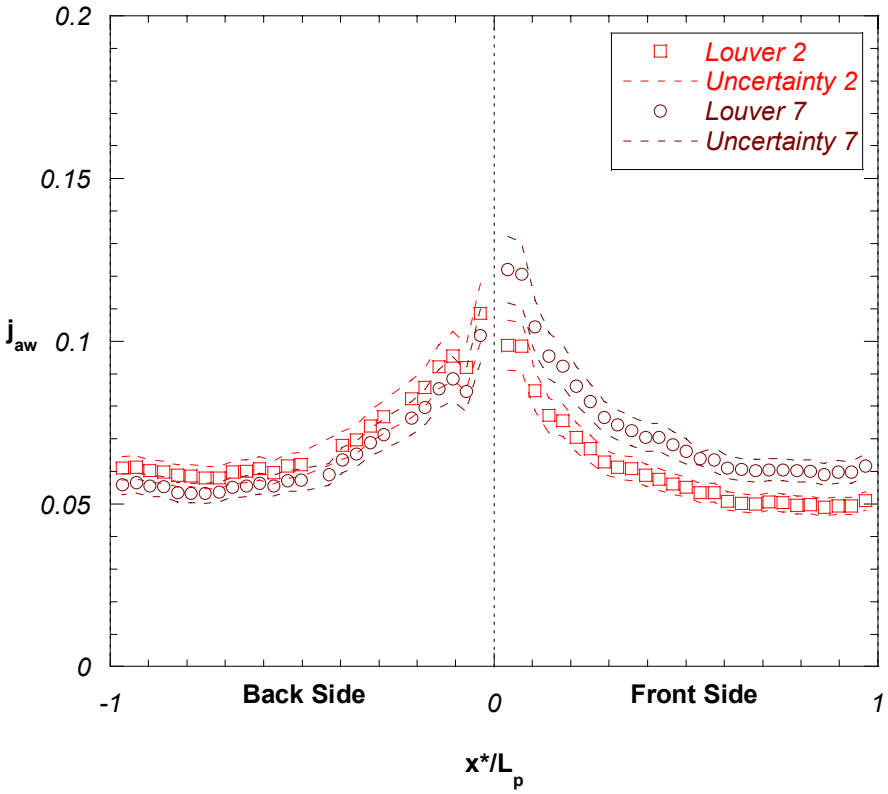

Figure 4.11b Colburn factor measurements based on adiabatic wall temperature and uncertainties for $\theta = 20°$, $F_p/L_p = 0.91$ louvered fin model at $Re_{Lp} = 230$.

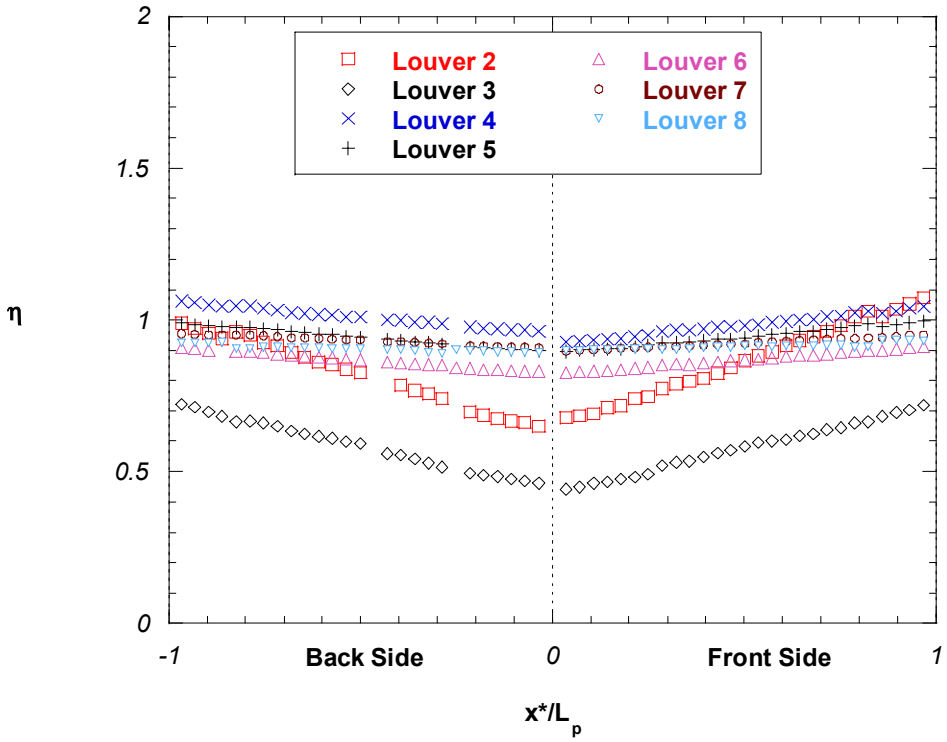

Figure 4.12 Non-dimensional adiabatic wall temperature measurements for the $\theta = 20°$, $F_p/L_p = 0.91$ louvered fin model at $Re_{Lp} = 230$.

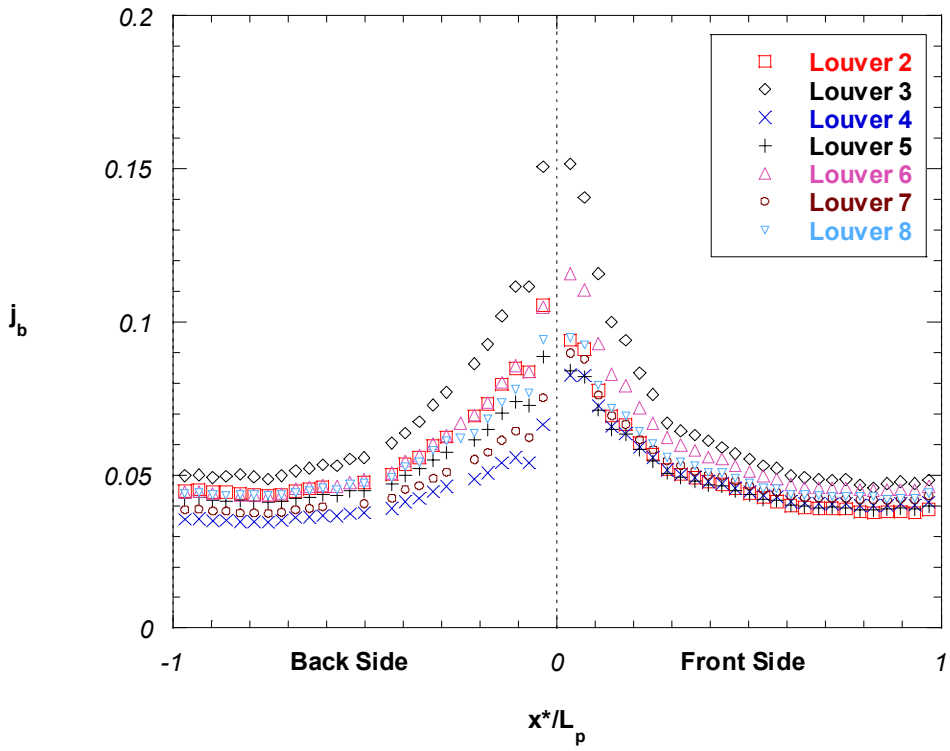

Figure 4.13 Colburn factor measurements based on the bulk flow temperature for the $\theta = 20°$, $F_p/L_p = 0.91$ louvered fin model at $Re_{Lp} = 370$.

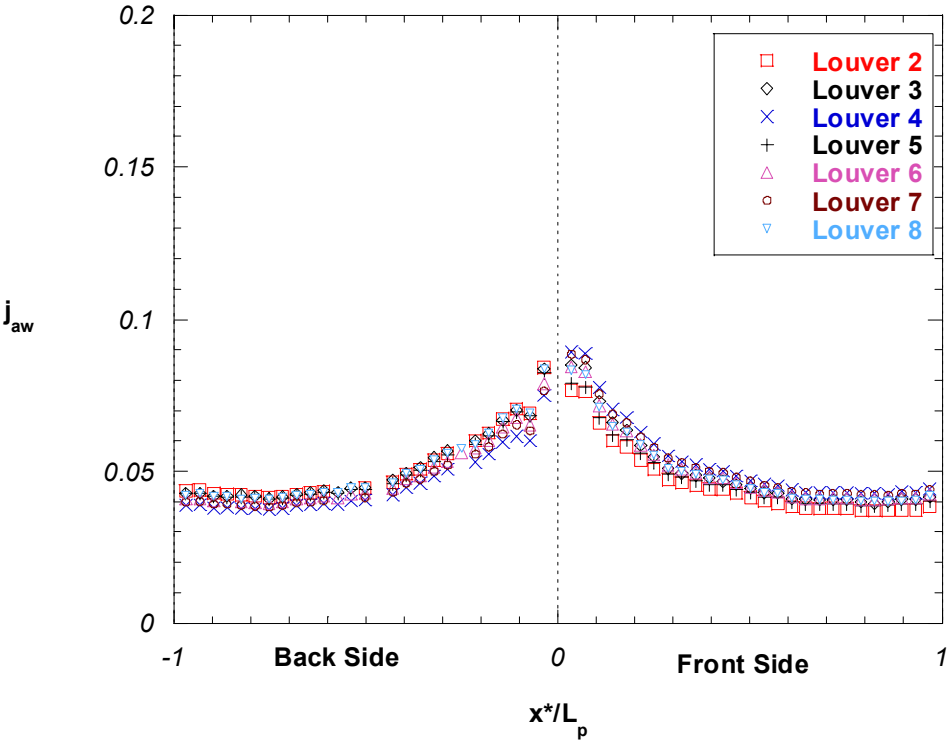

Figure 4.14 Colburn factor measurements based on the adiabatic wall temperature for the $\theta = 20°$, $F_p/L_p = 0.91$ louvered fin model at $Re_{Lp} = 370$.

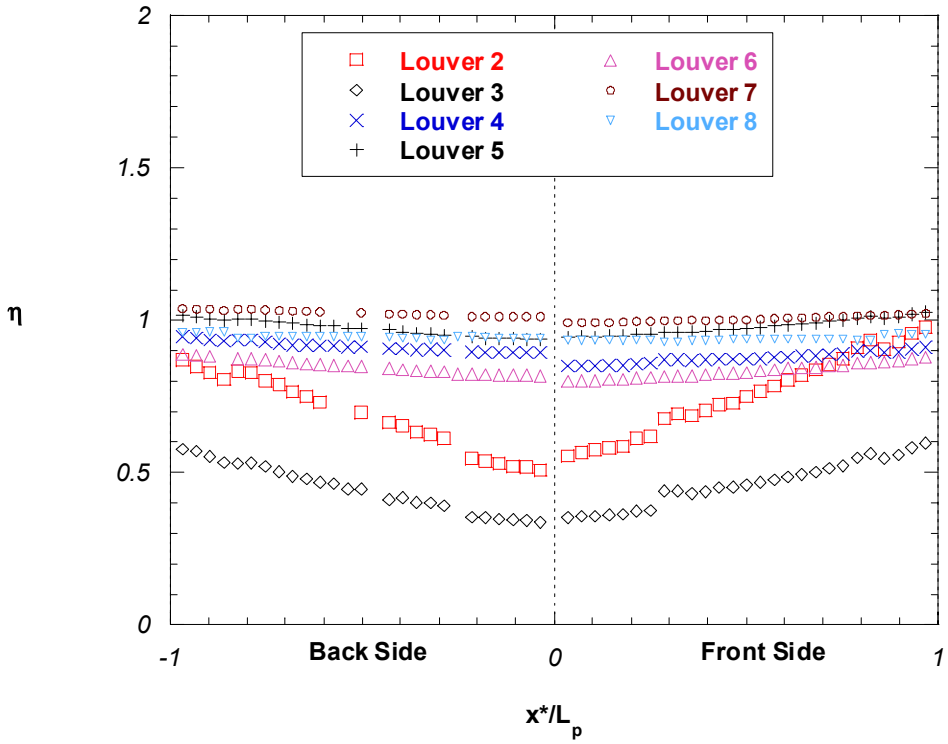

Figure 4.15 Non-dimensional adiabatic wall temperature measurements for the $\theta = 20°$, $F_p/L_p = 0.91$ louvered fin model at $Re_{Lp} = 370$.

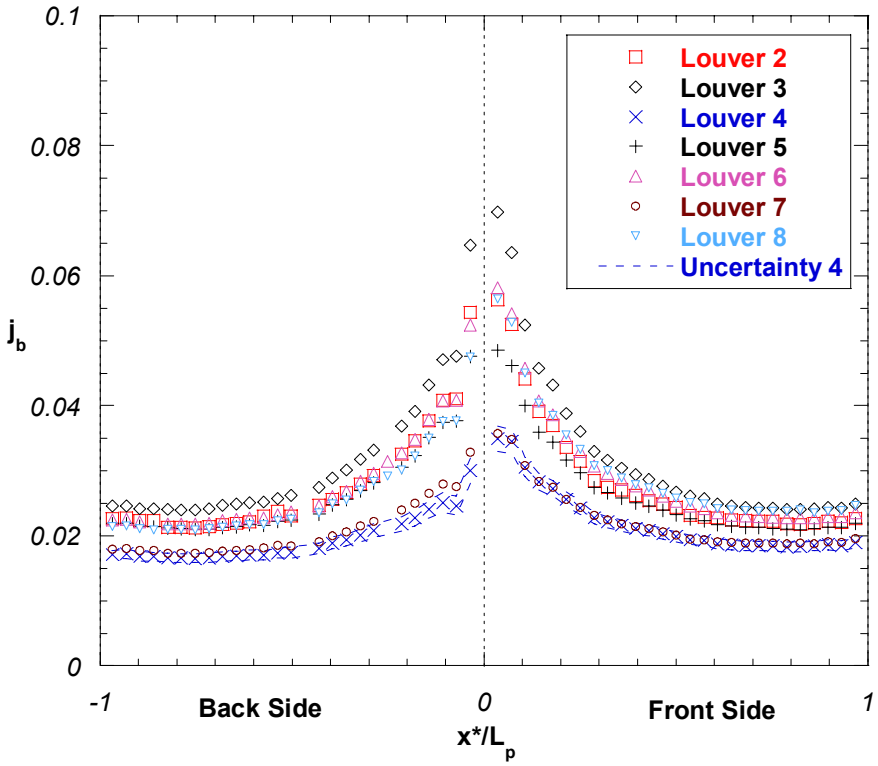

Figure 4.16 Colburn factor measurements based on the bulk flow temperature for the $\theta = 20°$, $F_p/L_p = 0.91$ louvered fin model at $Re_{Lp} = 1016$.

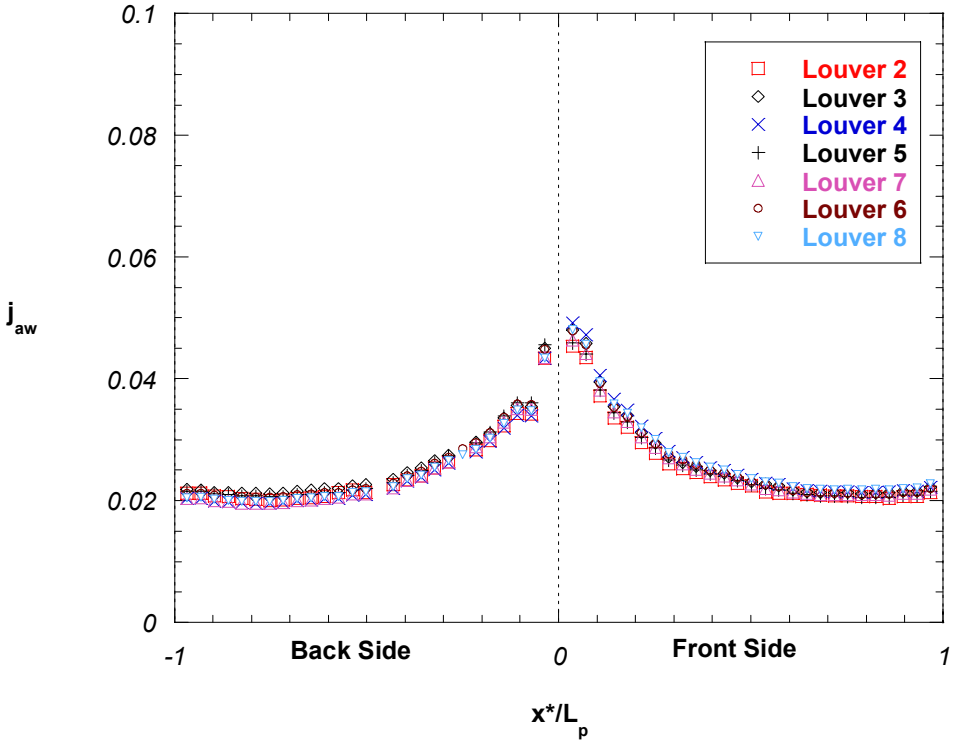

Figure 4.17a Colburn factor measurements based on the adiabatic wall temperature for the $\theta = 20°$, $F_p/L_p = 0.91$ louvered fin model at $Re_{Lp} = 1016$.

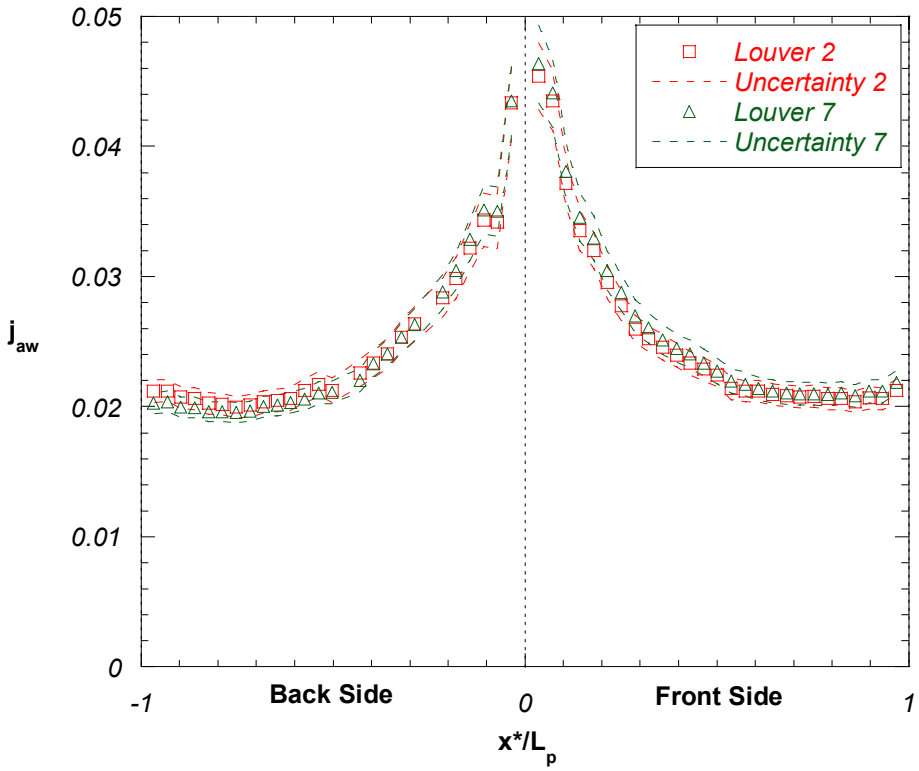

Figure 4.17b Colburn factor measurements based on the adiabatic wall temperature and uncertainties for $\theta = 20°$, $F_p/L_p = 0.91$ louvered fin model at $Re_{Lp} = 1016$.

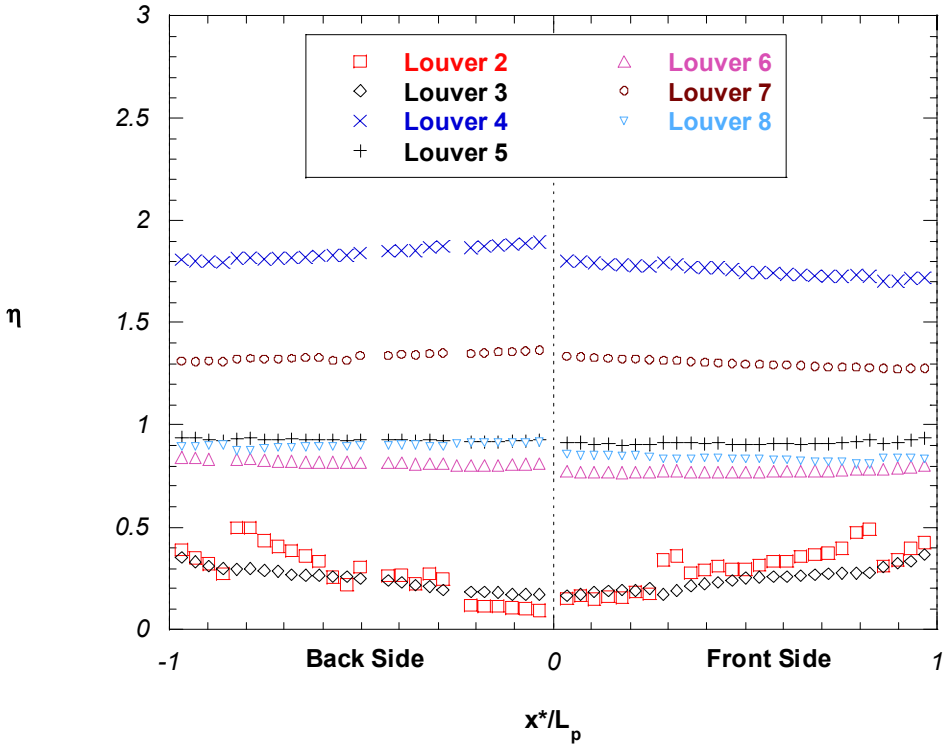

Figure 4.18 Non-dimensional adiabatic wall temperature measurements for the $\theta = 20°$, $F_p/L_p = 0.91$ louvered fin model at $Re_{Lp} = 1016$.

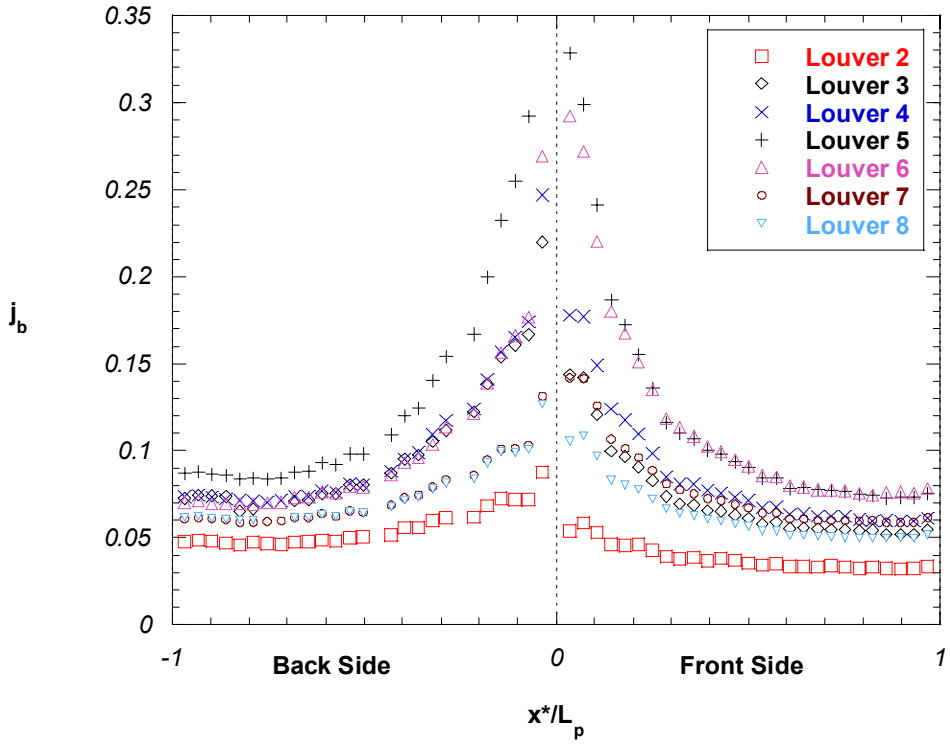

Figure 4.19 Colburn factor measurements based on the bulk flow temperature for the $\theta = 20°$, $F_p/L_p = 1.52$ louvered fin model at $Re_{Lp} = 230$.

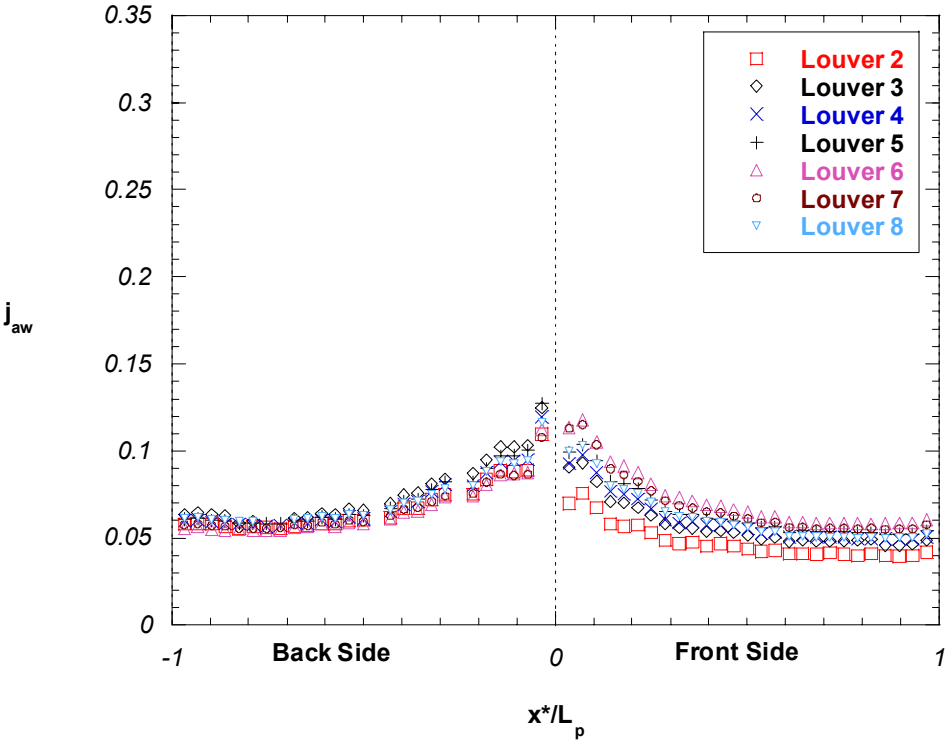

Figure 4.20 Colburn factor measurements based on the adiabatic wall temperature for the $\theta = 20°$, $F_p/L_p = 1.52$ louvered fin model at $Re_{Lp} = 230$.

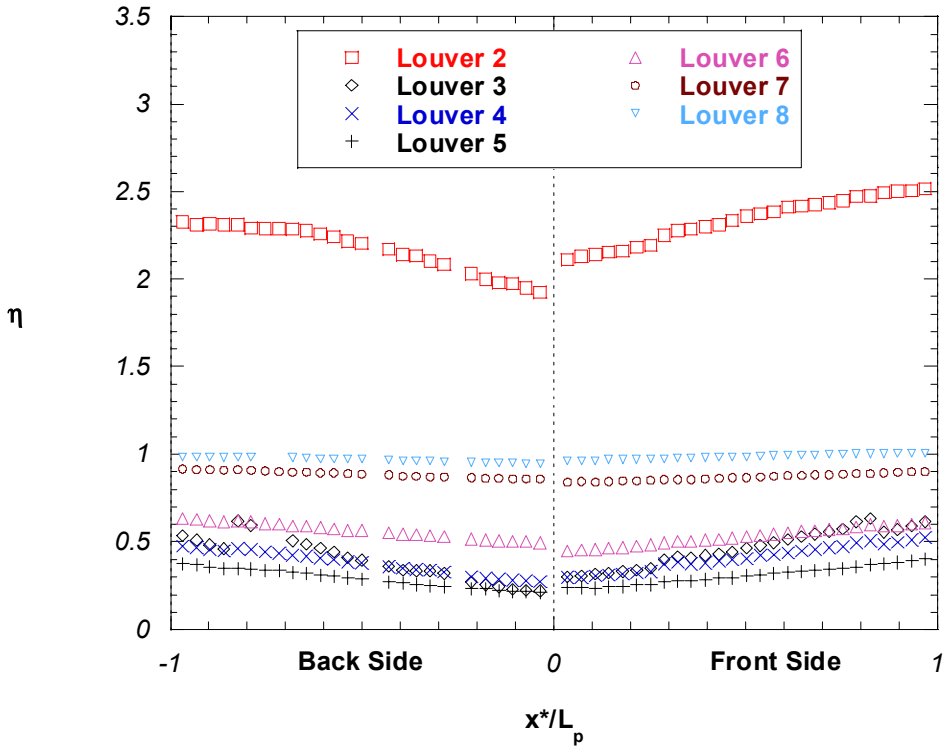

Figure 4.21 Non-dimensional adiabatic wall temperature measurements for the $\theta = 20°$, $F_p/L_p = 1.52$ louvered fin model at $Re_{Lp} = 230$.

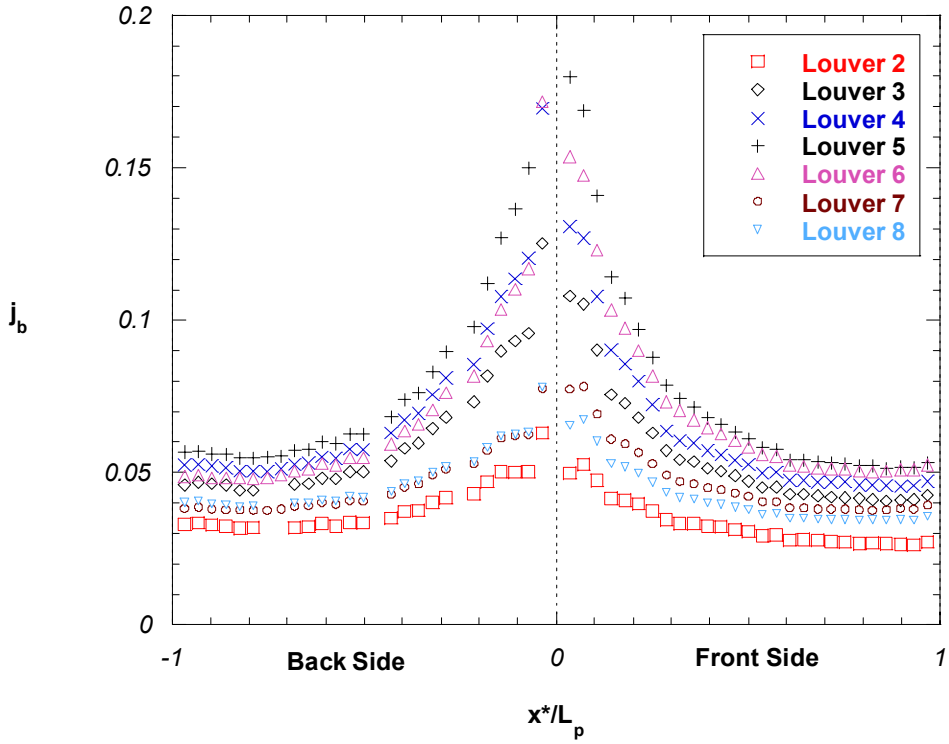

Figure 4.22 Colburn factor measurements based on the bulk flow temperature for the $\theta = 20°$, $F_p/L_p = 1.52$ louvered fin model at $Re_{Lp} = 370$.

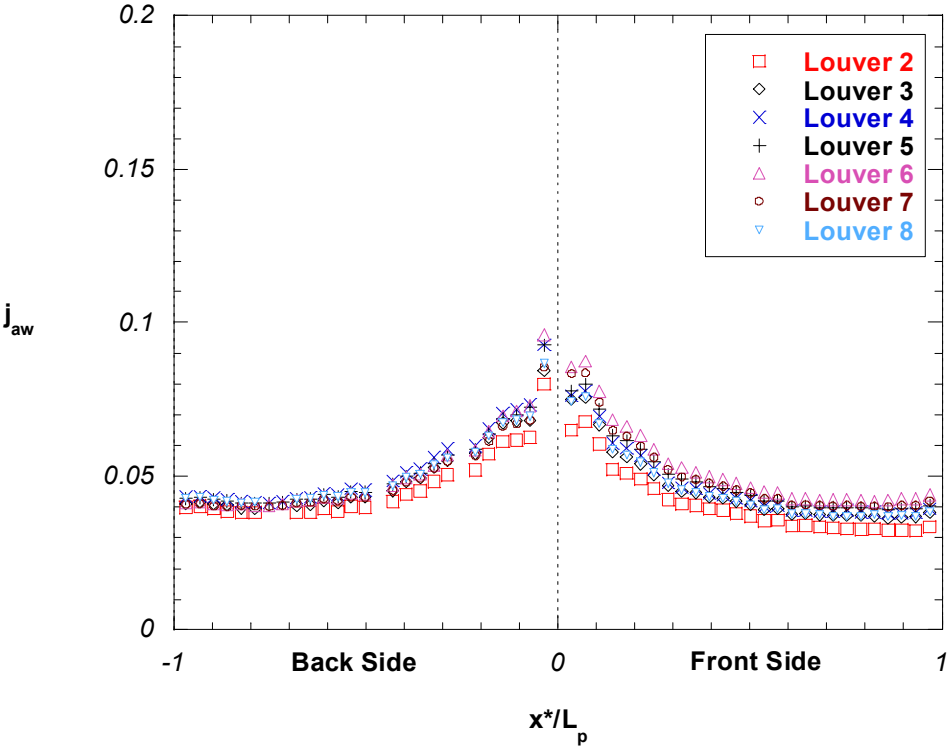

Figure 4.23 Colburn factor measurements based on the adiabatic wall temperature for the $\theta = 20°$, $F_p/L_p = 1.52$ louvered fin model at $Re_{Lp} = 370$.

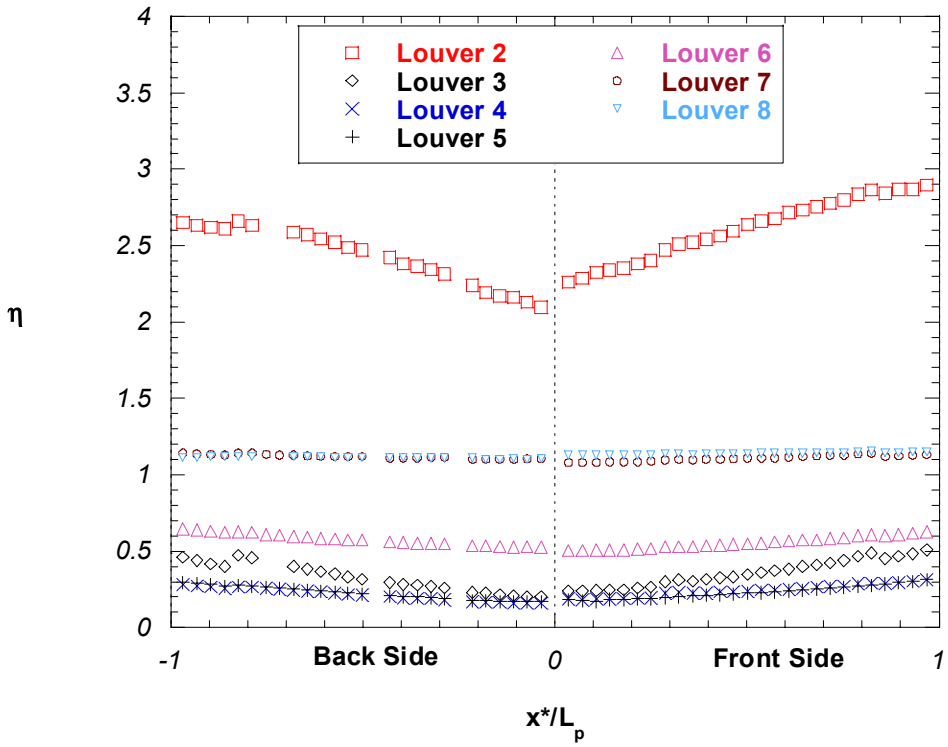

Figure 4.24 Non-dimensional adiabatic wall temperature measurements for the $\theta = 20°$, $F_p/L_p = 1.52$ louvered fin model at $Re_{Lp} = 370$.

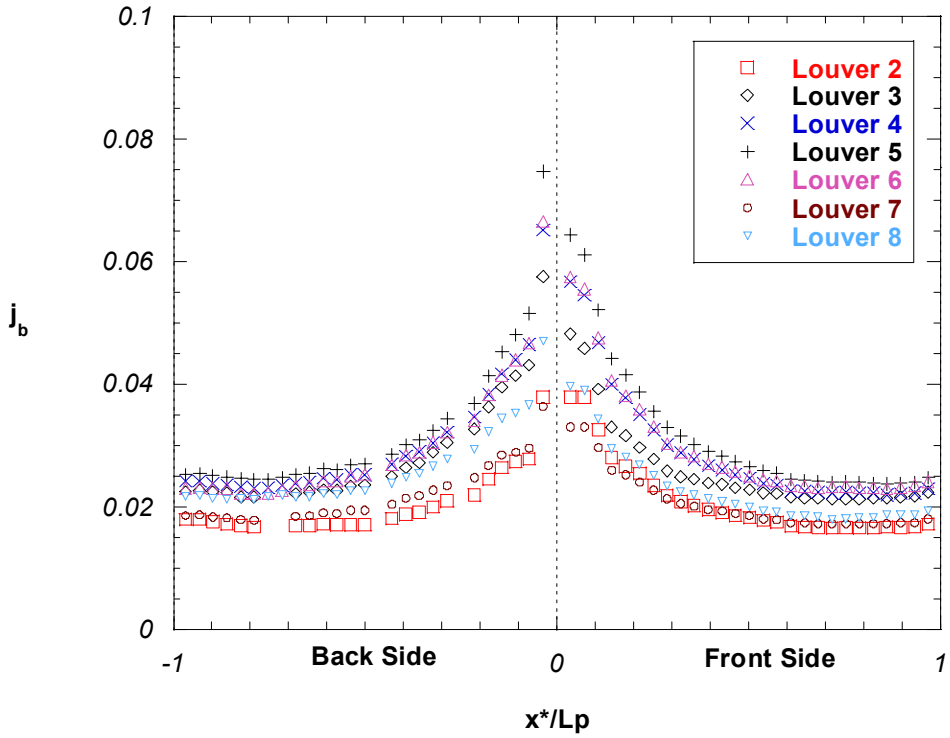

Figure 4.25 Colburn factor measurements based on the bulk flow temperature for the $\theta = 20°$, $F_p/L_p = 1.52$ louvered fin model at $Re_{Lp} = 1016$.

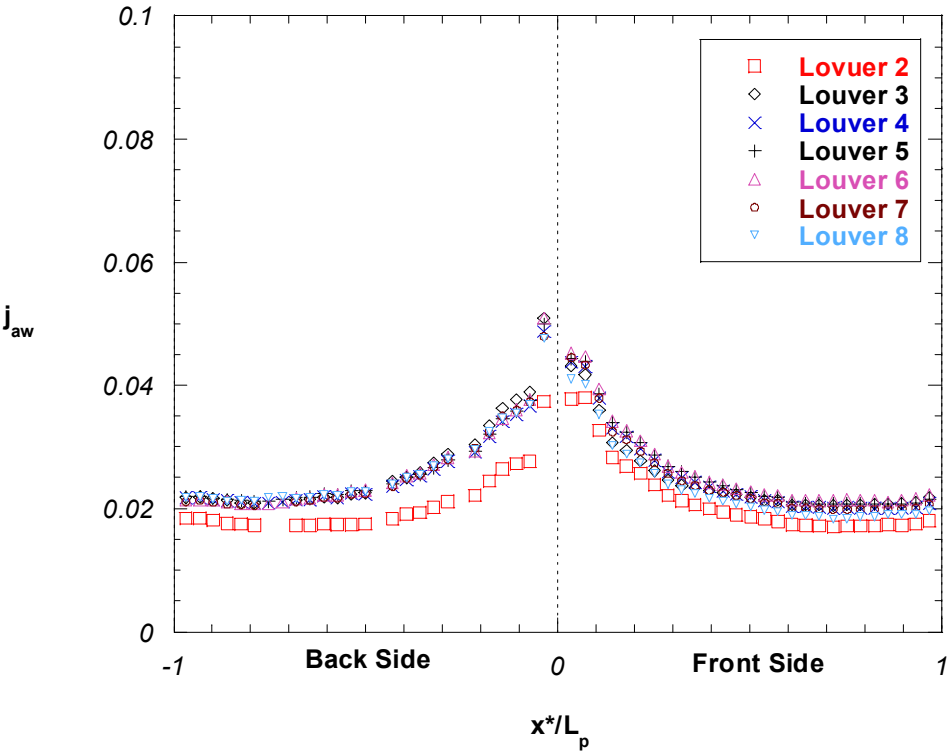

Figure 4.26 Colburn factor measurements based on the adiabatic wall temperature for the $\theta = 20°$, $F_p/L_p = 1.52$ louvered fin model at $Re_{Lp} = 1016$.

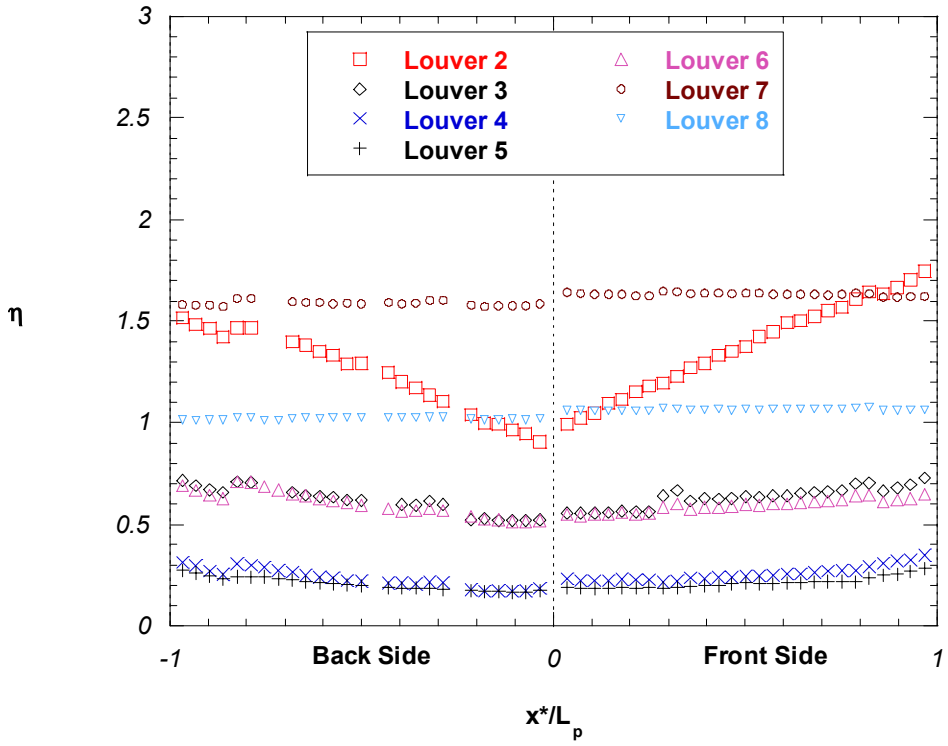

Figure 4.27 Non-dimensional adiabatic wall temperature measurements for the $\theta = 20°$, $F_p/L_p = 1.52$ louvered fin model at $Re_{Lp} = 1016$.

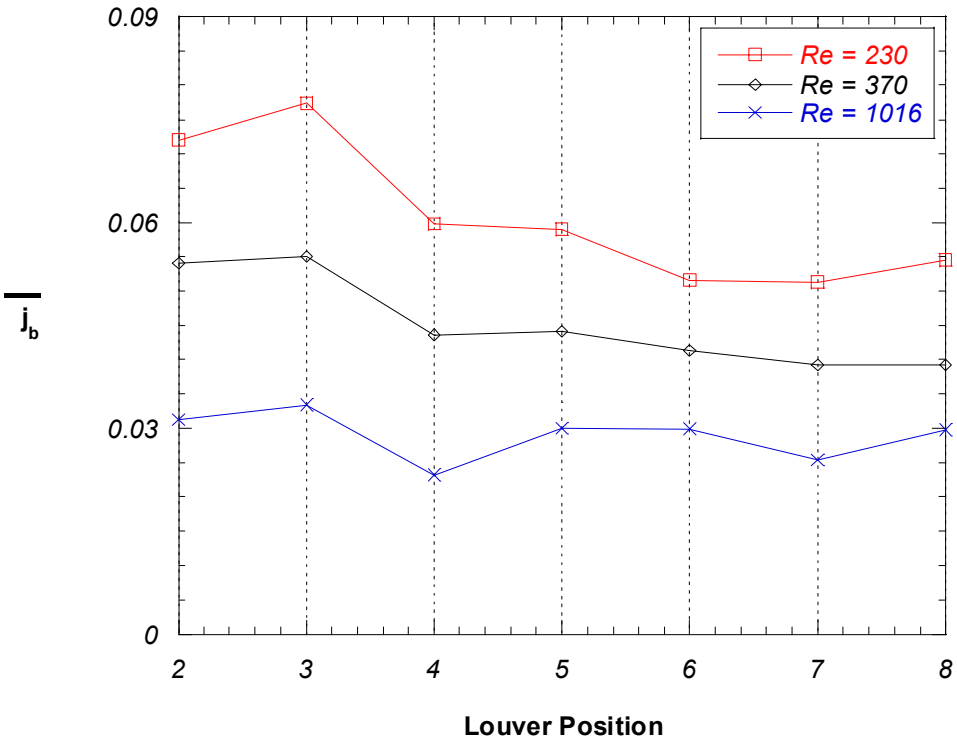

Figure 4.28 Louver-averaged Colburn factor measurements based on the bulk flow temperature for the $\theta = 20°$, $F_p/L_p = 0.54$ louvered fin model.

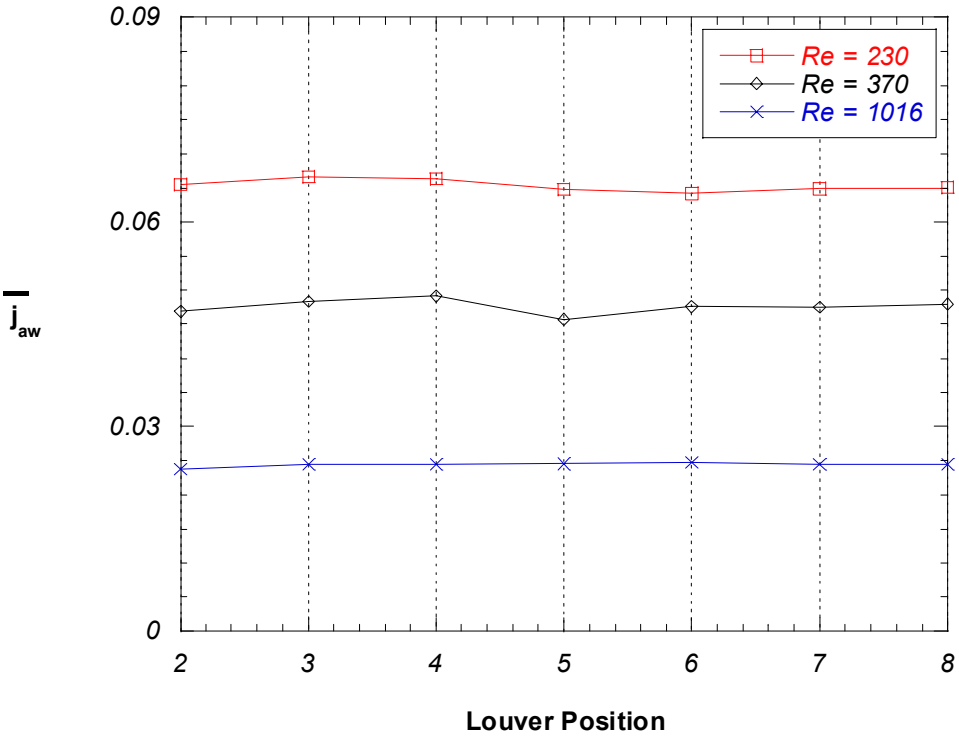

Figure 4.29 Louver-averaged Colburn factor measurements based on the adiabatic wall temperature for the $\theta = 20°$, $F_p/L_p = 0.54$ louvered fin model.

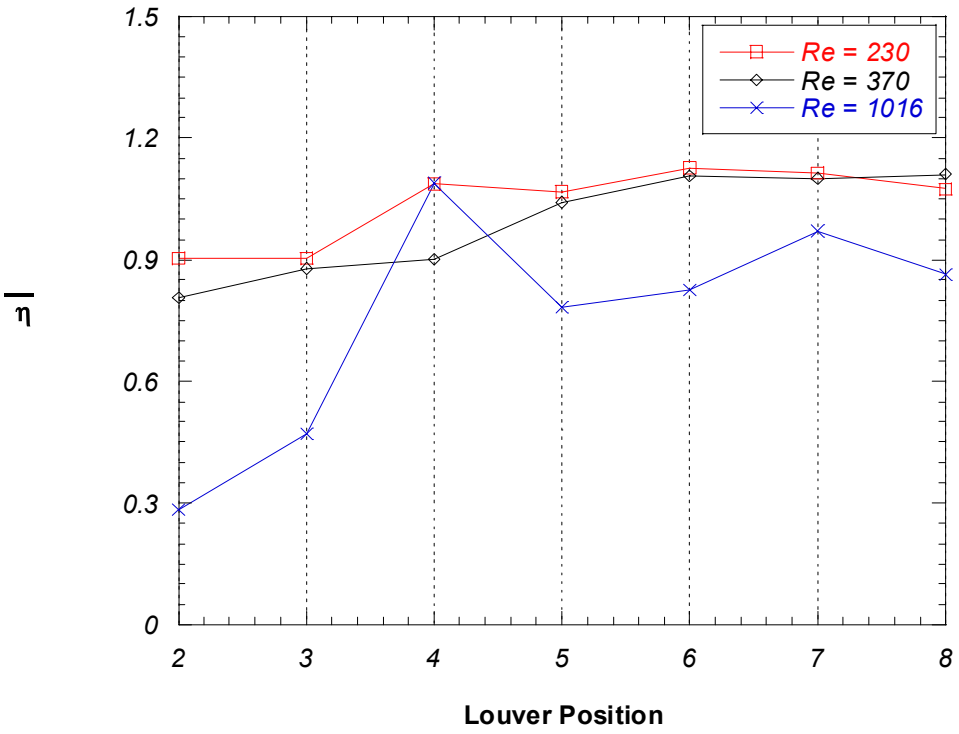

Figure 4.30 Louver-averaged non-dimensional adiabatic wall temperature measurements for the $\theta = 20°$, $F_p/L_p = 0.54$ louvered fin model.

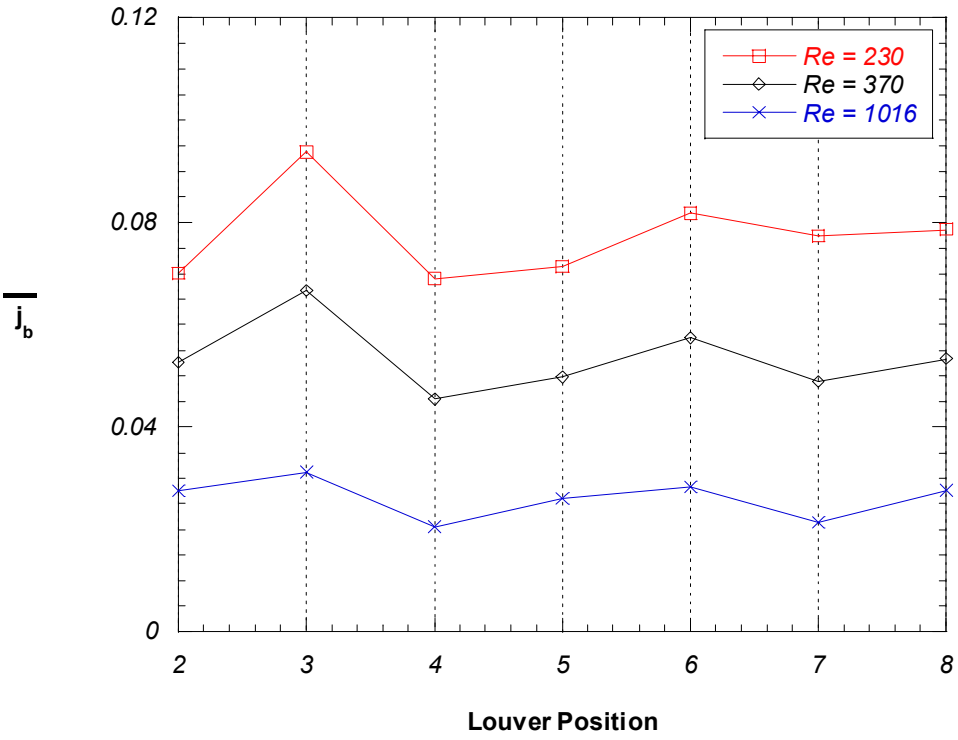

Figure 4.31 Louver-averaged Colburn factor measurements based on the bulk flow temperature for the $\theta = 20°$, $F_p/L_p = 0.91$ louvered fin model.

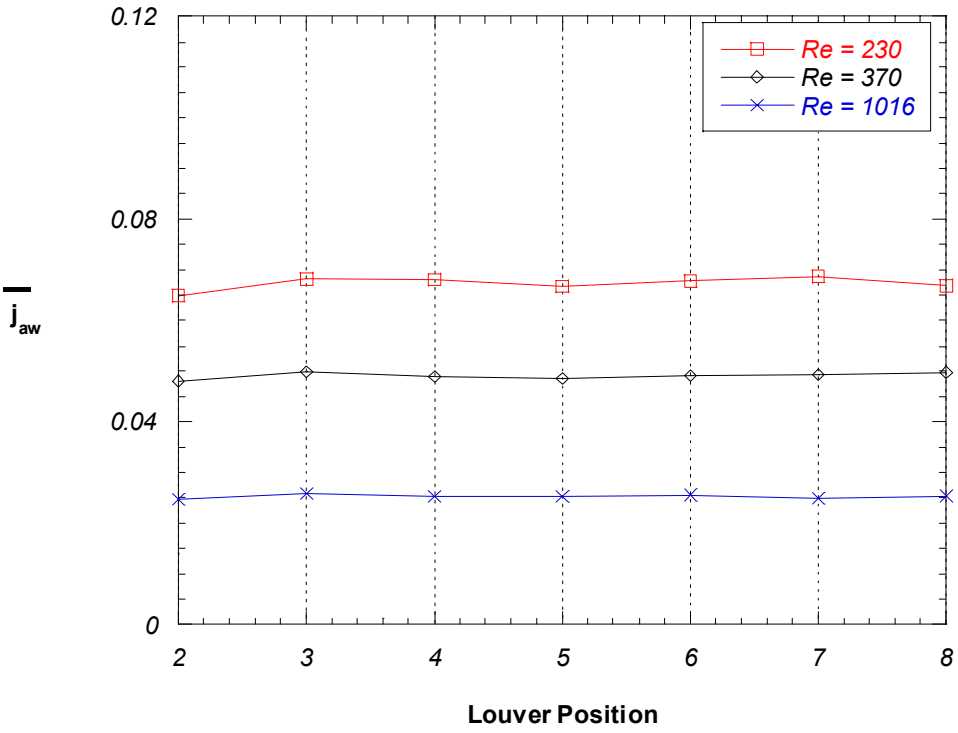

Figure 4.32 Louver-averaged Colburn factor measurements based on the adiabatic wall temperature for the $\theta = 20°$, $F_p/L_p = 0.91$ louvered fin model.

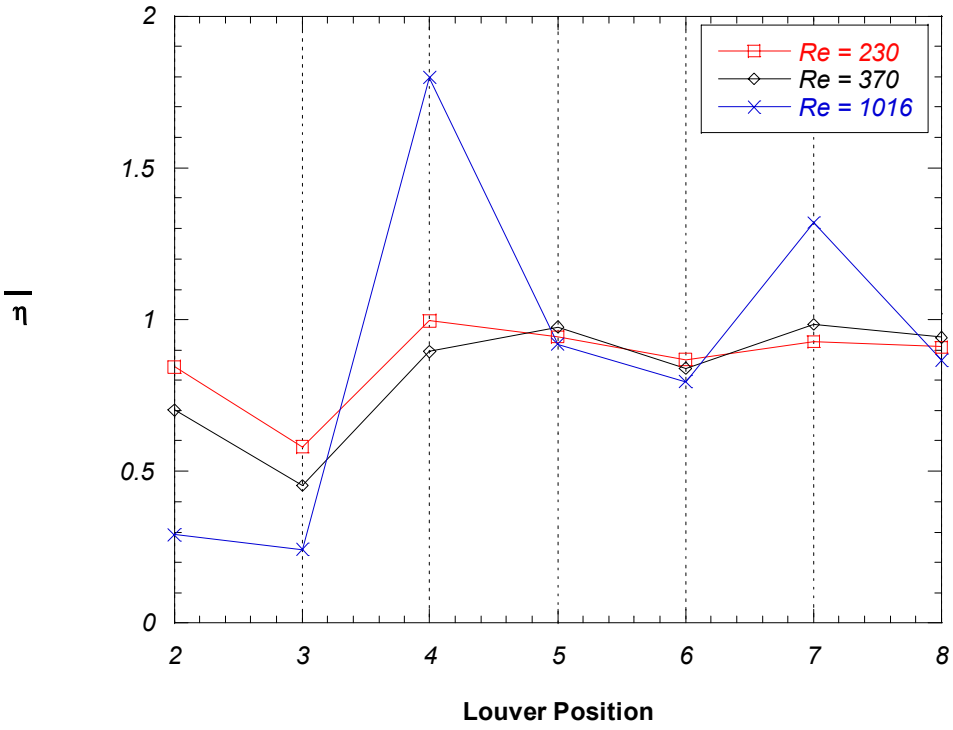

Figure 4.33 Louver-averaged non-dimensional adiabatic wall temperature measurements for the $\theta = 20°$, $F_p/L_p = 0.91$ louvered fin model.

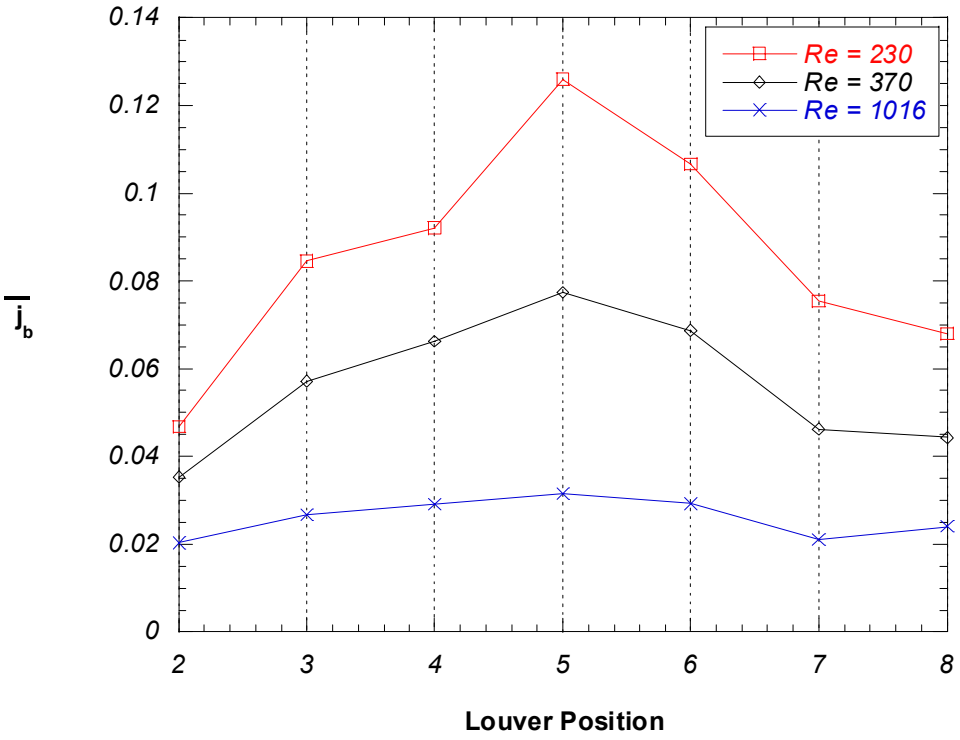

Figure 4.34 Louver-averaged Colburn factor measurements based on the bulk flow temperature for the $\theta = 20°$, $F_p/L_p = 1.52$ louvered fin model.

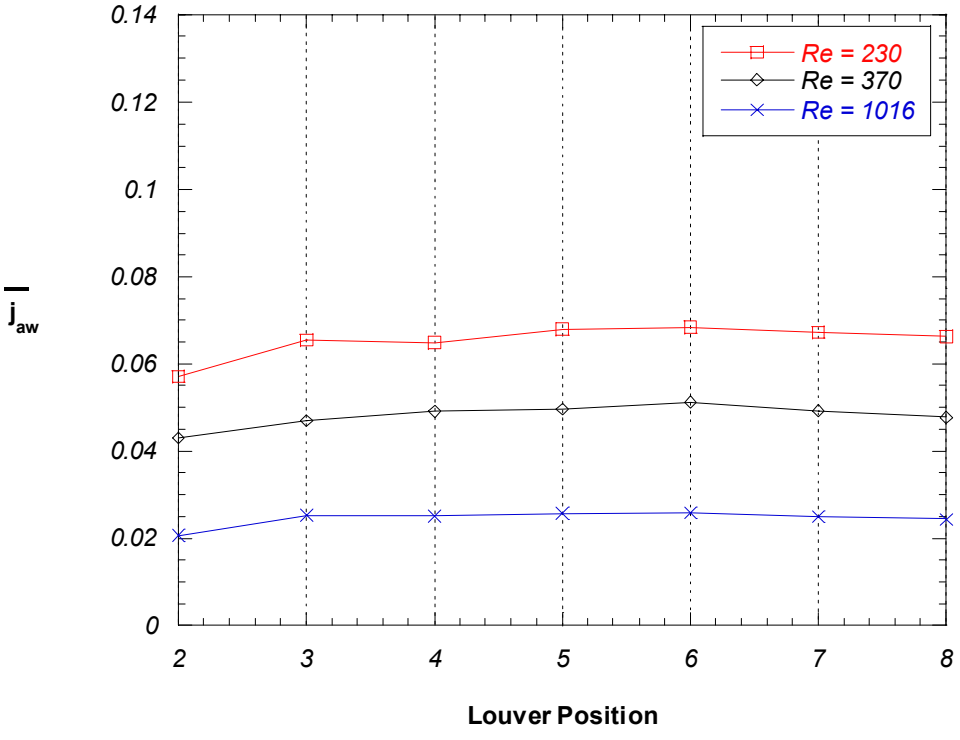

Figure 4.35 Louver-averaged Colburn factor measurements based on the adiabatic wall temperature for the $\theta = 20°$, $F_p/L_p = 1.52$ louvered fin model.

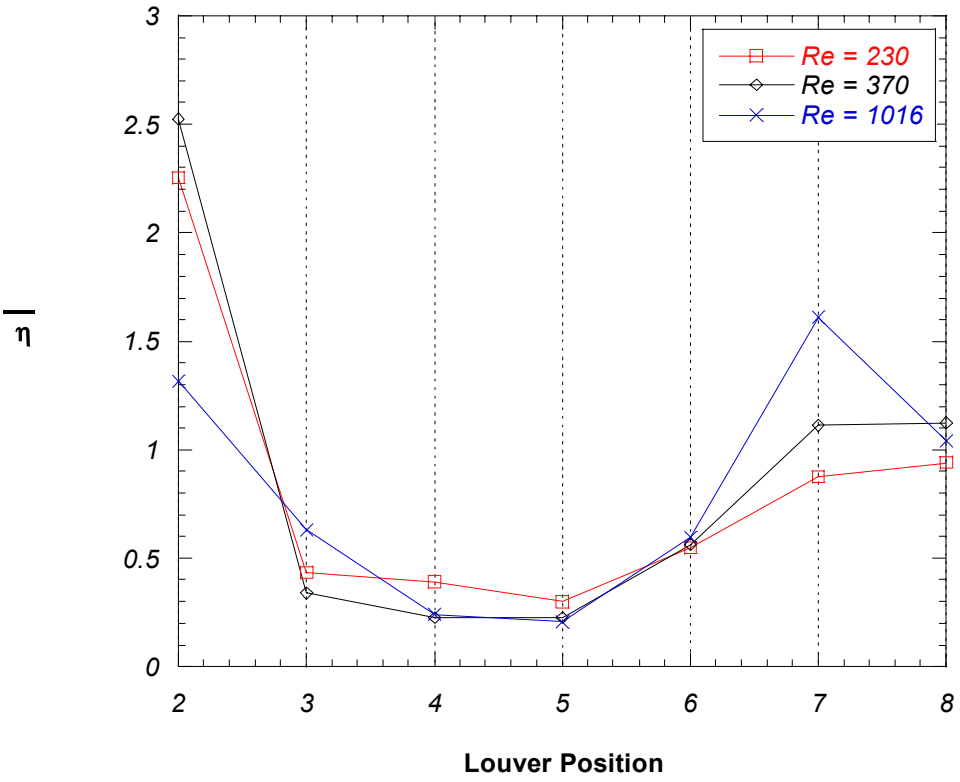

Figure 4.36 Louver-averaged non-dimensional adiabatic wall temperature measurements for the $\theta = 20°$, $F_p/L_p = 1.52$ louvered fin model.

Chapter 5

Comparison of the Nine Louver Models

As mentioned in the previous chapter, nine different scaled-up louver models were designed for this study. This chapter will compare the overall thermal performance of the nine models. The first segment of this chapter will present the expected heat transfer coefficients, as determined by a flat plate correlation, and compare these to the experimental heat transfer results obtained for the louvered fin models. Section 5.2 of Chapter 5 will describe how the thermal field surrounding each of the louvers affects the heat transfer of the louvers. The effects of both the fin pitch and the louver angle on the boundary layer development will be detailed throughout section 5.3. The effect of the Reynolds number on the heat transfer results in a louver-fin array will be discussed in section 5.4. Section 5.5 will show the progression of the entrance louver's wake through the louver passage. The final section will directly compare the nine different louver models based on overall heat transfer performance.

5.1 Flat Plate Correlations

After compiling the heat transfer results for the nine louver models, several basic trends were noticed and will be discussed throughout the following section. As discussed in Chapter 4, the detailed flow measurements performed by Springer and Thole (1998a, 1998b, 1999) showed how the fluid entering the louver array transitioned from being axially directed to louver directed. Once the fluid becomes strongly louver directed, the louvers essentially act as flat plates aligned parallel to the flow. To determine whether the array could be analyzed as a collection of small flat plates in the louver directed region, the experimental heat transfer results were compared with those obtained using a flat plate correlation. The correlation used was that derived for laminar flow over a flat plate with a uniform surface heat flux and is written as (Incropera and DeWitt, 1996)

$$Nu_x = 0.453 Re_x^{1/2} Pr^{1/3} \tag{5.1}$$

In Equation 5.1, Re_x and Pr represent the Reynolds and Prandtl number, respectively. The preceding equation is valid for Pr >0.6, which is the case for the air used in the current test facility. The velocity used in the definition of the Reynolds number was

determined by applying conservation of mass to the flow through a single louver passage. The velocity in a louver passage was slightly higher than that at the entrance of the louver array (0.72 m/s compared to 0.69 m/s) due to the area reduction caused by the finite thickness of the individual louvers. In terms of this study, the flat plate predicted Nusselt number is only a function of the fin pitch and the Reynolds number. The heat transfer coefficient used to define the Nusselt number calculated from Equation 5.1 is based on the freestream temperature. The bulk flow temperature for a louver passage is most analogous to the freestream temperature over a flat plate for the current application.

The Nu_b data at $Re_{Lp} = 230$ is compared with the flat plate predictions in Figures 5.1 and 5.2 for the $F_p/L_p = 1.52$, $\theta = 20°$ and the $F_p/L_p = 0.91$, $\theta = 39°$ models, respectively. From Figure 5.1, it is apparent that the flat plate correlation does not accurately predict the heat transfer coefficient for any of the louver positions. In fact, the louver-averaged difference between the predictions and the empirical data is greater than 50% for the first 6 louver positions. As expected, however, the louver-averaged differences are much less for the 2 louver positions located immediately upstream of the turning louver. The difference on louver 7 is approximately 22%, while the difference on louver 8 is only 10.5%. This convergence is expected because the flow tends to become more louver aligned as it progresses down the louver array. As mentioned above, as the flow transitions to being louver directed, the louvers essentially act as a flat plate in parallel flow. For the $F_p/L_p = 1.52$, $\theta = 20°$ model at $Re_{Lp} = 230$, the model-averaged difference between the flat plate predictions and the empirical data is almost 50% (47.4% to be exact).

Figure 5.2 shows the flat plate predictions and empirical data for the $F_p/L_p = 0.91$, $\theta = 39°$ model at $Re_{Lp} = 230$. For this model, the flat plate prediction is somewhat closer to the measured heat transfer coefficients. The louver-averaged difference is 56.5% at louver 2 and decreases to a value of only 0.75% at louver 7. Again, the difference gets smaller as the flow progresses through the louver array and becomes more louver directed. The model-averaged difference for this model decreases to a value of only 12.9%.

Figures 5.3 and 5.4 show the Nu_b data for the two louver models discussed above at $Re_{Lp} = 1016$. The flat plate predictions for the $F_p/L_p = 1.52$, $\theta = 20°$ model are shown

in Figure 5.3. The predictions are closer to that measured for the louver at the higher Reynolds number. The reason for this was briefly alluded to in the previous chapter. At a high Reynolds number, the flow becomes louver directed further upstream than at the low Reynolds number. For this model, the maximum louver-averaged difference is 27% and occurs for louver 2. The minimum louver-averaged difference is approximately 5% and the model-averaged difference is only 13.2%, a significant decrease from the 47.4% that occurs for $Re_{Lp} = 230$. Figure 5.4 shows the flat plate predictions for the $F_p/L_p = 0.91$, $\theta = 39°$ at $Re_{Lp} = 1016$. Of all the cases calculated, this is the one that the flat plate predictions are most accurate. The louver-averaged differences for this model did not exceed 18.5% for any of the seven louver positions and the model-averaged difference was approximately 11%. The most important observation form the previous four figures is that the heat transfer coefficients for the louvers in the array are greater than those predicted by the flat plate correlation. This shows that adding the louvers to the fins greatly enhances the heat transfer coefficient on those surfaces.

It is apparent from the above discussion that the flat plate predictions for the $F_p/L_p = 0.91$, $\theta = 39°$ model are somewhat closer than those for the $F_p/L_p = 1.52$, $\theta = 20°$ model. To explain this, the reader is referred to the louver geometry figures located in Chapter 2 (Figures 2.2-2.4). Of the 9 louver models, the $F_p/L_p = 0.91$, $\theta = 39°$ model is the louver array that most resembles a flat plate. From Figure 2.4 a, it appears as though all of the louvers are very close to being fully aligned. Figure 2.2 c shows the louver geometry for the $F_p/L_p = 1.52$, $\theta = 20°$ model and from this figure, one can see that this geometry is the one with the most variance in the louver alignment. For this reason, it is expected that the flat plate predictions would not accurately match the empirical data, which is indeed the case. It is also important to note that for both of the presented models, the flat plate predictions agree with the measurements more closely at $Re_{Lp} = 1016$ further supporting the claim made in the previous chapter that the flow is more louver aligned at high Reynolds numbers.

Figure 5.5 shows the Nusselt number based on the bulk flow temperature for each of the eight louver positions as well as the predicted Nusselt number for a duct geometrically equivalent to the $F_p/L_p = 0.91$, $\theta = 39°$ model. Incropera and DeWitt (1996) stated that the Nusselt number in a duct with a uniform surface heat flux is

constant for the entire length of the duct. For a duct with the same aspect ratio as the $F_p/L_p = 0.91$ model, the Nusselt number is given as $Nu_{Dh} = 5.99$. Notice that the Nusselt number is based on the hydraulic diameter, which is defined as

$$D_h = \frac{4A_c}{P} \tag{5.2}$$

where A_c is the cross-sectional area and P is the wetted perimeter. For the $F_p/L_p = 0.91$, $\theta = 39°$ model, the hydraulic diameter was calculated to be 39.9 mm and the experimental heat transfer coefficient based on the bulk temperature was normalized using this characteristic length. From Figure 5.5, it is quite obvious that the addition of the louvers to the array significantly increase the overall heat transfer performance when compared to the duct predictions. The average experimental Nu_b was calculated to be approximately 17.8 for $Re_{Lp} = 230$, an increase of almost 300%. This shows that the addition of louvers greatly enhances the heat transfer performance of a heat exchanger.

Figures 5.6 and 5.7 show the experimental Nu_{aw} values for each louver position compared to the Nusselt numbers for a flat plate with a length equivalent to the streamwise length of the entrance louver through louver 8. The Nusselt numbers for the flat plates were calculated using Equation 5.1. The heat transfer results in Figures 5.6 and 5.7 are for the $F_p/L_p = 0.91$, $\theta = 39°$ model. Figure 5.6 shows the resultant plot for the $Re_{Lp} = 230$ case. It is apparent from this figure that the louvers have a much higher average heat transfer coefficient than the equivalent flat plate. The average Nusselt number for the flat plate is only 36.4 while the model-averaged Nu_{aw} value is 119.1. The increase in heat transfer performance for the $Re_{Lp} = 1016$ is not as large, but it is still significant. The average Nusselt number for the flat plate correlation is 76.6 and the model-averaged Nu_{aw} is 216.6. The previous three figures show that the addition of louvers to a heat exchanger dramatically increase the heat transfer performance.

5.2 Thermal Field Effects

Louver wall temperatures measured with an adiabatic wall boundary condition provide insight to the thermal field surrounding a particular louver, as discussed in Chapter 3. Figures 5.8-5.10 show the louver-averaged, non-dimensional adiabatic wall temperatures ($\bar{\eta}$) for each of the 9 louver models. Remember from the definition of $\bar{\eta}$

that values greater than unity indicate that the fluid surrounding a particular louver is warmer than the calculated bulk flow temperature. Conversely, a $\bar{\eta}$ value less than one occurs when the fluid surrounding a louver is cooler than the bulk temperature.

The figures mentioned above show that the thermal field surrounding each louver is unique to the model being discussed, as no distinct pattern is evident in the $\bar{\eta}$ values. However, there are several interesting trends evident when Figures 5.8-5.10 are compared. The maximum $\bar{\eta}$ value for each of the models occurs when the wake from the entrance louver impacts a downstream louver. As discussed in the previous chapter, the $F_p/L_p = 0.91$, $\theta = 20°$ model experiences a maximum $\bar{\eta}$ value on louver 4 which is geometrically aligned with the entrance louver. The majority of the models follow this trend in that the highest $\bar{\eta}$ value corresponds to the louver most aligned with the entrance louver. The louver position that experiences the peak $\bar{\eta}$ value does not always, however, correspond to what one might expect if purely louver directed flow was assumed. An example of this is the $F_p/L_p = 1.52$, $\theta = 20°$ model where the fourth louver is aligned with the entrance louver, but the seventh louver is the one that experiences the maximum $\bar{\eta}$ value. The fourth louver experiences a relatively cool surrounding thermal field because the flow tends to remain duct directed for models with a large value of F_p/L_p.

Except for the model just discussed with a $F_p/L_p = 1.52$, $\theta = 20°$, the second louver position has a low $\bar{\eta}$ value for all of the models. The $\bar{\eta}$ value surrounding this louver position shows that the relatively cool fluid entering the array engulfs the louver. For the largest fin pitch at 20°, the $\bar{\eta}$ value is elevated because the mostly duct directed flow exiting from the entrance louver directly impinges onto the surface of louver 2.

For all of the louver angles, the models having the smallest fin pitch are the least affected by the thermal wakes emanating from the entrance louver as shown by the relatively flat lines in Figures 5.8-5.10 each of the three figures being discussed. The middle plot in Figure 5.8 shows the $\bar{\eta}$ values for the $F_p/L_p = 0.91$, $\theta = 20°$ model. From this plot, it can be seen that the $\bar{\eta}$ values for the $Re_{Lp} = 1016$ case are offset from those for the other two Reynolds numbers. This shows that the heated thermal wakes forming

at the entrance louver maintain form further downstream for the higher Reynolds number cases. The same trend can also be seen in the middle plot located in Figure 5.9. While the $\bar{\eta}$ values for the $F_p/L_p = 0.91$, $\theta = 27°$ model at $Re_{Lp} = 1016$ case appear to form a wavelike pattern, the thermal fields were relatively uniform at the other two Reynolds numbers.

Figure 5.11 shows the model-averaged $\bar{\bar{\eta}}$ values as a function of Reynolds number for each of the 9 louver models tested during this study. The lowest $\bar{\bar{\eta}}$ values occurred for the $F_p/L_p = 1.52$, $\theta = 27°$ at each of the three tested Reynolds numbers showing that this model has relatively cooler fluid surrounding the louvers in the array. The highest $\bar{\bar{\eta}}$ values occurred for different models depending upon the operating Reynolds number. The highest $\bar{\bar{\eta}}$ value for $Re_{Lp} = 230$ occurred in the $F_p/L_p = 0.54$, $\theta = 20°$ model. The high model-averaged $\bar{\bar{\eta}}$ value is caused by the high temperature fluid surrounding louver 2. At $Re_{Lp} = 370$ and 1016, the highest model-averaged $\bar{\bar{\eta}}$ values occurred for the $F_p/L_p = 0.91$, $\theta = 27°$ model. It should be noted that the louver geometry corresponding to $F_p/L_p = 0.91$, $\theta = 27°$ is the only model where the louvers are staggered with every other louver position being aligned with one another. This geometry creates a model in which there is a small streamwise distance between successive louver positions allowing the hot thermal wakes to have a greater effect on the downstream louvers as compared to the other louver models.

The Colburn factor based on the bulk flow temperature ($\bar{\bar{j}}_b$) is shown as a function of Reynolds number in Figure 5.12. As expected, the models with the highest model-averaged $\bar{\bar{j}}_b$ typically correspond to those with the lowest model-averaged $\bar{\bar{\eta}}$ values. The reason behind this is described in detail throughout the previous chapter. The worst performing model at the lower Reynolds numbers is the $F_p/L_p = 0.54$, $\theta = 20°$ model as shown by the low model-averaged j_b values in Figure 5.12. The best-performing model at these Reynolds numbers, on the other hand, is the $F_p/L_p = 1.52$, $\theta = 27°$ model. At the higher Reynolds number of $Re_{Lp} = 1016$, the most effective geometry is $F_p/L_p = 0.91$, $\theta = 39°$ while the worst performer is $F_p/L_p = 0.91$, $\theta = 27°$ model. The

findings at the lower two Reynolds numbers are in contrast to the correlations presented by Chang and Wang (1997) as well as Sunden and Svantesson (1990). Remember from Chapter 1 that Chang and Wang's correlation showed that the $F_p/L_p = 0.91$, $\theta = 39°$ model would be the best performer. Sunden and Svantesson's correlation, on the other hand, showed that the $F_p/L_p = 1.52$, $\theta = 39°$ model would excel in heat transfer performance. While both of these correlations do not agree at $Re_{Lp} = 230$ and 370, Chang and Wang's prediction does agree with the results from this study at $Re_{Lp} = 1016$, which showed that the $F_p/L_p = 0.91$, $\theta = 39°$ model is the optimal performer. It is important to note here that Sunden and Svantesson's correlation is not valid at $Re_{Lp} = 1016$. The model-averaged $\bar{\bar{\eta}}$ and $\bar{\bar{j}}_b$ values for the current study are located in Tables 5.1 and 5.2, respectively, at the end of this chapter.

5.3 Boundary Layer Development and Flow Field Effects

It was shown throughout Chapter 4 that using the adiabatic wall temperature as the reference temperature for the heat transfer coefficient typically collapsed the Colburn factors (j_{aw}) for each of the louver positions and models. Throughout most of the models, the j_{aw} did not collapse for the second louver position due to the entrance effects occurring at this louver position.

Figures 5.13-5.15 show the j_{aw} as a function of the F_p/L_p ratio at $Re_{Lp} = 1016$. In studying each of these figures, it is obvious that there are several major outliers. For each of the louver angles presented in these figures, the curve that corresponds to the largest F_p/L_p does not collapse to that of the smaller fin pitches. This is due to the fact that the flow does not become louver directed as quickly at large F_p/L_p ratios, which can cause a separation of the louver boundary layer. In comparing these figures, it can be surmised that the entrance effects are much more pronounced at the large louver angles. While there does appear to be separation on the largest F_p/L_p at $\theta = 20°$, the magnitude of the difference is not as large as that for the other two louver angles. The most obvious case of flow separation occurs for the $F_p/L_p = 1.52$, $\theta = 27°$ model on the back side of louver 2. The separation is caused by the primarily duct directed flow being deflected from and subsequently separating from the rear side of the louver. The most severe cases of

flowfield effects are evident in Figure 5.15. It can be seen from this figure that there is a considerable drop in j_{aw} between the front and back side of louver 2. The asymmetry in the data is due to the axial component of the momentum deflecting the flow from the back side of the louver and causing severe separation. On the front side of louver 2 however, the j_{aw} collapses to a tight band which means that there are no entrance effects on the front side of louver 2 in any of the three $\theta = 39°$ models.

Figures 5.16-5.18 show the j_{aw} values for louver 6 at $Re_{Lp} = 1016$ for each of the louver angles and values of F_p/L_p. The j_{aw} values collapsed to a tight band for all but two of the models ($F_p/L_p = 0.54$, $\theta = 20°$ and $F_p/L_p = 0.91$, $\theta = 39°$) for each of the three louver angles. The results show that the fin pitch does not have a significant effect on the boundary layer development on the louvers located in the fully developed flow region.

The $F_p/L_p = 0.54$, $\theta = 20°$ model has the closest fin spacing of all of the nine models tested. Because of the resulting geometry and close fin spacing, the flow is being blocked by the downstream louvers. Figure 5.16 shows a slight flow disturbance on the front side of the louver being discussed. The flow disturbance shown can be explained by studying the geometry of the array in Figure 2.2a. The flow disturbance on louver 6 is caused by flow blockage. There exists a small gap between the front surface of louver 5 and the back surface of louver 6. Rather than passing through the gap, the flow along the front surface of louver 5 tends to move upwards in the louver array and flow along the front surface of louver 6. The fluid is not parallel to louver 6 and that causes the boundary layer on the front surface of louver 6 to be thick thereby decreasing the heat transfer coefficient on that surface as shown in Figure 5.16.

As mentioned above, the other model whose j_{aw} values do not collapse to a tight band is the $F_p/L_p = 0.91$, $\theta = 39°$ model. The louvers of this array are nearly aligned causing the front side of the louver not to be affected by any upstream flow field wakes. Because the boundary layer along the front side of the louver is not affected by any wakes, the boundary layer is thinner. The thinner boundary layer causes a higher heat transfer coefficient as is evident in Figure 5.18. Also apparent from this figure is the substantially lower j_{aw} values located on the back side of each louver. This lower heat transfer is due to the interaction of the surface's boundary layer with the velocity wakes from the upstream louvers.

With the aid of Figures 5.19 and 5.20, the effect of the louver angle on the heat transfer from the second louver can be determined. Figure 5.19 shows the Colburn factors based on the adiabatic wall temperature (j_{aw}) for $F_p/L_p = 0.91$ and each of the 3 louver angles at louver 2. The j_{aw} data collapses to a tight band on the front side of the models with the high louver angle ($\theta = 27°$ and 39°). For the smallest louver angle of $\theta = 20°$, however, the j_{aw} data does not collapse to that single curve until $x^*/L_p = 0.6$. The reason behind this can be explained by studying the louver geometry in Figure 2.2b. The duct-directed flow that is attached the bottom side of the entrance louver impinges onto the front surface of louver 2 at about the half way point on the downstream louver causing the complete attachment to occur further down the louver surface. It is also quite apparent from Figure 5.19 that the heat transfer data for the $F_p/L_p = 0.91$, $\theta = 39°$ model does not collapse to a single curve on the back side of the louver being presented in this figure. The cause of this was previously discussed in detail above. For the larger $F_p/L_p = 1.52$ presented in Figure 5.20, a very similar trend occurs on the front side of the louver. For these models, the j_{aw} are very asymmetric between the front and back sides for the larger louver angles. The asymmetry of the data can be attributed to the fact that entrance effects are much more pronounced at large louver angles. Another characteristic of the entrance effects is shown in the "hook" that appears towards the trailing edge of the back side of louver 2. The j_{aw} data for both of the large louver angles appear to reattach towards the trailing edge with the heat transfer increasing dramatically for the largest louver angle of $\theta = 39°$.

Figures 5.21 and 5.22 show the j_{aw} data for the fully developed flow around louver 6 at $Re_{Lp} = 1016$. The first of these figures, Figure 5.21, shows the data for $F_p/L_p = 0.91$ at each of the three louver angles. From this figure, it is evident that the j_{aw} values collapse to a single curve for the two smaller louver angles of $\theta = 20°$ and 27° while the primary outlier is the data obtained for the $\theta = 39°$ model. The reason for the non-uniformity in the $\theta = 39°$ model was already discussed above. The symmetry of the $\theta = 20°$ and 27° data show that the flow field is the same for the front and back sides of louver 6. The j_{aw} data for the $F_p/L_p = 1.52$ model at $Re_{Lp} = 1016$ is shown in Figure 5.22. Unlike the previous figure, the j_{aw} values collapse to a single curve for each of the three louver angles tested.

5.4 Effect of Reynolds Number on the Heat Transfer

As expected, the magnitude of the heat transfer coefficient increased as the Reynolds number was increased. However, the magnitude of the Colburn factor actually decreased as the Reynolds number is increased. This change is rather misleading at first but can be explained by studying the definition of the Colburn factor (Equation 3.5). In the definition of the Colburn factor the maximum mass velocity (which increases with increasing Reynolds number) is in the denominator causing the Colburn factor to decrease with increasing Reynolds number.

The Reynolds number affected the heat transfer coefficients of all the louver positions in the array. The effect of the Reynolds number on the flowfield surrounding louver 2 is clearly shown in Figures 5.23-5.28. These figures show the localized j_{aw} normalized by the louver-averaged $\overline{j_{aw}}$ data for the front and back side of each louver in order to make a direct comparison between the differing Reynolds numbers. The data collapses to a single curve for most of the figures listed above. The primary outliers in the data occur for 4 of the models presented in Figures 5.23-5.28. The first model that contains an outlier in the data is the $F_p/L_p = 0.91$, $\theta = 20°$ model. The data collapses to a single curve for the two highest Reynolds numbers ($Re_{Lp} = 230$ and 370); however, the $Re_{Lp} = 230$ data strays from this curve on the front side of louver 2. As mentioned numerous times throughout this document, the flow requires a longer streamwise distance to become fully developed for low Reynolds number flows. The reason for the lower heat transfer on the front side of louver 2 in this model is that the duct directed flow at $Re_{Lp} = 230$ does not attach to the front surface of louver 2 as quickly as it does for the higher Reynolds numbers.

The next obvious outlier in the data occurs for $Re_{Lp} = 1016$ in the $F_p/L_p = 1.52$, $\theta = 27°$ model. The j_{aw} data collapses to a very tight curve on the front side of the louver for each of the Reynolds numbers. However, the j_{aw} data shows severe separation off of the back side of the louver at $Re_{Lp} = 1016$. At $Re_{Lp} = 230$, the momentum of the duct-directed component of the flow is relatively small leading to a minimal amount of flow separation on the louver. The momentum of the flow was much greater at $Re_{Lp} = 1016$ resulting in strong separation of the flow off of the back surface. The same trend is also

noticed in Figure 5.28. It is interesting to compare and contrast the data in Figure 5.25 with that in Figure 5.27. These figures show the data for the same value of F_p/L_p with the only difference being the louver angle. In viewing Figure 5.25, one can see a very small indicator of separated flow near the trailing edge of the back side of louver 2. Figure 5.27, on the other hand, shows severe flow separation near the trailing edge of the back side of louver 2. From the above data, it can be surmised that separation off of the back side of louver 2 generally became more significant as the Reynolds number, fin pitch, and louver angle were increased.

5.5 Thermal Wake Progression

As has been mentioned numerous times throughout this document, it is very important to understand the progression of the heated thermal wakes caused by the entrance louver in the array. This section will document the progression of this wake and discuss why the thermal wake does not always progress through the louver array as one might expect.

Figures 5.29 – 5.46 show the louver geometries for all nine models as well as information about the thermal wake's progression through the louver array for $Re_{Lp} = 230$ and $Re_{Lp} = 1016$. The solid black lines extending from the trailing edge of the entrance louver show how a thermal wake would progress if it were completely louver-aligned. All surfaces having a louver-averaged $\bar{\eta}$ greater than 1.0 are highlighted in red. Remember from the earlier sections that an $\bar{\eta}$ value greater than 1.0 occurs when a thermal wake impinges upon a louver surface. Therefore, the louver surfaces highlighted in red are those that are impacted by an upstream thermal wake. The elevated surface temperature is typically caused by the thermal wake emanating from the entrance louver because that wake is much stronger than those generated by the smaller louvers in the array. Because the progression of the entrance louver's wake is much more important than that of other louvers, this section will primarily focus on the progression of those thermal wakes. In studying Figures 5.29 – 5.46 it is difficult to make any generalized statements for all of the nine louver geometries, however several general trends are obvious and will be discussed in the following paragraphs.

Two general trends are apparent when studying these figures, one of which has already been briefly discussed in a previous section. The first of these trends is that the thermal wakes from the entrance louver are hotter and maintain form further downstream at high Reynolds numbers. There are several instances of this in the nine louver models shown in Figures 5.29 – 5.46. The first occurrence is shown in Figures 5.31 and 5.32. These figures show the thermal wake progression for the $F_p/L_p = 0.91$, $\theta = 20°$ model. For the higher Reynolds number of $Re_{Lp} = 1016$, the thermal wake beginning at the entrance louver impacts both louver 4 and louver 7. At $Re_{Lp} = 230$, however, none of the louvers are impacted by the thermal wake. Another prime example of the progression of a heated thermal wake is the $F_p/L_p = 0.91$, $\theta = 27°$ model in Figures 5.33 and 5.36. In this model, louver 3 is impacted by the thermal wake for both Reynolds numbers. However, for the $Re_{Lp} = 1016$ case, the thermal wake then proceeds to impact both louver 5 and 7 which clearly does not happen for the $Re_{Lp} = 230$ case.

The second of the two trends alluded to in the previous paragraph is the more duct-directed flow in the louvered fin array re-directing the thermal wake in the axial direction. This typically occurs for the models having a large F_p/L_p ratio because the flow entering the array tends to remain duct-directed. The effect was also more pronounced at $Re_{Lp} = 1016$ because the flow entering the array had more momentum in the streamwise direction. The first figure that shows evidence of this phenomenon is Figure 5.32, which shows the wake progression for the $F_p/L_p = 0.91$, $\theta = 20°$ model at $Re_{Lp} = 1016$. The black line extending from the entrance louver shows that the entrance louver is geometrically aligned with louver 6, however the thermal wake impacts louvers 4 and 7 as shown by the red surfaces. The reason can be attributed to the flow being slightly duct-directed causing it to impact louvers located below louver 6.

A very similar trend can be seen in all of the louver geometries having a large F_p/L_p ratio. In Figures 5.43 and 5.44, which shows the $F_p/L_p = 1.22$, $\theta = 39°$ model geometry, louvers 4 and 7 are geometrically aligned with the entrance louver, but the thermal wake from the entrance louver follows a more duct-directed path causing the wake to impact the front and back surfaces of louver 3 instead. As mentioned before, the redirection of entrance louver's thermal wake did not typically occur for the models with a small F_p/L_p ratio as shown by Figures 5.30 and 5.36. Figure 5.30 shows the thermal

wake progression for the $F_p/L_p = 0.54$, $\theta = 20°$ model at $Re_{Lp} = 1016$. In this figure, the black line showing the geometric alignment of the entrance louver coincides with the louver surface shown in red (louver 4). Figure 5.36 shows the progression for the $F_p/L_p = 0.76$, $\theta = 27°$ model at $Re_{Lp} = 1016$. As was the case in the previous model, the black line coincides with the red surfaces (louvers 4 and 7). Because there is not a large gap between successive entrance louvers, the flow entering the louver array becomes louver-directed more quickly at small fin pitches.

5.6 Summary of the Nine Louver Model Comparison

The discussion of the heat transfer and fluid mechanics of the nine louver models presented in this chapter give valuable insight into the performance of a louvered fin heat exchanger. Several very important points were shown throughout this chapter and will be summarized in this section of the document.

Louver-directed flow is desired to maximize the performance of a louver array and there are several geometric properties that aide to obtain louver-directed flow. The flow through a louver array becomes louver-directed in a smaller streamwise distance at large louver angles. However, entrance effects are much more pronounced at the larger louver angles. In terms of an operating Reynolds number, flow tends to remain duct (axially) directed at lower values of Reynolds number. Finally, the flow requires a longer streamwise distance to become louver-directed at high fin pitch values.

For the lower Reynolds numbers of $Re_{Lp} = 230$ and 370, the best performing geometry is the $F_p/L_p = 1.52$, $\theta = 27°$ model. The worst performing model for the lower two Reynolds numbers is the $F_p/L_p = 0.54$, $\theta = 20°$ model. For the largest Reynolds number tested of $Re_{Lp} = 1016$, the best performing model is the $F_p/L_p = 0.91$, $\theta = 39°$ model while the worst performing model is the $F_p/L_p = 0.91$, $\theta = 27°$ model. The optimal performer averaged over all three of the Reynolds numbers is the $F_p/L_p = 1.52$, $\theta = 27°$ model.

Louver Model	Re_{Lp} = 230	Re_{Lp} = 370	Re_{Lp} = 1016	All Reynolds Numbers
F_p/L_p = 0.54, θ = 20°	1.04	0.99	0.75	0.93
F_p/L_p = 0.91, θ = 20°	0.87	0.83	0.89	0.86
F_p/L_p = 1.52, θ = 20°	0.82	0.87	0.81	0.83
F_p/L_p = 0.76, θ = 27°	0.88	0.86	0.80	0.85
F_p/L_p = 0.91, θ = 27°	0.90	0.99	1.31	1.07
F_p/L_p = 1.52, θ = 27°	0.65	0.66	0.69	0.67
F_p/L_p = 0.91, θ = 39°	0.96	0.93	0.80	0.90
F_p/L_p = 1.22, θ = 39°	0.81	0.88	1.03	0.91
F_p/L_p = 1.52, θ = 39°	0.83	0.96	0.86	0.88

Table 5.1 Model-averaged $\bar{\bar{\eta}}$ values for the nine models discussed throughout Chapter 5.

Louver Model	Re_{Lp} = 230	Re_{Lp} = 370	Re_{Lp} = 1016	All Reynolds Numbers
F_p/L_p = 0.54, θ = 20°	0.0608	0.0453	0.0290	0.0450
F_p/L_p = 0.91, θ = 20°	0.0774	0.0535	0.0261	0.0524
F_p/L_p = 1.52, θ = 20°	0.0857	0.0565	0.0260	0.0561
F_p/L_p = 0.76, θ = 27°	0.0805	0.0571	0.0283	0.0553
F_p/L_p = 0.91, θ = 27°	0.0734	0.0497	0.0236	0.0489
F_p/L_p = 1.52, θ = 27°	0.0928	0.0604	0.0269	0.0600
F_p/L_p = 0.91, θ = 39°	0.0711	0.0539	0.0303	0.0518
F_p/L_p = 1.22, θ = 39°	0.0850	0.0583	0.0283	0.0572
F_p/L_p = 1.52, θ = 39°	0.0768	0.0492	0.0271	0.0510

Table 5.2 Model-averaged $\bar{\bar{j}}_b$ values for the nine louver models discussed throughout Chapter 5.

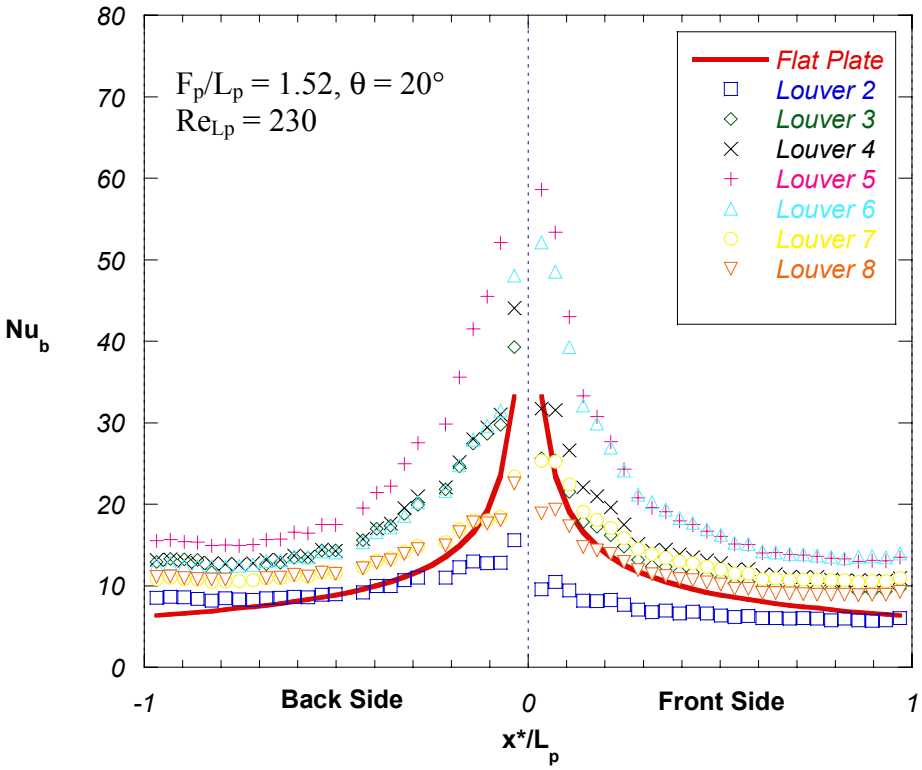

Figure 5.1 Local Nusselt number based on the bulk flow temperature compared to flat plate predictions for the $F_p/L_p = 1.52$, $\theta = 20°$ model at $Re_{Lp} = 230$.

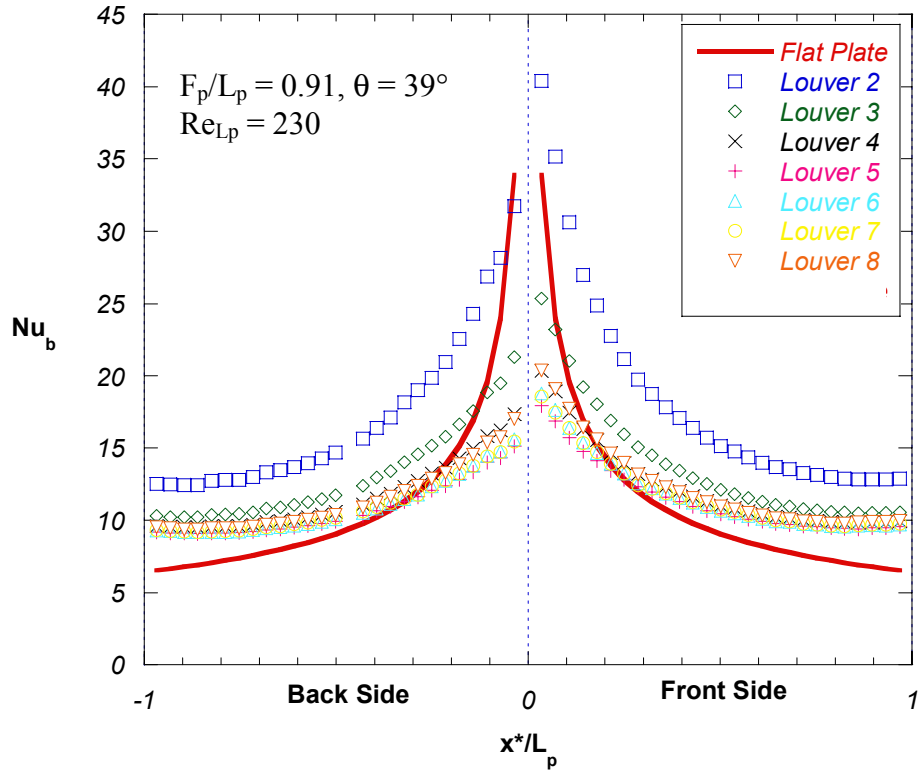

Figure 5.2 Local Nusselt number based on the bulk flow temperature compared to flat plate predictions for the $F_p/L_p = 0.91$, $\theta = 39°$ model at $Re_{Lp} = 230$.

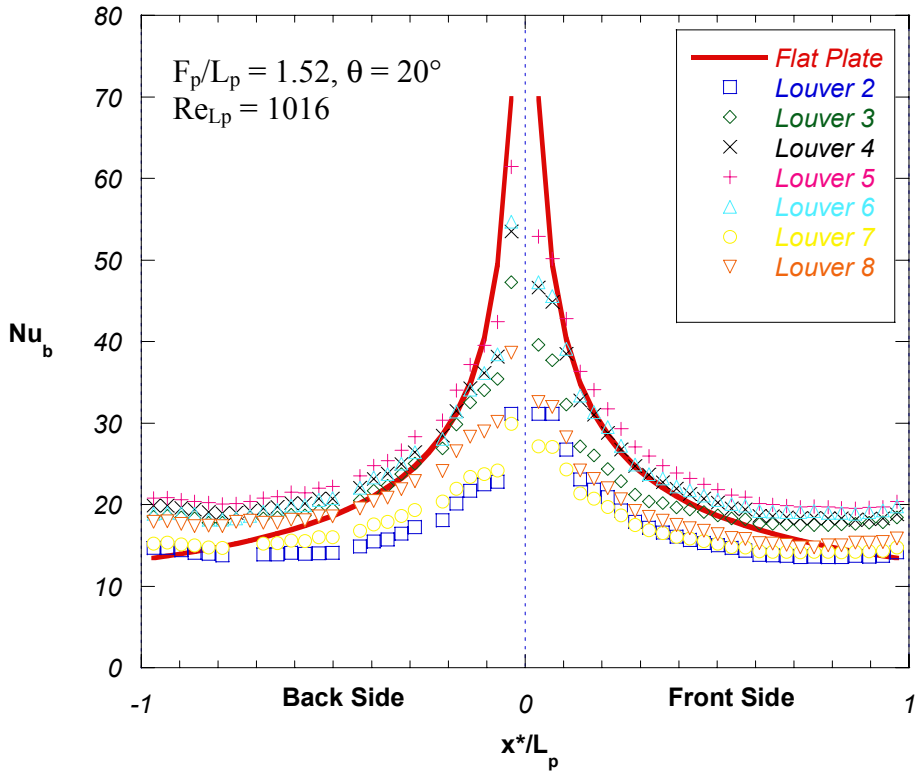

Figure 5.3 Local Nusselt number based on the bulk flow temperature compared to flat plate predictions for the $F_p/L_p = 1.52$, $\theta = 20°$ model at $Re_{Lp} = 1016$.

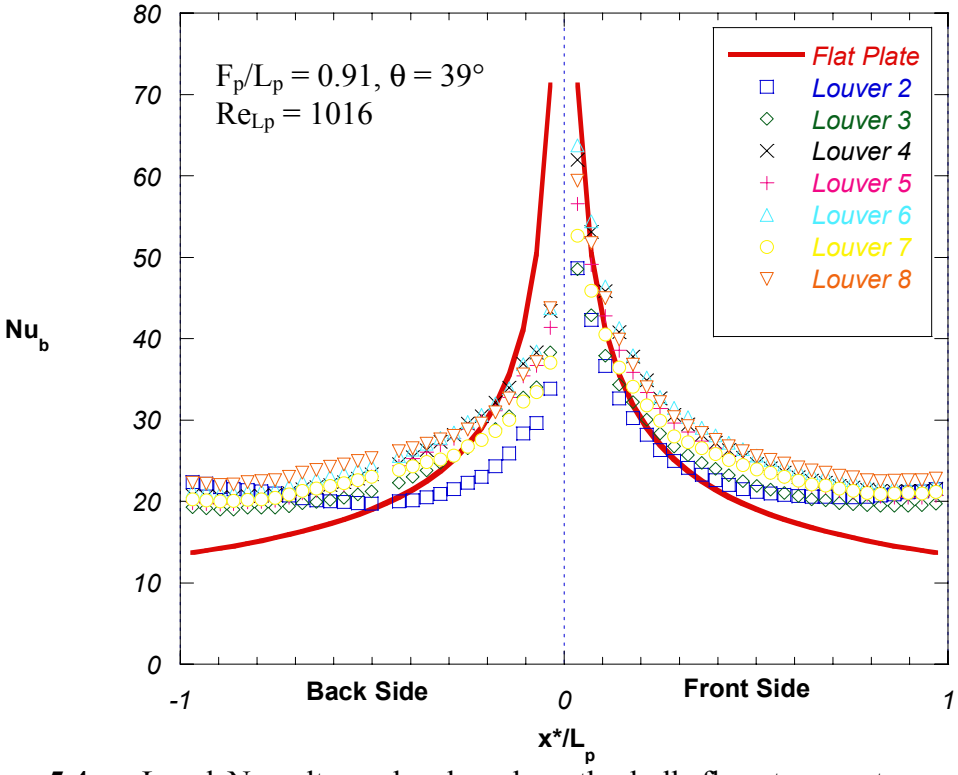

Figure 5.4 Local Nusselt number based on the bulk flow temperature compared to flat plate predictions for the $F_p/L_p = 0.91$, $\theta = 39°$ model at $Re_{Lp} = 1016$.

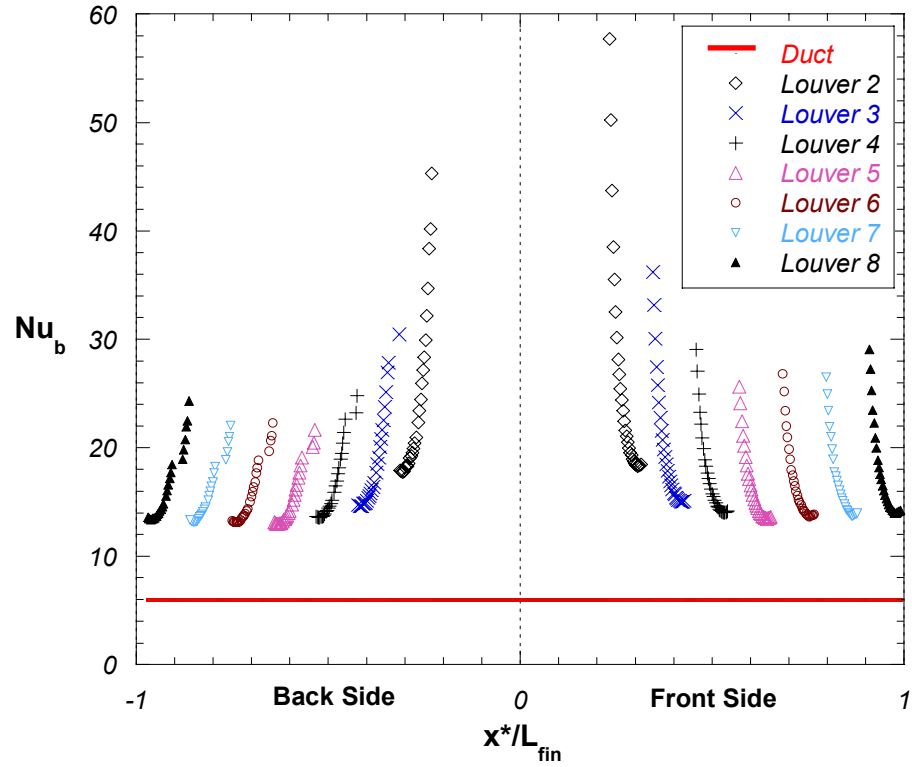

Figure 5.5 Nu_b for each louver shown with the Nusselt number for a duct equivalent to $F_p/L_p = 0.91$, $\theta = 39°$ model at $Re_{Lp} = 230$

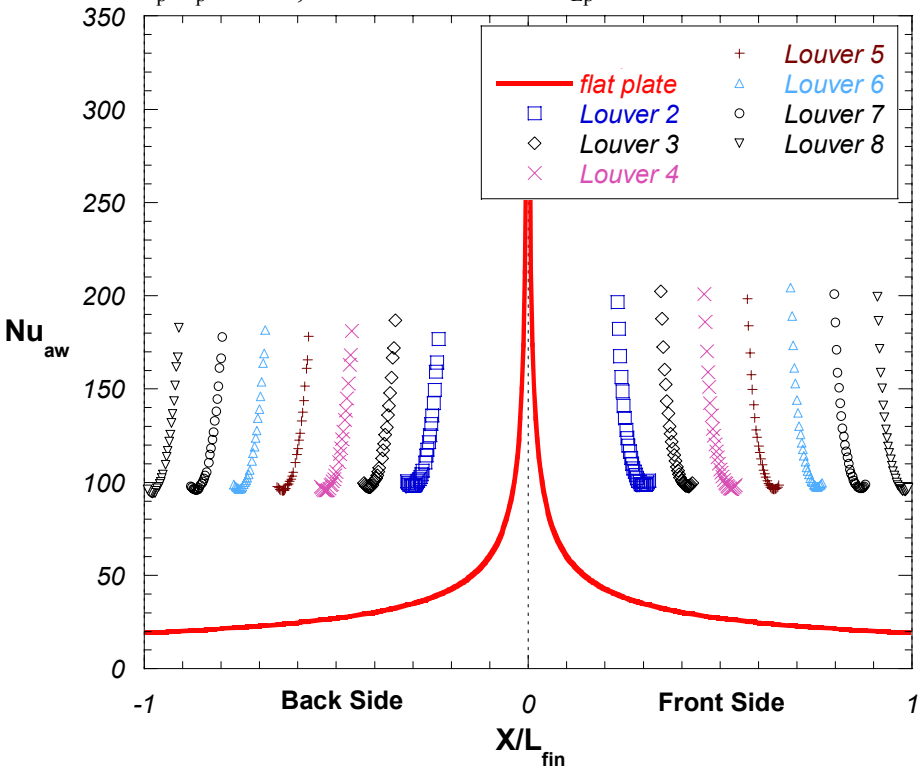

Figure 5.6 Nu_{aw} for each louver position shown with the Nusselt number prediction for a flat plate with the length of one fin. Experimental data shown for $F_p/L_p = 0.91$, $\theta = 39°$ model at $Re_{Lp} = 230$.

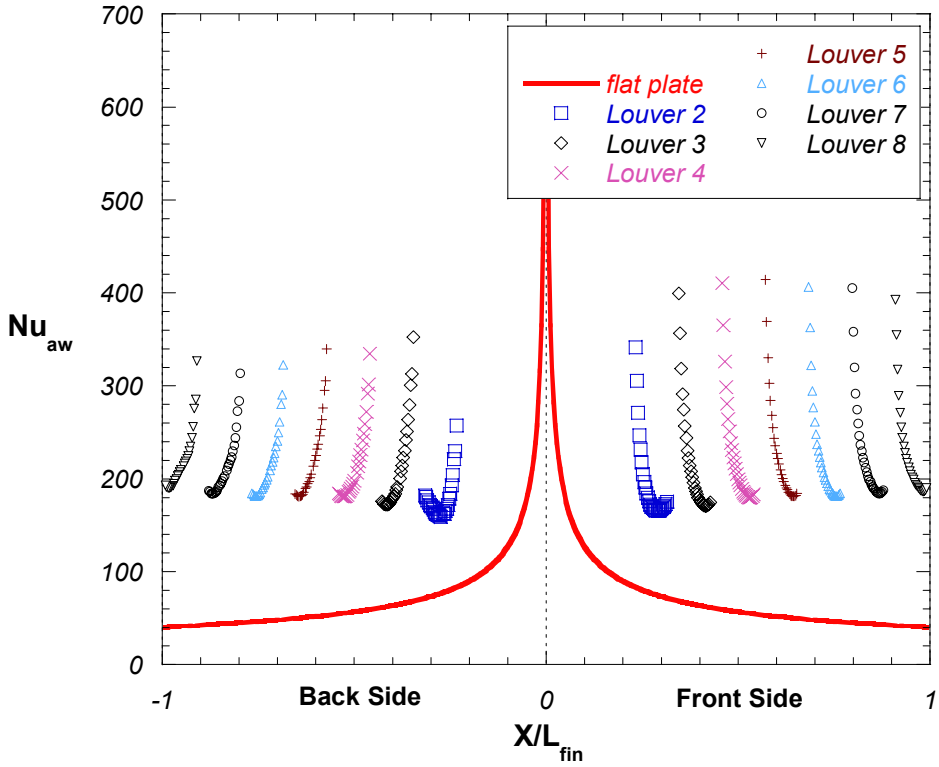

Figure 5.7 Nu_{aw} for each louver position shown with the Nusselt number prediction for a flat plate with the length of one fin. Experimental data shown for $F_p/L_p = 0.91$, $\theta = 39°$ model at $Re_{Lp} = 1016$.

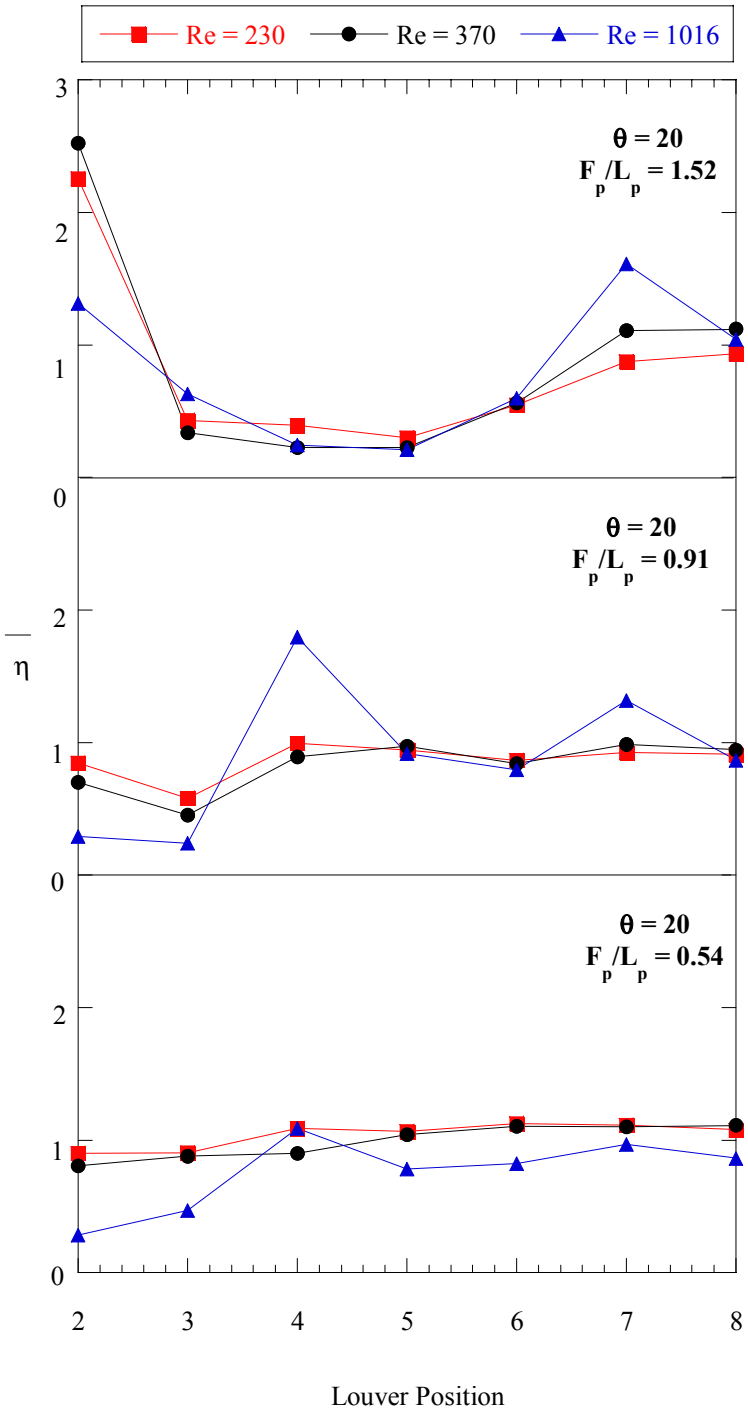

Figure 5.8 Louver-averaged non-dimensional adiabatic wall temperatures at each louver position in the θ = 20° models at all of the tested Reynolds numbers.

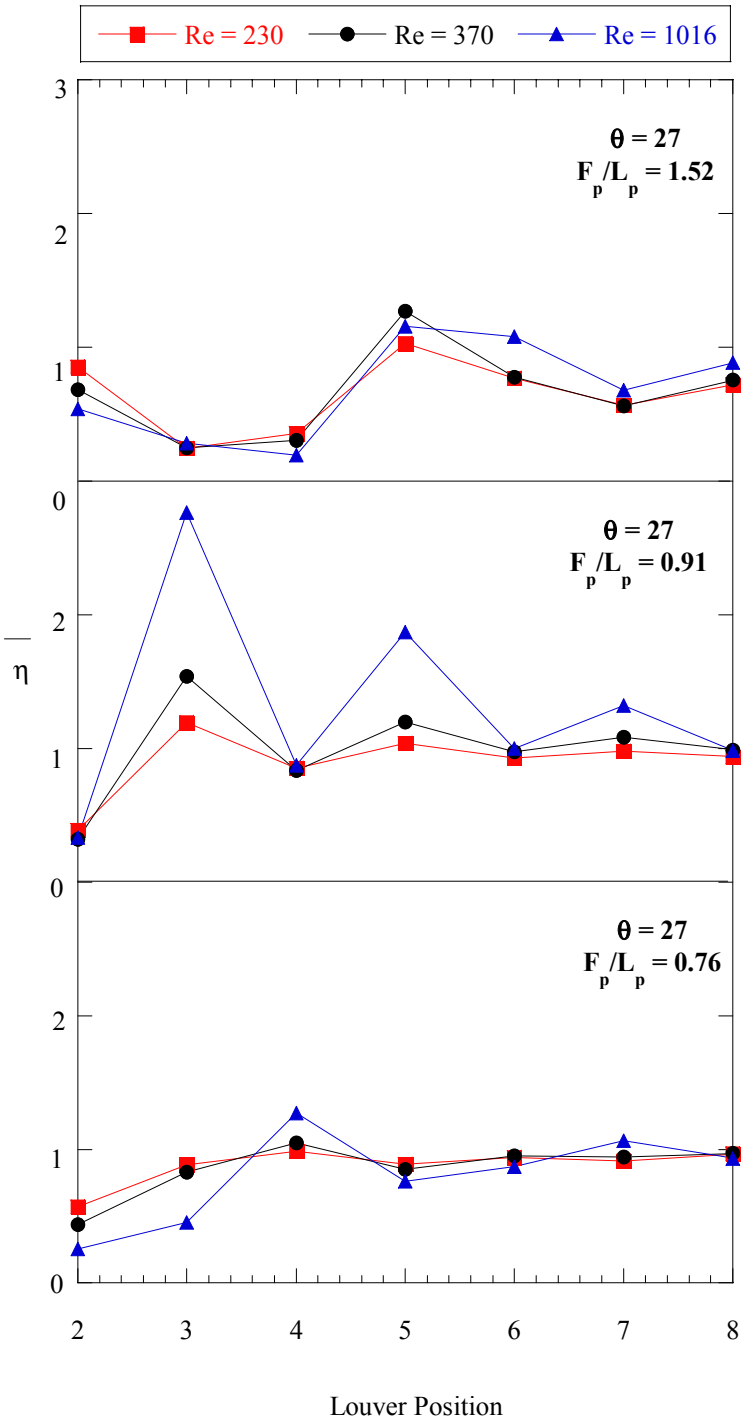

Figure 5.9 Louver-averaged non-dimensional adiabatic wall temperatures at each louver position in the θ = 27° models at all of the tested Reynolds numbers.

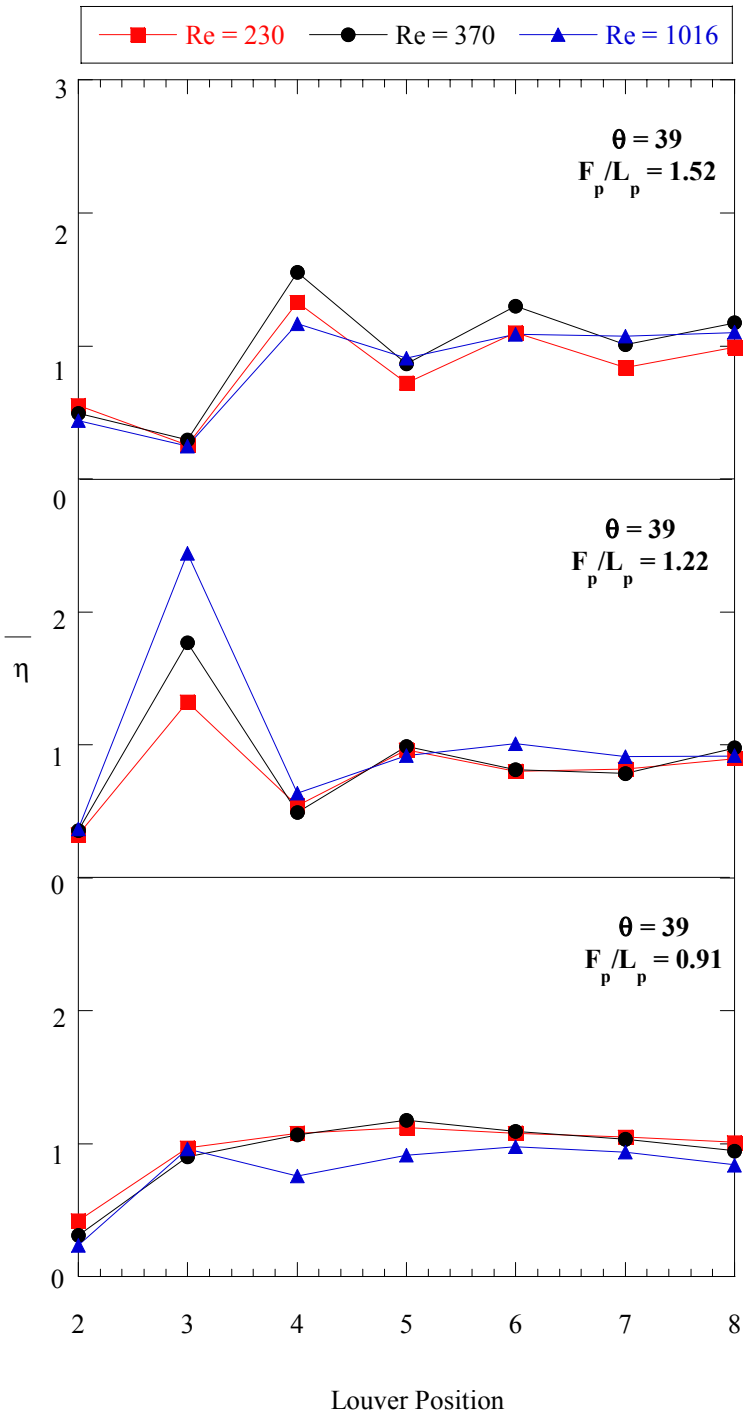

Figure 5.10 Louver-averaged non-dimensional adiabatic wall temperatures at each louver position in the θ = 39° models at all of the tested Reynolds numbers.

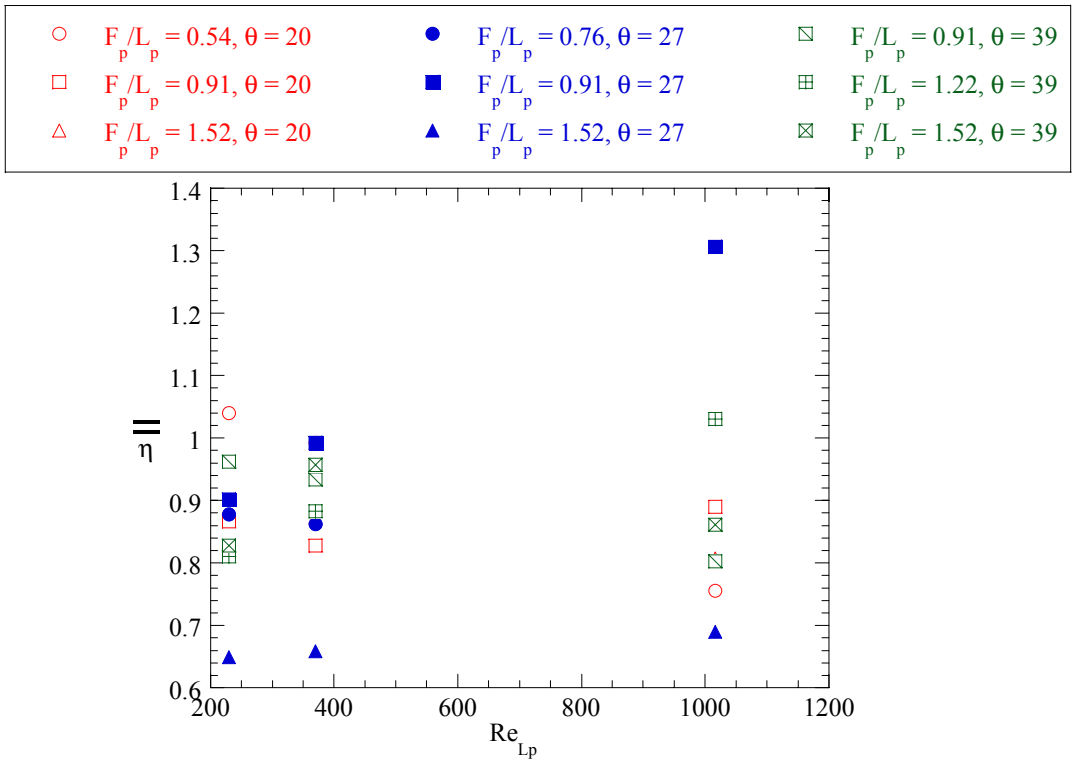

Figure 5.11 Model-averaged non-dimensional adiabatic wall temperatures for all of the tested models.

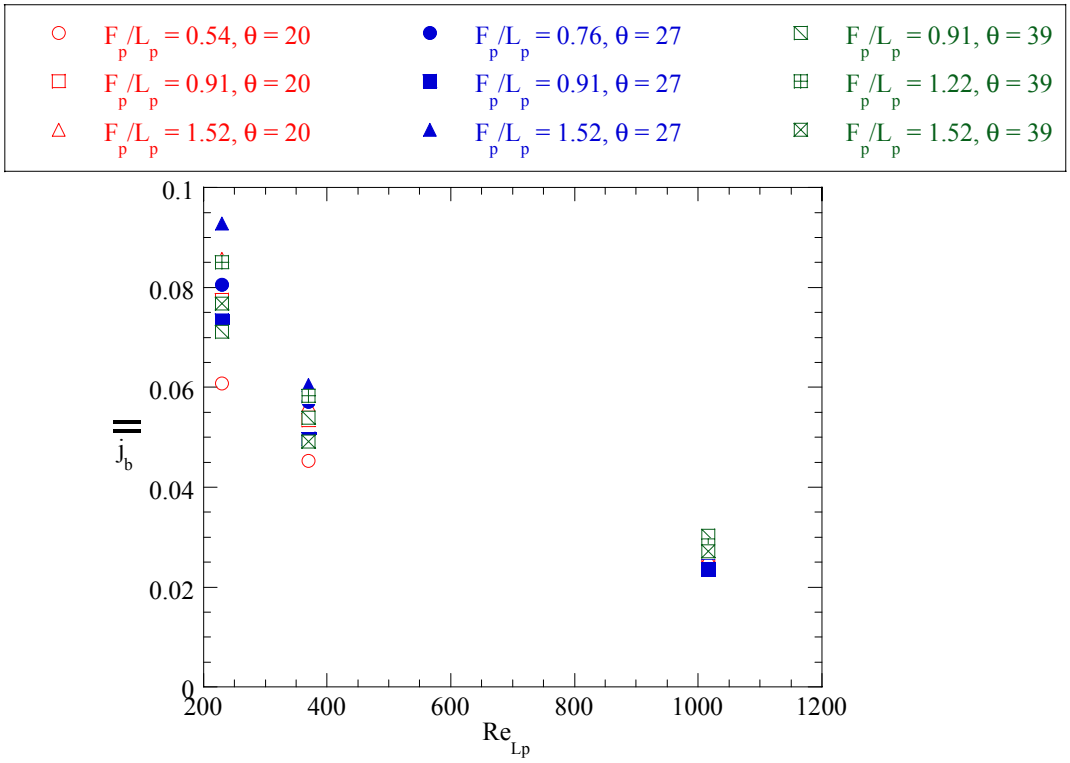

Figure 5.12 Model-averaged Colburn factor based on the bulk flow temperature for each of the nine tested models.

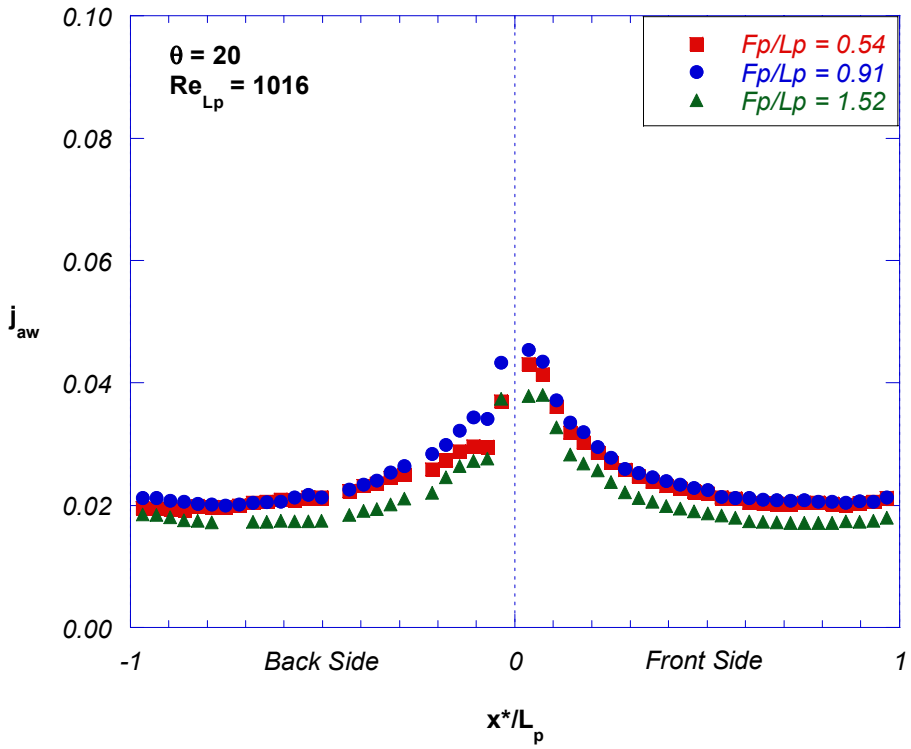

Figure 5.13 Colburn factor measurements based on the adiabatic wall temperature at louver position 2 for Re_{Lp} = 1016 in the θ = 20°and all values of F_p/L_p.

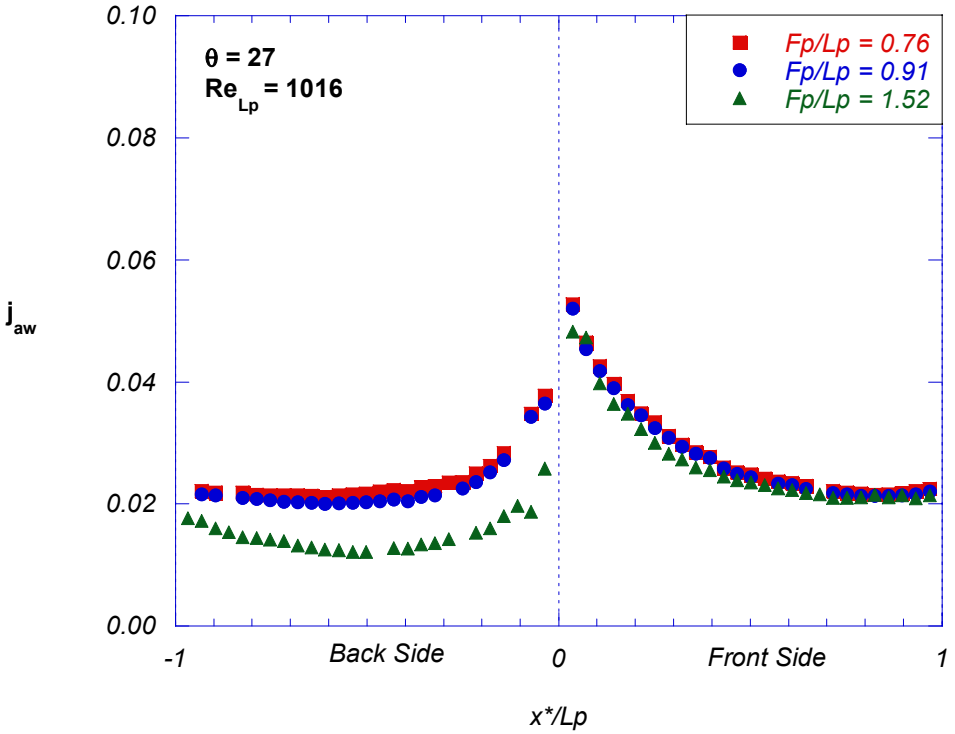

Figure 5.14 Colburn factor measurements based on the adiabatic wall temperature at louver position 2 for Re_{Lp} = 1016 in the θ = 27° and all values of F_p/L_p.

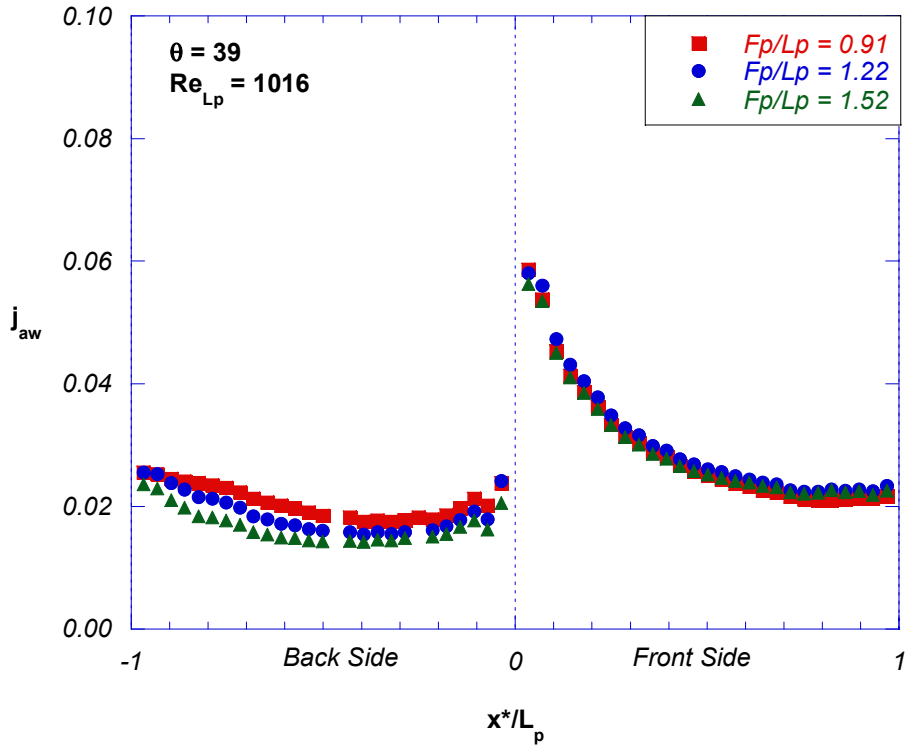

Figure 5.15 Colburn factor measurements based on the adiabatic wall temperature at louver position 2 for Re_{Lp} = 1016 in the θ = 39° and all values of F_p/L_p.

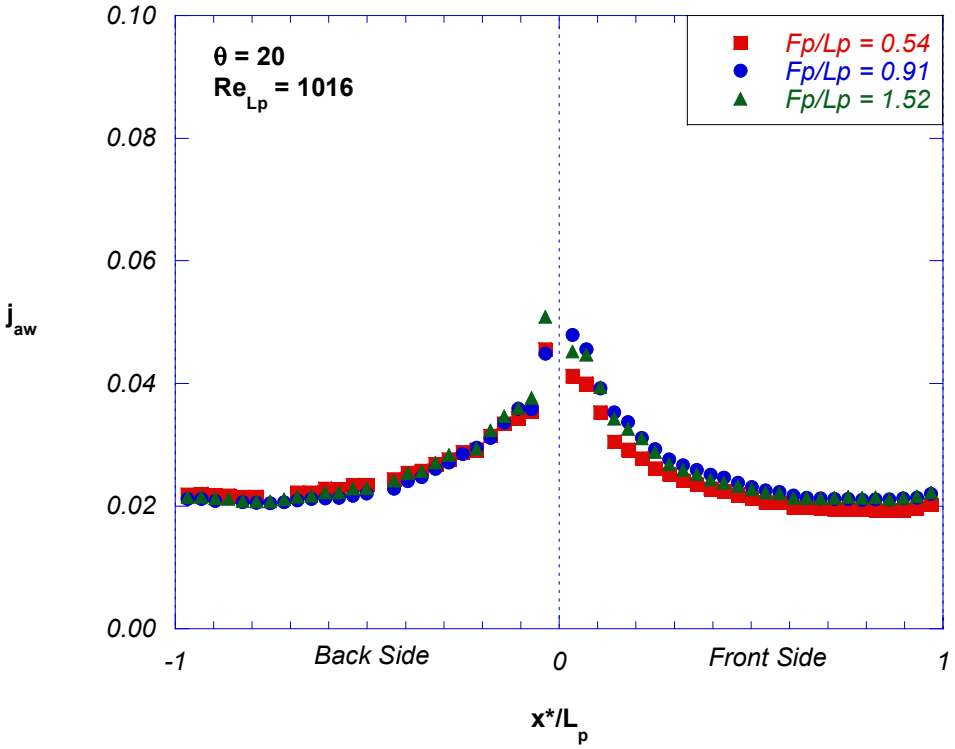

Figure 5.16 Colburn factor measurements based on the adiabatic wall temperature at louver position 6 for Re_{Lp} = 1016 in the θ = 20° and all values of F_p/L_p.

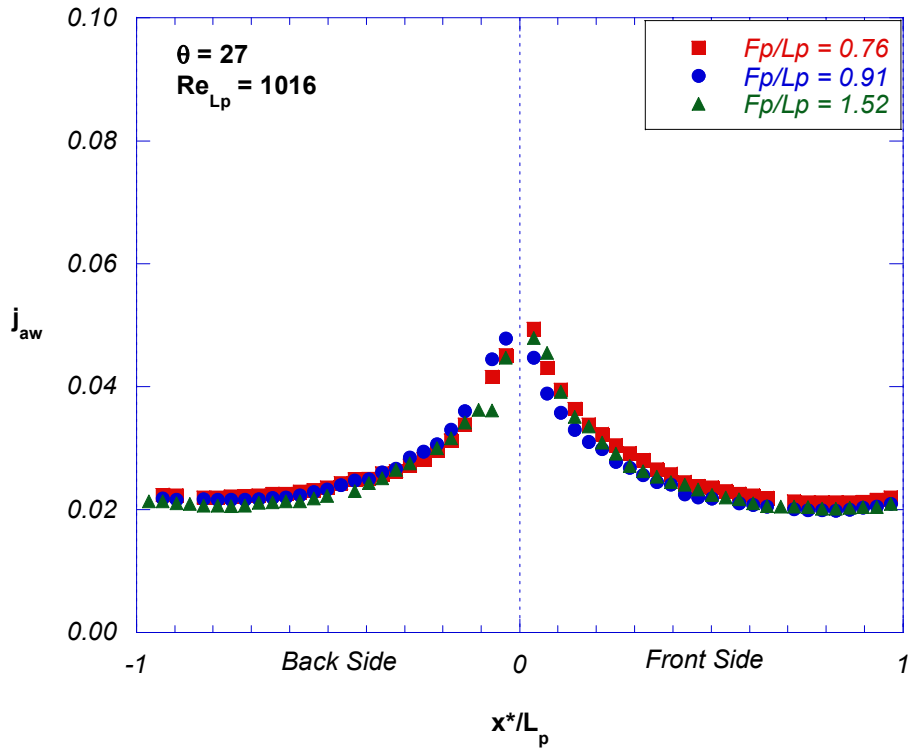

Figure 5.17 Colburn factor measurements based on the adiabatic wall temperature at louver position 6 for Re_{Lp} = 1016 in the θ = 27° and all values of F_p/L_p.

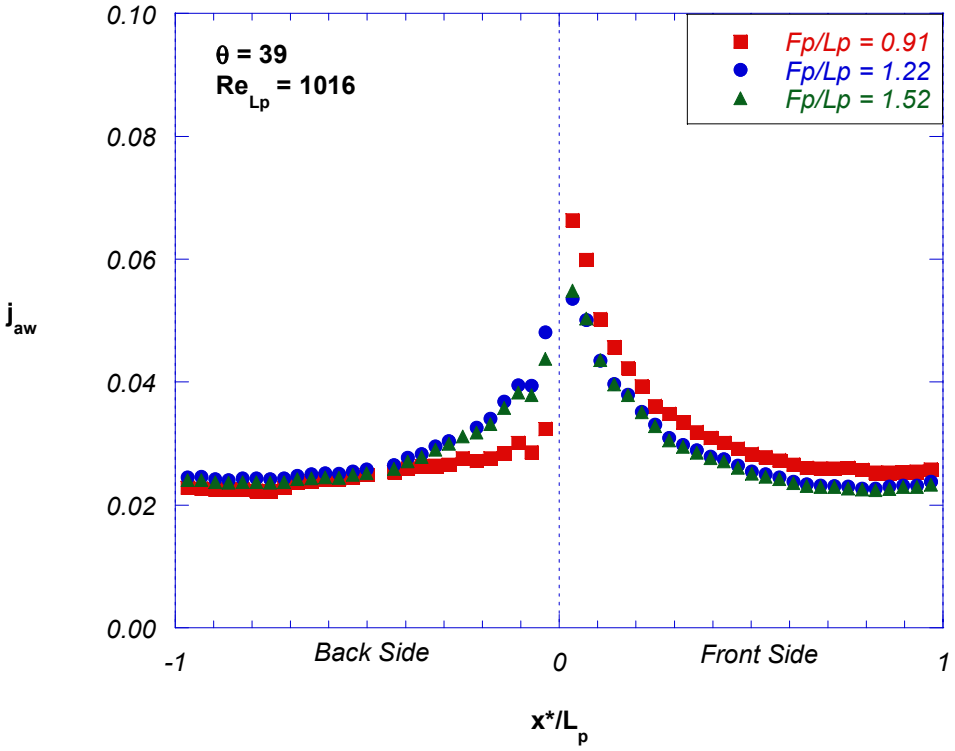

Figure 5.18 Colburn factor measurements based on the adiabatic wall temperature at louver position 6 for Re_{Lp} = 1016 in the θ = 39° and all values of F_p/L_p.

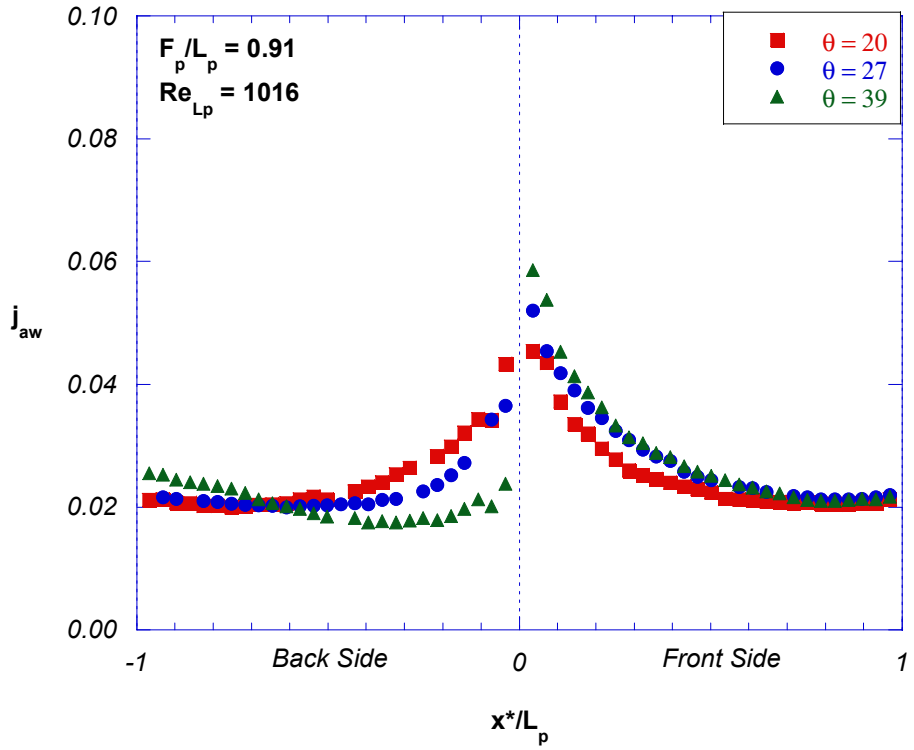

Figure 5.19 Colburn factor measurements based on the adiabatic wall temperature at louver position 2 for Re_{Lp} = 1016 in the F_p/L_p = 0.91 and all values of θ.

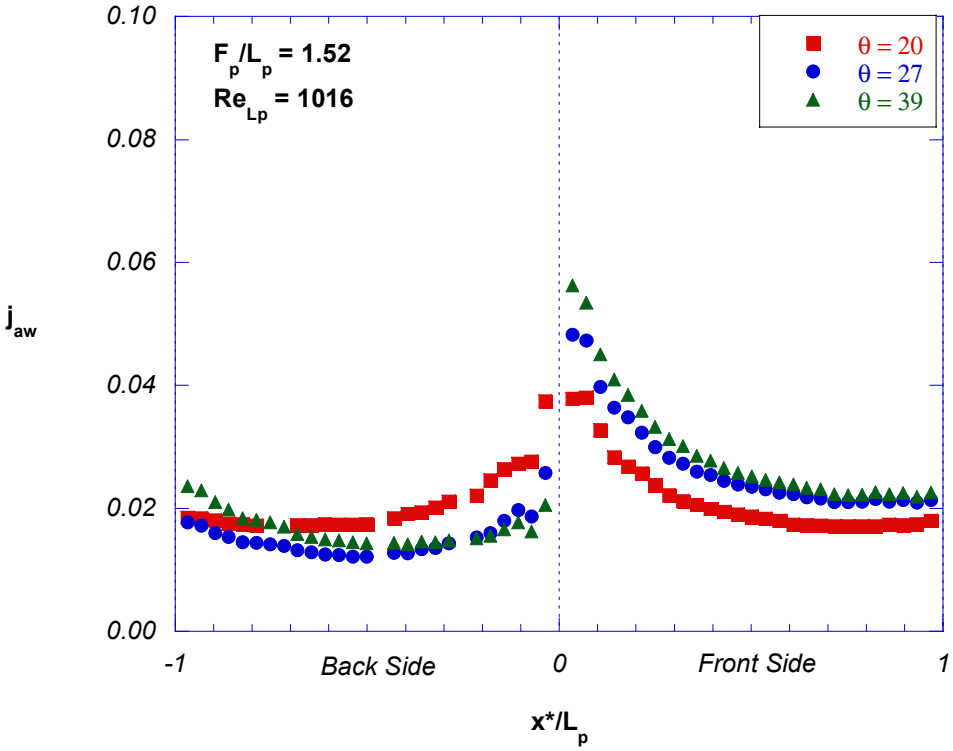

Figure 5.20 Colburn factor measurements based on the adiabatic wall temperature at louver position 2 for Re_{Lp} = 1016 in the F_p/L_p = 1.52 and all values of θ.

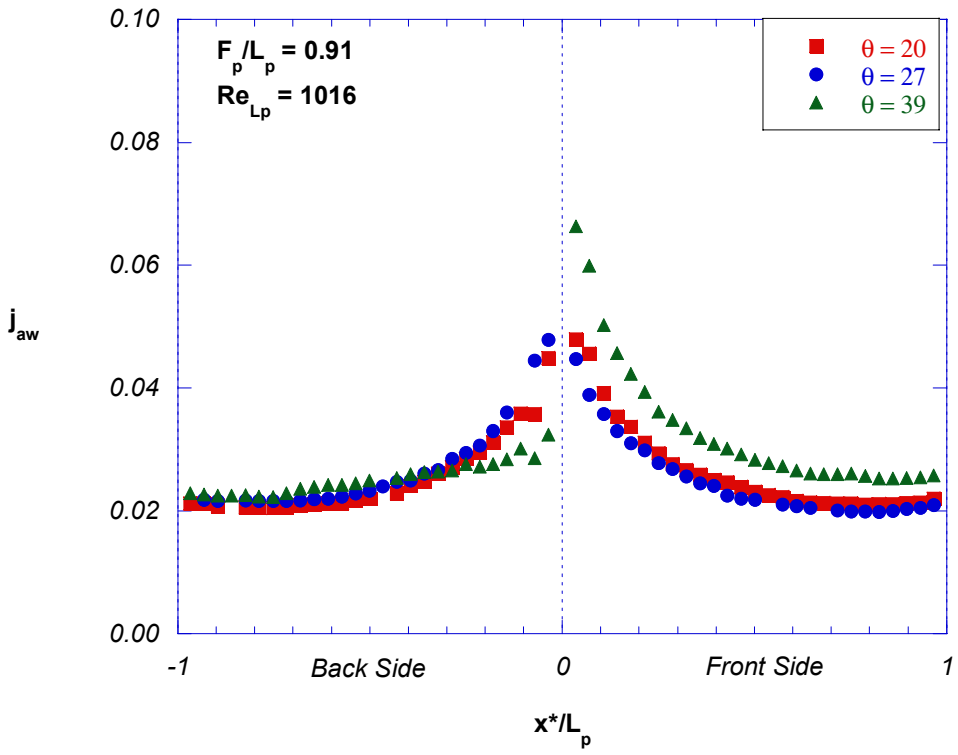

Figure 5.21 Colburn factor measurements based on the adiabatic wall temperature at louver position 6 for Re_{Lp} = 1016 in the F_p/L_p = 0.91 and all values of θ.

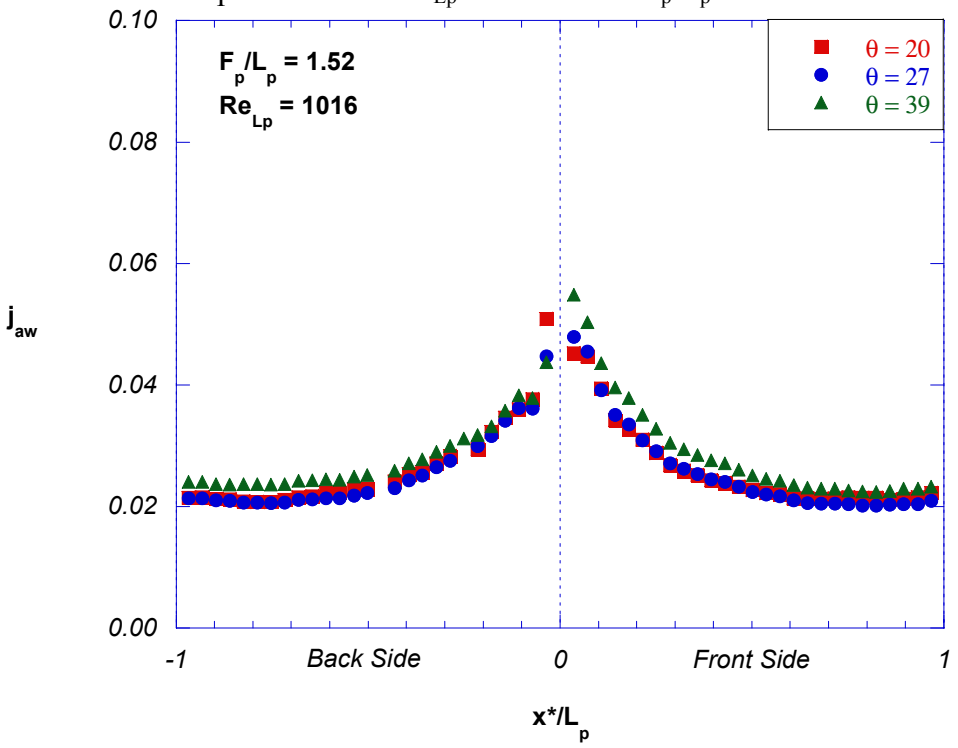

Figure 5.22 Colburn factor measurements based on the adiabatic wall temperature at louver position 6 for Re_{Lp} = 1016 in the F_p/L_p = 1.52 and all values of θ.

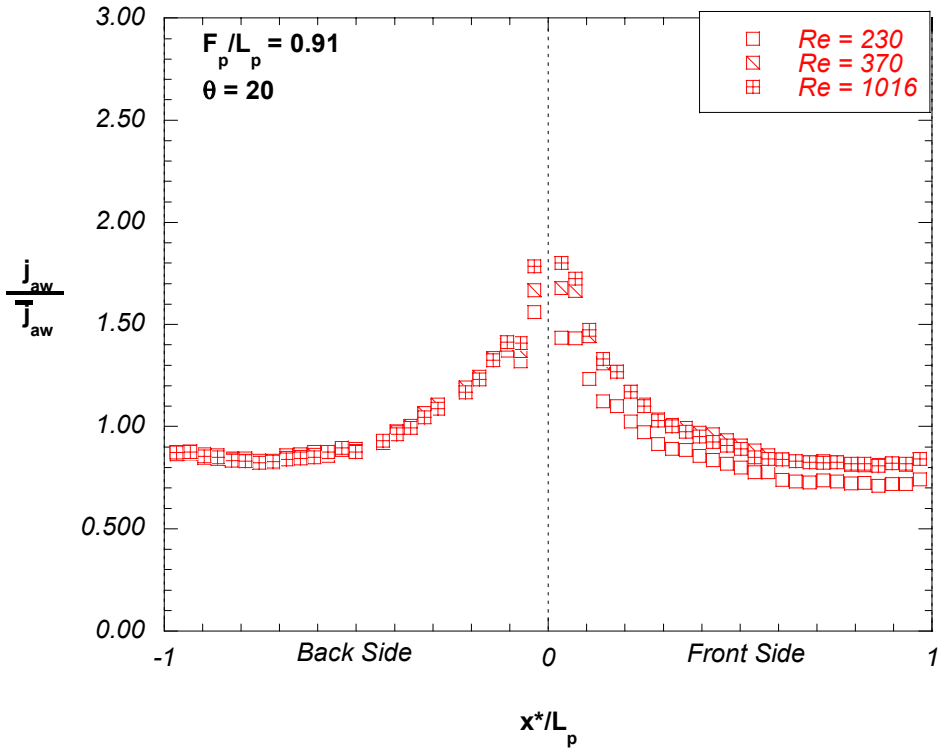

Figure 5.23 Colburn factor based on the adiabatic wall temperature normalized by $\overline{j_{aw}}$ at louver 2 in the $\theta = 20°$, $F_p/L_p = 0.91$ model.

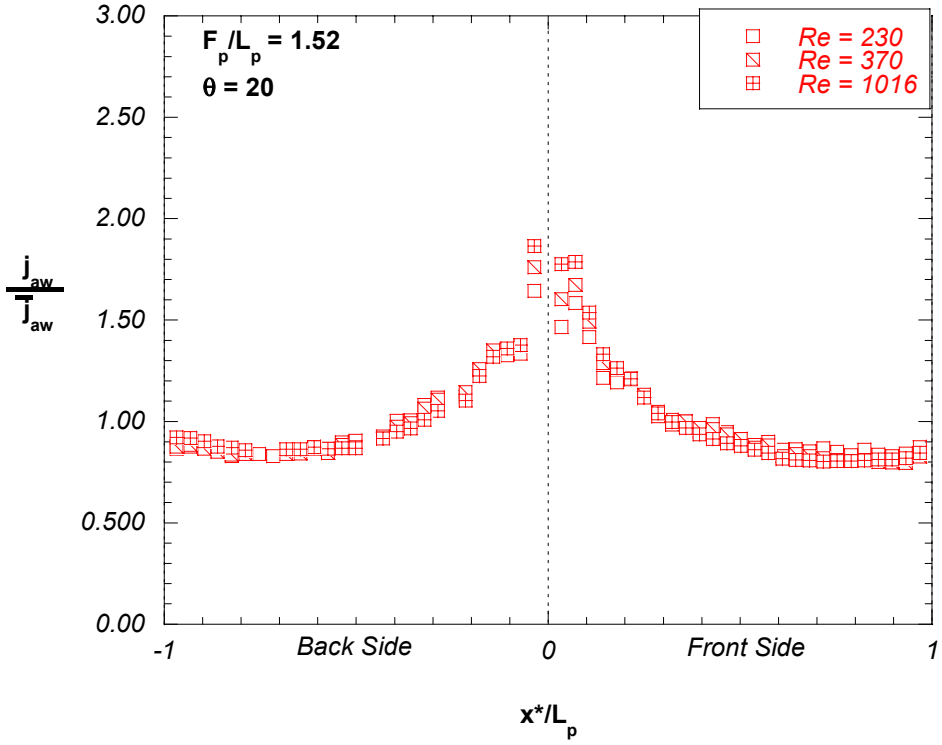

Figure 5.24 Colburn factor based on the adiabatic wall temperature normalized by $\overline{j_{aw}}$ at louver 2 in the $\theta = 20°$, $F_p/L_p = 1.52$ model.

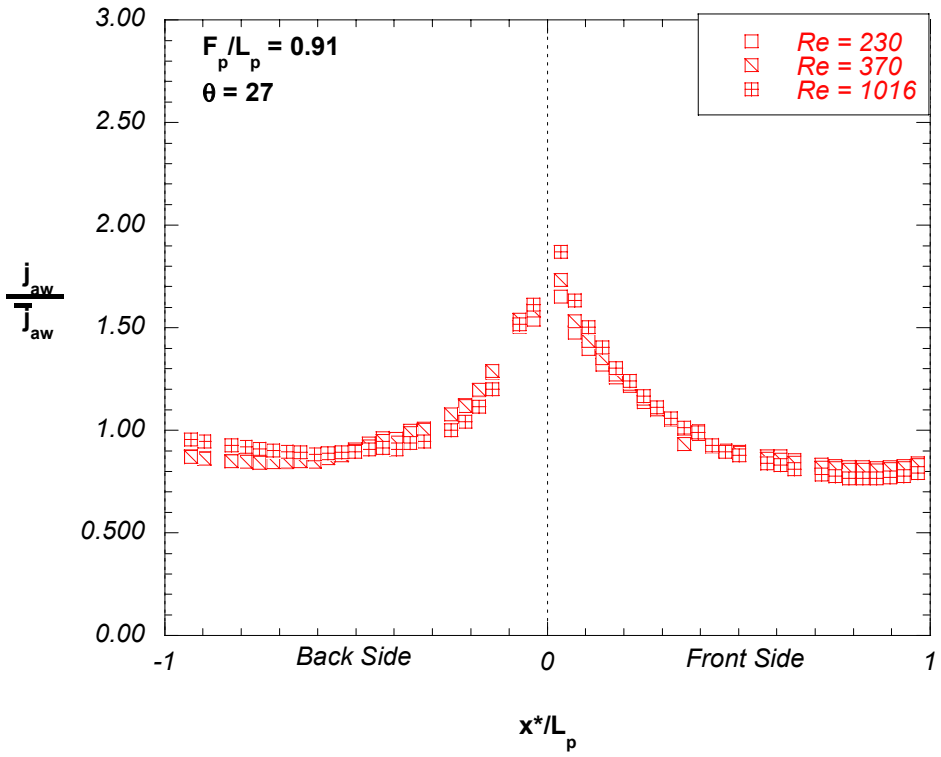

Figure 5.25 Colburn factor based on the adiabatic wall temperature normalized by $\overline{j_{aw}}$ at louver 2 in the $\theta = 27°$, $F_p/L_p = 0.91$ model.

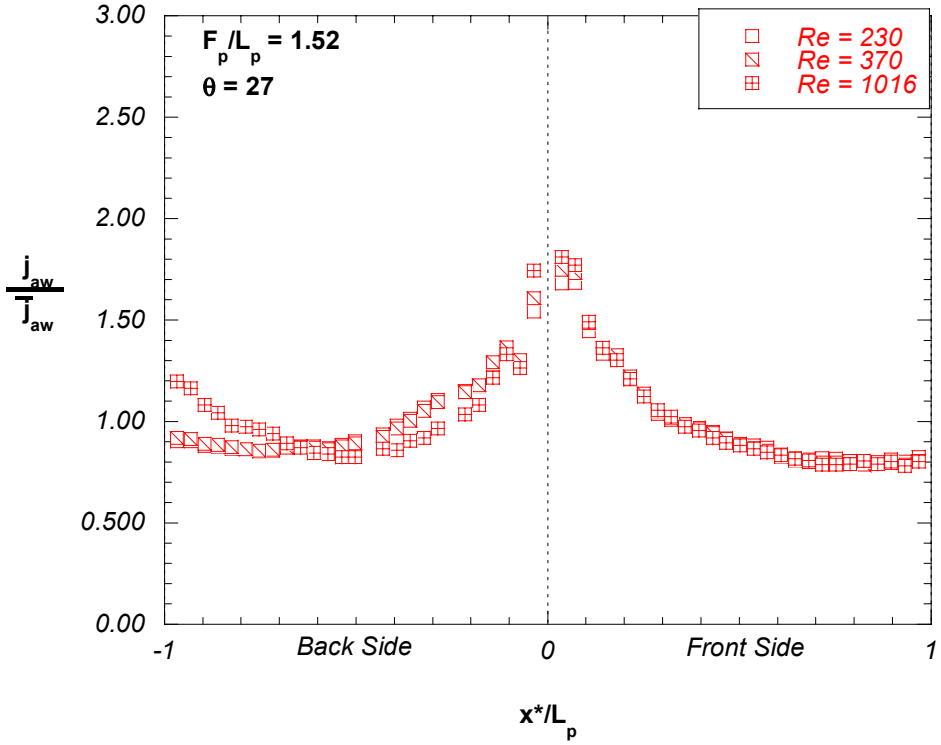

Figure 5.26 Colburn factor based on the adiabatic wall temperature normalized by $\overline{j_{aw}}$ at louver 2 in the $\theta = 27°$, $F_p/L_p = 1.52$ model.

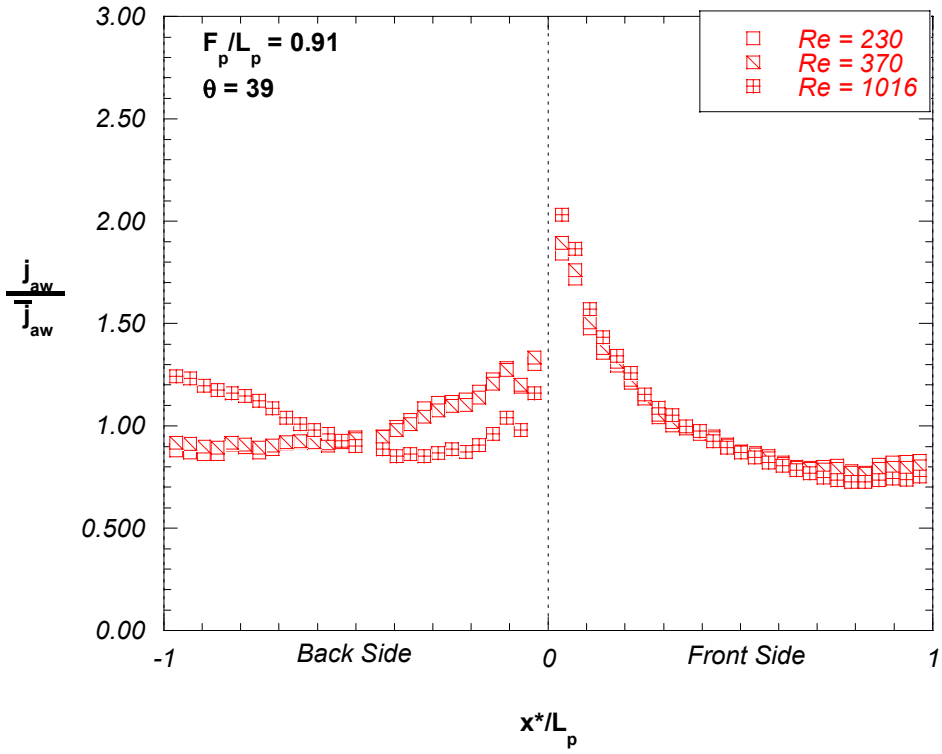

Figure 5.27 Colburn factor based on the adiabatic wall temperature normalized by $\overline{j_{aw}}$ at louver 2 in the $\theta = 39°$, $F_p/L_p = 0.91$ model.

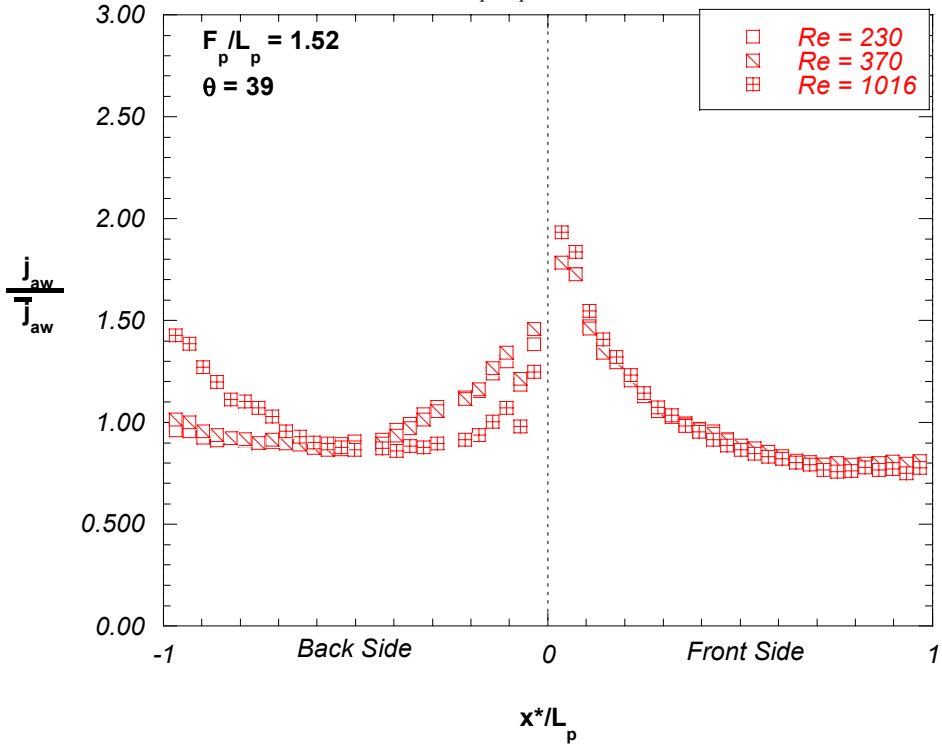

Figure 5.28 Colburn factor based on the adiabatic wall temperature normalized by $\overline{j_{aw}}$ at louver 2 in the $\theta = 39°$, $F_p/L_p = 1.52$ model.

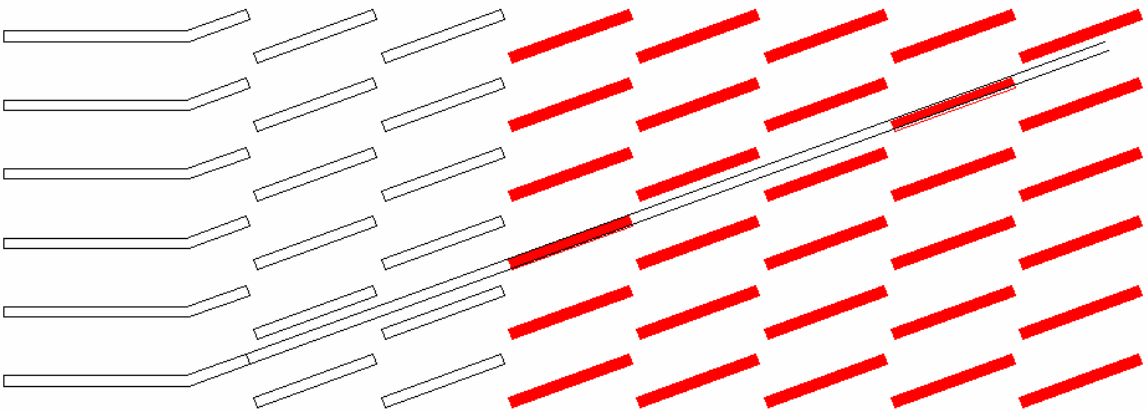

Figure 5.29 Entrance louver's alignment shown with the louvers impacted by thermal wakes for the $F_p/L_p = 0.54$, $\theta = 20°$ model at $Re_{Lp} = 230$.

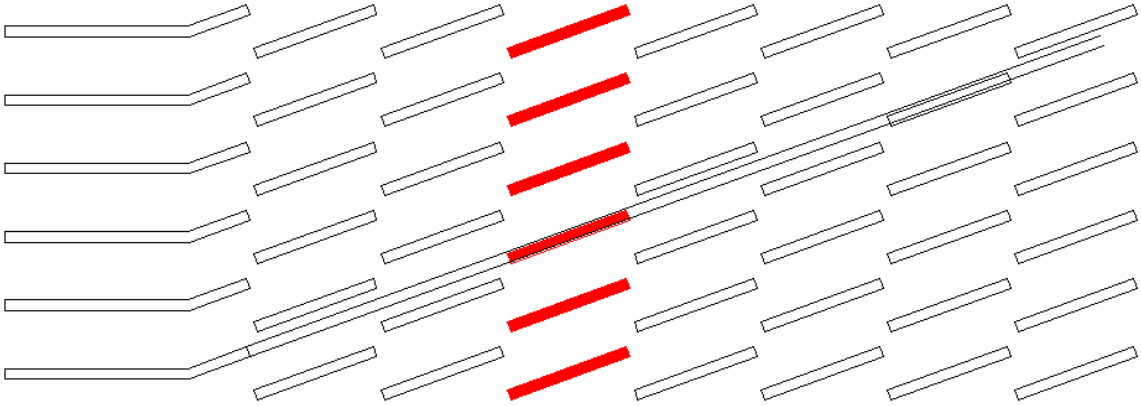

Figure 5.30 Entrance louver's alignment shown with the louvers impacted by thermal wakes for the $F_p/L_p = 0.54$, $\theta = 20°$ model at $Re_{Lp} = 1016$.

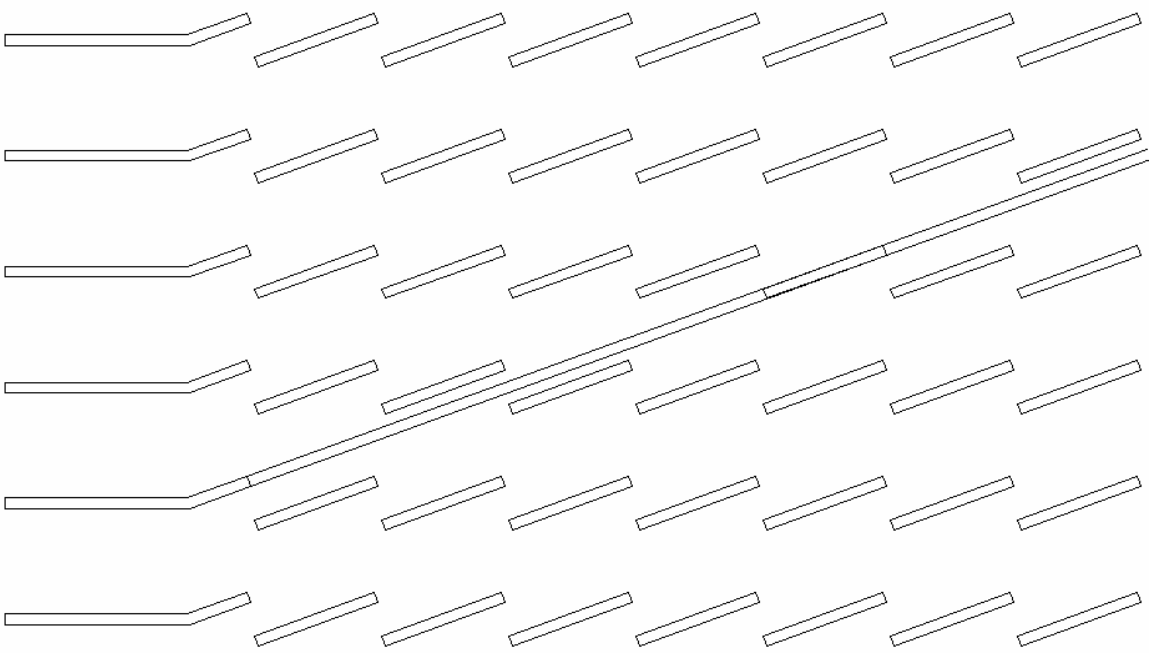

Figure 5.31 Entrance louver's alignment shown with the louvers impacted by thermal wakes for the $F_p/L_p = 0.91$, $\theta = 20°$ model at $Re_{Lp} = 230$.

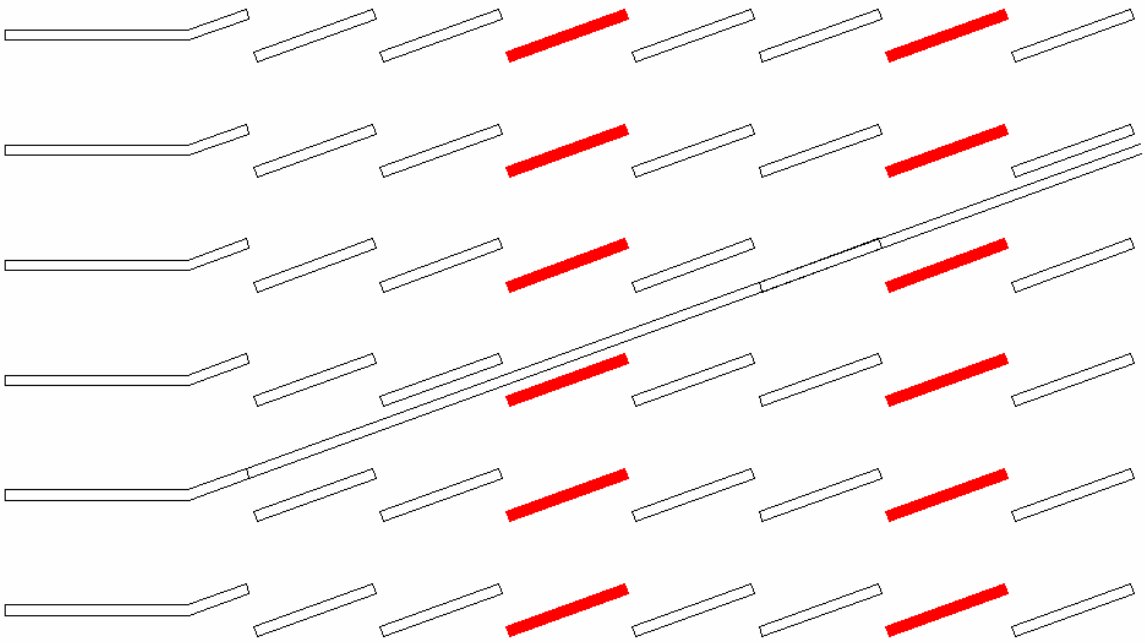

Figure 5.32 Entrance louver's alignment shown with the louvers impacted by thermal wakes for the $F_p/L_p = 0.91$, $\theta = 20°$ model at $Re_{Lp} = 1016$.

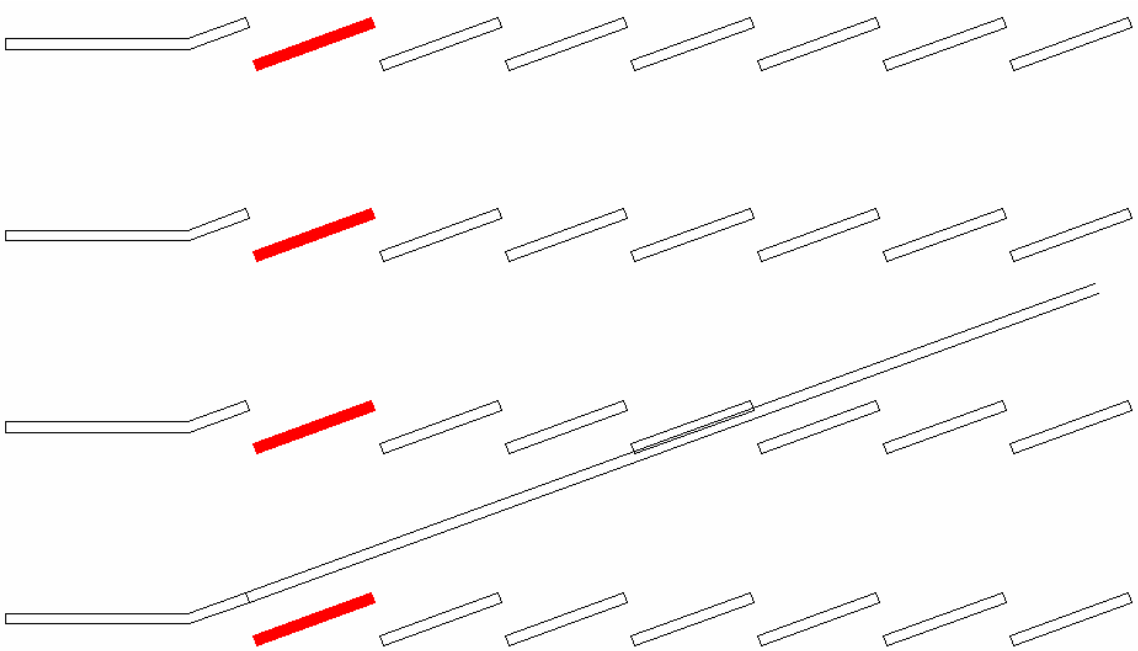

Figure 5.33 Entrance louver's alignment shown with the louvers impacted by thermal wakes for the $F_p/L_p = 1.52$, $\theta = 20°$ model at $Re_{Lp} = 230$.

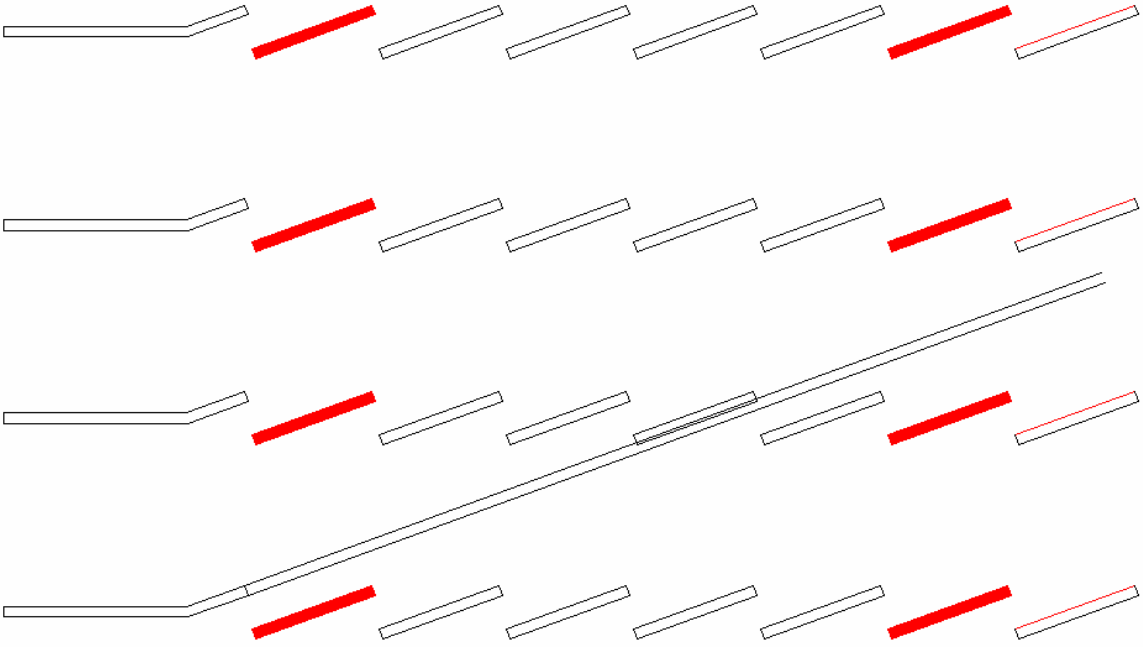

Figure 5.34 Entrance louver's alignment shown with the louvers impacted by thermal wakes for the $F_p/L_p = 1.52$, $\theta = 20°$ model at $Re_{Lp} = 1016$.

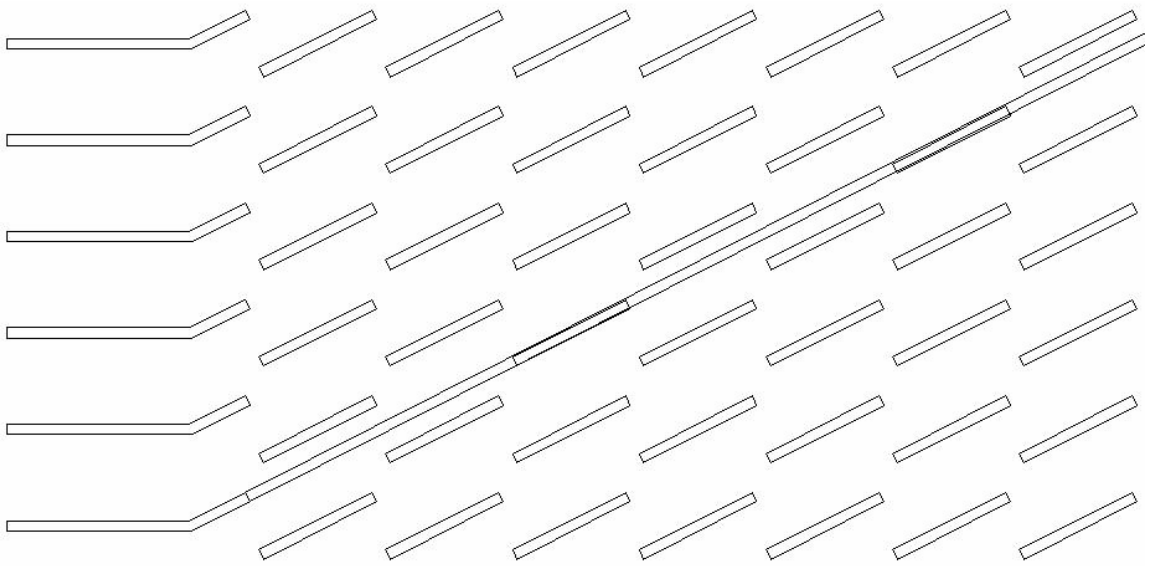

Figure 5.35 Entrance louver's alignment shown with the louvers impacted by thermal wakes for the $F_p/L_p = 0.76$, $\theta = 27°$ model at $Re_{Lp} = 230$.

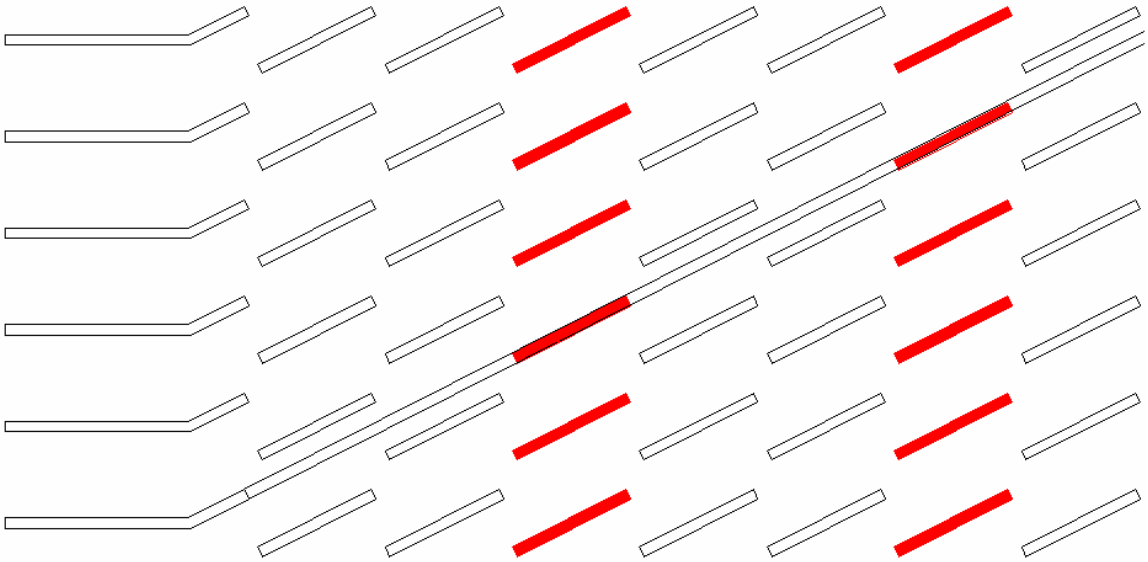

Figure 5.36 Entrance louver's alignment shown with the louvers impacted by thermal wakes for the $F_p/L_p = 0.76$, $\theta = 27°$ model at $Re_{Lp} = 1016$.

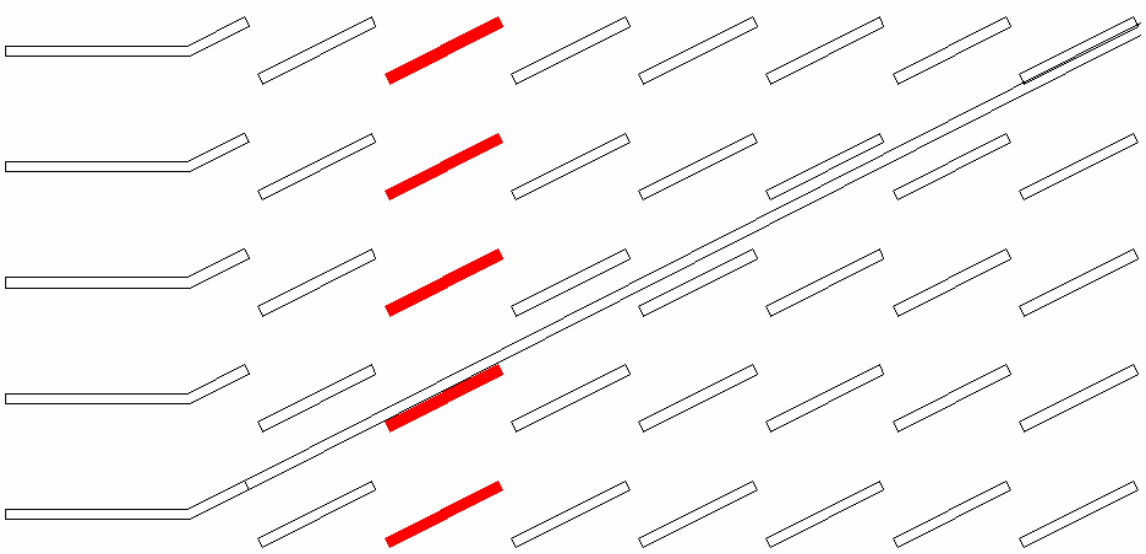

Figure 5.37 Entrance louver's alignment shown with the louvers impacted by thermal wakes for the $F_p/L_p = 0.91$, $\theta = 27°$ model at $Re_{Lp} = 230$.

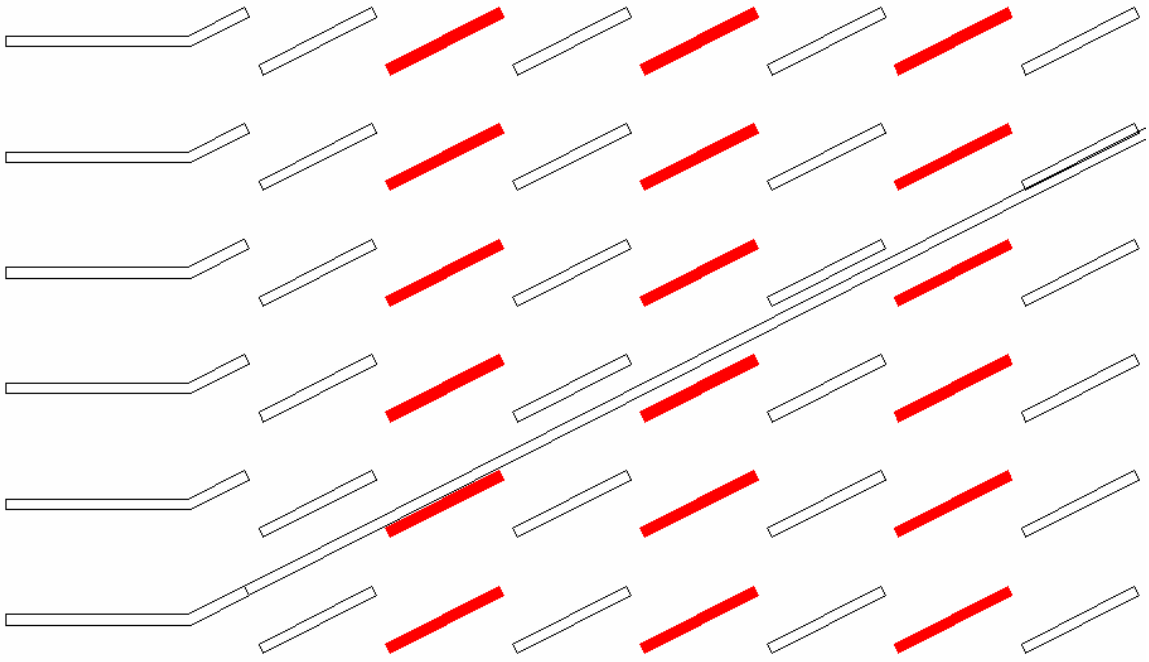

Figure 5.38 Entrance louver's alignment shown with the louvers impacted by thermal wakes for the $F_p/L_p = 0.91$, $\theta = 27°$ model at $Re_{Lp} = 1016$.

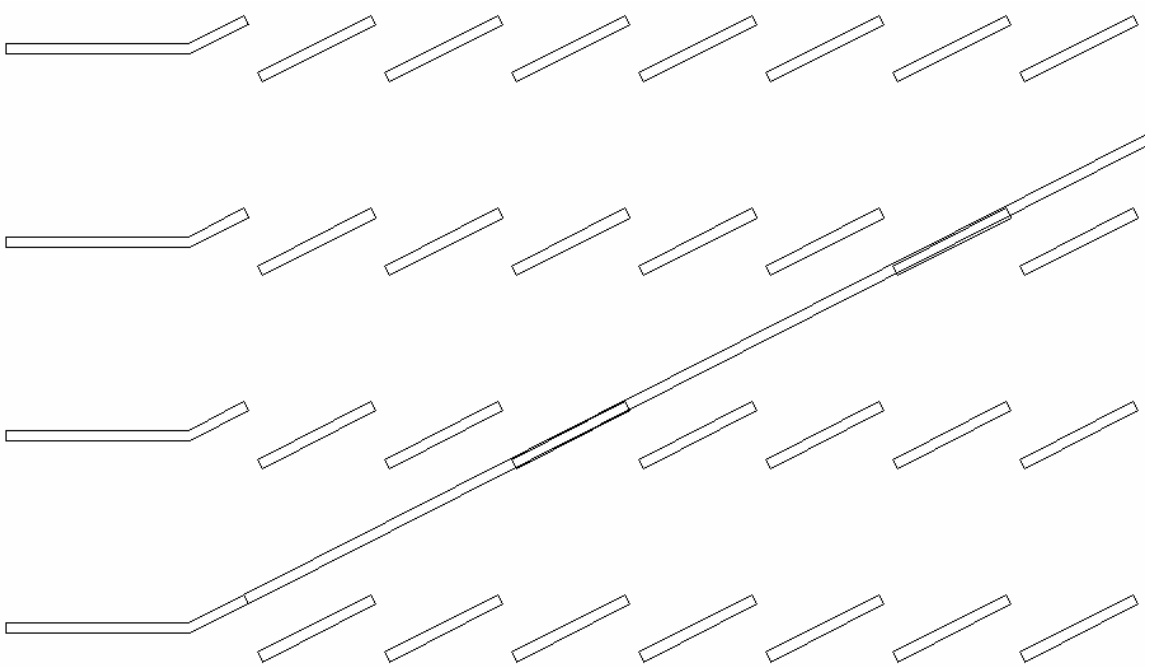

Figure 5.39 Entrance louver's alignment shown with the louvers impacted by thermal wakes for the $F_p/L_p = 1.52$, $\theta = 27°$ model at $Re_{Lp} = 230$.

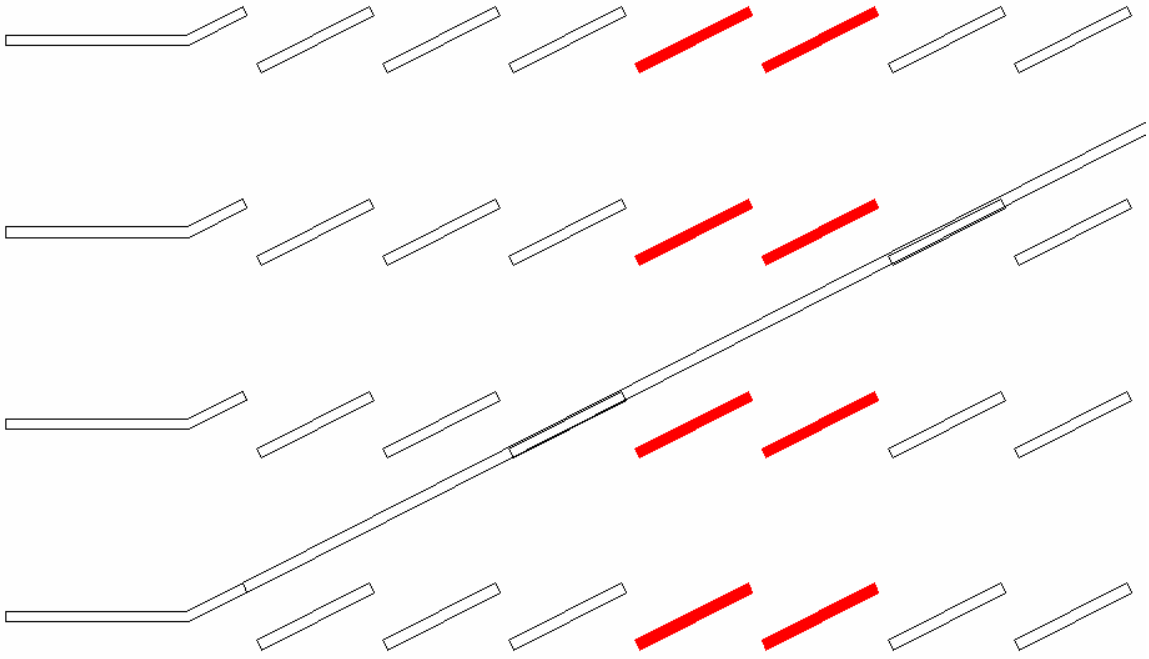

Figure 5.40 Entrance louver's alignment shown with the louvers impacted by thermal wakes for the $F_p/L_p = 1.52$, $\theta = 27°$ model at $Re_{Lp} = 1016$.

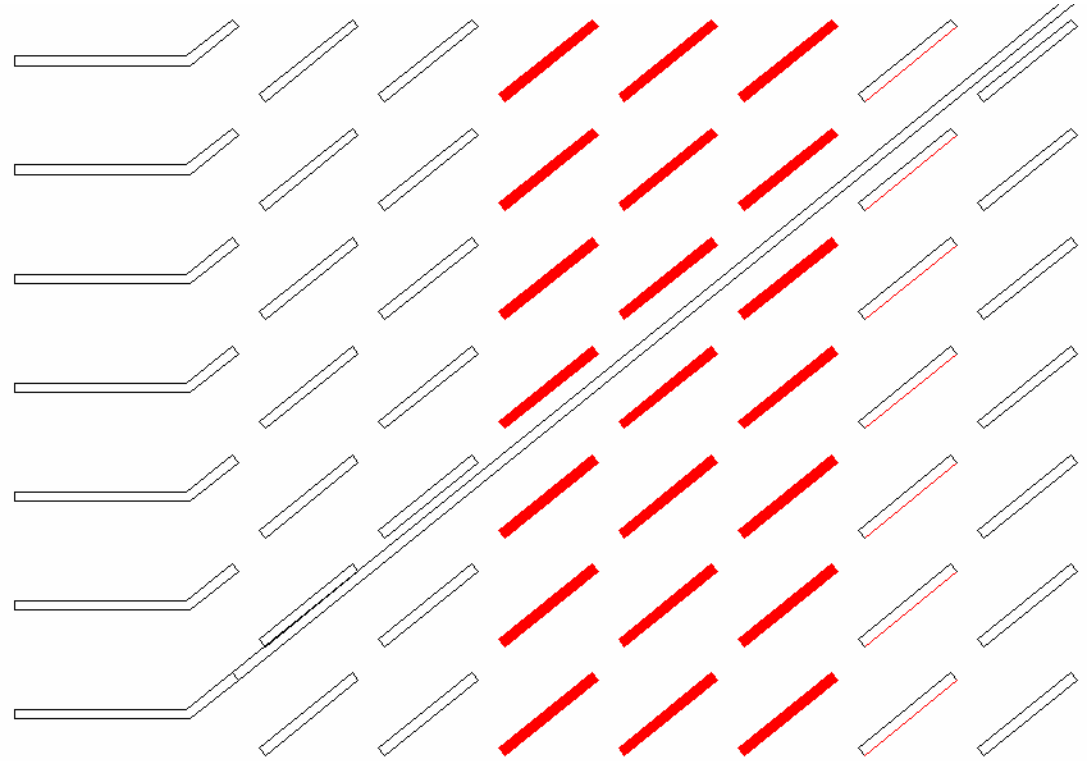

Figure 5.41 Entrance louver's alignment shown with the louvers impacted by thermal wakes for the $F_p/L_p = 0.91$, $\theta = 39°$ model at $Re_{Lp} = 230$.

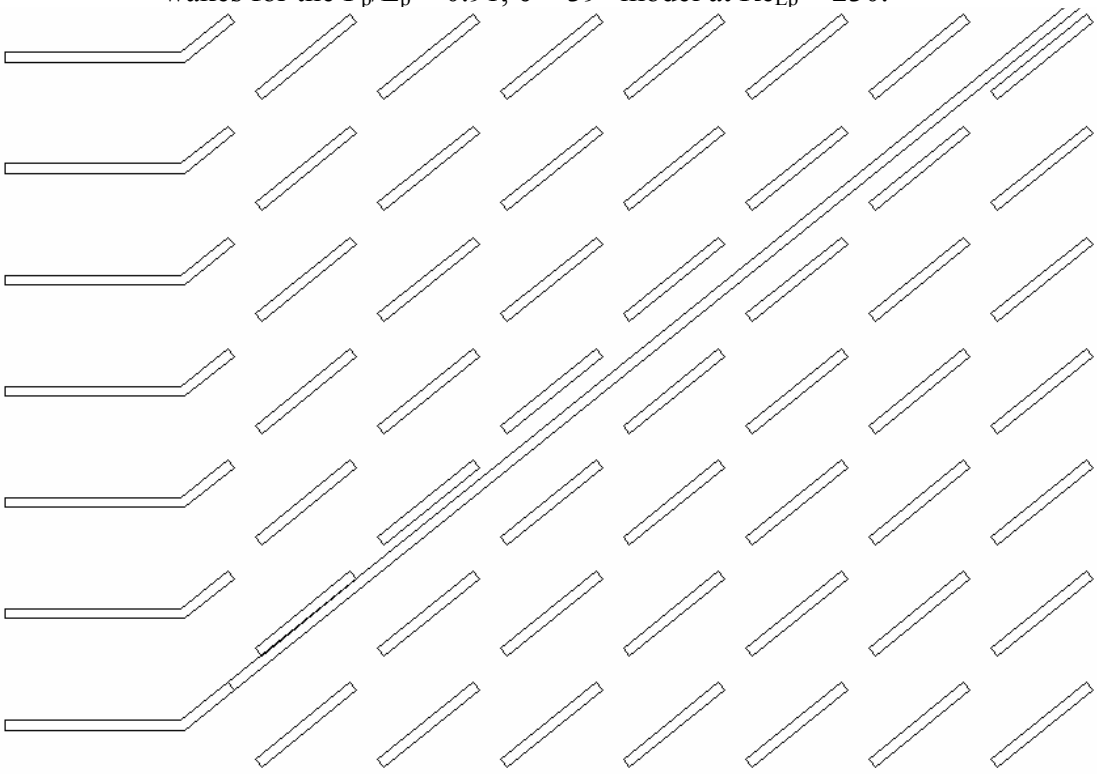

Figure 5.42 Entrance louver's alignment shown with the louvers impacted by thermal wakes for the $F_p/L_p = 0.91$, $\theta = 39°$ model at $Re_{Lp} = 1016$.

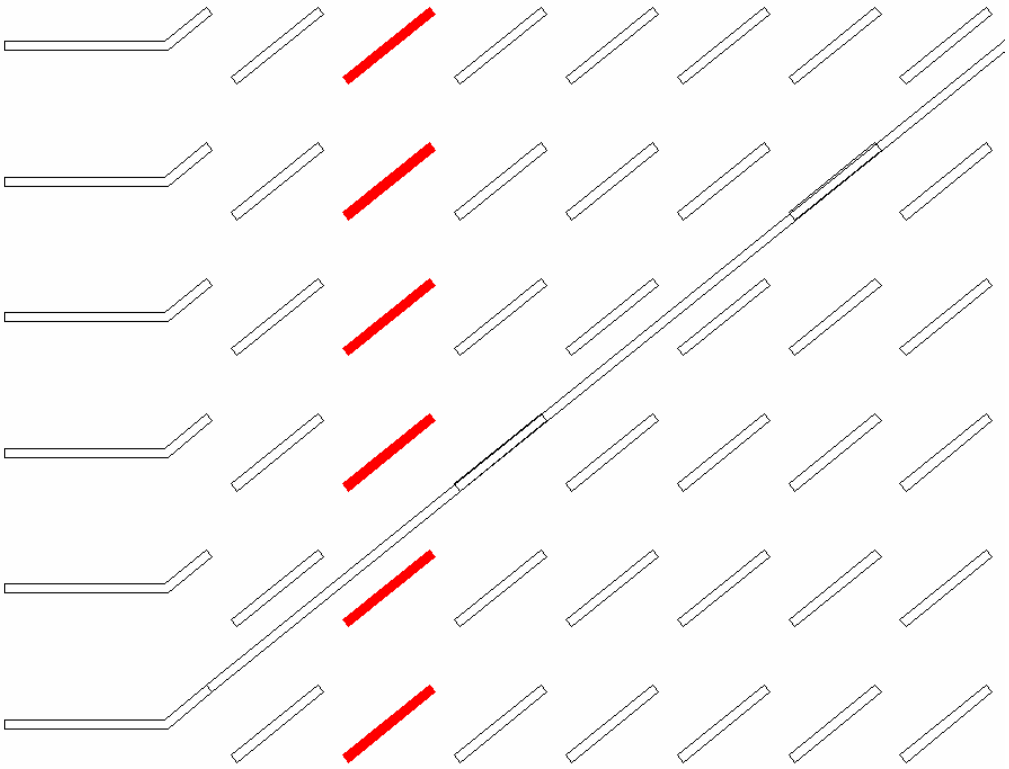

Figure 5.43 Entrance louver's alignment shown with the louvers impacted by thermal wakes for the $F_p/L_p = 1.22$, $\theta = 39°$ model at $Re_{Lp} = 230$.

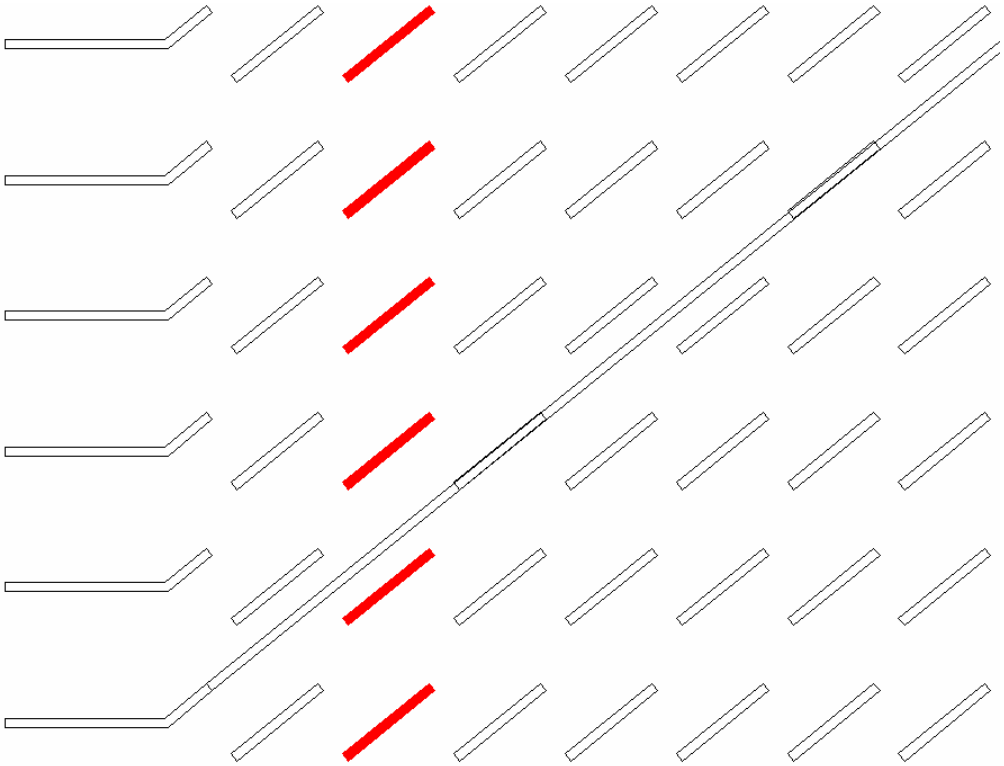

Figure 5.44 Entrance louver's alignment shown with the louvers impacted by thermal wakes for the $F_p/L_p = 1.22$, $\theta = 39°$ model at $Re_{Lp} = 1016$.

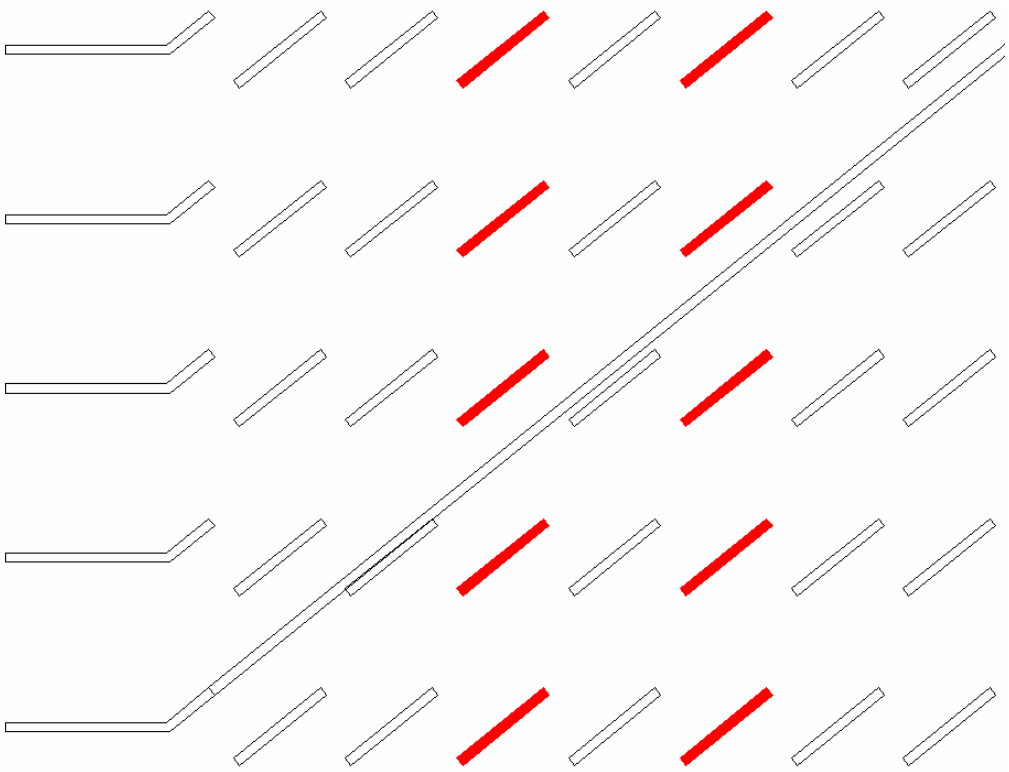

Figure 5.45 Entrance louver's alignment shown with the louvers impacted by thermal wakes for the $F_p/L_p = 1.52$, $\theta = 39°$ model at $Re_{Lp} = 230$.

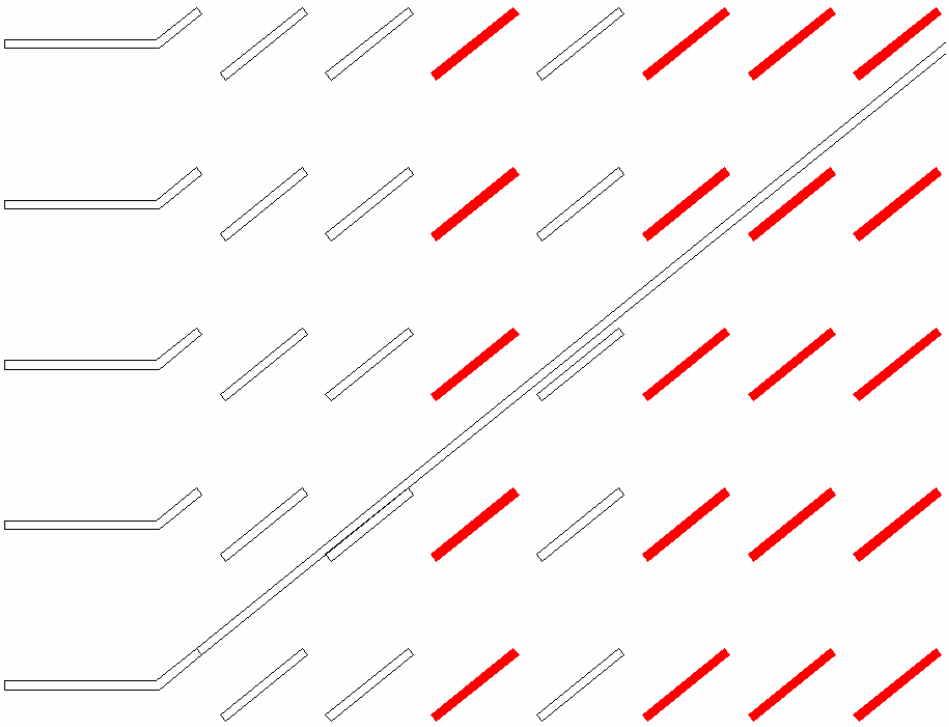

Figure 5.46 Entrance louver's alignment shown with the louvers impacted by thermal wakes for the $F_p/L_p = 1.52$, $\theta = 39°$ model at $Re_{Lp} = 1016$.

Chapter 6

Optimization Study

The final two sections of Chapter 2 briefly discussed the methodology behind the computational and optimization simulations. The current chapter, Chapter 6, will give a more detailed description of the CFD simulations performed for the current study. Section 6.1 will present a comparison of the CFD results with the experimental data discussed in the previous chapters of this document. Section 6.2 will detail the optimization methodology. The objective function that was used for the optimization study will be derived and discussed in the third section of this chapter. The fourth section will present the results from the optimization study. Chapter 6 will conclude by reviewing the important findings from the optimization study.

6.1 Comparison of CFD and Experimental Results

In an effort to validate the use of a CFD code for the optimization study, it was imperative to show that the CFD code could accurately predict the heat transfer in the experimental apparatus used for this study. The use of a CFD code for an optimization study has several advantages over performing a similar study using the experimental methodology described throughout this document. The most obvious and important reason for using CFD is the amount of time and money that is saved. A typical CFD solution for the current geometries can be obtained in approximately 8 hours. Conversely, it can take as long as two weeks to measure and reduce a full set of experimental data for one model. Another important advantage to using a computational methodology for an optimization study is that a computer can quickly analyze trends in the data and determine how to vary parameters according to preprogrammed user logic.

A description of the computational methodologies can be found in section 2.5 of this document. Lyman (2000) performed a CFD simulation for the $F_p/L_p = 0.76$, $\theta = 27°$ model and found excellent agreement between the CFD predictions and his experimental data. For the current study, the $F_p/L_p = 0.91$, $\theta = 20°$ model was chosen for the comparison of the CFD and experimental results. The resultant computational runs (as well as the optimization results) were completed for $Re_{Lp} = 1016$.

A triangular mesh was used throughout the majority of the flow domain. However, a quadrilateral mesh (or a boundary layer mesh) was used around the surfaces of the louvers to capture, in detail, the thermal gradients that occurred near the louver surfaces. This was necessary to ensure the most accurate computational predictions. A representative portion of the quadrilateral grid used around the louver surface can be found in Figure 6.1. Figure 6.1 also shows the triangular grid used on the majority of the flow domain.

The predicted Nusselt numbers based on the bulk flow temperature for louvers 2, 3, and 7 can be found in Figure 6.2. The results shown are for the $F_p/L_p = 0.91$, $\theta = 20°$ model at $Re_{Lp} = 1016$. As would be expected from the experimental data and an empirical flat plate correlation, Nu_b is very high near the leading edge of the louvers and decreases dramatically in the streamwise direction. The heat transfer coefficients on the front side of louvers 2 and 3 are much higher than those predicted at the other locations. For example, Nu_b as measured on the front side of louver 7 is much lower than the predictions on the front side of louvers 2 and 3. The variation in the heat transfer coefficients can be explained by investigating the thermal field surrounding each of the louver surfaces in question. In studying Figure 6.4, which shows the computationally predicted temperature contours through the louver array, it is apparent that the thermal wake emanating from the entrance louver impinges onto the surface of louver 7. The streamlines shown in Figure 6.3 indicates the louver directed flow in the array. By tracing the streamline beginning at the trailing edge of the entrance louver through the array, one can see that it impacts the front side of both louvers 4 and 7 thereby decreasing the heat transfer coefficients on these surfaces. Figures 6.3 and 6.4 also help to explain the increased heat transfer on the front surface of louvers 2 and 3. From Figure 6.4, it is clear that the thermal field surrounding these surfaces is relatively cool due to the fact that the cooler flow entering the louver array impinges onto these louver surfaces. The claim is further supported by the streamline predictions shown in Figure 6.3. Another cause for the high Nu_b on the front side of louver 2 is the impingement of the axially directed flow onto that surface. This causes the boundary layer on that surface to be much thinner, thereby increasing the convective heat transfer coefficient on that surface.

Figure 6.2 shows that the Nu_b is lower on the back side of louver 2 than on the front side of the same surface. The cause of this decreased heat transfer coefficient on the back side of louver 2 is a slight deflection of the flow away from that surface. The deflection causes a thicker boundary layer on that surface, which decreases the overall heat transfer. The deflection of the flow away from the back side of louver 2 is caused by the flow not being completely louver aligned and is shown by the predicted streamlines in Figure 6.3. The streamlines are very close to the front side of louver 2 but are much further away on the back side.

Figures 6.5 through 6.7 show a comparison between the experimental data and the CFD predictions for the $F_p/L_p = 0.91$, $\theta = 20°$ model at $Re_{Lp} = 1016$. The most obvious difference between the predictions and the experimental data exists at the leading edge of the second position. In addition, the CFD predictions show a heat transfer curve whose slope approaches a near infinite value at the leading edge. While the experimental data indicates a high heat transfer coefficient near the leading edge, it is much lower than that predicted by CFD. The cause of this discrepancy is most likely streamwise heat conduction that occurs in the experimental louvers. The other major discrepancy between the predictions and experiments occur on the back side of louvers 2 and 3. The CFD predictions show severe separation off of these surfaces, which did not appear to be as severe in the experiments. Other than the regions mentioned above, CFD appeared to accurately predict the local heat transfer coefficients for both the entrance region (louvers 2 and 3) and the fully developed region (louver 7). Apart from the leading edge regions and the back side of louvers 2 and 3, the CFD predictions were typically well within the uncertainty bands shown by the dotted lines in Figures 6.5 through 6.7.

The $\overline{Nu_b}$ values averaged over each surface individually can be found in Figure 6.8 for each of the three louver positions. The general trends of the lines are very similar but, in most instances, the CFD predicted averages are much higher than the experimentally measured averages. The CFD predicts a much higher $\overline{Nu_b}$ because of the extremely high predictions near the leading edges of the louvers. The only case where the CFD predicted $\overline{Nu_b}$ is lower than the experimental data is the back side of louver 2. The experimental $\overline{Nu_b}$ is higher because of the severe separation that CFD

predicts on this surface. Figure 6.9 shows the $\overline{Nu_b}$, which were averaged over the entire louver (both front and back side). Again, the general trends in the curves match up very well but the magnitudes of the numbers are very off.

To compare the $\overline{Nu_b}$ values outside of the leading edge region, the average values were calculated from $x^*/L_p = \pm 0.25$ to $x^*/L_p = \pm 1.00$. These new average values are shown in Figures 6.10 and 6.11. Figure 6.10 shows the average values on both the front and back side of each of the three louver positions reported. As before, the general trends of the CFD predicted curves and the experimental curves match up quite well. The predicted data and the experimental data match up very well on the front side of all three louver positions as well as the back side of louver 7. The CFD predictions on the back side of louvers 2 and 3 are lower than the experimental values. This discrepancy can be attributed to the fact that Fluent predicted severe separation off of the back side of louvers 2 and 3 that did not occur during the experiments. Figure 6.11 shows the $\overline{Nu_b}$ values averaged over both the front and back surfaces of the three louver positions. Again, the prediction is quite accurate for louver 7, but the CFD under predicts the heat transfer on louvers 2 and 3. The cause of this is again due to the prediction of separation off of the back sides of these louvers.

6.2 Optimization Methodology

After the verification of the CFD methodology used for the current study, the optimization study was set up. The optimization of the louver geometry was completed by integrating the optimization software, iSIGHT, with the Gambit and Fluent journal files (Lethander, 2003). The Gambit journal files are read by the executable and they describe how the geometry should be created and meshed. The aforementioned Fluent journal files existed in order to run the CFD predictions. The optimization process began with iSIGHT entering the input parameters describing the louver geometry into the Gambit journal files. After the geometry was created and meshed in Gambit, Fluent ran the code to solve the two-dimensional Navier-Stokes equations. The optimization objectives were then obtained from the Fluent output files and the geometric parameters were changed according to the optimization technique being used by iSIGHT.

The optimization of the louver array was performed using the same computational set-up that was described in the previous section. The existing journal files were modified in order to define the geometry creation in terms of variables rather than quantitative values specific to a geometry. Several values were held constant throughout the optimization. The entire study was performed for a single inlet velocity corresponding to a $Re_{Lp} = 1016$. The temperature of the fluid entering the louver array was 295 K. In order to maintain consistency between the optimization simulations and the experiments, the louver pitch was held at a constant value of 27.9 mm and a constant heat flux of 160 W/m^2 was applied to each side of the louver. The louver thickness also remained constant for the simulations. The optimization variables were the fin pitch and the louver angle. The ratio of the fin pitch to the louver pitch (F_p/L_p) was allowed to vary between 0.58 and 2.00. The louver angle was allowed to take on values between 15° and 45°. In order to prevent the louvers from one row to overlap with the vertically adjacent louver row, it was necessary to perform the optimization in 10° increments. Table 6.1 shows the louver angle ranges along with the allowable values of the F_p/L_p.

6.3 Definition of the Objective Function

The first step in performing the optimization on a louvered fin heat exchanger geometry was to define the objective function that needed to be used. In order to define this function, it is first necessary to define the optimization goals. The initial goal was to maximize the heat dissipated by the louver array (Q), which is given as

$$Q = q'' * A_{louvers} \tag{6.1}$$

Where q'' represents the heat flux applied to the surface of each louver and $A_{louvers}$ represents the sum of all the louver surface areas exposed to the flow. As mentioned above, the heat flux applied to the surface of each louver is held constant for each of the louver geometries (q'' = constant). The total surface area exposed to the flow is also a constant between the different louver geometries since L_p = 27.9 mm ($A_{louvers}$ = constant) therefore, Equation 6.1 is equal to a constant.

$$Q = C_1 \tag{6.2}$$

In the preceding equation, C_1 is an arbitrary constant. The second optimization goal for this study was to minimize the volume of the core (V). Minimizing the volume of the core is done to reduce the amount of space that a heat exchanger takes up as well as reduce the overall weight of the system. The volume of the core is defined by the following relationship

$$V = F_p * w * L \tag{6.3}$$

In Equation 6.3, w is the spanwise width of the louvers, which because the CFD solution assumes 2-dimensional flow, w is a constant (unity). L, on the other hand, represents the streamwise length of the entire louver array that is also a constant. After performing these simplifications, Equation 6.3 reduces to

$$V = C_2 * F_p \tag{6.4}$$

As before, C_2 represents some arbitrary constant. The third, and final, optimization goal was to minimize the pumping power required to push the flow through the louvered array. The pumping power required (P) is given as

$$P = U_{in} * F_p * w * \Delta p \tag{6.5}$$

Where U_{in} is the inlet velocity to the louver array and Δp represents the pressure drop through the entire louver array. As before, several of the terms in Equation 6.5 are constant between the louver geometries. Both U_{in} and w are constants. Therefore, Equation 6.5 reduces to

$$P = C_3 * F_p * \Delta p \tag{6.6}$$

To review, there were three goals of the optimization simulation. The first goal was to maximize the heat dissipated by the heat exchanger. Secondly, it was important to minimize the volume of the core. The third, and final, objective of the optimization function was to minimize the pumping power required to push the flow through the louver array. An optimization function was defined by combining Equations 6.2, 6.4, and 6.6 and is shown as follows

$$\frac{Q}{V * P} = \frac{C_1}{C_2 F_p C_3 F_p \Delta p} \tag{6.7}$$

By removing the constants from the preceding equation, it is possible to simplify the optimization function. To accomplish the goals of the optimization, the function that was maximized is defined as

$$\frac{Q}{V * P} \propto \frac{1}{F_p^2 \Delta p} \tag{6.8}$$

6.4 Results of the Optimization Study

The optimization study that was performed yielded results from approximately 120 different sets of louver geometries. As mentioned above, the goal of the optimization study was to maximize the right hand side of the relationship defined in Equation 6.8. Figure 6.12 shows the optimization results with the optimization function divided into two parts. The first part, which is shown on the right axis, is $1/F_p^2$ while the second part is simply $1/\Delta p$ as shown on the left axis. The reason for evaluating the optimization function as two separate parts is to show the magnitude of the parts. The $1/F_p^2$ has values that range between 250 and 4000, while the $1/\Delta p$ maintains values between 0.5 and 2.5. From the above discussion and Figure 6.12, it is apparent that the $1/F_p^2$ value dominates the optimization function in terms of order of magnitude.

Figures 6.13 and 6.14 show the optimization function plotted as a function of louver angle (θ) for small bands of F_p/L_p. Figure 6.13 shows that as the louver angle (θ) is increased, the value of the optimization function appears to decrease. There is a much

wider spread of the optimization function at the lower louver angle values indicating more of a F_p/L_p dependence, whereas at higher louver angle values the data is collapsing to an overall lower value of the optimization function.

Figure 6.14 also shows selected F_p/L_p ranges. For the $1.1 < F_p/L_p < 1.2$ band, the values of the optimization function maintain a decreasing value as the louver angle is increased for the louver angle range of $15° < \theta < 30°$. However, as θ is increased beyond 30° the optimization function significantly decreases. The same trend can be seen for the other two F_p/L_p bands. Table 6.2 also shows the effect of the louver angle on the optimization function for constant values of F_p/L_p. For constant values of F_p/L_p, the optimization function is always greater for smaller louver angles. As discussed before, there exists a higher tendency for flow separation for large values of louver angle. This effect causes the pressure drop through the louver array to increase as the louver angle is increased.

Figures 6.15 through 6.17 show the optimization function plotted as a function of F_p/L_p for each of the three louver angle bands that were studied. The first figure, Figure 6.15, shows the optimization function for $15° < \theta < 25°$, which was the smallest louver angle band that was studied. It is apparent from this figure that the optimization function decreases at a relatively constant slope for the overwhelming majority of the data. While this is obviously true, there are several data points that do not fall within the linear trend of the data. The outliers on the plot correspond to the louver angles near the upper limit of $\theta = 25°$. The outliers begin at a louver angle of approximately $\theta = 21°$. The reason for these outliers, as alluded to earlier in this section, is the impact of the large louver angles on the pressure drop through the louver array. For these large louver angles, the pressure drop has a bigger impact on the optimization function. The data for $25° < \theta < 35°$ can be found in Figure 6.16. Unlike Figure 6.15, the data does easily lend itself to any particular trends. For the smaller louver angles, the optimization function does decrease with increasing values of F_p/L_p. This is not necessarily true at the higher louver angle values such as $33° < \theta < 34°$. For this data, the optimization function actually increases with increasing values of F_p/L_p ($1/F_p^2\Delta p = 650$ to 800 for $F_p/L_p = 1.5$ to 1.6). The same trend can be found in Figure 6.17 with the optimization function actually increasing with

increasing F_p/L_p for $40° < \theta < 42°$ due to the increased pressure drop associated with the large louver angles.

6.5 Summary of Optimization Study

As shown in the previous section of this chapter, an optimization methodology is a viable technique for designing compact heat exchangers. Using this approach, a design engineer can save a large amount of time in the design phase of a louvered fin array and be able to explore the entire solution domain. For the optimization function used throughout the current study, the optimal design was a very strong function of F_p/L_p for the given problem constraints. The optimization function was only dependent on the louver angle for value of $\theta > 21°$. For the given optimization function, the best heat exchanger geometry would be one with a small F_p/L_p value and a small louver angle. The analysis described above also shows that optimization methods used in conjunction with CFD can be used to improve the local heat transfer performance on a given louver.

θ (degrees)	F_p/L_p
15° < θ < 25°	0.58 < F_p/L_p < 2.0
25° < θ < 35°	0.73 < F_p/L_p < 2.0
35° < θ < 45°	0.88 < F_p/L_p < 2.0

Table 6.1 Fin pitch and louver angle ranges for optimization study.

F_p/L_p	θ (degrees)	$1/(F_p^2\Delta p)$	F_p/L_p	θ (degrees)	$1/(F_p^2\Delta p)$
1.1952	36.5651	785.9394	1.5648	26.6850	879.7037
	43.4338	499.0220		33.5537	815.5091
1.4880	27.0187	901.1355	1.5354	26.8666	909.4079
	33.8874	659.6531		33.7354	750.0891
1.4996	28.8242	1008.0480	1.5677	30.6827	1041.8136
	28.9237	995.6324		30.7822	943.8110
1.4909	41.6148	470.2938	1.5044	25.4524	908.1176
	41.7143	462.7274		32.3212	838.6899
1.5274	31.5440	983.2006	1.5285	31.3581	1005.9165
	31.6434	955.9959		31.4575	993.8292
1.3175	27.6150	1151.9352			
	30.6159	858.4307			
	34.4837	827.5589			

Table 6.2 CFD optimization results showing the louver angle effect on the optimization function for a constant F_p/L_p.

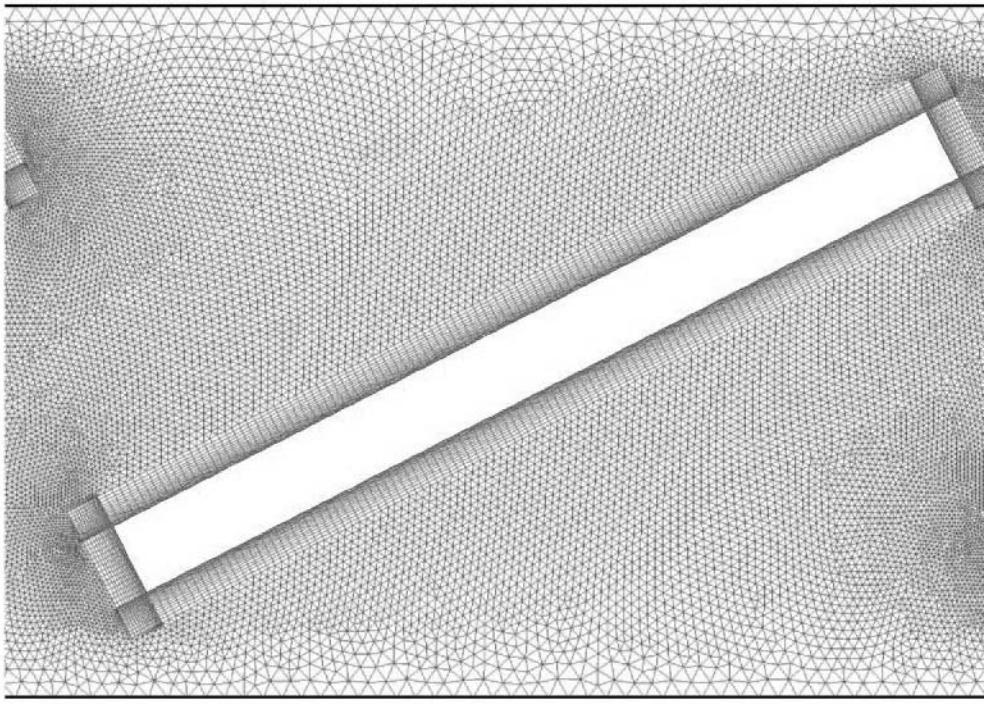

Figure 6.1 A portion of the CFD grid showing a detailed section of the quadrilateral (boundary layer) grid used around each of the louvers.

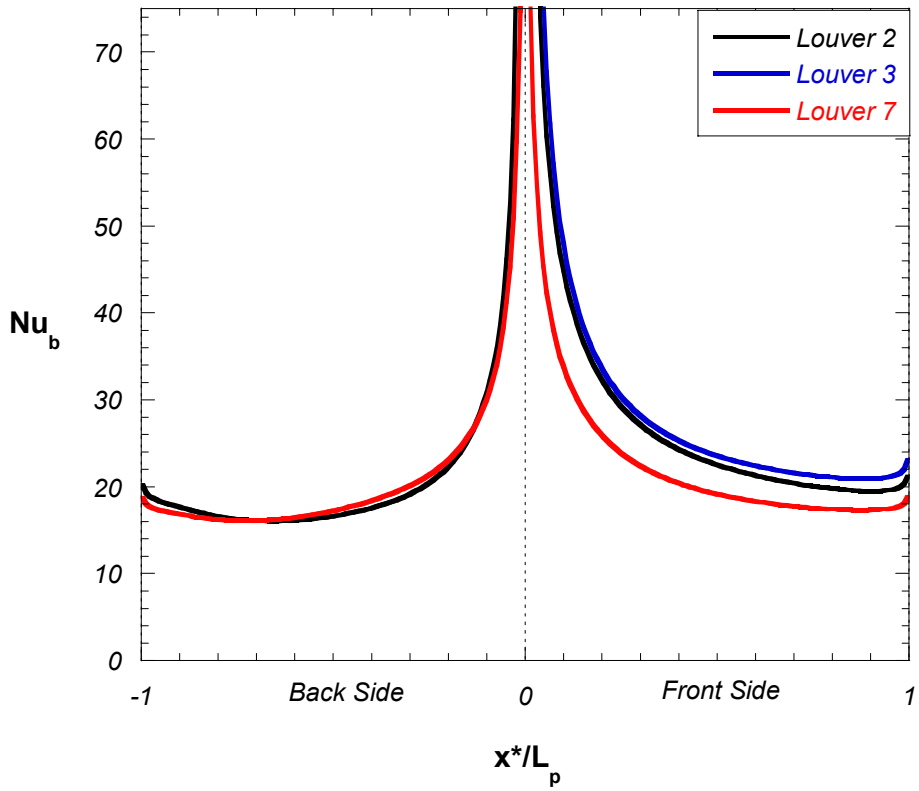

Figure 6.2 Nusselt number predictions on louvers 2, 3, and 7 for the $F_p/L_p = 0.91$, $\theta = 20°$ model geometry at $Re_{Lp} = 1016$.

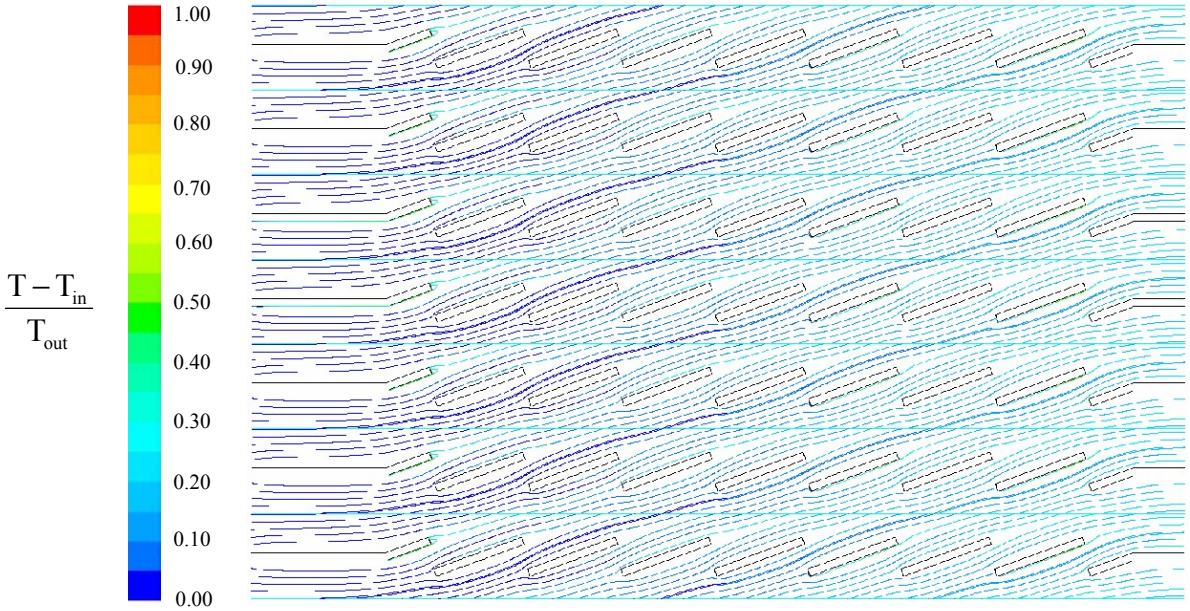

Figure 6.3 Predicted streamlines through the $F_p/L_p = 0.91$, $\theta = 20°$ model geometry at $Re_{Lp} = 1016$.

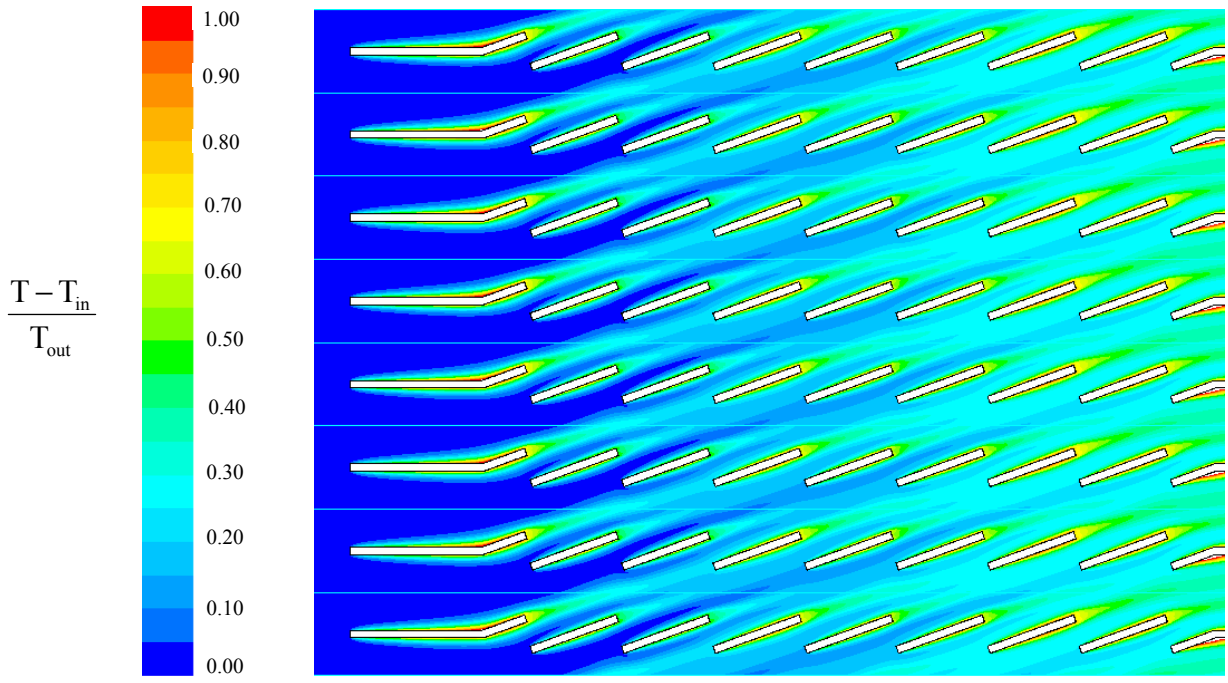

Figure 6.4 Predicted temperature contours through the $F_p/L_p = 0.91$ model geometry at $Re_{Lp} = 1016$.

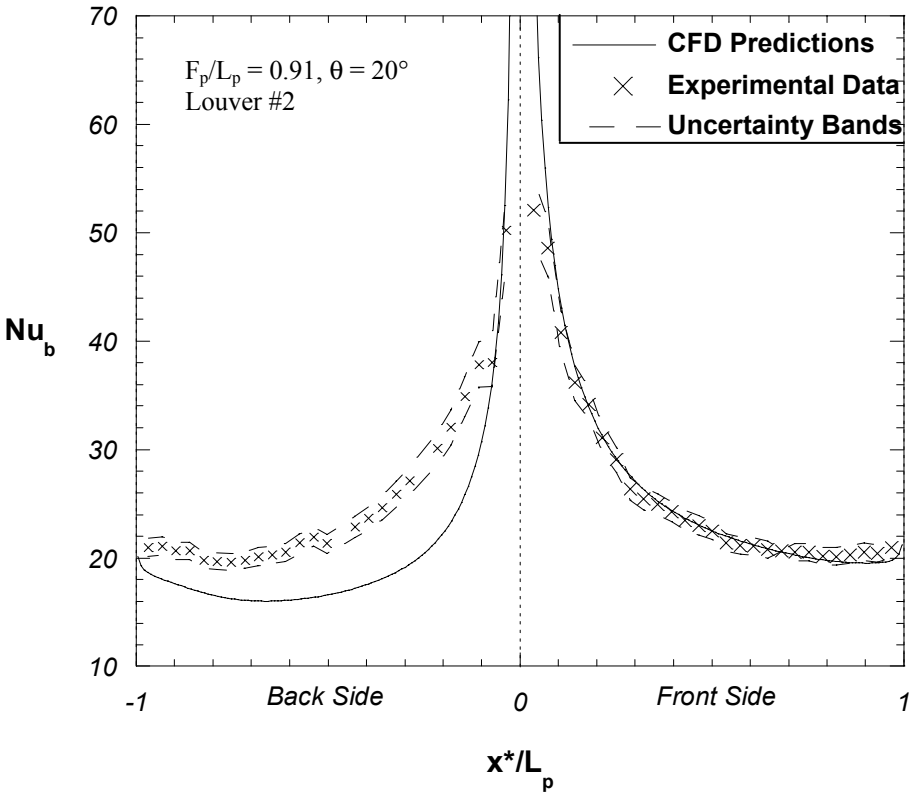

Figure 6.5 Comparison of the experimental data and the CFD predicted data of the Nusselt number based on the bulk flow temperature at louver 2 for the $F_p/L_p = 0.91$, $\theta = 20°$ model at $Re_{Lp} = 1016$.

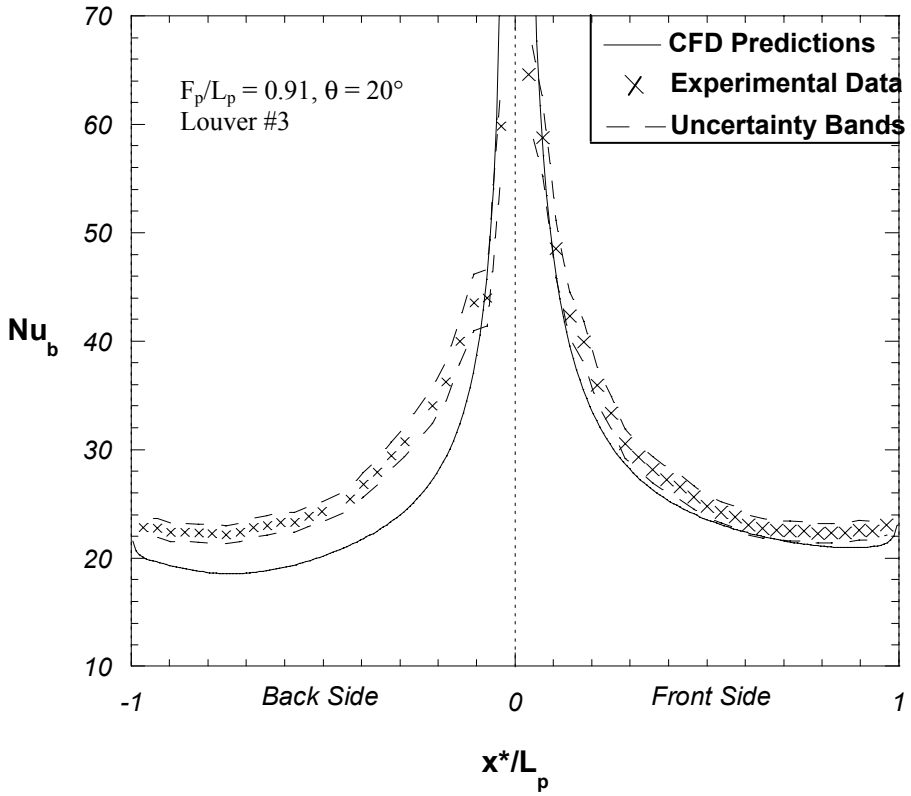

Figure 6.6 Comparison of the experimental data and the CFD predicted data of the Nusselt number based on the bulk flow temperature at louver 3 for the $F_p/L_p = 0.91$, $\theta = 20°$ model at $Re_{Lp} = 1016$.

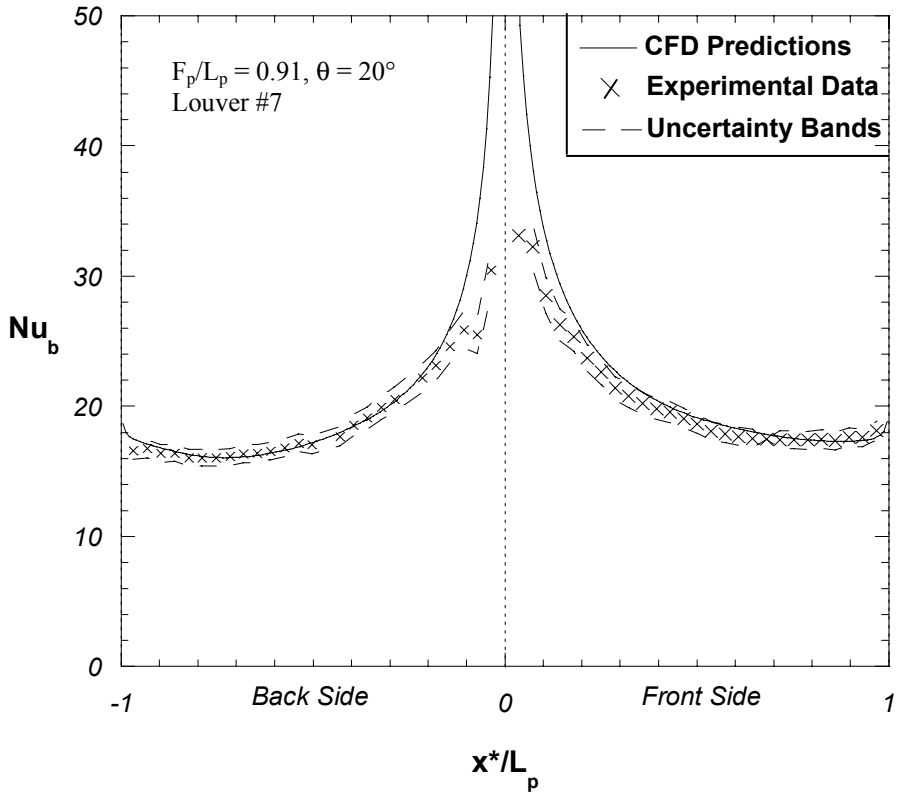

Figure 6.7 Comparison of the experimental data and the CFD predicted data of the Nusselt number based on the bulk flow temperature at louver 7 for the $F_p/L_p = 0.91$, $\theta = 20°$ model at $Re_{Lp} = 1016$.

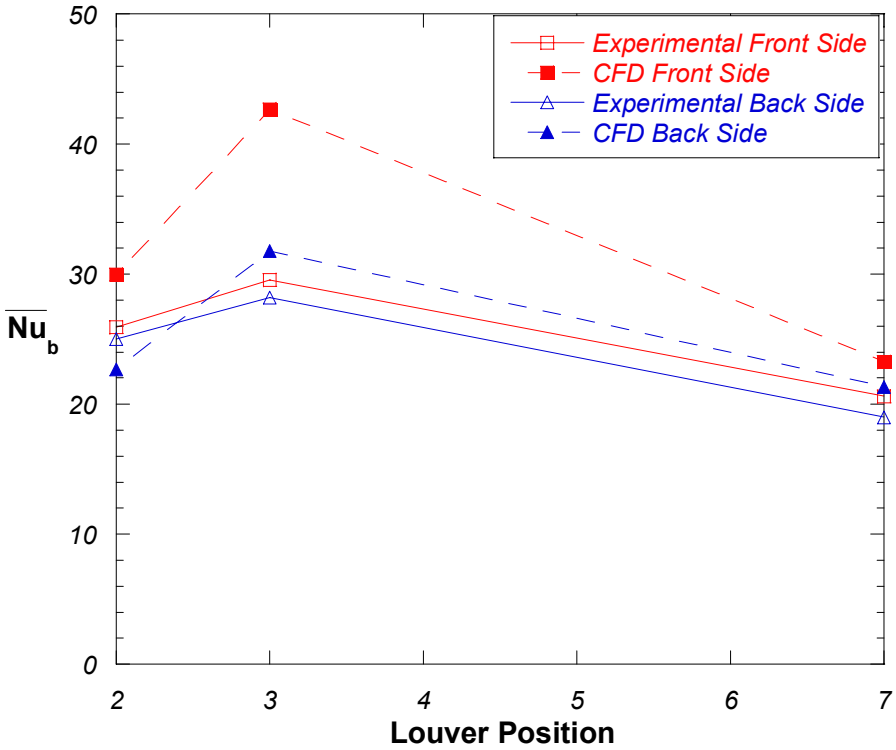

Figure 6.8 Predicted and experimentally measured average Nusselt numbers based on the bulk flow temperature for both sides of louvers 2, 3, and 7 for the $F_p/L_p = 0.91$, $\theta = 20°$ model at $Re_{Lp} = 1016$.

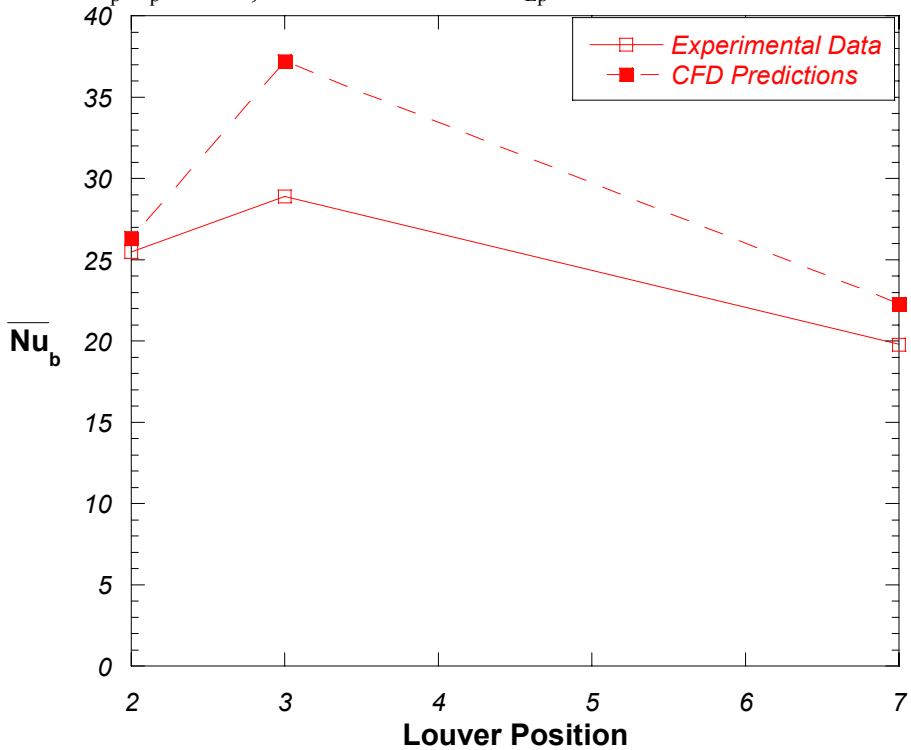

Figure 6.9 Predicted and experimentally measured average Nusselt numbers (averaged over front and back side) based on the bulk flow temperature on louvers 2, 3, and 7 for the $F_p/L_p = 0.91$, $\theta = 20°$ model at $Re_{Lp} = 1016$.

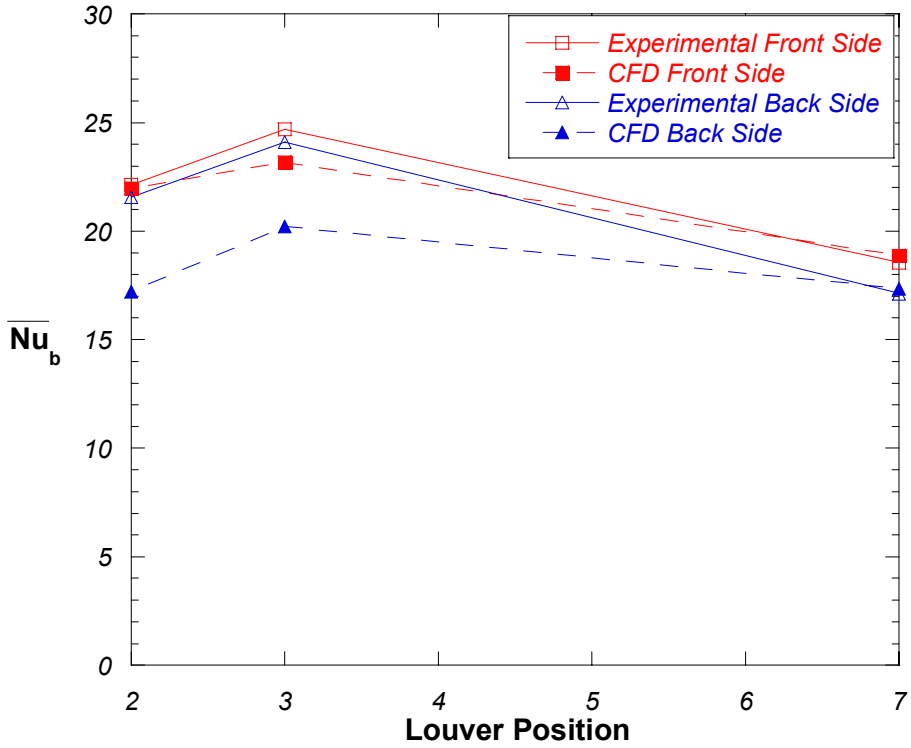

Figure 6.10 Predicted and experimentally measured average Nusselt numbers based on the bulk flow temperature calculated for $0.25 < x^*/L_p < 1.00$ for the $F_p/L_p = 0.91$, $\theta = 20°$ model at $Re_{Lp} = 1016$.

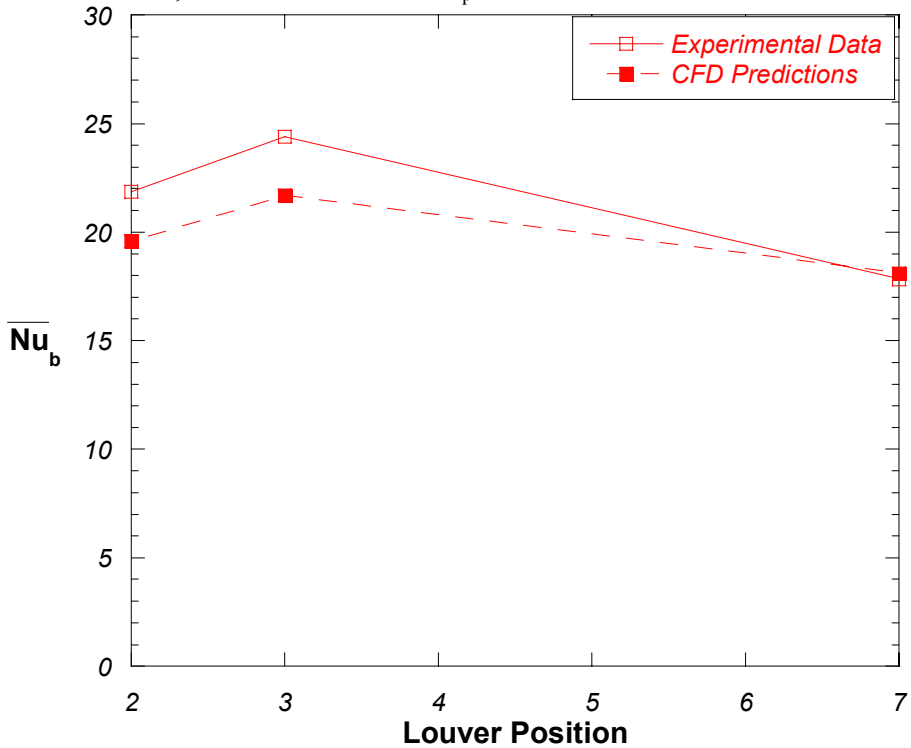

Figure 6.11 Predicted and experimentally measured average Nusselt numbers (averaged on front and back) based on bulk flow temperature calculated for $0.25 < x^*/L_p < 1.00$ for $F_p/L_p = 0.91$, $\theta = 20°$ model at $Re_{Lp} = 1016$.

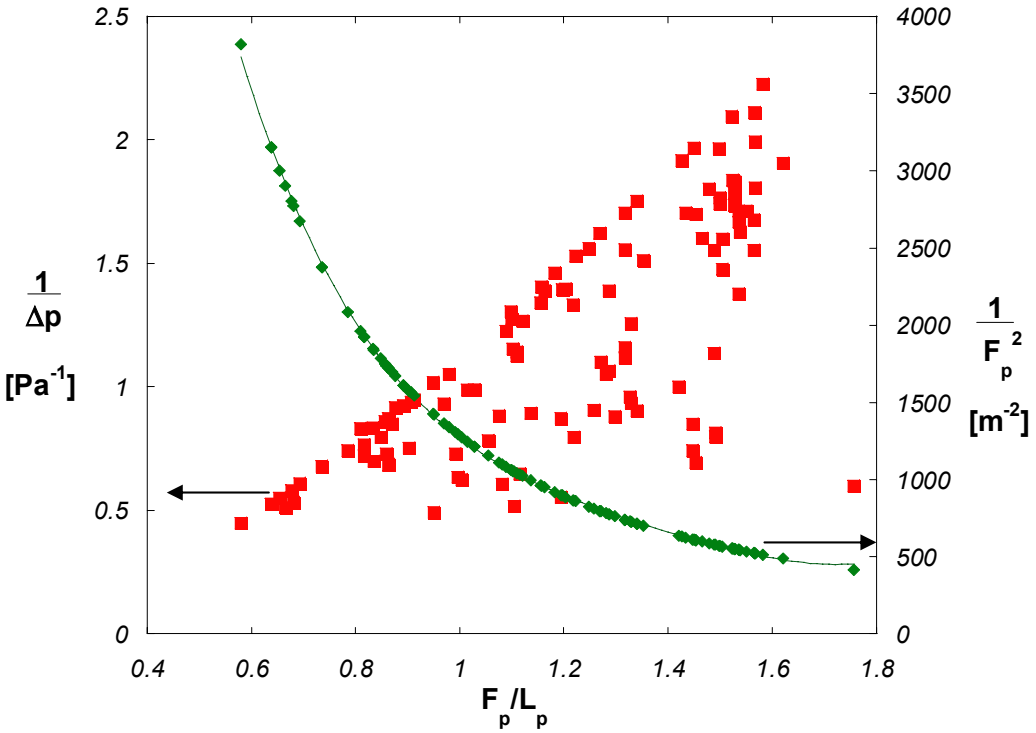

Figure 6.12 CFD optimization results with the optimization function shown as two parts.

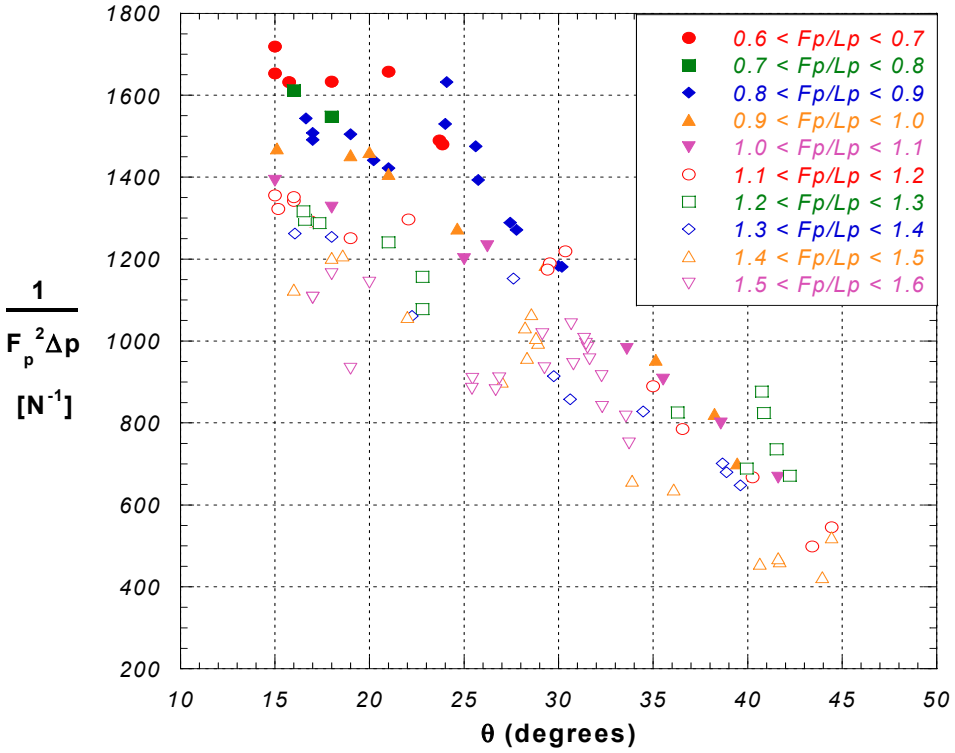

Figure 6.13 CFD optimization results showing the louver angle effect on the optimization function.

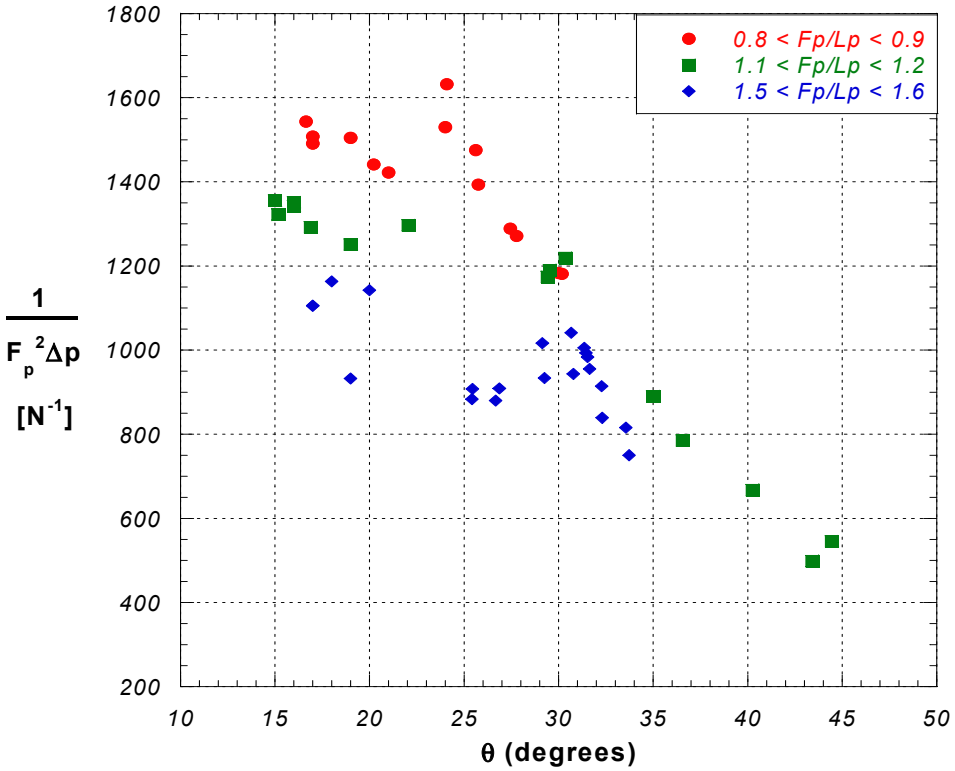

Figure 6.14 CFD optimization results showing the louver angle effect on the optimization function for selected F_p/L_p bands.

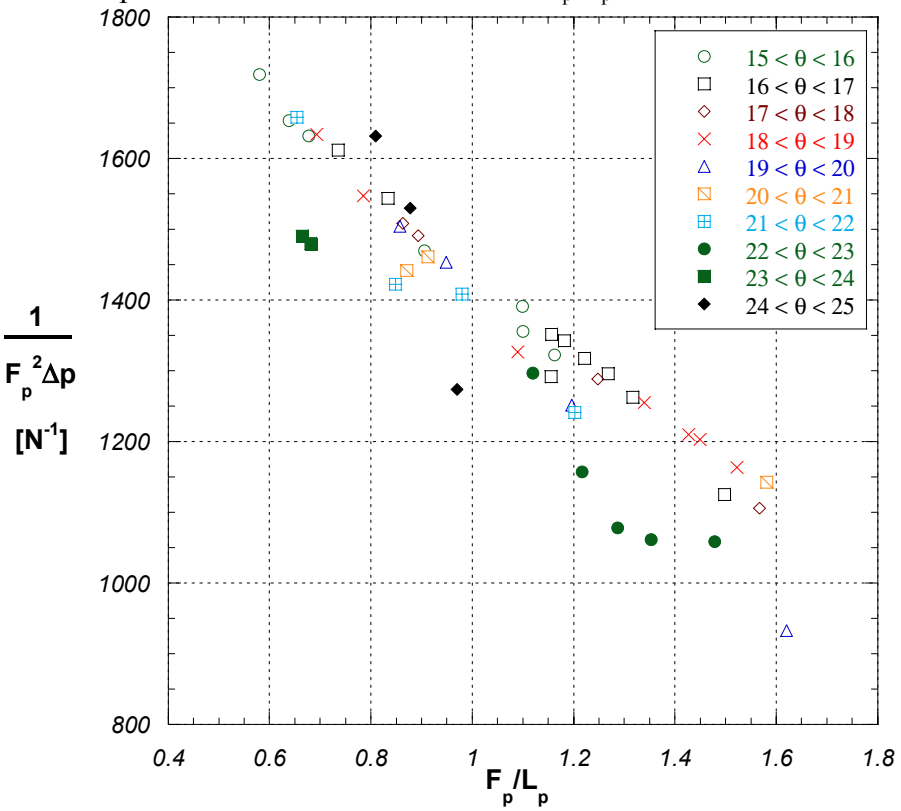

Figure 6.15 CFD optimization results showing the effect of F_p/L_p on the optimization function for $15° < \theta < 25°$.

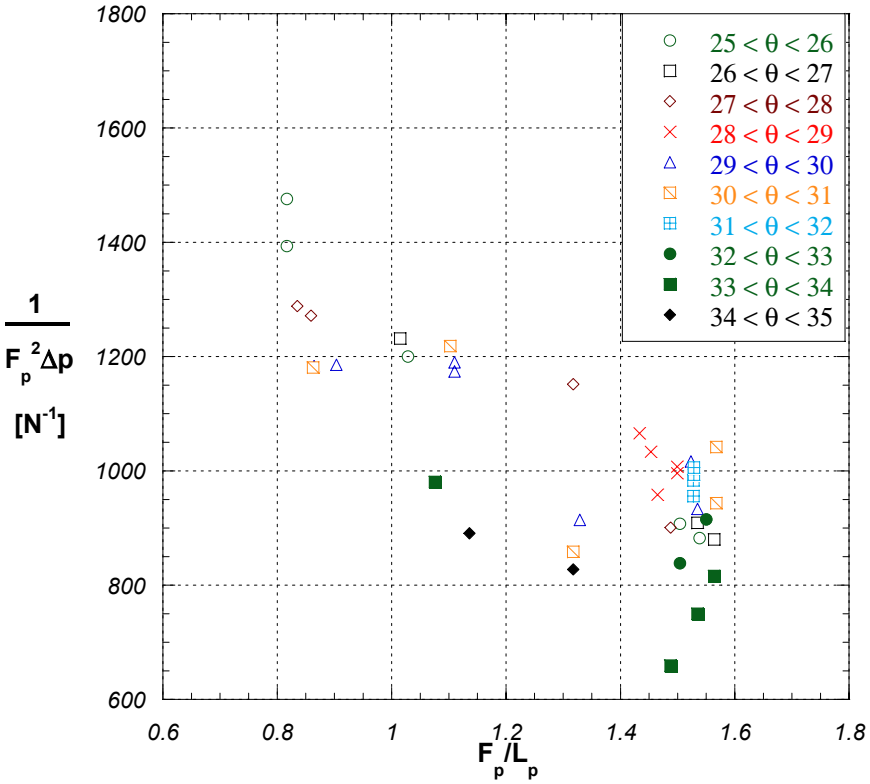

Figure 6.16 CFD optimization results showing the effect of F_p/L_p on the optimization function for $25° < \theta < 35°$.

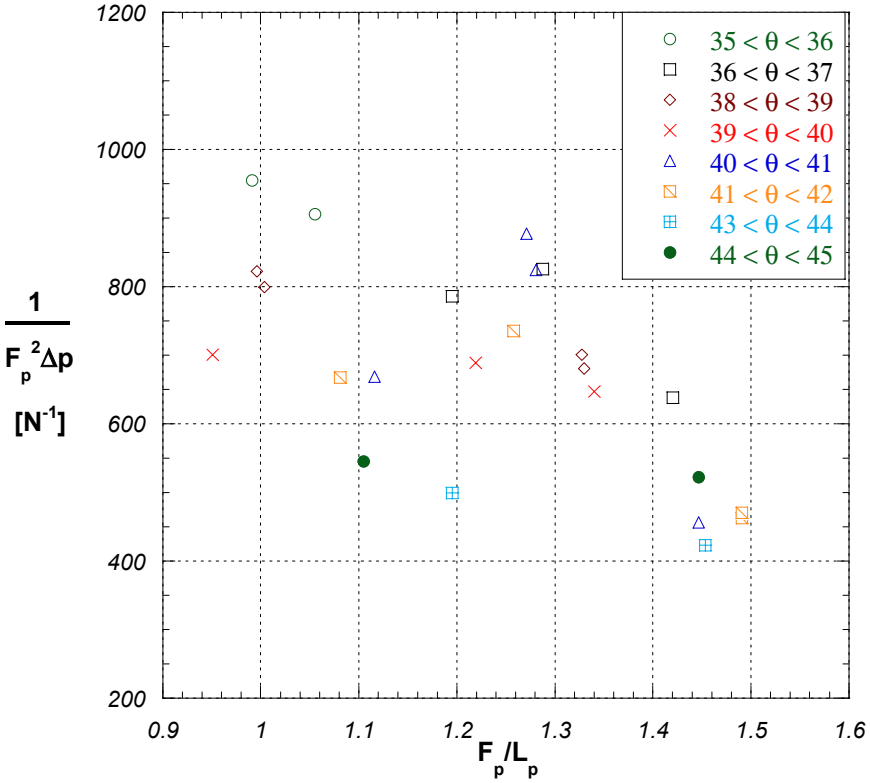

Figure 6.17 CFD optimization results showing the effect of F_p/L_p on the optimization function for $35° < \theta < 45°$.

Chapter 7

Conclusions and Recommendations for Future Work

As shown in detail throughout this entire document, an experimental study was performed to measure the local heat transfer coefficients for three louver geometries. The findings from this study were compared with the results obtained by Lyman (2000) for six other louver geometries and an optimal geometry was found and recommended for each Reynolds number. In parallel with this experimental investigation, a computational optimization study was performed using a combination of optimization and computational fluid dynamics packages. The studied louver arrays were representative of two-dimensional louver geometries found in many louvered fin heat exchangers used in the automotive industry.

Detailed heat transfer coefficients were measured on louver surfaces with a constant surface heat flux. The measurements were taken for three inlet velocities, which corresponded to Re_{Lp} = 230, 370, and 1016. The heat transfer coefficients presented throughout this document were computed using two different reference temperatures. The first reference temperature used was the bulk flow temperature at the inlet to a particular louver position, which was obtained by performing an energy balance. Using the bulk flow temperature as the reference temperature the combined effects of the thermal and flow field were identified. The second reference temperature used was the measured adiabatic wall temperature. This temperature was obtained by performing a second experiment in which the louver of interest had a zero heat flux boundary condition imposed. The adiabatic wall temperature as the reference temperature allowed the effects of the thermal field to be distinguished from that of the flow field effects.

The parallel optimization study that was performed was completed for a two-dimensional model that replicated the experiments using a constant heat flux boundary condition applied to the louvers. Unlike the experiments, the optimization study was performed for only one inlet velocity, which corresponded to Re_{Lp} = 1016. The optimization function was defined with three goals in mind. The first of these was to maximize the amount of heat dissipated by the louvered fins. The second goal was to minimize volume of the heat exchanger core allowing it to take up less space and weigh less. The third goal of the study was to minimize the pumping power required for the

louver array. The optimal geometry was found to be one with a small fin pitch and a small louver angle. The current chapter will summarize the primary findings of the study and give recommendations for future research in louvered fin heat exchanger studies.

7.1 Summary of Heat Transfer Measurements

Several very interesting trends were apparent after analyzing the data obtained from this large scale louver study. Using the adiabatic wall temperature as the reference temperature in defining the heat transfer coefficient allowed the effects of the flow field, such as separation and boundary layer thickness, to be isolated and studied. From this parameter, several important observations were made and they are as follows:

1.) Flow field effects are much more apparent at the entrance region of the louver array and these effects are much more pronounced for louver models with large louver angles and large fin pitches.

2.) The transition of the flow from duct directed to louver directed depends on several parameters. The flow becomes louver directed in a shorter streamwise distance at large louver angles. It takes a longer streamwise distance for the flow to become fully louver directed in models with a large fin pitch. Finally, the flow remains duct directed over a longer streamwise distance at lower Reynolds numbers.

3.) The Colburn factor based on the adiabatic wall temperature collapses to a single curve for louvers in the fully developed region in models with a common fin pitch and louver angle. This effect shows that the flow field does not affect the boundary layer development along a louver surface after the flow becomes fully louver directed.

Using a non-dimensional adiabatic wall temperature, several trends were also deduced. These trends were indication of the thermal field surrounding a louver surface. The surface area of the entrance louver is twice as large as that of the downstream louvers; therefore, the thermal wakes that begin at the entrance louver are heated to levels much higher than the downstream louvers due to the constant heat flux boundary

condition. The thermal wakes that impact the surface of the downstream louvers have an adverse effect on the heat transfer from that surface. Throughout this study, the effect of the thermal wakes on the heat transfer from a surface was determined using two parameters. The first parameter used was the non-dimensional adiabatic wall temperature, which was simply a ratio of the adiabatic wall temperature to the bulk temperature. The other parameter used to measure the impact of the thermal wakes was the heat transfer coefficient based on the bulk flow temperature. Using these parameters, several observations were made concerning the thermal wakes and they are as follows:

1.) The thermal wakes emanating from the entrance louver do not follow the louver angle at large fin pitches because the flow tends to remain duct directed. The wakes are re-directed further downstream by the duct directed flow entering the louver passages thereby making their angle of progression slightly less than the louver angle.

2.) The thermal wakes maintain form further downstream at higher Reynolds numbers.

The best performing louver geometry was found to be Reynolds number dependent. For the lower Reynolds number of Re_{Lp} = 230 and 370, the best performing geometry based on the Colburn factor defined by the bulk flow temperature was the F_p/L_p = 1.52, $\theta = 27°$ model. The worst performing model for the same Reynolds numbers was the F_p/L_p = 0.54, $\theta = 20°$ model. For the highest Reynolds number tested of Re_{Lp} = 1016, the best performing model was the F_p/L_p = 0.91, $\theta = 39°$ model while the worst performing model was the F_p/L_p = 0.91, $\theta = 27°$ model.

Interestingly, Suga and Aoki (1991) predicted the optimal geometry, from a perspective of combined heat transfer and pressure drop, to be the F_p/L_p =0.50, $\theta = 20°$ model. As mentioned above, for Re_{Lp} = 230 and 370, the worst performing geometry was found to be the F_p/L_p =0.54, $\theta = 20°$ louver geometry, which appears to disagree with the conclusion of Suga and Aoki (1991). It is important to note that the current study only focused on the heat transfer performance of a louver array and neglected the pressure drop through the array. As mentioned in Chapter 1, the correlation by Chang and Wang (1997) predicted that the F_p/L_p = 0.91, $\theta = 39°$ model would be the best

performer, which agrees with the experimental data discussed earlier. It was shown that the $F_p/L_p = 0.91$, $\theta = 39°$ model was the optimal performance for $Re_{Lp} = 1016$. Sunden and Svantesson (1990) predicted through their correlation that the $F_p/L_p = 1.52$, $\theta = 39°$ would be the best performing model. The current study showed that this model was not the best performing model from a heat transfer perspective for any of the tested Reynolds numbers.

7.2 Summary of Optimization Study

As noted throughout the previous section of this report, an optimization study was performed on the louver geometries in an effort to determine the optimal louver array geometry. The current study showed that a combined CFD-optimization approach was a viable technique for maximizing louvered fin heat exchanger performance. For the optimization function that was defined, the optimal design was a very strong function of the fin pitch for the constraints used during this study. The effect of the louver angle on the optimization function was minimal for louver angles less than 20°. However, as the louver angle was increased beyond 20°, the effect was substantial. High louver angles decrease the heat exchanger performance. For these reasons, the best performing geometry for the optimization function that was used was one with small fin pitches and small louver angles. As mentioned in the previous section, Suga and Aoki showed that the optimal geometry would be one with a small fin pitch and small louver angle from a combined perspective of heat transfer and pressure drop. Their conclusion agrees with the results from the current optimization study.

7.3 Recommendations for future work

This study presented the spatially resolved heat transfer coefficients for three louver geometries. The heat transfer results from the current study were then compared with the six models tested by Lyman (2000) during his very similar study. The combination of these two studies gave a representative experimental database of several louver geometries. Future experimental work should focus on altering the fluid mechanics along the louver surface to increase the heat transfer from those surfaces. There are several possible options for doing this such as incorporating a dimpled surface

into the design of the louvers, or small delta fins located at the leading edge of the louvers. The most obvious drawback of employing these designs is the increased pressure drop through the array.

The current study also showed that the heat transfer performance of the arrays can be accurately predicted using CFD and that an optimization technique is viable approach to designing louvered fin heat exchangers. Future efforts at using these techniques should incorporate the adiabatic wall temperature into the optimization function. The primary goal of this effort would be to minimize the average adiabatic wall temperature throughout the entire array. This would help to eliminate the interaction of thermal wakes from the entrance louver with subsequent downstream louver surfaces. Any of the aforementioned efforts would help to maximize the overall thermal performance of a compact louvered fin heat exchanger.

References

Achaichia, A. and Cowell, T. A. (1988) "Heat Transfer and Pressure Drop Characteristics of Flat Tube and Louvered Plate Fin Surfaces," *Experimental Thermal and Fluid Science,* Vol.1, pp. 147-157.

Beauvais, F.N. (1965), "An Aerodynamic Look at Automotive Radiators", SAE Paper No. 650470.

Chang, Y. and Wang, C. (1997) "A Generalized Heat Transfer Correlation for Louver Fin Geometry," *International Journal of Heat and Mass Transfer*, Vol. 40, No. 3, pp. 533-544.

Davenport, C.J. (1980) "Heat Transfer and Fluid Flow in Louvered Triangular Ducts", PhD. Thesis, CNAA, Lanchester Polytechnic, Coventry, UK, 1980.

Davenport, C. J. (1983) "Correlation for Heat Transfer and Flow Friction Characteristics of Louvered Fin", *AIChE Symp. Ser.* 79, 19-27.

Fluent User's Guide (1998) Release 5.0, Fluent, Inc., Lebanon, New Hampshire.

Huihua, Z., and Xuesheng L. (1989) "The Experimental Investigation of Oblique Angles and Interrupted Plate Lengths for Louvered Fins in Compact Heat Exchangers," *Experimental Thermal and Fluid Science*, Vol. 2, pp. 100-106.

Incropera, F.P., and DeWitt, D.P., *Fundamentals of Heat and Mass Transfer*, 4th ed., John Wiley & Sons, New York, 1996.

Kline, S. J., and McClintock, F. A. (Jan. 1953) "Describing Uncertainties in Single Sample Experiments," *Mech. Engineering*, pp. 3-8.

Kurosaki, Y., Kashiwagi, T., Kobayashi, H., Uzuhashi, H., and Tang, S. (1988) "Experimental Study on Heat Transfer from Parallel Louvered Fins by Laser Holographic Interferometry," *Experimental Thermal and Fluid Science*, Vol. 1 pp. 59-67.

Lethander, A.T. (2003), PhD. Thesis, Mechanical Engineering, Virginia Polytechnic and State University.

Lyman, A.C. (2000) "Spatially Resolved heat Transfer Studies in Louvered Fins for Compact Heat Exchangers," *Master of Science Thesis*, Mechanical Engineering, Virginia Polytechnic and State University.

Moffat, R. J. (1998) "What's New in Convective Heat Transfer?," *International Journal of Heat and Fluid Flow*, Vol. 19, pp. 90-101.

Rugh, J. P., Pearson, J. T., and Ramadhyani, S. (1992) "A Study of a Very Compact Heat Exchanger Used for Passenger Compartment Heating in Automobiles," *Compact Heat Exchangers for Power and Process Industries*, ASME Symp. Ser., HTD-Vol. 201, pp. 15-24 ASME, New York.

Sparrow, E. M. and Hajiloo, A. (1980) "Measurements of Heat Transfer and Pressure Drop for an Array of Staggered Plates Aligned Parallel to an Air Flow," *Journal of Heat Transfer*, Vol. 102, pp. 426-432.

Springer, M. E. (1998a) "Flowfield Studies in Louvered Fins Relevant to Compact Heat Exchangers," *Master of Science Thesis*, Mechanical Engineering, University of Wisconsin.

Springer, M. E., and Thole, K. A. (1998b) "Experimental Design for Flowfield Studies of Louvered Fins," *Experimental Thermal and Fluid Science*, Vol. 18, pp. 258-269.

Springer, M. E. and Thole, K. A. (1999) "Entry Region of Louvered Fin Heat Exchangers," *Experimental Thermal and Fluid Science*, Vol. 19, pp. 223-232.

Suga, K. and Aoki, H. (1991) "Numerical Study on Heat Transfer and Pressure Drop in Multilouvered Fins," *ASME/JSME Thermal Engineering Proceedings*, Vol. 4., pp. 361-368.

Webb, R. L., and Jung, S. H. (1992) "Air-Side Performance of Enhanced Brazed Aluminum Heat Exchangers," *ASHRAE Trans.* 98, Pt 2, pp. 391-401.

Zhang, L. W., Balachandar, S., Tafti, D. K., Najjar, F. M. (1997) "Heat Transfer Enhancement mechanisms in Inline and Staggered Parallel-Plate in Heat Exchangers," *International Journal of Heat and Mass Transfer*, Vol. 40, No. 10, pp. 2307-2325.

Zhang, X., Tafti, D.K. (2001) "Classification and Effects of Thermal Wakes on Heat Transfer in Multilouvered Fins," *International Journal of Heat and Mass Transfer*, Vol. 44, No. 13, pp. 2461-2473

Vita

Ryan Stephan was born in Massillon, Ohio on 10 June 1978. Ryan became a huge sports fan at a very early age. Due to his close proximity to Cleveland, Ohio, he took a liking to the Cleveland Browns and Indians. Unfortunately, he had to endure some pretty rough seasons of Cleveland Indians baseball and he also had to deal with the loss of his beloved Cleveland Browns to Baltimore. Throughout his life in Massillon, he enjoyed playing many sports both organizationally and at the park near his home. Ryan became very competitive at a very early age and he attributes that competitiveness to his success in the academic arena.

Ryan began college in the fall of 1996 at Tri State University in Angola, Indiana and at first, he struggled with the new environment. At the end of his first year of college, he realized that he missed his girlfriend too much and he had to move closer to her. That fall, he enrolled in Ohio Northern University in Ada, Ohio, which was much closer to the girl that he met in seventh grade English class. Ryan settled into his new life at Ohio Northern rather quickly and graduated with a Bachelor's of Science degree in Mechanical Engineering on 16 May 2000.

On month after graduation, on 17 June 2000, Ryan married his high school sweetheart Kim Stephan (formerly Sheil). Ryan and Kim moved to Blacksburg, Virginia only 2 days after their wedding and Ryan, with Kim's never ending support, began his Master's degree at Virginia Tech. In January of 2001, Ryan was offered a job at NASA Langley Research Center in Hampton, Virginia and he accepted immediately.

Ryan plans to return to Virginia Tech to receive his PhD in Mechanical Engineering in the very near future.